

# POLITECNICO DI MILANO

Facoltà di Ingegneria Industriale

Corso di Laurea Specialistica in Ingegneria Spaziale



CubeSat formation flying mission as Wi-Fi data transmission and GPS  
based relative navigation technology demonstrator

Supervisor: Michèle LAVAGNA

Authors:

Alessandro Ferrario      matr. 725016

Beatrice Furlan          matr. 708421

Academic Year 2010-2011



## Summary

<b>List of figures</b> .....	<b>VII</b>
<b>List of tables</b> .....	<b>XIV</b>
<b>List of acronyms</b> .....	<b>XVII</b>
<b>Abstract</b> .....	<b>XIX</b>
<b>Sommario</b> .....	<b>XX</b>
<b>Chapter 1 - Introduction</b> .....	<b>1</b>
Section 1.1 - New trends in space system technology .....	1
Section 1.2 - Objectives .....	2
<i>Subsection 1.2.1 - Mission requirements</i> .....	2
Section 1.3 - Wireless technology in space.....	3
<i>Subsection 1.3.1 - State of the art and related mission</i> .....	3
<i>Subsection 1.3.2 - Wireless technology application within Inter-Satellite and Intra-Satellite Networking</i> .....	5
Section 1.4 - GPS implementation in Formation Flying.....	5
<i>Subsection 1.4.1 - GPS in LEO</i> .....	5
<i>Subsection 1.4.2 - Formation flying, definitions and main characteristics</i> .....	7
<i>Subsection 1.4.3 - Guidance, Navigation and Attitude Control with GPS within a formation</i> .....	10
<i>Subsection 1.4.4 - Low accuracy GPS application in LEO close formations</i> .....	12
Section 1.5 - CubeSat package characteristics, low cost and power COTS.....	13
<i>Subsection 1.5.1 - Technological demonstrator: CubeSat platform</i> .....	13
<i>Subsection 1.5.2 - PCI-104 form factor characteristics</i> .....	13
<i>Subsection 1.5.3 - Power generation</i> .....	14
<i>Subsection 1.5.4 - Related mission: CubeSat technological demonstrator</i> .....	15
Section 1.6 - Work plan .....	16
<i>Subsection 1.1.1 - Mission constrains</i> .....	16
<i>Subsection 1.6.1 - Paper structure</i> .....	16
<b>Chapter 2 - Payload design</b> .....	<b>19</b>
Section 2.1 - Wireless inter-satellite network .....	19
<i>Subsection 2.1.1 - ISL architecture</i> .....	19

<i>Subsection 2.1.2 - Component list</i> .....	20
<i>Subsection 2.1.3 - ISL dimensioning</i> .....	21
<i>Subsection 2.1.4 - Transceiver trade off (ISL)</i> .....	27
Section 2.2 - Wireless Temperature sensor .....	27
<i>Subsection 2.2.1 - SENSEOR TSE ASI0 Wireless Temperature SAW Sensor</i> .....	27
<i>Subsection 2.2.2 - SENSEOR interrogation unit</i> .....	29
<i>Subsection 2.2.3 - Comments</i> .....	29
<i>Subsection 2.2.4 - Alternative transceiver</i> .....	29
<b>Chapter 3 - Mission analysis and system architecture .....</b>	<b>31</b>
Section 3.1 - Operative orbit definition .....	31
<i>Subsection 3.1.1 - Mission analysis requirements</i> .....	31
<i>Subsection 3.1.2 - Sun-synchronous conditions</i> .....	31
Section 3.2 - Launch opportunities.....	33
<i>Subsection 3.2.1 - Launcher interface</i> .....	34
<i>Subsection 3.2.2 - Short term scheduled launches</i> .....	35
<i>Subsection 3.2.3 - ADM-Aeolus</i> .....	36
Section 3.3 - Launch selection criteria .....	37
<i>Subsection 3.3.1 - Atmospheric drag</i> .....	37
<i>Subsection 3.3.2 - Continuous sun visibility propagation including drag</i> .....	39
<i>Subsection 3.3.3 - Preliminary analysis for spacecraft charging</i> .....	40
<i>Subsection 3.3.4 - Lifetime</i> .....	42
Section 3.4 - Relative position control strategy.....	44
<i>Subsection 3.4.1 - Disturbance mitigation strategies</i> .....	44
<i>Subsection 3.4.2 - Operative relative trajectory definition</i> .....	45
<i>Subsection 3.4.3 - Risk reduction strategies</i> .....	45
<i>Subsection 3.4.4 - Relative control architecture trade-off</i> .....	46
<i>Subsection 3.4.5 - Commissioning and formation acquisition</i> .....	47
<i>Subsection 3.4.6 - Relative attitude configuration</i> .....	49
Section 3.5 - System configuration.....	50
<i>Subsection 3.5.1 - Critical issues</i> .....	50
<i>Subsection 3.5.2 - CubeSat X-U bus trade-offs</i> .....	50
<i>Subsection 3.5.3 - Summary: Baseline definition</i> .....	52
<b>Chapter 4 - Relative position determination and control.....</b>	<b>53</b>

Section 4.1 - Formation control requisites .....	53
<i>Subsection 4.1.1 - Guidance Navigation and Control subsystem requisites .....</i>	<i>53</i>
<i>Subsection 4.1.2 - Propulsion subsystem requisites .....</i>	<i>53</i>
Section 4.2 - Uncontrolled dynamics analysis .....	53
<i>Subsection 4.2.1 - Disturbance accelerations within formation.....</i>	<i>53</i>
<i>Subsection 4.2.2 - Uncontrolled relative dynamic.....</i>	<i>55</i>
Section 4.3 - Guidance, Navigation and Control with GPS .....	58
<i>Subsection 4.3.1 - Single frequency spaceborne GPS receivers trade-off.....</i>	<i>58</i>
<i>Subsection 4.3.2 - GPS position measurement implementation .....</i>	<i>60</i>
<i>Subsection 4.3.3 - Discrete-time filtering .....</i>	<i>60</i>
<i>Subsection 4.3.4 - Kalman filtering.....</i>	<i>61</i>
<i>Subsection 4.3.5 - Digital Implementation .....</i>	<i>62</i>
Section 4.4 - Optimal control .....	64
<i>Subsection 4.4.1 - Discrete time implementation .....</i>	<i>64</i>
<i>Subsection 4.4.2 - Optimum control with integral feedback.....</i>	<i>65</i>
Section 4.5 - Propulsion subsystem, relative position control .....	68
<i>Subsection 4.5.1 - Chemical thrusters .....</i>	<i>68</i>
<i>Subsection 4.5.2 - Pulsed Plasma Thrusters.....</i>	<i>69</i>
<i>Subsection 4.5.3 - Analyzed propulsion subsystems.....</i>	<i>71</i>
<i>Subsection 4.5.4 - Simulation implementation.....</i>	<i>72</i>
<i>Subsection 4.5.5 - Actuation with Cold Gas Micropropulsion.....</i>	<i>73</i>
<i>Subsection 4.5.6 - Actuation with Pulsed Plasma Thruster.....</i>	<i>73</i>
Section 4.6 - Collision avoidance strategy .....	76
<i>Subsection 4.6.1 - Passive collision avoidance nominal trajectory.....</i>	<i>76</i>
<i>Subsection 4.6.2 - Effects on control performance, simulation results .....</i>	<i>76</i>
Section 4.7 - Formation acquisition and reconfigurations .....	79
<i>Subsection 4.7.1 - Relative dynamic after second spacecraft releasing.....</i>	<i>79</i>
<i>Subsection 4.7.2 - Formation acquisition with continuous control.....</i>	<i>79</i>
<i>Subsection 4.7.3 - Formation acquisition with impulsive control .....</i>	<i>83</i>
<i>Subsection 4.7.4 - Reconfigurations with continuous control .....</i>	<i>83</i>
Section 4.8 - Effects of parameters on control performance.....	86
<i>Subsection 4.8.1 - Separation effects.....</i>	<i>86</i>
<i>Subsection 4.8.2 - Altitude variation effects.....</i>	<i>87</i>

Section 4.9 - Summary .....	88
<b>Chapter 5 - Attitude Determination and Control subsystem.....</b>	<b>91</b>
Section 5.1 - Pointing requisites .....	91
Section 5.2 - Attitude control architectures .....	91
<i>Subsection 5.2.1 - Maximum torques estimation.....</i>	<i>91</i>
<i>Subsection 5.2.2 - Some considerations on passive stabilization.....</i>	<i>92</i>
<i>Subsection 5.2.3 - Attitude control possible solutions.....</i>	<i>92</i>
<i>Subsection 5.2.4 - Disturbance torques at nominal attitude .....</i>	<i>93</i>
<i>Subsection 5.2.5 - Free dynamic .....</i>	<i>95</i>
Section 5.3 - Attitude determination.....	95
<i>Subsection 5.3.1 - Magnetometer.....</i>	<i>96</i>
<i>Subsection 5.3.2 - Sun sensor.....</i>	<i>97</i>
<i>Subsection 5.3.3 - Determination method .....</i>	<i>98</i>
<i>Subsection 5.3.4 - Star tracker .....</i>	<i>99</i>
Section 5.4 - Attitude control .....	100
<i>Subsection 5.4.1 - Dynamic model for nadir-pointing attitude spacecraft .....</i>	<i>100</i>
<i>Subsection 5.4.2 - Discrete time linear quadratic regulator implementation .....</i>	<i>101</i>
<i>Subsection 5.4.3 - Actuators trade off.....</i>	<i>102</i>
<i>Subsection 5.4.4 - Operative mode.....</i>	<i>104</i>
<i>Subsection 5.4.5 - Thrust misalignment disturbances.....</i>	<i>106</i>
<i>Subsection 5.4.6 - Desaturation strategy .....</i>	<i>108</i>
<i>Subsection 5.4.7 - Detumbling, commissioning mode.....</i>	<i>109</i>
<i>Subsection 5.4.8 - Altitude variation effects.....</i>	<i>111</i>
Section 5.5 - Final considerations.....	112
<b>Chapter 6 - On-Board Data Handling and Communication subsystem .....</b>	<b>113</b>
Section 6.1 - On Board Data Handling subsystem .....	113
Section 6.2 - Telemetry Tracking & Command subsystem.....	113
<i>Subsection 6.2.1 - Satellite – Ground station link.....</i>	<i>114</i>
<i>Subsection 6.2.2 - Inter-Satellite Link backup .....</i>	<i>120</i>
<b>Chapter 7 - Power generation and Thermal Control subsystems .....</b>	<b>121</b>
Section 7.1 - Components breakdown .....	121
Section 7.2 - Operative Modes .....	122
Section 7.3 - Electric Power Subsystem .....	124

<i>Subsection 7.3.1 - Power solar panel generation and battery sizing</i> .....	124
<i>Subsection 7.3.2 - Power Budget</i> .....	125
Section 7.4 - Thermal Control Subsystem .....	127
<b>Chapter 8 - System overview</b> .....	<b>133</b>
Section 8.1 - Configuration requisites.....	133
<i>Subsection 8.1.1 - Components masses and envelopes</i> .....	133
<i>Subsection 8.1.2 - System Chart</i> .....	133
Section 8.2 - Primary structure .....	134
<i>Subsection 8.2.1 - CubeSat structures</i> .....	134
<i>Subsection 8.2.2 - Propulsion pointing and structural integration</i> .....	135
Section 8.3 - Secondary structures.....	136
<i>Subsection 8.3.1 - Reaction wheels</i> .....	137
<i>Subsection 8.3.2 - WiFi payload</i> .....	137
<i>Subsection 8.3.3 - GPS receiver</i> .....	138
Section 8.4 - Spacecraft configuration .....	138
Section 8.5 - Mass & Cost budgets .....	140
<i>Subsection 8.5.1 - Single spacecraft mass and cost budgets</i> .....	140
<i>Subsection 8.5.2 - Launch cost budget</i> .....	142
<i>Subsection 8.5.3 - Risks assessment</i> .....	142
<b>Chapter 9 - Conclusion</b> .....	<b>143</b>
Section 9.1 - Considerations and analysis results .....	143
<i>Subsection 9.1.1 - Formation performances</i> .....	143
<i>Subsection 9.1.2 - CubeSat integration</i> .....	144
<i>Subsection 9.1.3 - Wireless payloads</i> .....	144
Section 9.2 - Conclusion and next development.....	145
<b>Appendix A - Global Positioning System overview</b> .....	<b>i</b>
Section A.1 - Signal characteristics .....	i
Section A.1 - Signal processing .....	ii
<i>Subsection A.1.1 - Code Phase method</i> .....	ii
<i>Subsection A.1.2 - Carrier Phase method</i> .....	iii
Section A.2 - Coverage .....	iii
<b>Appendix B - Notions of relative position dynamics and adopted conventions</b> .....	<b>v</b>
Section B.1 - Relative rotating frame.....	v

<i>Subsection B.1.1 - Cartesian coordinates LVLH</i> .....	v
<i>Subsection B.1.2 - Curvilinear coordinates</i> .....	v
<i>Subsection B.1.3 - Relative orbital elements</i> .....	vi
Section B.2 - Unperturbed dynamic models .....	vi
<i>Subsection B.2.1 - Projected equation of motion</i> .....	vi
<i>Subsection B.2.2 - Hill-Clohessey-Wiltshire equations HCW</i> .....	vii
<i>Subsection B.2.3 - Tshaurer-Hempel equations</i> .....	viii
Section B.3 - Perturbed motion .....	ix
<i>Subsection B.3.1 - Gauss variational equation</i> .....	ix
<i>Subsection B.3.2 - J2 effect</i> .....	ix
<i>Subsection 9.2.1 - Commensurability condition</i> .....	x
<b>Appendix C - ADM-Aeolus PoliMi communication accesses</b> .....	<b>xi</b>
<b>Bibliography</b> .....	<b>xiii</b>



## List of figures

Figure 1.1 - Distributed spacecraft optical and RF systems concept with little or no structure to obtain wide aperture optical system [1].....	2
Figure 1.2 – From left to the right: NANOSAT-01 (INTA), FOTON-M3, OPTOS (INTA). ....	4
Figure 1.3 – NUTS satellite (left), STRaND satellite (center), Delfi-C3 (right).....	4
Figure 1.4 - Maximum theoretical Doppler frequency shift and shift rate on received GPS signal in LEO circular orbits .....	6
Figure 1.5 - Possible example relative trajectories in EH frame, obtainable varying phase difference between $\alpha_x$ . $\alpha_z$ in HCW solution, adopting example values: $\rho_x=4m$ , $\rho_y=-10m$ , $\rho_z=10m$ , .....	9
Figure 1.6 - PRISMA satellites and features .....	11
Figure 1.7 - FASTRAC (left), GRACE (center) and CHAMP (right) satellites artist’s impressions.....	12
Figure 1.8 – PC/104 modules package. Figure 1.9 – PCI-104 module front view.....	14
Figure 1.10 – Common EPS components: 3J solar cells 1U side (left), Li-Ion battery pack (center) and commercial Li-Po battery pack (right).....	14
Figure 1.11 – CanX satellite: CanX-1 (1U), CanX-2 (3U), CanX-4 (20x20x20 cm <sup>3</sup> ). .....	15
Figure 1.12 – RAX-1 and RAX-2 satellites. ....	15
Figure 1.13 - Main issues and relationship.....	16
Figure 2.1 – ISL possible network architectures: A) Client-server, B) Peer-to-Peer, C) Client-server and Peer-to-Peer, D) Hybrid Peer-to-Peer. ....	20
Figure 2.2 – ZigBee, from left to right: RF300PD1 [33], TelosB [34], CC2420 [35], SM200P81 [36], JN5 148-001 [37]......	21
Figure 2.3 – IEEE802.11b ISL transceiver, from the left to the right: WiBear [38], TiWi-R2 [39], SM700PC1 [40], XG880MU [41], HW86052 [42], GS1011M [43]......	21
Figure 2.4 – $E_b/N_0$ of the signal vs. BER for various modulations. ....	23
Figure 2.5 – ISL data block diagram. ....	25
Figure 2.6 – DSSS Physical Protocol Data Unit (PPDU).....	26
Figure 2.7 – FHSS Physical Protocol Data Unit (PPDU).....	26
Figure 2.8 – TSE AS10 Wireless SAW Temperature Sensor. ....	27
Figure 2.9 – Typical conductance of TSE AS10 at 25°C with regard to frequency.....	28
Figure 2.10 – MICRF620 [45], TDA 7255V [46], RFM12B [47], CC1100 [48], SRW1011 [49] (left to right). ....	30
Figure 3.1 – Sunsynchronous nominal inclination for circular orbit as function of altitude.....	32

Figure 3.2 - Sun orientation respect to orbit plane at boreal summer solstice, in dawn dusk sun-synchronous conditions with  $\Omega = \alpha_{\text{sun}} + 90^\circ$  (left) or  $\Omega = \alpha_{\text{sun}} - 90^\circ$  (right)..... 32

Figure 3.3 – Eclipse orbit period percentage over a sidereal year, for circular sun-synchronous orbits at various altitudes, for  $\Omega = \alpha_{\text{sun}} + 90^\circ$ . Time axis starts at vernal equinox. .... 33

Figure 3.4 - Example of secondary payload accommodations. .... 34

Figure 3.5 – Cal Poly's and NovaNano FlyMate Picosatellite Deployers..... 35

Figure 3.6 – Visualization of dawn dusk RAAN condition: the sun visibility in Aeolus orbit (Left) is continuous, while eclipse occurs for a RAAN different to 6.00 h (Right)..... 36

Figure 3.7 – ADM-Aeolus orbit sun visibility during lifetime. Only immediately before final atmospheric re-entry eclipses can occur, even nearby sun-synchronous RAAN and inclination. .... 36

Figure 3.8 – ADM-Aeolus orbital parameters time evolution due to atmospheric drag..... 37

Figure 3.9 - STK propagation results for lifetime at various initial semiaxis and eccentricity. 39

Figure 3.10 – STK and Matlab propagation results comparison, for circular orbit lifetime at 0.005 initial eccentricity, with various model and hypothesis ..... 39

Figure 3.11 - Continuous daylight periods start times and end times, in elapsed days since 2014 vernal equinox. Simulation are started at each considered altitude at the corresponding visibility period start time and then propagated till atmospheric re-entry or first eclipse period occurred. .... 40

Figure 3.12 – Shielding configuration. .... 41

Figure 3.13 – Total Dose vs. aluminium shielding thickness. .... 41

Figure 3.14 – Dose Equivalent vs. areal density. .... 41

Figure 3.15 – Total Dose vs. Al thickness: comparison between PCB and Al shielding performance. .... 42

Figure 3.16 - Lifetime respect to initial altitude summary, at occurring of considered critical effects..... 43

Figure 3.17 – Sun visibility analysis over entire lifetime (below) and zoom in (above) that highlight the loss of continuous visibility after 228 days. Only a short penumbra condition is earlier experienced. .... 43

Figure 3.18 –LOP propagation results for desired 450 km altitude sunsynchronous circular orbit, starting from an hypothetical launch date of March 2014..... 44

Figure 3.19 – Relative position measurement and control scheme for geometric control methods..... 47

Figure 3.20 – Left: 6-Pack ISIPOD (ISIS [65]), Right: double P-POD design (CalPoly)..... 48

Figure 3.21 – UHF/VHF dipole antenna disposition (left) and nadir pointing relative attitude between spacecraft in the current leader-follower configuration (right)..... 50

Figure 3.22 - Deployable solar panels architectures ..... 51

Figure 3.23 – Isis family modular CubeSat structures [65].....	51
Figure 4.1 – Effects of including Earth gravity harmonics (left) and atmospheric acceleration (right) respect to unperturbed keplerian problem, for a 400 km circular orbit, over a sidereal day. ....	55
Figure 4.2 – STK (below) and MATLAB Simulink (above) perturbed uncontrolled relative dynamic propagation over a sidereal day .....	56
Figure 4.3- Reference (above) and differential (center) semiaxis and eccentricity, and differential classical and modified orbital angle parameters (below), on uncontrolled relative dynamic of a 100 m separation L-F formation, at 400 km circular 98° inclined LEO.....	57
Figure 4.4 – Differential disturbance accelerations acting on uncontrolled relative dynamic of a 100 m separation L-F formation over 10 orbit periods, with 2% ballistic coefficient mismatch, at 400 km 98° inclined LEO.....	58
Figure 4.5 – SSTL SGR-05U hardware (left) and host interfacing diagram (right).....	59
Figure 4.6 - NovAtel OEM4-G2L hardware .....	59
Figure 4.7 - Envelope of relative position measurement accuracy with onboard GPS receivers, for a 100m leader-follower nominal configuration respect to the chief position. ....	60
Figure 4.8 - Discrete-time Kalman filter position error respect to integration time period, during an uncontrolled dynamic propagation over 5 orbit periods. ....	63
Figure 4.9 – Differential aerodynamic (above) and radiant pressure (below) time trends, in case of DLQR, with 2% ballistic coefficient mismatch, over 30 orbit periods. ....	65
Figure 4.10 - Relative position propagation in case of DLQR (T=4s) .....	66
Figure 4.11 - Relative position errors time trend in EH frame (above) and control thrust (below), in case of DLQR (T <sub>s</sub> =4s), over 30 orbit periods .....	66
Figure 4.12 - Relative position propagation in case of DLQR (T=4s) with integral error feedback. ....	67
Figure 4.13 - Relative position errors time trend in EH frame (above) and control thrust (below), in case of DLQR with integral error feedback (T=4s), over 30 orbit periods.....	67
Figure 4.14 - MicroSpace Cold Gas Micropropulsion, nozzles module (left) and control PCB (right) [80].....	68
Figure 4.15 - Vacco MiPS propulsion system, system diagram (left) and enclosures, with (center) and without (right) extended tank [80] .....	69
Figure 4.16 –Pulsed Plasma Thruster, nozzle section CAD [84] .....	70
Figure 4.17 – Clyde Space CubeSat Pulsed Plasma, external (nozzle) side view (a), internal view (b) and nozzle close up view (c) and its lateral nozzle version, during vibration tests (d) and CAD model (e) [84].....	70
Figure 4.18 – Single (left) and cluster (right) configuration of 8 PPT thruster within PC104 form factor.....	71
Figure 4.19 - Relative position propagation in case of DLQR (T=4s) with Micro Space cold gas (left) and zoom in (right), over 30 orbit periods .....	74

Figure 4.20 - Relative position errors time trend in EH frame (above) and control thrust (below), in case of DLQR ( $T=4s$ ) with Micro Space cold gas (left) and zoom in (right), over 30 orbit periods ..... 74

Figure 4.21 - Relative position propagation in case of DLQR ( $T=4s$ ) with Clyde Space PPT (left) and zoom in (right), over 30 orbit periods ..... 75

Figure 4.22 – Relative position errors time trend in EH frame (above) and control thrust (below), in case of DLQR ( $T=4s$ ) with Clyde Space PPT (left) and zoom in (right), over 30 orbit periods ..... 75

Figure 4.23 - Passive collision avoidance strategy. Propagation over a sidereal day of uncontrolled relative motion, setting initial  $\delta e$  and  $\delta i$ ..... 77

Figure 4.24 - Relative out-of-plane and in-plane motion synchronization ..... 77

Figure 4.25 – Controlled relative position propagation (left) and projection in radial-normal plane (right), in case of DLQR ( $T=4s$ ) with Clyde Space PPT (left) and zoom in (right) , over 30 orbit periods, with Collision Avoidance Relative Orbit (CARO) starting conditions ..... 78

Figure 4.26 - Relative position errors time trend in EH frame (above) and control thrust (below), in case of DLQR ( $T=4s$ ) with Clyde Space PPT (left) and zoom in (right) , over 30 orbit periods, with Collision Avoidance Relative Orbit (CARO) starting conditions ..... 78

Figure 4.27 – Relative uncontrolled trajectory evolution in EH frame, after deputy releasing with 0.2 m/s radial (left) or in-track (right) velocity , for 1 km separation L-F formation ..... 79

Figure 4.28 - Relative trajectory in EH frame during formation initialization, with Cold Gas Micropropulsion, for 0.2 m/s intrack velocity error..... 81

Figure 4.29 - Formation initialization with Cold Gas Micropropulsion. Position in EH frame (above) and control thrust (below) time-trend for 0.2 m/s in-track velocity error..... 81

Figure 4.30 – Relative trajectory (left) in case of formation acquisition after deputy and chief undocking, highlighted in close up view (right), with an in-track 1 cm/s impulse..... 82

Figure 4.31 – Acquisition performance position (above) and required control acceleration (below) in case of L-F formation acquisition after Deputy undocking from Chief, with an in-track 1 cm/s impulse. .... 82

Figure 4.32 - Relative trajectory in EH frame (left) and projection on normal-radial plane, during reconfiguration from leader follower to a 10 m aperture periodic relative motion relative trajectory. .... 84

Figure 4.33 - Relative trajectory in EH frame (left) and projection on intrack-radial plane, during reconfiguration from 100 m to a 200 m intrack separation in a leader follower configuration..... 84

Figure 4.34 – Relative position in EH components (above) and required control acceleration (center) during reconfiguration from L-F to a 10 m aperture periodic relative motion relative trajectory (below)..... 85

Figure 4.35 – Steady state distance error respect to target relative position and maximum value experienced during transient ..... 86

Figure 4.36 – Steady state relative position measurement (above) and control (below) statistical values over a sidereal day, respect to target L-F in-track separation in all three EH frame direction. .... 87

Figure 4.37 - Daily  $\Delta V$  budget (left) and mean accelerations (right) respect to reference orbit altitude..... 87

Figure 4.38 – Steady state relative position measurement (left) and control (right) respect to reference orbit altitude, in all three EH frame direction..... 88

Figure 5.1 – Maximum disturbance torques respect to LEO altitude, on a 3U nadir-pointing CubeSat ..... 91

Figure 5.2 – Attitude control analyzed architectures..... 93

Figure 5.3 - Environmental conditions at nominal nadir-pointing attitude, at 400 km altitude LEO, over an orbit period. Aerodynamic (a), radiation pressure (b) and magnetic (c) torques. .... 94

Figure 5.4 –Uncontrolled attitude angles rates over short time period, expressed as small angles rotations, starting from unperturbed nominal attitude..... 95

Figure 5.5 – Uncontrolled attitude angles rates over short time period, expressed as small angles rotations, starting from unperturbed nominal attitude , in case of pitch axis inertia wheel ( $h_i= 4$  mNm). .... 95

Figure 5.6 - Relative angle (d) between sun direction (e) and Earth magnetic field vector (f). 96

Figure 5.7 - SSBV Magnetometer hardware (left, sensor only), Sparkfun Electronics MicroMag3 sensor (center) and its dedicated interface provided in Pumpkin ADCS package (right)..... 96

Figure 5.8 - Isis Analog Fine Sun Sensor (a), Solar MEMS SSOC-D60 (b), SSBV CubeSat Sun Sensor (c) and Sinclair Digital Fine Sun Sensor (d) ..... 98

Figure 5.9 - Angles and angular rates measurements (dashed line) over short period free dynamic, with direct determination from sun sensor and magnetometer measurements (left). Angle rates (right) are calculated via finite differences. .... 99

Figure 5.10 - Angles and angular rates measurements (dashed line) over short period free dynamic with Sinclair S3S star tracker (left). Angle rates are calculated via finite differences. .... 100

Figure 5.11 - Space technology RW1 wheel and its 4x cluster configuration (left), Maryland Aerospace complete MAI 100 ADCS (center) and the only MAI-101 3x wheels cluster enclosure (right) [91]..... 103

Figure 5.12 - Sinclair Interplanetary RW-0.01-4 wheel hardware (above) drawing (left-below) and power consumption (right-below) [92]..... 103

Figure 5.13 – Power consumption comparison for the considered solutions, without spin (left), and more detailed power consumption chart [92] respect to required torque and nominal angular speed..... 103

Figure 5.14 – Attitude respect to LVLH frame (above) and power consumption (center) performances, in case of operative mode 3-axis control. .... 105

Figure 5.15 - Zoom in views (below) highlight attitude errors and control torques short period time trend. .... 105

Figure 5.16 – Attitude respect to LVLH frame (above) and power consumption (center) performances, in case of operative mode dual spin. .... 106

Figure 5.17 – Power (above) and attitude (below) performance in case of 3-axis control, during MicroSpace Cold Gas continuous firing at 25% of maximum thrust. .... 107

Figure 5.18 – Power (above) and attitude (below) performance in case of dual-spin control, during MicroSpace Cold Gas continuous firing at 25% of maximum thrust. .... 108

Figure 5.19 – Wheel angular momentum storage time trend over an orbit, without desaturation control (a) and with proportional desaturation control, in Chief operative mode (b) and in Deputy operative mode (c)..... 109

Figure 5.20 – Attitude (above), stowed angular moment (center) and power consumption (above) performance during transient response after spacecraft releasing with 5° and 5%/s attitude and rate errors. .... 110

Figure 5.21 - Attitude error (left) and power consumption (right) trend respect to reference orbit altitude. .... 111

Figure 6.1 – 32-bit Microcontroller: LPC1102 (left) and NanoMind A712C (right). .... 113

Figure 6.2 – ADM-Aeolus PoliMi accesses, over 10 days. .... 114

Figure 6.3 – Telemetry data flow..... 115

Figure 6.4 – Source Packet Format ..... 115

Figure 6.5 – Transfer Frame Format ..... 116

Figure 6.6 – TT&C Transceiver: at left AstroDev Helium Radios, at right NanoCom U480. 118

Figure 6.7 – Atmospheric losses diagram. .... 120

Figure 7.1 – Power consumption: absolute values and percentage of available power. .... 126

Figure 7.2 – Geometries relative to the analyzed cases: A) equinox, B) summer solstice, C) winter solstice, D) passage on the orbital node. All the figures are relative to the north position on orbit ..... 128

Figure 7.3 – Albedo (Left): view factor (F) in function of high on mean Earth radius ( $h/R_p$ ) and  $\beta$  angle; IR radiation (Right): view factor (F) in function of angle between normal to S/C panel and planet center direction and high on mean Earth radius ( $h/R_p$ )..... 128

Figure 8.1 - System block diagram. .... 134

Figure 8.2 – Cold Gas and PPT propulsion system accommodation for lateral thrust ..... 135

Figure 8.3 – Bus stacking continuity and routing possible solutions, discrete wire and header Samtec products for PCI-104 (left) and Pumpkin breakout board for I/O routing (right) [103] ..... 136

Figure 8.4 – Sinclair 3x cluster enclosure (under development [106]) (left) and Sinclair wheels readjustment within Maryland IMI-100 enclosure (right). Solids have been sliced to aid viewing..... 137

Figure 8.5 – Sinclair wheels cluster PCB stack 3D representation (left) and first vibration mode deformed view of the only interface PCBs (right)..... 137

Figure 8.6 – WiFi payload (left) and GPS receiver (right) direct PCB mounting configurations ..... 138

Figure 8.7 – Explode view of the overall configuration, with all components correctly stacked within structures rails. .... 139

Figure 8.8 – Mass and cost budget comparison: PPT and cold gas thruster. .... 142

Figure A.1 - GPS data format [105] ..... i

Figure A.2 - GPS signal encoding and modulation [105] ..... ii

Figure A.3 - Main lobe coverage of GPS signal [105] ..... iii

Figure A.4 - Cartesian and curvilinear EH frame coordinates ..... vi

Figure A.5 - Relative orbital elements representation..... vi

## List of tables

Table 1.1- Typical performances comparison of single frequency GPS receivers and their dual frequency most common competitors for space applications [26].....	12
Table 2.1 – Comparison of wireless technologies. ....	19
Table 2.2 – IEEE802.15.4 transceiver. ....	20
Table 2.3 – IEEE802.11b transceiver. ....	21
Table 2.4 – Parameters for the ISL design.....	23
Table 2.5 – IEEE802.15.4 transceivers calculated outdoor range. ....	24
Table 2.6 – IEEE802.11b transceivers calculated outdoor range. ....	24
Table 2.7 – ISL Data packet.....	25
Table 2.8 – DSSS packet format details. ....	26
Table 2.9 – FHSS packet format details. ....	26
Table 2.10 – SENSEOR system temperature specifications .....	28
Table 2.11 – SENSEOR electrical specifications of the sensor .....	28
Table 2.12 – SENSEOR transceiver parameters .....	29
Table 2.13 – Transceiver investigated for wireless sensor network .....	30
Table 3.1 – Deployment systems (POD) .....	35
Table 3.2 – Secondary payload launch opportunities .....	35
Table 3.3 – Small launcher vehicles typical injection orbital parameters accuracy for LEO circular orbit, comprising polar and sun-synchronous orbits. (Rockot user manual [58]).....	38
Table 3.4 – Aluminium and PE density features for a reference 80 cSv/yr equivalence dose..	42
Table 3.5 – Main relative position control architecture performances .....	46
Table 3.6 – Releasing conditions constraints.....	48
Table 3.7 - Properties and performances depending on modules architecture.....	50
Table 4.1 – Single frequency Spaceborne GPS receiver benchmark [73] .....	58
Table 4.2 - Characteristics of on board GPS receiver.....	59
Table 4.3 – Standard deviation comparison of relative position and velocity and propagation on differential classical and modified orbital parameters with and without filtering. ....	63
Table 4.4- Available CubeSat chemical propulsion subsystems .....	69
Table 4.5- Available CubeSat PPT propulsion subsystems .....	71
Table 4.6- Existing CubeSat propulsion subsystem driving selection criteria summary .....	72



Table 4.7 – Performance indexes, calculated from propagation data over 30 orbit periods, in case of DLQR, with and without integral error feedback, with and without PPT or cold gas actuation .....	73
Table 4.8 – Performance indexes, calculated from propagation data over 30 orbit periods, for the only case of PPT actuation, at different relative orbit apertures.....	77
Table 4.9 – Formation acquisition performance, calculated from propagation data over 10 orbit periods, for a relative velocity error of 0.2 m/s initial conditions. ....	80
Table 4.10 – STK Astrogator results for a 2-impulse maneuver formation acquisition, for an initial relative velocity error of 0.2 m/s (after 1 orbit free dynamics, with 2 orbit coast phase between the two firings). ....	83
Table 4.11 – Performance indexes, calculated from propagation data over the three different input target signal phases, in case of PPT actuation, for a reconfiguration strategy, starting from a leader follower steady state.....	84
Table 4.12 – Propulsion solution trade off. ....	88
Table 5.1 - Attitude control architecture comparison.....	93
Table 5.2 – Magnetometer performances for CubeSat applications .....	97
Table 5.3 – Sun sensors performances for CubeSat applications (see also Figure 5.8) .....	97
Table 5.4 – Attitude determination direct method performances in operative orbit conditions, with SSBV CubeSat Sun Sensor and Sparkfun Electronics MicroMag3 magnetometer. Angle rates results from random simulations and are calculated via finite differences (FD). ....	98
Table 5.5 – Sinclair Interplanetary S3S Star tracker performances .....	99
Table 5.6 – Attitude determination solutions and performances summary .....	100
Table 5.7 – Optimal control performance comparison attitude determination with sun sensor and magnetometer .....	101
Table 5.8 – Reaction Wheels for CubeSat applications performances.....	102
Table 5.9 – Magnetic actuators performance comparison for CubeSat applications at 400 km. ....	104
Table 5.10 – Performance comparison between dual spin and three axis architectures, in case of optimal control and attitude determination with sun sensor and magnetometer .....	107
Table 5.11 – Performance during detumbling transient and steady state, in case of optimal control three axis architecture and attitude determination with sun sensor and magnetometer .....	111
Table 5.12 – Architecture trade-off results. Panel integrated magnetotorquers (2×top/bottom + 4×lateral) on both configuration plus inertia wheel or reaction wheel cluster. ....	112
Table 6.1 – OBDH microcontroller data. ....	113
Table 6.2 – Telemetry data every sampling time. ....	116
Table 6.3 – Telemetry data collected during maximum waiting time.....	116
Table 6.4 – Source Packet Ground link.....	117

Table 6.5 – Transfer Frame Ground link. ....	117
Table 6.6 – TT&C transceiver. ....	118
Table 6.7 – Deployable Dipole Antenna System. ....	118
Table 6.8 – Ground station data. ....	119
Table 6.9 – Data for ground link calculation. ....	119
Table 6.10 – Ground link budget calculation. ....	119
Table 6.11 – Data for ISL backup link calculation. ....	120
Table 6.12 – ISL backup link budget calculation. ....	120
Table 7.1 – Satellite components specifications. ....	121
Table 7.2 – Mission Operative Modes vs. Subsystems. ....	122
Table 7.3 – Solar panel power generation. ....	124
Table 7.4 – Clyde Space battery board data. ....	125
Table 7.5 – Battery power supply. ....	125
Table 7.6 – Subsystem Power Consumption vs. Operative Mode. ....	125
Table 7.7 – Power budget: summary. ....	127
Table 7.8 – Data relative to thermal analysis. ....	129
Table 7.9 – Solar cell and substrates Thermal Properties [102]. ....	129
Table 7.10 – Solar panel Thermal Properties. ....	130
Table 7.11 – One node analysis results. ....	130
Table 7.12 – Satellite materials specific heats and percents. ....	130
Table 7.13 – Non-stationary analysis results for eclipse case. ....	131
Table 8.1 – Satellite components physical specifications and cost. ....	133
Table 8.2 – Mechanical interface natural frequencies. ....	138
Table 8.3 – Mass distribution within cubes. ....	140
Table 8.4 – Mass budget for each satellite. ....	141
Table 8.5 – Cost budget for each satellite. ....	141
Table 8.6 – Cost per kilogram for some launcher. ....	142
Table A.1 - GPS code frequencies [105] ....	i
Table A.2 – CubeSat–Ground station PoliMi access. ....	xi
Table A.3 – CubeSat–Ground station PoliMi access statistic. ....	xii

## List of acronyms

AECA	Arms Export Control Act
BPSK	Binary Phase-Shift Keying
C/A	Coarse/Acquisition
CAN	Control Area Network
CCK	Complementary Code Keying
CDGPS	Carrier-phase Differential GPS
CDMA	Code Division Multiple Access
CoCom	Coordinating Committee for Multilateral Export Controls
COTS	Component Off The Shelf
DSSS	Direct Sequence Spread Spectrum
DIP	Dual In-line package
DLQR	Discrete-time Linear Quadratic Regulator
ECEF	Earth-Centered Earth-Fixed
ECI	Earth-Centered Inertial
EH	Euler-Hill
EKF	Extended Kalman Filter
FF	Formation Flying
FHSS	Frequency-Hopping Spread Spectrum
FOV	Field Of View
GNSS	Global Navigation Satellite System
GPS	Global Positioning System
I <sup>2</sup> C	Inter Integrated Circuit
ISL	Inter-Satellite Link
ITAR	International Traffic in Arms Regulations
LEO	Low Earth Orbit
L-F	Leader-Follower
LOS	Line Of Sight
LQR	Linear Quadratic Regulator
LVLH	Local Vertical - Local Horizontal
MEMS	Micro Electro Mechanical System
OBDH	On Board Data Handling
OEM	Original Equipment Manufacturer
OFDM	Ogonal Frequency-Division Multiplexing
P2P	Peer-to-Peer
PCB	Printed Circuit Board
PCB	Polychlorinated biphenyls
PCO	Projected Circular Orbit
PPT	Pulsed Plasma Thruster
PPU	Power Processing Unit
PRN	Pseudo Random Noise
QPSK	Quadrature Phase Shift Keying
RF	Radio Frequency
RSS	Root Sum Square
RTOS	Real-time Operating System

SAW	Surface Acoustic Wave
SEU	Single-Event Upset
SGPS	Spaceborne GPS
SMD	Surface Mounting Device
SPI	Serial Peripheral Interface
TBD	To Be Defined
TSE	Temperature System Equipment
UT	Universal Time
UTC	Universal Time Constant
WLAN	Wireless Local Area Network
WPAN	Wireless Personal Area Network
WMAN	Wireless Metropolitan Area Network

## Abstract

The purpose of this thesis is to report the feasibility study for a technological demonstrator mission using CubeSat platform. The scope is to verify wireless Commercial-Off-The-Shelf technology performances in Low Earth Orbit (LEO) environment. To implement this task two wireless network are considered: an Inter-Satellite Link (ISL), performed by a Wireless Local Area Network, and an Intra-Satellite Link, by a Wireless Personal Area Network. The selected payload consist on a WiFi transceiver used for the ISL and on a wireless temperature sensors network. In order to perform the project scope, a two CubeSat formation flying is required with a localization system based on GPS, whose received signal is filtered by a dynamic model. Formation dimension must be kept below kilometer order, to remain in the wireless network outdoor range, these dimensions are lower than distances usually used in formation flying. This analysis covers the phase A of mission design, exploring also in details some critical issues and subsystems, that is relative position and attitude determination and control, their impacts on on-board computing and inter-satellite communication performances. Cost budget and launch possibility are also treated, defining two main mission architectures in respect of propulsion subsystem options. In conclusion, wireless networks within a spacecraft formation is affordable even at nanosatellite class level. Each of these three main aspects are well known and flight proven, but when they coexist in the same mission, some conflicting requirements emerge, in relation to power generation and need of fine thrust levels.

Keywords: Wireless Local Area Network, Wireless Sensor Network, formation flying, global positioning system, nanosatellite, CubeSat, Low Earth Orbit.

## Sommario

Lo scopo di questo lavoro è documentare lo studio di fattibilità di una missione di test di dispositivi wireless Commercial-Off-The-Shelf con l'ausilio di piattaforme CubeSat. La logica di progetto consta nel realizzare due wireless network su scale diverse, in particolare si è voluto realizzare un Inter-Satellite Link tramite una rete WLAN e un link intra-satellitare tramite una rete WPAN. Il payload selezionato consiste in un ricetrasmittitore WiFi utilizzato per il link inter-satellitare e in un sistema di misura basato su sensori di temperatura wireless. Al fine di raggiungere lo scopo si è utilizzata una formazione di due CubeSat con un sistema di localizzazione basato sul GPS, il cui segnale viene filtrato con un modello dinamico. La dimensione della formazione è dell'ordine del chilometro, molto inferiore a quelle normalmente utilizzate, al fine di rimanere nel campo di vista della rete wireless. L'analisi copre un progetto di missione di fase A, esplorando anche in dettaglio aspetti critici e sottosistemi, come posizione relativa e determinazione e controllo d'assetto, il loro impatto sulle prestazioni del computer di bordo e sulla comunicazione intersatellitare. Il budget di costi e le opportunità di lancio sono stati affrontati, definendo due proposte di configurazione che differiscono per il sistema propulsivo scelto. In conclusione, una rete wireless inserita in un contesto di nanosatelliti in formazione è possibile. Tuttavia, nonostante ciascuno di questi aspetti sia provato e verificato in volo, la combinazione dei tre fa insorgere dei requisiti discordanti, in particolare relativamente alla generazione di potenza e alla necessità di un livello di spinta fine.

Thesaurus: Wireless Local Area Network, Wireless Sensor Network, volo in formazione, global positioning system, nanosatelliti, CubeSat, Low Earth Orbit.

# Chapter 1 - Introduction

## Section 1.1 - New trends in space system technology

Since the beginning of space age, a very few enhancement in space capability has been achieved and generates a very gloomy prospect several decades to the future. In particular, launch cost will still be several thousand dollars per kilogram of payload, implementing at least partially expendable launch vehicles. Power availability in space will continue to be tens of thousand dollars per kilogram. Spacecraft masses and costs will not be significantly lower than today for the same functions and performances.

However, there are many technological trends and concepts which will enable new capabilities in future systems: electric and magnetic propulsion, tethers, microelectronics, nano-materials, Micro-Electro-Mechanical Systems (MEMS), gossamer structures. Their main characteristic is to enable a magnitude-order enhancement respect to traditional technology. Some of these are known from years, but not yet fully pursued for a variety of reason. In some case they still require development and demonstration before being seriously adopted in a space program.

Another concept, which shall be defined a trend rather than a technology, is to “*replace structure with information*”, that means the possibility to achieve the same tasks and performance, obtained with a unique huge spacecraft, with distributed space systems, implementing coherent cooperating spacecraft formations.

As depicted in a wide literature [1], a cluster or formation of many small, nano- or pico-satellite theoretically permits to implement wide space apertures antennas at radiofrequencies (RF) and microwaves, filled aperture optical systems, large interferometers, and so on, as depicted in Figure 1.1, enhancing available dimensions in optical and radiofrequency system, much more than it can be even obtained using gossamer technologies.

This concept can be applied to many space mission as:

- Cooperation between a large mother ship and a cluster of slave nodes
- Earth coverage for multipoint remote sensing, monitoring or communication in LEO
- Planetary exploration

This concept would allow:

- Mass saving and higher performances than using a unique large spacecraft
- Higher redundancy, reducing failure effect of a single element respect to the whole formation functionality lowering total mission risk
- Easy replacement of spacecraft become inoperative, easy augmentation by addition of new elements, due to intrinsic mission architecture modularity
- Mission flexibility and possibilities of geometrical reconfigurations, with orbital maneuvers
- Production and testing cost reduction, taking advantage of modular design

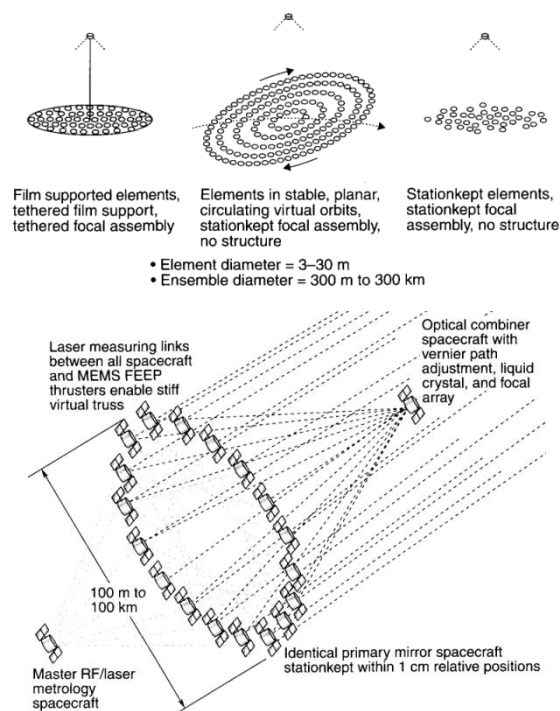


**Figure 1.1 - Distributed spacecraft optical and RF systems concept with little or no structure to obtain wide aperture optical system [1]**

## Section 1.2 - Objectives

### Subsection 1.2.1 - Mission requirements

The present work aims to explore formation flight feasibility of two main Commercial Off-the-Shelf (COTS) technologies: Wi-Fi and GPS in LEO, onboard a nanosatellite class platform. That means:

- To verify multiple spacecraft coordinated communication feasibility, such as a Local Area Network, testing at least a two-head link, involving **commercial low-cost wireless transceivers**.
- To verify relative dynamic control feasibility, that is to determine achievable performance in terms of spacecraft relative position determination and control, using **commercial low-cost GPS receivers**.

Then a technological demonstration space mission is proposed, which has the following **mission requirements**:

1. To establish and maintain a leader-follower formation flight and investigate performance in terms of separation and relative geometry possibilities.
2. To verify correct functioning and performance of a selected COTS wireless transceiver for ISL within formation flight control system. (a back-up traditional link must still be provided).
3. To verify correct functioning and performance of a selected COTS GPS receiver within formation flight control system. (a back-up GPS receiver which has already flown must be mounted).



4. To verify a selected wireless devices' remote activation and control within an intra-satellite link, even exploring performance and power transmission capabilities in a short range inter-satellite link. We choose for this purpose a temperature sensor network system, applied on ground tests, which has never flown.

## Section 1.3 - Wireless technology in space

A distributed satellite system is analogous to the concept of wireless sensor network, so a formation flying mission or a sensor network are of particular interest from the point of view of using wireless COTS protocol. This technology has several advantages as: low cost, mass, power and volume that are very important features for space mission and in particular for CubeSat systems, in addition Wi-Fi enables Ad-hoc network and permits to remove cables and supporting infrastructure. A wireless network can be classified as:

- **Wireless personal area network (WPAN):** used to transmit over short distances. This allows small, power efficient, inexpensive solutions. Data rates up to 1 Mbps.
- **Wireless local area network (WLAN):** hundreds of meters order transmission range. Data rates up to 54 Mbps.
- **Wireless metropolitan area network (WMAN):** tens of kilometres order transmission range. Data rates up to 120 Mbps.

The two main application domains applicable to a cluster of satellites or to a sensors network are the intra-vehicle network (environmental, physical and structural monitoring, intra-spacecraft communications, process and scientific monitoring) for which a WPAN is enough, and the inter-vehicle network (vehicle-to-vehicle communication) for which a WLAN is needed to guarantee the inter satellite link. Despite the fact that standard wireless COTS protocols are widely used terrestrially, they are not used in the space application domain. Suitability of COTS wireless devices for communication inside spacecraft and between satellites must be investigated in space weather. See ref. [2] and [3].

### Subsection 1.3.1 - State of the art and related mission

The potential uses of wireless technology are extremely broad. This ubiquity of use is also expected in the space domain and as a result wireless communications will cross the boundaries of existing areas of discipline where wireless transmission was typically limited to space-to-ground links. Wireless communication is an enabling technology for both manned and unmanned spacecraft; it enables un-tethered mobility of crew and instruments, increasing safety and science return, and decreasing mass and maintenance costs by eliminating expensive cabling.

In recent years wireless communication in space has become an important research topic. However the applications aren't widespread yet. Technologies already in use in few space missions are optical wireless communication and RF wireless communication, both only for intra-satellite application.

At the end of the 90's, the National Institute for Aerospace Technique of Spain (INTA) proposed optical wireless as a solution for interconnections between future micro/nano devices. The name given to this initiative was OWLS (Optical Wireless Links for intra-Satellite communications)[4]. NANOSAT-01[5] was the first in-orbit experience of OWLS, which purpose were: to perform an in-orbit demonstration of a wireless application, and

characterize some aspects related to the behaviour of OWLS in Space. Also FOTON-M3[6], a 2m diameter spherical Russian capsule used for scientific experimentation in micro-gravity, and OPTOS[7], a demonstrator satellite of optical wireless link, mounted OWLS system.

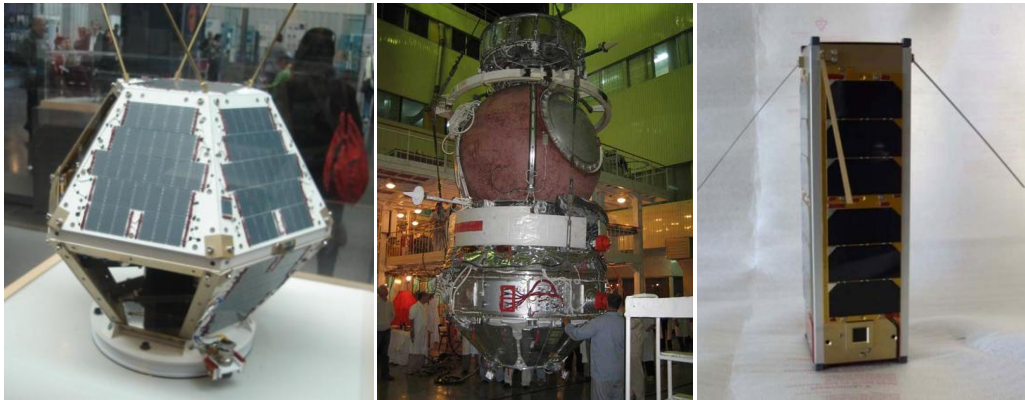


Figure 1.2 – From left to the right: NANOSAT-01 (INTA), FOTON-M3, OPTOS (INTA).

International Space Station uses RF wireless technology inter-module communication, but the link range is of few meters.

Another example of RF wireless link is given by NUTS [8] (test satellite, 2U CubeSat) which project was started in September 2010 and the launch is foreseen in the 2014. NUTS goal is, apart the other, the RF intra-satellite bus.

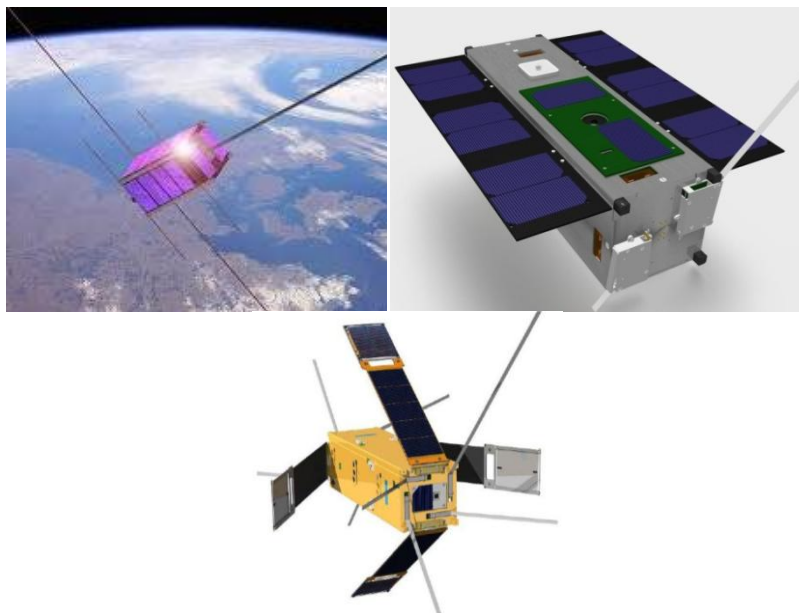


Figure 1.3 – NUTS satellite (left), STRaND satellite (center), Delfi-C3 (right).

STRaND-1 [9] [10] is a demonstrator satellite that mounts a COTS Android smartphone. The smartphone has been integrated into the STRaND-1 with the initial aim of providing the main imaging payload but with the ultimate intention to assess the opportunity to assess the smartphone's capabilities to perform the primary on-board computer role. One experiment to be conducted in the mission is the intra-satellite link between the mobile phone and on board computer using WiFi.

Delfi-C3[11], a two-year student satellite project of the Faculty of Aerospace Engineering and the Faculty of Electrical Engineering, Mathematics and Computer Sciences of Delft University of Technology in the Netherlands, act as such a technology qualification test-bed for two payloads. A Thin Film Solar Cell experiment will be performed to verify the performance of these cells in the space environment. In addition, an autonomous Sun Sensor using a wireless data link will be demonstrated. OPTOS, STRaND and Delfi-C3 are all 3U CubeSat platform.

None of satellite missions already designed or flown tests Wireless Inter Satellite Link. In next subsection, mission objectives for the wireless technology demonstrator will be presented.

### **Subsection 1.3.2 - Wireless technology application within Inter-Satellite and Intra-Satellite Networking**

#### **Inter-Satellite Networking**

In last five years inter-satellite wireless communication was a topic of particular interest for the main universities and space agencies. In particular University of Surrey has developed many researches on this matter [2] and some COTS wireless devices were also tested [12].

The inter-satellite link is established via wireless communication protocols and based on the terrestrial IEEE 802.11 and IEEE 802.15.4 standards. These standards normally support a typical communication range within 100m or 1000m. For space applications, the separation between satellites usually is more than at least 1 Km. Hence a few notes will be investigated to verify the applicability of these devices to formation flying system.

#### **Intra-Satellite Networking**

One new area of applying wireless networking in satellites is intra-satellite communication. A satellite is comprised of many different subsystems and sensors. In traditional construction, each subsystem is networked with the others, and sensors are connected with their respective subsystems over wired interfaces.

In next pages will be discuss the design of an Intra-Satellite Network using COTS temperature sensors. In particular SENSEOR TSE AS10 Wireless Temperature SAW (Surface Acoustic Wave) [13] Sensor integration will be investigated thanks to their very little dimensions and no power needed.

## **Section 1.4 - GPS implementation in Formation Flying**

### **Subsection 1.4.1 - GPS in LEO**

Global Positioning System (GPS) has a wide and consolidated reliability for ground applications in position determination. The GPS constellation coverage and emitted signal is expressly designed to permit to a receiver at any latitude to lock and identify at least four satellites at the same time and measure received signal time delay (See Appendix A).

#### **Environmental effect**

In LEO conditions, signal doesn't suffer effects typical of Earth surface, such as atmospheric degradations and delay, but position determination greatly suffers high relative velocity between transmitters and receiver, which orbits absolute velocities are nearby several thousand of meters per second. Positioning method is based on the assumption that the spacecraft

receives delayed signals in the same position, but that hypothesis falls if it's rapidly moving. Fortunately, satellite orbits are relatively predictable and although Kepler's equations can be used to give a very good approximation to the satellites' orbits, and only deviations from that predicted orbit need to be measured and accounted for. Better predictions, accounting for gravitational and drag effects, may be necessary.

### Doppler effects

The biggest stumbling block to implement a LEO GPS receiver is the extreme dynamics of the receiver compared to terrestrial ground-based and low-altitude applications. Normal terrestrial receivers Doppler search spaces do not adequately provide for the large frequency shifts and shift rates. These shifts occur as a result of the high velocities associated with satellites. Doppler shift is calculated as follows:

$$f' = f_0 \sqrt{\frac{1+v/c}{1-v/c}} = f_0 + f'_d$$

where  $v$  is the velocity component along signal path and  $c$  the speed of light. The Doppler offsets for a terrestrial receiver can be as much as  $\pm 5$  kHz [14][15], that lead, for the carrier frequency L1 of 1575.42 MHz, to a maximum allowed relative velocity of 951.5 m/s.

Otherwise, we can calculate the maximum theoretical Doppler shift, assuming the worst case in which a LEO receiver is in the same orbital plane of the GPS spacecraft, but in retrograde motion respect to it. Figure 1.4 shows this results as function of altitude, assuming circular orbit, but it's clearly one order of magnitude greater than on ground, that is over  $\pm 50$  kHz. Another issue to take in consideration is the Doppler frequency variation rate, because the GPS signal has to be locked and followed during its visibility window.

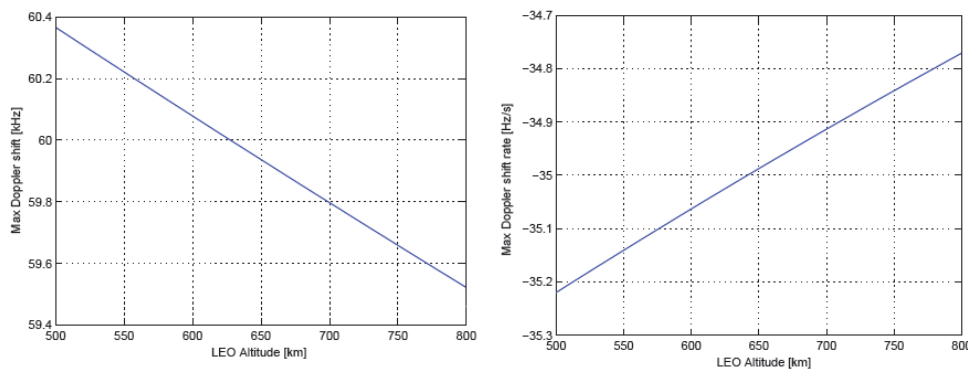


Figure 1.4 - Maximum theoretical Doppler frequency shift and shift rate on received GPS signal in LEO circular orbits

### Receiver legal restrictions and limitations

The GPS system is controlled, maintained and operated by the U. S. Department of Defense. GPS receivers are subject to degradations of position and velocity accuracies under Department of Defense imposed Selective Availability.

GPS commercial tracking devices should disable tracking when the device realizes itself to be moving faster than 1,000 knots (514 m/s) at an altitude higher than 60000 ft (18,3 km), whereas typical LEO altitudes above 200 km and orbital velocity of about 7 km/s exceed this limit. This was intended to avoid the use of GPS in intercontinental ballistic missile-like

applications. It's usual to refer to this restriction with the phrasing "CoCom Limits". In the United States, Coordinating Committee for Multilateral Export Controls (CoCom) compliance was implemented in the 1960s via the Arms Export Control Act (AECA) and the State Department's regulatory supervision on AECA via International Traffic in Arms Regulations (ITAR), which are still in effect.

#### **Subsection 1.4.2 - Formation flying, definitions and main characteristics**

The definition of spacecraft *formation flying*, proposed by NASA's Goddard Space Flight Center (GSFC) is *the tracking or maintenance of a desired relative separation, orientation or position between or among spacecraft*. Formation flying spacecraft are therefore a particular case of a more general category, termed *distributed space systems*, defined by NASA GSFC as follows: *an end-to-end system including two or more space vehicles and a cooperative infrastructure for science measurement, data acquisition, processing, analysis and distribution*. GSFC proposed a number of other important distinctions: A *constellation* is a collection of space vehicles that constitutes the space element of a *distributed* space system; *virtual aperture* is an effective aperture generated by physically independent spacecraft; and *virtual platform* is a spatially distributed network of individual vehicles collaborating as a single functional unit, and exhibiting a common system-wide capability to accomplish a shared objective [16].

A *formation*, distinguishes from a constellation, consisting in more than one satellite in a closed distance flight path, which typically means quasi-coplanar orbits and distances below few kilometers, where relative motion is in linear domain, so spacecraft states are directly coupled and relative position and velocity are accurately controlled. Multiple spacecraft architectures enable objectives that cannot be fulfilled by a single spacecraft, either because a immediate subsequent passage on the same location is required, to synthesize a larger aperture than could be sensibly be carried on a single platform, and so on.

Depending on the application, all formation flying architectures can be classified in few typical geometries: *trailing formations* (in track formations or pendulum formation) and *clusters* (Cartwheel configurations).

#### **Trailing formations**

Trailing formations, also called Leader-Follower (L-F) are formed by multiple satellites orbiting on the same path, typically a leader satellite and one or more followers. They are displaced from each other at a specific distance to produce either varied viewing angles of one target or to view a target at different times. Trailing satellites are especially suited for meteorological and environmental applications such as viewing the progress of a fire, cloud formations, and making 3D views of hurricanes.

Typically, in track formations are, are composed by spacecrafts with similar orbit parameters, with the same orbital period, or rather the same semi-major axis, but drifted in time (GRACE, PRISMA [17] [18] and so on). For spacecraft operating in the same orbit track, the worst secular disturbance effects on relative state is from atmospheric drag (and in some case from solar pressure, for the same reasons), because these perturbations depend on each spacecraft ballistic coefficient and produce differential effects.

A similar solution is a ground track oriented leader-follower formation, also called a pendulum formation, due to the shape of relative periodic motion. In such this configuration, orbits are

generally near circular, with the same semi-axis, with slight difference in plane orientation that is in ascending node and true anomaly, to obtain repeated and opportunely delayed ground tracks on the same location.

### Clusters

Cluster formations are formed by satellites in a relatively tightly spaced arrangement, in a bounded periodic motion around a master satellite or a reference orbit. Slight eccentric orbits in different planes are needed, to obtain a periodic motion both in the in-track and cross-track direction, obtaining elliptical relative trajectories around references slightly inclined respect to local horizon. This arrangement has been proposed for the first time in TechSat-21 mission (ref), never flown. It has been implemented in InSAR measures (TerraSAR-L) (ref), because it is best for high resolution interferometry and allows acquisition of one in track and two across track components, even if a formation reconfiguration is needed to acquire a different component measurement.

### Relative trajectory

Usually Deputy satellite position refers to a reference orbit or Chief spacecraft centered Local-Vertical Local-Horizontal (LVLH) Cartesian frame, also called Euler-Hill (EH) frame.

There are several studies in literature, as resumed in Appendix B. To make some simple geometrical considerations regarding to obtainable geometries within a formation, let's consider the HCW equations state space model, that express relative motion, under the hypothesis of low eccentricity keplerian reference orbit and low distance respect to orbit semiaxis :

$$\begin{cases} \ddot{x} = 2n_0\dot{y} + 3n_0^2x \\ \ddot{y} = -2n_0\dot{x} \\ \ddot{z} = -n_0^2z \end{cases}$$

which have bounded periodic solutions:

$$x(t) = \rho_x \sin(n_0t + \alpha_x)$$

$$y(t) = \rho_y + 2\rho_x \sin(n_0t + \alpha_x)$$

$$z(t) = \rho_z \sin(n_0t + \alpha_z)$$

$$\rho_x = \frac{1}{n_0} \sqrt{\dot{x}^2(0) + n_0^2 x^2(0)}$$

$$\rho_y = y(0) + \frac{2\dot{x}(0)}{n_0}$$

$$\rho_z = \frac{1}{n_0} \sqrt{\dot{z}^2(0) + n_0^2 z^2(0)}$$

$$\alpha_x = \tan^{-1} \left( \frac{n_0 x(0)}{\dot{x}(0)} \right)$$

$$\alpha_z = \tan^{-1} \left( \frac{n_0 z(0)}{\dot{z}(0)} \right)$$

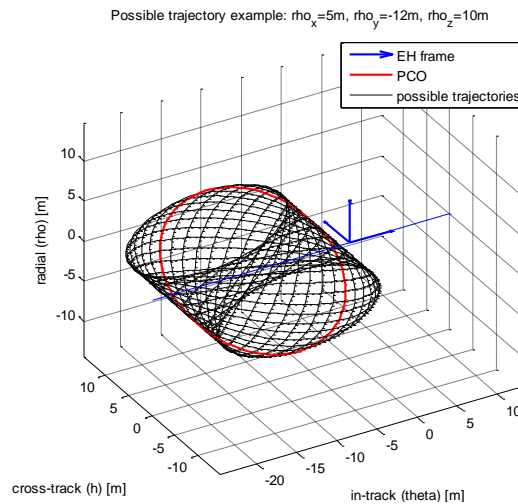


**Figure 1.5 - Possible example relative trajectories in EH frame, obtainable varying phase difference between  $\alpha_x, \alpha_z$  in HCW solution, adopting example values:  $\rho_x=4m, \rho_y=-10m, \rho_z=10m$ ,**

Some constants, depending only on initial conditions can be conveniently individuated and associated to relative trajectory geometry. The in-plane motion defines an ellipse with minor semiaxis  $\rho_x$  and major semiaxis  $\rho_y$ , with constant in-track offset  $\rho_z$  respect the origin, which, combined to out of plane  $\rho_z$  amplitude oscillation, lead to a cylindrical region of possible trajectories, varying in plane and out of plane phases  $\alpha_x$  and  $\alpha_z$ , as shown in Figure 1.5. This cylinder can be translated along in-track direction and stretched in height and amplitude, but still maintaining its semiaxis 2/1 ratio. Some common geometry definitions are:

- **Leader follower:** only along track offset  $\rho_y$ , with no periodic motion
- **Pendulum:** with along track offset  $\rho_y$  out-of plane periodic motion of  $\rho_z$  but no in-plane motion ( $\rho_x=0$ )
- **Projected Circular Orbit:** no along track offset  $\rho_y$ , and  $\rho_z=2\rho_x$  condition to obtain circular projected relative motion in horizontal plane. The 3D trajectory is not circular and it's  $30^\circ$  inclined respect to the horizon around along track direction.

### Relative position control system objective

The task of a formation control system is to maintain relative positions between spacecrafts within acceptance limits, determined by whole cluster functionality. Widely speaking, in this analysis we will take in consideration most common formation relative geometry, and reconfiguration strategies, to entirely investigate possibilities and limitation of the nanosatellite category. To this aim, it's necessary:

- To plan the formation architecture.
- To maintain each formation architecture.
- To reconfigure each formation architecture in another one
- To define a collision avoidance strategy

### Relative position control maneuvers

Ordinary maneuvers necessary in a relative position control are:

- **Maintenance:** continuously or periodically performed firings to negate perturbation drift effects, in order to maintain each spacecraft nearby its relative nominal trajectory within a prefixed tolerance.
- **Reconfiguration:** impulsive firing to modify relative position geometry, stepping from certain bounded periodic motion to another. If the two trajectories have any intersection, it's possible to perform a single impulse maneuver, otherwise of a two impulse transfer is the only solution, generally solving an optimization problem to minimize fuel consumption. Usually, for this purpose, the relative motion is modeled neglecting disturbance forces, due to relatively short transfer time. Also acquisition maneuvers after launcher releasing, even with uncertain initial state conditions, can be considered in this category.
- **Safety:** triggered only in case of certain control condition are satisfied, for instance whenever relative distances between spacecraft for any reason fall below a prefixed limit, to avoid risk of collision.

### **Subsection 1.4.3 - Guidance, Navigation and Attitude Control with GPS within a formation**

Guidance and control navigation requirements are typically high to very high. With an on board computer and dedicated algorithm, satellites may autonomously position themselves into a formation. Previously, ground control would have to adjust each satellite to maintain formations. In orbit, satellites may arrive at and maintain formations with faster response time and have the ability to change the formation for varied resolution of observations.

Within a relative close formation, typically with all spacecraft in line of sight, coordination of navigation and attitudes data and commands transmission can be fulfilled by ISL, whatever the network is configured, instead of involving ground segment to spacecraft links, in order to fasten the whole system time response [19].

Within a wireless local area network it's also possible to collect telemetry data necessary for attitude and navigation determination and control of the whole formation on a single module and distribute commands to the whole formation.

That enables multiple choices in information handling between inter-satellite communication subsystem and position and attitude determination and control subsystems on each spacecraft. The same principle can be applied, when it's necessary, also on each spacecraft attitude determination and control, to implement a relative attitude determination and control subsystem.

### **Augmented GPS**

There are several techniques to increment position determination accuracy. The most efficient, on Earth surface, consist in augmented GPS concept that is a bias errors correction by receiving information from a nearby ground station, whose position is accurately known. In a restricted area, different GPS devices are affected by the same environmental disturbing factors, such as ground reflections, atmospheric signal delays, and so on, that produces similar bias errors. In simple terms, if a second GPS receiver is placed in a known position, it can evaluate such those errors and communicate them to other devices.



In a LEO environment, this advantage may decrease significantly, having poor atmospheric interaction and substantially no ground reflections, but spacecraft relative velocity effects can be negated.

In orbit, this concept still applies to relative positioning. Communicating results coming from different GPS devices, mounted on each satellite, would automatically cancel bias errors deriving from orbital velocity, which is substantially the same for all spacecraft within a formation. That is called Differential GPS.

### Differential GPS

Code-based pseudorange measurements typically produce differential accuracies of several meters, which are not sufficient for formation flying missions. Carrier techniques offer much higher accuracy by calculating pseudoranges from the phase measurement of the Radio Frequency (RF) carrier wave. If carrier measurements from a mobile receiver and a base station are differenced, forming a Carrier-phase Differential GPS (CDGPS) measurement, the motion can be observed accurately. If the base is also moving, as in the case of target and chaser vehicles in a satellite formation, the CDGPS observable leads to relative position and velocity [15] [16].

In addition to the code and carrier pseudoranges, a Doppler measurement, which can be related to velocity, is available from the GPS receiver. The Doppler measurement is created inside the receiver by differencing carrier phase measurements. Because this is not a truly independent measurement, previous research has found that adding Doppler measurements does not significantly improve the state estimate [16].

A lot of related mission implement Differential GPS in formation flying control, such GRACE CHAMP and most of all PRISMA missions, which formation flying control system implement both a RF positioning system (shown in Figure 1.6) and Carrier-phase Differential GPS, within a separation range from 3 m up to 30 km [20]. Most of these missions cannot be recognized as nanosatellite category.

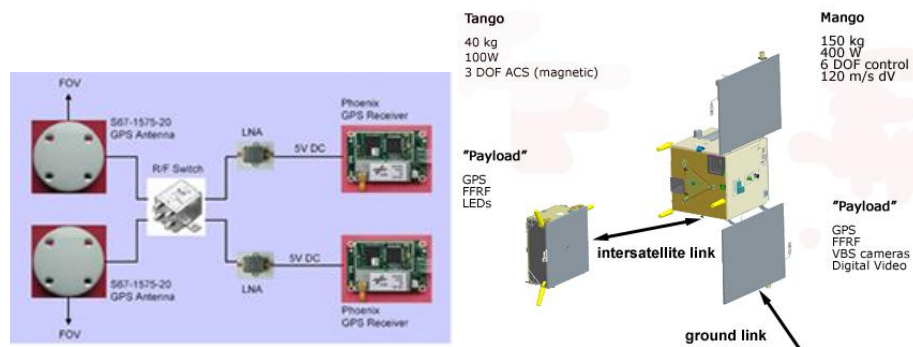


Figure 1.6 - PRISMA satellites and features

There are also numerous university research projects involving nanosatellites, FASTRAC (Figure 1.7) [21] and Emerald/Orion [22], but CanX-4 & 5 [23] can be considered the smallest dual formation, even if not flown yet. These two satellites, shown in Figure 1.11, will be launched together, commissioned together, and then separated in orbit, examining Projected Circular Orbit (PCO) and Leader-Follower (L-F) orbits and a maneuver to move from the latter to the former geometry. Relative position determination will be accurate to a few

centimetres using CDGPS techniques. Relative position control will be accurate to within one meter. Their primary mission is the demonstration of on-orbit formation flying.

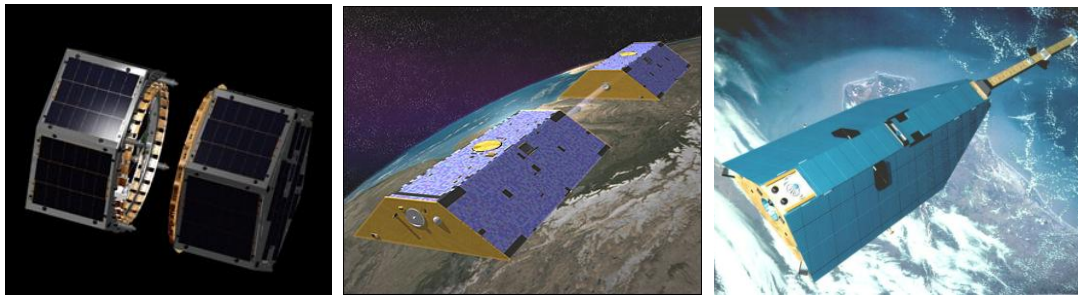


Figure 1.7 - FASTRAC (left), GRACE (center) and CHAMP (right) satellites artist's impressions

#### Subsection 1.4.4 - Low accuracy GPS application in LEO close formations

Spaceborne GPS receiver accuracy strongly depends on GPS signal processing method and, therefore, has impacts on mass and power consumption. Single frequency GPS receivers, such as Satellite Technology Limited (SSTL) [24], or the equivalent DLR Phoenix [25], Spaceborne (SGPS) series, are generally used for small satellite missions when medium navigational precision is required in relation to their very low dimension and power, but unfortunately it implements a Coarse/Acquisition (CA) or code-phase method, based on the only L1 GPS frequency (See Appendix A for more information) and then they have poor accuracies. In Table 1.1, their typical performances are compared to most frequently used product family for formation flying application applications.

Table 1.1- Typical performances comparison of single frequency GPS receivers and their dual frequency most common competitors for space applications [26]

	Ch.	Signal process.	Mass, power	Accuracy	Specifications, missions
<b>Single freq. SGPS receivers</b>	12-24	Single L1, CA	0.02-1.5 kg, 0.8-5 W	<10 m	not rad-hard (TIR >10 kRad), LEO
<b>JPL BlackJack, BRE Igor</b>	48	L1/L2, CA, P1/2	3.2-4.6 kg, 10 W	cm-level (CDGPS)	(TerraSAR-X, CHAMP, GRACE missions)
<b>NovAtel OEM4-G2l [27]</b>	24	L1/L2, CA, P2	0.05 kg, 1.5 W	0.45 m (CDGPS)	not rad-hard, LEO (CanX-2), ITAR restrictions

Several studies [20] have been proved the potential of real-time navigation at sub-meter level using single frequency GPS receiver. Using appropriate batch of Kalman Filter (KF) estimation techniques, the entire relative state can be determined from position output. By incorporating more sophisticated models, it's furthermore possible to compensate disturbance forces.

At LEO altitude, all GPS satellite which are visible from ground at the same latitude and longitude, at the same time, without atmospheric effect that impose the line of sight minimum elevation. Even a single antenna, pointed in radially direction and designed to have low directivity and Field Of View (FOV) is sufficient to have receive all GPS signal in Line Of

Sight (LOS). Typically (see Appendix A) cardioids directivity patterns are preferred, to have primary lobe angles nearby  $90^\circ$ , to be oriented towards nadir direction, with almost the same gain.

## **Section 1.5 - CubeSat package characteristics, low cost and power COTS**

A CubeSat is a low cost nanosatellite 10 cm cubic shaped and weight less than 1kg (1-Unit or 1U), and typically uses commercial off-the-shelf components. In 1999 Professor Twiggs of Stanford University and California Polytechnic State University developed the CubeSat to allow universities space access and create opportunities for low cost space tests and studies.

Central to the CubeSat concept is the standardization of the interface with the launch vehicle, which allows developers to pool together different modules for launch and so reduce costs and increase opportunities. Also internal and external interfaces, subsystems, products and services are today standardized to make quick and easy the development of the project. The advantages of CubeSat platform are:

- Access to more lower cost launch opportunities thanks to POD launch system
- Rapid development cycles thanks to the modular subsystem
- Use of COTS components
- Use of students labour
- Reduction in project management and quality assurance roles
- Limited or no built-in redundancy

These satellites can have different dimensions, commonly they are parallelepiped shaped. The smallest is 0.5 U ( $10 \times 10 \times 5 \text{ cm}^3$ ), than we can create modular structure up to 3U. This is the limit imposed by the POD launch system ( $10 \times 10 \times 30 \text{ cm}^3$ ).

### **Subsection 1.5.1 - Technological demonstrator: CubeSat platform**

CubeSat meet the demand for new technology validation missions. It allows doing on-orbit experience for characterization at an earlier stage in development minimizing costs. It's possible to put on orbit technologies with low TRL that requires in-orbit experience and test them in space environment.

The institutions who are interested in CubeSat are universities, the military, major space engineering and space service companies. In particular they are interested in various types of technology validation such as proof-of-concept for advanced or miniaturized platform technologies, demonstration of new operational concepts and related technology, characterization of specific components for inclusion in the baseline of agency level mission, and complete proof-of-concept missions.

### **Subsection 1.5.2 - PCI-104 form factor characteristics**

As already said CubeSat is characterized by standard structure, subsystems and interfaces. This is an advantage because the satellite is easy to assemble and a low cost system. However it also imposes some constrains that the system Satellite must observe. First of all, due to little dimensions, the power generated by solar panel is very low and the subsystems available volume is much shrunk.

Another feature of CubeSat platform is the PC/104 form factor bus. In particular PCI-104 modules are generally used (Figure 1.9). Modules utilizing the 104-pin Bus are stackable in 15mm and 25mm inter-module distances as shown in Figure 1.8.

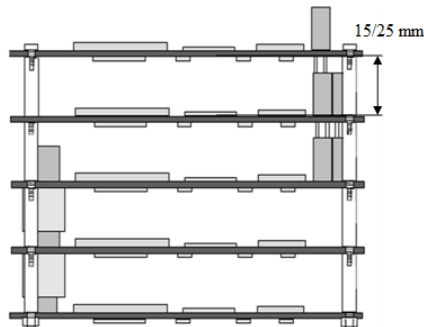


Figure 1.8 – PC/104 modules package.

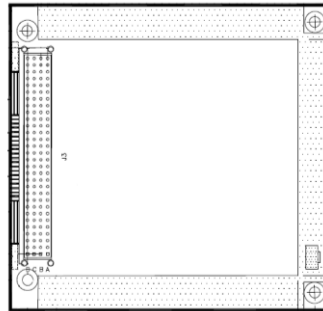


Figure 1.9 – PCI-104 module front view.

The satellite architecture is versatile. The main features are:

- Modular approach 90 x 96mm Printed Circuit Board (PCB) form factor
- 104-pin stackable bus connectors form a backplane: I/O, power, control, status, network, switching, user-defined
- 48 I/O pins directly on bus
- +5V, +3.3V voltage supply on bus

CubeSat standard subsystem already respect power, volume and interface features. In the matter of payload or not CubeSat compliant devices (usually MEMS), they must respect system's constrains or is necessary to use interface devices. The interface between bus and payload must be the following:

- Conform to PCB module specification (footprint).
- Power from +5V or +3.3V
- On Board Computer interface: standard Inter Integrated Circuit (I<sup>2</sup>C), SPI and asynchronous serial interfaces (all +3.3V I/O).

### Subsection 1.5.3 - Power generation

The only available power sources, for CubeSat class volumes and masses, are photovoltaic solar cells. Most common solutions are space qualified triple junction cells from AzurSpace giving an efficiency of 28% or more.

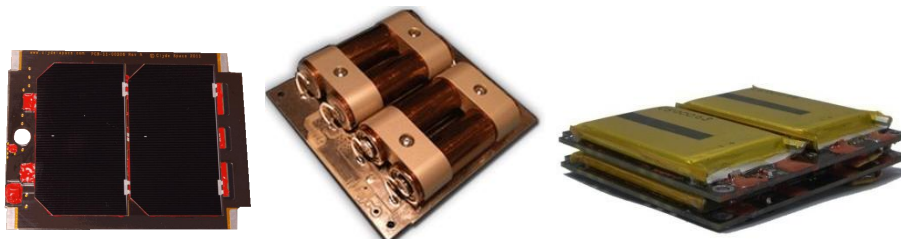


Figure 1.10 – Common EPS components: 3J solar cells 1U side (left), Li-Ion battery pack (center) and commercial Li-Po battery pack (right)

Two cells are usually reflow soldered to a single 1U side panel, reported in Figure 1.10, and connected in series to achieve an output voltage of approximately 4.7 V. Battery packs are

available in different sizes, as additional boards or plug-in. Each two cells side panel, in LEO condition, provides roughly 2.1 W, but extended structures can combine more cells in series, in order to achieve higher voltages and power outputs.

#### Subsection 1.5.4 - Related mission: CubeSat technological demonstrator

In CubeSat missions already flown rarely a propulsion or ADCS systems were implemented. A few interesting cases are now presented:

CanX [23] is the first nano satellite mission. The Canadian Advanced Nanospace eXperiment (CanX) program at the UTIAS Space Flight Laboratory provides cost-effective access to space for the research and development community at home and abroad through the use of nanosatellites. Four satellites of CanX mission are interesting for our goals:

CanX-1 (launched in 2003): It has a mass less than 1 kg, 1U size. Its mission is to evaluate several novel technologies in space, including, among others, GPS-based position determination.

CanX-2 (launched in 2008): It is a 3.5 kilograms, 3U size. The technologies to be tested include a novel propulsion system, custom radios, innovative attitude sensors and actuators, and a commercial GPS receiver. The first objective was to demonstrate key technologies required for the CanX-4 and CanX-5 formation flight mission. These technologies include a novel SFL-designed cold gas propulsion system and miniature attitude determination and control subsystem sensors and actuators to name a few.

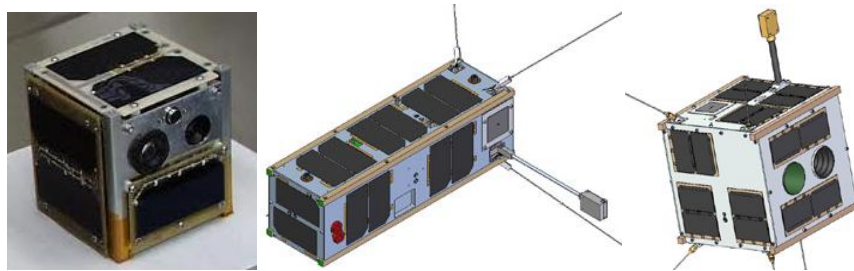


Figure 1.11 – CanX satellite: CanX-1 (1U), CanX-2 (3U), CanX-4 (20x20x20 cm<sup>3</sup>).

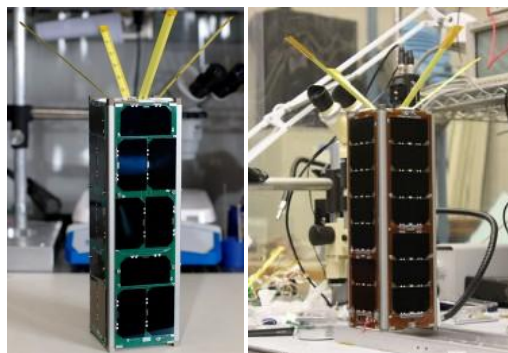


Figure 1.12 – RAX-1 and RAX-2 satellites.

RAX [28] mission is a demonstration of the mission's technological capabilities. This mission is characterized by a passive Attitude Control and it doesn't carry a propulsion system. Position determination is performed by a dual frequency GPS receiver, providing high precision navigation and timing, for payload data.

As already described, Delfi-C3 is a technological demonstrator. It carries a Thin Film Solar Cell (TFSC) payload and an Autonomous Wireless Sun Sensor. Its Attitude Control Subsystem is also passive and the spacecraft doesn't present a propulsion subsystem.

In addition to verify 802.11g WiFi space application, STRaND satellite objectives include also two different propulsion systems. The propulsion module on STRaND is split into two parts; the Surrey Satellite Technology Ltd. (SSTL) butane resistojet and the Surrey Space Centre (SSC) Pulsed Plasma Thruster (PPT).

## Section 1.6 - Work plan

### Subsection 1.1.1 - Mission constraints

First of all payload devices to be tested in LEO environment will be selected, among commercial low cost components, not expressly designed for space application. Then their feasibility among typical formation flying geometries and ranges and their integration in a nanosatellite class spacecraft will be investigated. In particular, the principal issues to investigate are the relationship between payload and these two application field, resumed as follows:

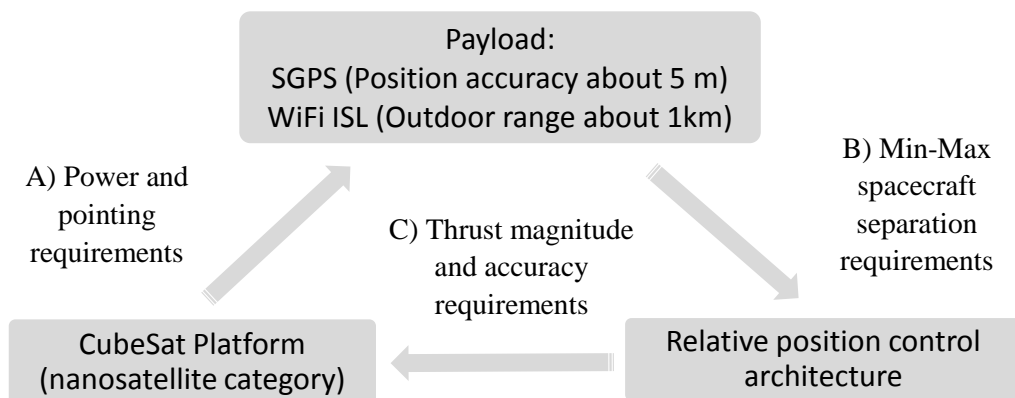


Figure 1.13 - Main issues and relationship

- A. The very limited power and volume capability of CubeSat package are the major issue in payload selection, as well as attitude control pointing accuracy regarding to inter satellite link
- B. Wi-Fi outdoor maximum range and GPS accuracy limit the architecture and performance of achievable formation control
- C. The same CubeSat platform must provide thrust within magnitude level and pointing accuracy adequate to operate fine relative position control

### Subsection 1.6.1 - Paper structure

In the present work, main issues are investigated as follows:

- In Chapter 2, payloads will be examined and the link designed, distinguishing inter-satellite and intra-satellite wireless devices, different protocol are selected and investigated
- In Chapter 3, requirements out coming from reference orbit are outlined and then applied in formation flying and bus configuration definition. A baseline spacecraft

architecture is finally proposed to fulfill all requisites beyond common CubeSat package possibilities

In next Chapters, subsystems are investigated, focusing on application outside CubeSat standards.

- In Chapter 4, relative position determination and control and close operations possibilities are investigated in detail, evaluating sensor and actuation devices performance for CubeSat application
- In Chapter 5, attitude determination and control performance are investigated, again, paying attention to nanosatellite application
- In Chapter 6, On Board Data Handling and communication systems are dimensioned for the specific mission, tacking care on the inter satellite link redundancy
- In Chapter 7, power generation is showed referring to the mission operational mode, and a simple thermal control are developed
- In Chapter 8, the resulting mission configuration is resumed and mass, power and cost budget are examined
- In conclusion, in Chapter 9, all critical considerations about mission feasibility, future developments and applications are discussed.





# Chapter 2 - Payload design

## Section 2.1 - Wireless inter-satellite network

Each satellite of a cluster needs to communicate with every other satellite to combine data readings from the instruments and the sensors, and to transmit that data to the Earth ground station. A satellite cluster operating as a "virtual satellite" is a group of satellites within very close range of each other (100m). Using distributed architectures for the different payloads among the satellites of the formation, and by using one satellite as the executive controller for transmitting data to the ground, we require a wireless bus among the satellites for data transmission, with higher data rates compared with CAN (Control Area Network).

The link type depends on the distances between the satellites and the amount of data that needs to be transferred.

Table 2.1 – Comparison of wireless technologies.

	Wi-Fi	Bluetooth	ZigBee	WiMAX
<b>Type</b>	WLAN	WPAN	WPAN	WMAN
<b>Protocol</b>	IEEE 802.11	IEEE 802.15.1	IEEE 802.15.4	IEEE 802.16
<b>Range [m]</b>	Up to 1000	Up to 100	100s	10000s
<b>Band [GHz]</b>	2.4	2.4	2.4 – 0.866/0.9	2.5 – 3.4
<b>Data rate [Mbps]</b>	11 – 54	1	0.25	280
<b>Network topology</b>	Point-to-multipoint	Ad-hoc	Mesh, point-to-multipoint, cluster tree	Point-to-multipoint, mesh

WPAN may be used for ranges up to 100s of meters. However, if the distances exceed 100 m or the data rate exceeds 250 kbps than WLAN or WMAN is a better choice. In the case of this paper, ZigBee and Wi-Fi have been examined for inter-satellite communication. See [2], [3] and [12].

### Subsection 2.1.1 - ISL architecture

For space mission applications the main network architectures that can be considered are:

- Client-server (Point-to-multipoint)
- Peer-to-peer (P2P) (mesh)
- Client-server and P2P (Ad-hoc)
- Hybrid P2P (cluster tree)

In the client-server network, the server manages the data storage of all the clients connected to him, the data transfer between server and client and between clients, the communications between clients. In this structure the server is the single point of failure, redundancy must be considered. In P2P architecture, every peer has the same importance. All network peers are connected each other to permit communications and data exchange. Considering the combination of these two architectures (client-server and P2P), every peer is in connected with the server and can exchange particular types of data with the other peers. The server coordinates the interactions between peers. Hybrid P2P network presents a mesh of super-peers that manages and shares the data of the peers connected to the super-peers.

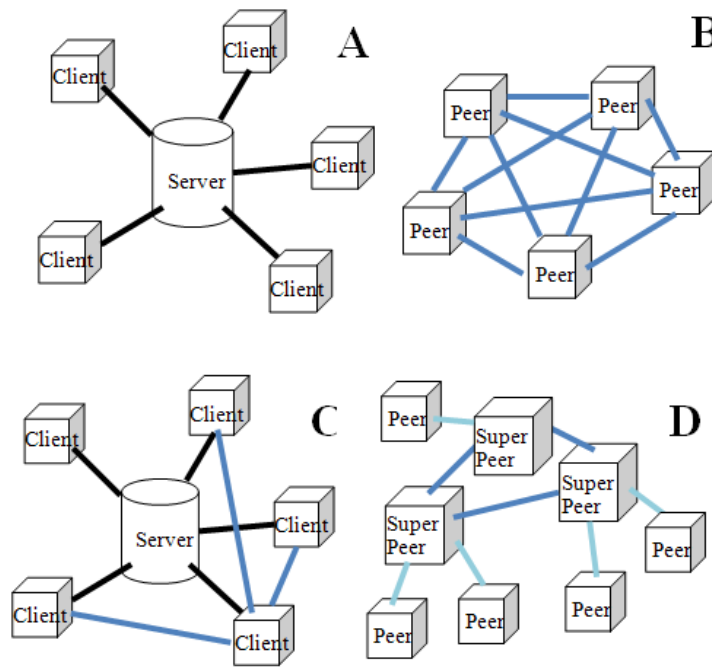


**Figure 2.1 – ISL possible network architectures: A) Client-server, B) Peer-to-Peer, C) Client-server and Peer-to-Peer, D) Hybrid Peer-to-Peer.**

The idea for our link is to implement a P2P network between the two satellites in order to maintain the system symmetry. See [3], [29], [30] and [31].

### Subsection 2.1.2 - Component list

The transceivers were selected in according to ultra low power and very low physical dimensions. Data and physical interfaces must be investigated to ensure the possibility of the payload integration in the spacecraft system. Data packets relative to the wireless protocols considered are enough and even excessive in respect of the amount of data that must be transmitted. In particular, eleven devices were investigated: five ZigBee transceivers, ultra low power but very short outdoor range, and six WiFi transceivers, outdoor range greater than ZigBee ones to the detriment of low power supply. In Table 2.2 and Table 2.3 are listed respectively the ZigBee and WiFi devices features.

**Table 2.2 – IEEE802.15.4 transceiver.**

	<b>RF300PD1</b>	<b>TelosB</b>	<b>JN5 148</b>	<b>CC2420</b>	<b>SM200P81</b>
<b>Data rate [kbps]</b>	150	250	500	250	250
<b>Frequency [GHz]</b>	0.915	2.4	2.4	2.4	2.4
<b>Power supply</b>					
<b>RX[W]</b>	0.061	0.076	0.076	0.062	0.068
<b>TX[W]</b>	0.281	Not specified	0.363	0.058	0.074
<b>Voltage [V]</b>	3.3	3.3	3.3	3.3	3.3
<b>Output power [dBm]</b>	20	-24 / 0	20	0	3
<b>Sensitivity [dBm]</b>	-121	-94	-98	-95	-100
<b>Bus</b>	I2C	I2C	SPI	SPI	I2C
<b>Size [mm<sup>2</sup>]</b>	34x47	65 x 31	18x41	7x7 (Chip)	29.8x19
<b>Outdoor range [m]</b>	Up to 4800	75 / 100	Up to 4000	100	300



Figure 2.2 – ZigBee, from left to right: RF300PD1[32], TelosB[33], CC2420[34], SM200P81[35], JN5 148-001[36].

Table 2.3 – IEEE802.11b transceiver.

	WiBear	TiWi-R2	SM700PC1	XG880MU	HW86052	GS1011M
Data rate [Mbps]	1	11	0.25	6	11	1
Frequency [GHz]	2.4	2.4	2.4	2.4	2.4	2.4
<b>Power supply</b>						
RX[W]	0.990	0.36	0.108	0.825	0.584	0.462
TX[W]	1.155	1.008	0.695	1.485	0.825	0.825
Voltage [V]	3.3	3.3	3.3	3.3	3.3	3.3
Output power [dBm]	19	20	20	17	15	18
Sensitivity [dBm]	-98	-89	-96	-82	-85	-92
Bus	SPI	I2C	I2C	TBD	I2C	I2C
Size [mm <sup>2</sup> ]	50x20	18x13	25x36	20x23	47x37	34x25
Outdoor range [m]	TBD	TBD	2400	300	300	TBD



Figure 2.3 – IEEE802.11b ISL transceiver, from the left to the right: WiBear[37], TiWi-R2[38], SM700PC1[39], XG880MU[40], HW86052[41], GS1011M[42].

### Subsection 2.1.3 - ISL dimensioning

#### Link budget

The link budget is calculated adding all the gains and losses from the transceiver to the receiver. It accounts for the attenuation of the transmitted signal due to propagation, as well as the antenna gains, waveguide loss, medium loss and miscellaneous loss. For a line-of-sight radio system, the primary source of loss is the decrease of the signal power due to uniform propagation, proportional to the inverse square of the distance.

A link budget equation expressed logarithmically might look like this:

$$P_r = P + L_t + G_t + L_{FS} + L_M + G_r + L_r$$

where:

- $P_r$  is the received power
- $P$  is the transmitter output power
- $L_l$  includes all the transmitter to antenna line losses
- $G_t$  is the transmit antenna gain
- $L_{FS}$  is the free-space loss
- $L_M$  are miscellaneous losses (misalignment, polarization mismatch, other losses...)
- $G_r$  is the receive antenna gain
- $L_l$  includes all the antenna to receiver line losses

The loss due to propagation between the transmitting and receiving antennas can be written in dimensionless form by normalizing the distance to the wavelength:

$$L_{FS} = 20 \cdot \log_{10} \left( \frac{4\pi \cdot r}{\lambda} \right)$$

In which  $r$  is the transmitting and receiving antennas distance and  $\lambda = c/f$  is the wavelength ( $c$  is the light velocity and  $f$  is the frequency).

The ratio of received Energy-per-bit to noise-density is defined as:

$$\frac{E_b}{N_0} = \frac{P \cdot L_l \cdot G_t \cdot L_{FS} \cdot L_M \cdot G_r}{k \cdot T_s \cdot R}$$

where  $k$  is the Boltzmann's constant ( $1.38 \cdot 10^{-23}$  J/K),  $T_s$  is the system noise temperature and  $R$  is the data rate. The same expression in dB is (power, losses and gains are express in dB):

$$\frac{E_b}{N_0} = P + L_l + G_t + L_{FS} + L_M + G_r - 10 \cdot \log_{10} k - 10 \cdot \log_{10} T_s - 10 \cdot \log_{10} R$$

that can be written as:

$$\frac{E_b}{N_0} = EIRP + L_{FS} + L_M + \frac{G_r}{T_s} + 228.6 - 10 \cdot \log_{10} R$$

The threshold power incoming to the receiver antenna is:

$$P_{required} = P + L_l + G_t + L_{FS} + L_M$$

so, it can be substituted in link budget equation as:

$$P_{required} = \frac{E_b}{N_0} + 10 \cdot \log_{10} k + 10 \cdot \log_{10} T_s + 10 \cdot \log_{10} R - G_r$$

From Figure 2.4 the BER level of  $10^{-6}$ , commonly used for space application, refers to a  $E_b/N_0$  value comprised between 10 and 11. A value of 11 will be used to be conservative. Comparing the received power with the threshold power we can dimension the link budget varying the design variables: in the case of ISL they are antennas gains, free space loss depending on link range and  $E_b/N_0$  (varying data rate).

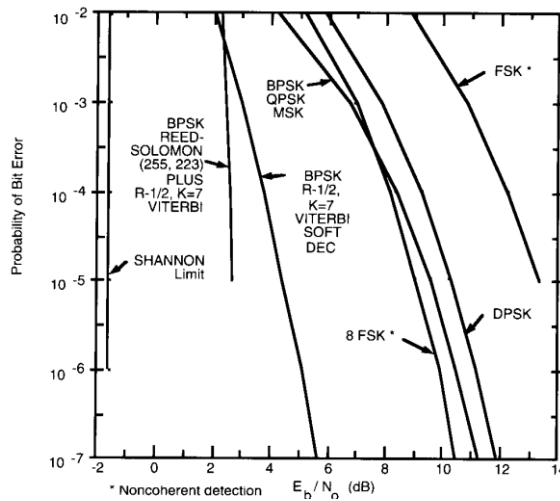


Figure 2.4 –  $E_b/N_0$  of the signal vs. BER for various modulations.

Link budget design steps are:

- Select carrier frequency and transmitter power from transceiver datasheet
- Estimate RF losses between transmitter and antenna: usually between -1 and -3 dB, due to very short cable lengths (maximum satellite dimension is 0.3 m) we consider a value of -1 dB
- Estimate the maximum antenna pointing offset angle: due to the short distance between the two satellites, we consider them on the same plane, so the offset angle depends on the ADCS accuracy (less than  $5^\circ$ ) and on the relative position. Setting an angle of  $30^\circ$  we permit to the satellites to realize the main formation geometries.
- The transmitting and receiving gains antennas are given by the antennas datasheets.
- Calculate space loss
- Estimate the system noise temperature
- Calculate BER for the specific system
- Calculate  $E_b/N_0$  for the selected modulation and coding technique (Figure 2.4)
- Add 1 dB to the theoretical value for implementation loss
- Calculate the link margin: difference between the expected value of received power calculated and the required power (threshold power)
- Adjust input parameters until the margin is at least 3dB greater than the threshold power.

In Table 2.4 are reported the design parameters common to every transceiver that will be investigated.

Table 2.4 – Parameters for the ISL design.

Parameter	Value	Comments
TX and RX waveguide loss	-1dBm	Estimate RF losses between transmitter and antenna
Misalignment angle ( $\theta$ )	$30^\circ$	
Directivity function	0.6667	For a dipole antenna ( $l=\lambda/2$ ): $f = \cos^2\left(\frac{\pi}{2} \sin \theta\right) / \cos^2 \theta$
Gt	0 dBi	Omnidirectional antennas

Parameter	Value	Comments
<b>Gr</b>	0 dBi	Omnidirectional antennas
<b>Noise temperature</b>	10000 K	Expected noise temperature of the antenna exposed to the Sun
<b>BER</b>	10 <sup>-6</sup>	Means value for space application
<b>Eb/N0</b>	11	BPSK – QPSK modulations
<b>Implementation loss</b>	1 dB	
<b>Boltzmann's constant</b>	1.38·10 <sup>-23</sup> WsK <sup>-1</sup>	
<b>Pr margin</b>	+3 dBm	

In Table 2.5 and Table 2.6 are shown the design results respectively for the IEEE802.15.4 protocol transceivers and for the IEEE802.11b protocol one:

Table 2.5 – IEEE802.15.4 transceivers calculated outdoor range.

	RF300PD1	TelosB	JN5 148	CC2420	SM200P81
<b>Output power [dBm]</b>	20	0	20	0	3
<b>Frequency [GHz]</b>	0.915	2.4	2.4	2.4	2.4
<b>Data rate [kbps]</b>	150	250	500	250	250
<b>Sensitivity [dBm]</b>	-121	-94	-98	-95	-100
<b>Calculated outdoor range [m]</b>	Over 100000	200	3200	220	550

Table 2.6 – IEEE802.11b transceivers calculated outdoor range.

	WiBear	TiWi-R2	SM700PC1	XG880MU	HW86052	GS1011M
<b>Output power [dBm]</b>	19	20	20	17	15	18
<b>Frequency [GHz]</b>	2.4	2.4	2.4	2.4	2.4	2.4
<b>Data rate [Mbps]</b>	1	11	0.25	6	11	1
<b>Sensitivity [dBm]</b>	-98	-89	-96	-82	-85	-92
<b>Calculated outdoor range [m]</b>	2800	1100	2400	350	400	1200

### Data packet

The inter-satellite link must be designed to permit the communication of coordinates, attitude and time to perigee to the second satellite. These data are useful to avoid collision and to maintain the alignment to guarantee the communication link. In the eyes of formation flying there is a slave satellite that must follow the master satellite motion, so the first one has to implement a relative position control using position vectors in the inertial reference system of both satellites ( $r_{IN}^M$  master position vector,  $r_{IN}^S$  slave position vector) and the rotational matrix from inertial to Hill systems ( $A_{EH-IN}$ ). Master satellite could communicate to the slave one his own position vector and rotational matrix, that must be calculated on board of master. Depending on accuracy of the transmitted data and the number of data, a data packet dimension can be calculated.

Table 2.7 – ISL Data packet.

	Data	One data dimension	Total data dimension	Data accuracy
<b>Coordinates</b>	Position ( $r_{IN}^M$ )	24	3x24	1m
	Rotational matrix ( $A_{EH-IN}$ )	24	6x24	
<b>Attitude</b>	Quaternions	16	4x16	0.01deg
<b>Time to perigee</b>		24	24	0.001sec
<b>Total data packet</b>			<b>304</b>	

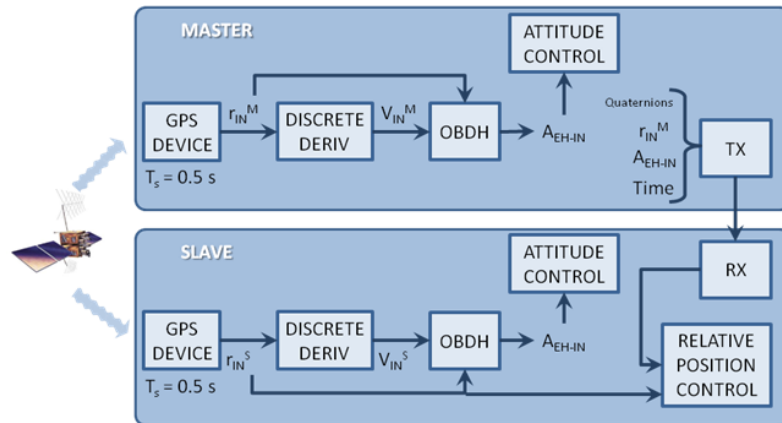


Figure 2.5 – ISL data block diagram.

In Table 2.7 are showed the data packet composition and dimension and in Figure 2.5 is represented the logic block diagram.  $T_s$  is the GPS receiver sampling time. The transmission is every 4 s, according to Kalman filter time step, so the data rate must be almost 76 bps. The wireless data packet is almost 1 Mbps, so data string can be repeated several times in the same data packet to correct errors.

### Packet Format

802.11b uses a Direct Sequence Spread Spectrum (DSSS) Physical layer for signal modulation and coding, and maintains the same frequency usage over time while using only a specific channel within the 2.4 GHz ISM band. The maximum raw data rate for 802.11b is 11 Mb/s. ZigBee terrestrial wireless technology operates in the ISM band: 868 MHz in Europe, 915 MHz in the United States and 2.4 GHz all over the world. 802.15.4 protocol uses a DSSS or a Frequency-Hopping Spread Spectrum (FHSS) Physical layers.

Figure 2.6 show the data packet relatives to the DSSS coding and Binary Phase-Shift Keying (DBPSK) or Quadrature Phase-Shift Keying (DQPSK) modulation. In the Table 2.8 are summarized dimension, data rate and description of every field of the packet format. Both the preamble and the header are transmitted at 1 Mbps, so the transmission time is 192  $\mu$ s. The PSDU block can be transmitted at deferent speed according to the modulation (DBPSK or DQPSK). Figure 2.7 and Table 2.9 describe the FHSS data packet.

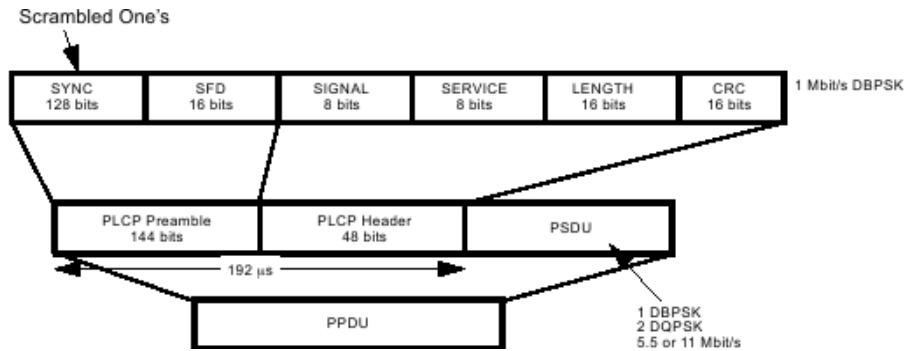


Figure 2.6 – DSSS Physical Protocol Data Unit (PPDU).

Table 2.8 – DSSS packet format details.

Field	Size	Data Rate	Description
<b>SYNC</b>	128 bits	1 Mbps	Synchronize the receiver's carrier tracking and timing prior to receiving the start of frame delimiter.
<b>SFD</b>	16 bits	1 Mbps	Start of frame delimiter: information marking the start of a PPDU frame.
<b>Signal</b>	8 bits	1 Mbps	Defines which type of modulation must be used for demodulate (DBPSK or DQSK modulation).
<b>Service</b>	8 bits	1 Mbps	Reserved for future use.
<b>Length</b>	16 bits	1 Mbps	Indicates the number of microseconds necessary to transmit the frame.
<b>CRC</b>	16 bits	1 Mbps	Contains the results of a calculated frame check sequence.
<b>PSDU</b>	Dependent on Length field	1 Mbps DBPSK 2 Mbps DQPSK 5.5-11 Mbps CCK	Data

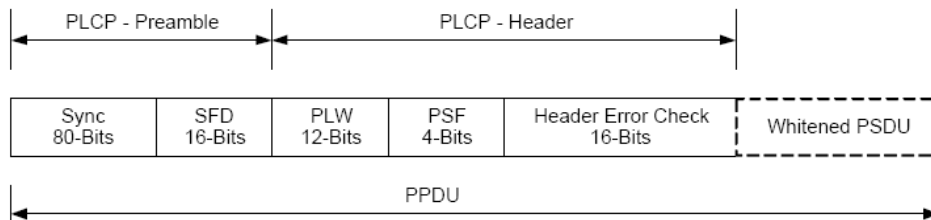


Figure 2.7 – FHSS Physical Protocol Data Unit (PPDU).

Table 2.9 – FHSS packet format details.

Field	Size	Data Rate	Description
<b>SYNC</b>	80 bits	1 Mbps	
<b>SFD</b>	16 bits	1 Mbps	
<b>PLW</b>	12 bits	1 Mbps	Specifies the length of the PSDU in octets.
<b>PSF</b>	4 bits	1 Mbps	PLCP (Physical Layer Convergence Procedure) signaling field: identifies the data rate of the whitened PSDU ranging from 1 Mbps to 4.5 Mbps in increments of 0.5 Mbps. The PLCP preamble and header are transmitted at the basic rate.
<b>Header Check Error</b>	16 bits	1 Mbps	Contains the results of a calculated frame check sequence from the sending station.
<b>PSDU</b>	4095 byte	1 to 4.5 Mbps	Data



### Subsection 2.1.4 - Transceiver trade off (ISL)

The features on which the trade off is based are, in order of importance: the power consumption, the outdoor range and the data bus type. Despite of all the transceiver considered are ultra low power supplied, few of them require lower power level. From this point of view ZigBee are very interesting. WiFi devices that waste less power are (in order of interest) SM700PC1, GS1011M, TiWi-R2 and HW86052. The outdoor range is a formation flying dimensioning data. To permit more freedom of relative motion geometries and to test the wireless technology at different distances, we prefer the devices characterized by outdoor range over 1 km. In particular RF300PD1 and JN5 148 ZigBee devices and WiBear, TiWi-R2, SM700PC1 and GS1011M WiFi ones are selected. In conclusion, the most interesting transceivers are RF300PD1, TiWi-R2, SM700PC1, JN5 148 and GS1011M.

## Section 2.2 - Wireless Temperature sensor

### Subsection 2.2.1 - SENSEOR TSE AS10 Wireless Temperature SAW Sensor

#### Wireless passive robust SAW temperature sensor

SENSeOR's SAW sensors [13] are wireless and batteryless temperature sensors. Their key features of this device are:

- Flexible use for testing in various configurations and environments wireless, batteryless, robust.
- Measuring temperature range:  $-15^{\circ}\text{C}$ ,  $165^{\circ}\text{C}$ .
- Various mountings available.
- Dimensions:  $5 \times 5 \times 1.5$  mm.



Figure 2.8 – TSE AS10 Wireless SAW Temperature Sensor.

According to application requirements, appropriate antennas are provided with the mounted SAW sensor. Various types of antennas have already been conceived and optimized for SAW sensors, like microstrip antennas, patch antennas, slot antennas, meander antennas, PIFA etc., depending on environment constraints, like interrogation, distance and size constraints.

The sensing system must also include a transceiver for wireless interrogation of the sensors. With appropriate configuration, up to 24 sensors can be interrogated simultaneously.

#### Working principle

The transceiver sends an electromagnetic pulse to the sensor which is converted into a mechanical wave on the surface of the acoustic wave chip (piezoelectric effect). Properties of the acoustic wave will be modified under the effect of the physical parameter which is sensed. The SAW sensor reflects these modified signals back to the transceiver, which translates the

results and provides digital output. The frequency dependence with regard to temperature is given by following equation:

$$f(\vartheta) = f(\vartheta_0) \cdot [1 + C_1 \cdot (\vartheta - \vartheta_0) + C_2 \cdot (\vartheta - \vartheta_0)^2]$$

where  $\vartheta$  is the temperature expressed in °C and  $\vartheta_0$  is 25°C. Table 2.10 reports the operating and measuring temperature range and the values of the temperature coefficient  $C_1$  and  $C_2$ . TSE AS10 is based on two resonators working at two different frequencies in the 434 MHz ISM band [433.05 MHz, 434.79 MHz]. Table 2.11 reports the resonant frequency of both resonators.

Table 2.10 – SENSEOR system temperature specifications

Temperature specifications	
Operating temperature range	-40°C, 200°C
Measuring temperature range	-15°C, 165°C
Accuracy	+/- 2°C
Typical first order temperature coefficient C1 resonator 1	6.5 ppm/°C
Typical second order temperature coefficient C2 resonator 1	-20.3 ppb/°C
Typical first order temperature coefficient C1 resonator 2	1.2 ppm/°C
Typical second order temperature coefficient C2 resonator 2	-33.8 ppb/°C
Differential temperature sensitivity (typ.)	- 2.3 kHz /°C

Table 2.11 – SENSEOR electrical specifications of the sensor

Resonator electrical specifications at 25°C	
Resonant frequency resonator 1	433.63MHz ± 0.2MHz (Figure 2.9)
Resonant frequency resonator 2	434.36MHz ± 0.15MHz (Figure 2.9)
Unloaded quality factor resonator 1 (min)	10000 (typical value 12 000)
Unloaded quality factor resonator 2 (min)	10000 (typical value 12 000)

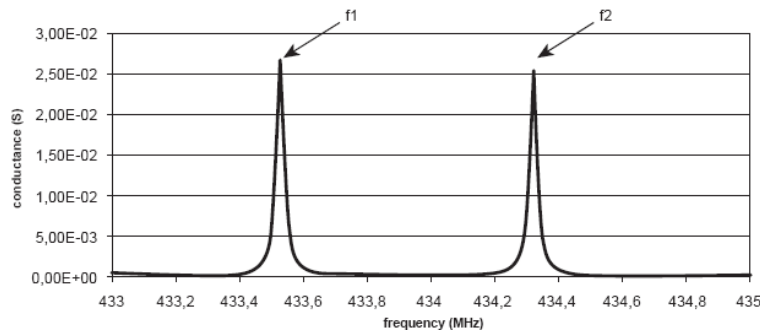


Figure 2.9 – Typical conductance of TSE AS10 at 25°C with regard to frequency.

## Applications

The SENSEOR Wireless Temperature SAW Sensor has many benefits. It enables new measurement for OEM's (Original Equipment Manufacturer) and end-users in Energy, Transportation and Aerospace:

- On moving and rotating parts
- In explosive, corrosive, electromagnetic fields, radiated environments
- In confined and inaccessible places
- Where cabling costs too much or is impossible


- In multisensor or multitasking configurations
- For process optimization and better equipment through condition monitoring and process control

### Subsection 2.2.2 - SENSEOR interrogation unit

SENSeOR's wireless interrogator (transceiver) at 434MHz is designed for wireless interrogation of SAW resonator sensors. The device considered is the WR E010 Ultra-compact [43]. It emits no more than 10 dBm peak power in the 433 MHz band. The Table 2.12 shows the SENSEOR transceiver features.

Table 2.12 – SENSEOR transceiver parameters

Transceiver parameters	Specifications
Consumption	85 mA / 5 V (powered by USB port)
Frequency band	[433.05 MHz, 434.79 MHz]
Digital output	Mini USB
Maximum RF Power	+ 10 dBm
Antenna connection	SMA connector
Operating temperature range	-10°C, 70°C
Interrogator distance	0.03 m, 2 m
Dimension	102 x 72 x 22 mm



### Subsection 2.2.3 - Comments

In order to adapt the Wireless Temperature SAW Sensor System to a CubeSat mission, it is fundamental to consider the imposed constraints of low available power and small volumes. Sensors are very small and easy to place on the inner side of the solar panels. Each sensor requires an antenna. SENSEOR can provide numerous types of antenna according to customer requirements. Microstrip and patch antennas are good solutions. The transceiver shows some inappropriate features. The power consumption declared from the device datasheet and reported in Table 2.12 is more than 0.425 W, so acceptable for this mission. However geometrical dimensions exceed the satellite envelope. So the interrogation unit could be replaced with a smaller transceiver.

### Subsection 2.2.4 - Alternative transceiver

To select the alternative solution to SENSEOR one few COTS devices were investigated according to mission requirements. First criteria to select the components are the transmitting frequencies: the temperature sensors impose that the transceiver sends the electronic pulse in the 434 MHz ISM band. Geometrical dimensions must be very small to permit the device assembly in the CubeSat and the power consumption must be very low. The result of the research is a selection of five very small and ultra low power transceivers. Also the costs are very low. The outdoor ranges are such as to allow an inter-satellite sensor interrogation, so that to test a power transmission between the two satellite.

### Transceiver list and properties

In Table 2.13 are showed the transceiver considered to substitute the SENSEOR interrogator.

Table 2.13 – Transceiver investigated for wireless sensor network

	MICRF620	TDA7255V	RFM12B	CC1100	SRW1011
<b>Physical layer</b>	FSK-FHSS	ASK/FSK	FSK-FHSS	FSK-FHSS	FSK/OOK
<b>Data rate [kbps]</b>	2.4	4	1.2	2.4	1.2
<b>Frequency [MHz]</b>	410 - 450	433 - 435	430 - 440	400 - 464	240 - 930
<b>Power supply</b>					
<b>RX [W]</b>	0.03	0.027	0.043	0.047	0.061
<b>TX [W]</b>	0.0575	0.040	0.050	0.088	0.099
<b>Voltage [V]</b>	2 - 2.5	2.1 - 5.5	2.2 - 3.8	1.8 - 3.6	1.8 - 3.6
<b>Output power [dBm]</b>	10	Up to 13	0	10	13
<b>Sensitivity [dBm]</b>	-110	-112/-115	-109	-111	-121
<b>Bus</b>	SPI	I <sup>2</sup> C	SPI	SPI	SPI
<b>Outdoor range [m]</b>	~500	~500	> 200	~1000	~1000
<b>Host board interface</b>	SMD	SMD	DIP/SMD	SMD	DIP/SMD

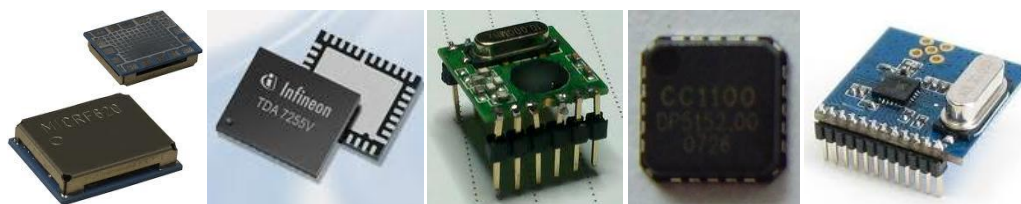


Figure 2.10 – MICRF620 [44], TDA 7255V [45], RFM12B [46], CC1100 [47], SRW1011 [48] (left to right).

### Transceiver comparison

Comparing the investigated devices we realize that the elements with lower power consumption are MICRF620 and TDA 7255V, despite the good outdoor range. The RFM12B has an output power of 0 dBm and the lower sensitivity, for which reason its outdoor range is relatively low. SRW1011 and CC1100 transceiver are immediately rejected because of their higher power consumption in comparison with the other devices features. They also need a bus adapter. The TDA 7255V, on the other hand, has a very low power consumption and a long outdoor range. The proposed antenna is the Antenna Factor ANT-433-SP [49], a 434 MHz frequency band.

# Chapter 3 - Mission analysis and system architecture

## Section 3.1 - Operative orbit definition

### Subsection 3.1.1 - Mission analysis requirements

In order to fulfill mission requirements, the operative orbit, that is reference orbit for the whole formation:

- Must investigate payloads performance within LEO altitudes along as wide as possible latitude spans
- Must maximize daylight duration, because of small available surface for power photovoltaic generation and stringent predicted power budget deriving from propulsion and attitude control subsystems, outside of common CubeSat mission capabilities
- Shall naturally satisfy End-of-Life (EOL) disposal norms without maneuvering, that means that lifetime due to atmospheric re-entry shall be no longer than 25 years.
- Shall ensure plasma and radiation effects does not overcome acceptance limit of COTS components.
- Must ensure periodical visibility windows with ground station, set at Politecnico di Milano. In a LEO scenario, ground station visibility is quite unaffected by orbital parameters, except for inclination, because of short orbital periods permits frequent passage above a particular region.

Unless it's necessary to ensure a formation flying between at least two spacecraft and a relative position control system and dedicated propulsion and attitude control subsystem are required, the reference orbit can still be uncontrolled, accommodating disturbance effects in initial orbit determination.

### Subsection 3.1.2 - Sun-synchronous conditions

The obvious choice that meet all mentioned requisites consists in a **LEO dusk-dawn sun-synchronous** orbit, which initial altitude is determined in order to maximizes available lifetime, taking in account altitude degradation due to atmospheric drag and radiation hazards. This kind of orbit ensures continuous sun visibility and is characterized by inclinations over 90°. Since it is very close to polar inclinations, this type of orbit has ground track that covers a great span in latitude and guarantees at least two passages per day nearby any location on the globe, even including the selected ground station.

A sun-synchronous orbit has a  $\Omega$  precession rate, such that it maintains an almost constant orientation with respect to the sun, matching with Earth orbital mean angular rate, which is equal to 0.9856°/day. Major semi-axis, eccentricity and inclinations can be related by the following constraint [50]:

$$\dot{\Omega} = -\frac{3}{2} J_2 \left( \frac{R_{Earth}}{a(1-e^2)} \right)^2 \sqrt{\frac{\mu}{a^3}} \cos(i) = -\frac{3}{2} J_2 \left( \frac{R_{Earth}}{p} \right)^2 n \cos(i)$$

Where  $p$  is the semi-latus rectum,  $n$  is the mean motion,  $\mu$  is the Earth's gravitational constant,  $J_2$  is the zonal harmonic coefficient ( $J_2= 0.0010863$ ),  $a$  is the semi-major axis,  $e$  the eccentricity and  $i$  the orbit inclination.

In absence of other perturbations other than  $J_2$  Earth gravitational harmonic effect, a sun-synchronous orbit can be obtained at every altitude within LEO range, setting orbit inclination, which is necessarily higher than  $90^\circ$  degrees (a sun-synchronous orbit is always a retrograde orbit). Eccentricity has a minor effect, even for highest values obtained till perigee and apogee altitudes remain within LEO ranges, as shown in Figure 3.1. According to low eccentricity dependence, subsequent analysis will be conducted assuming circular orbits.

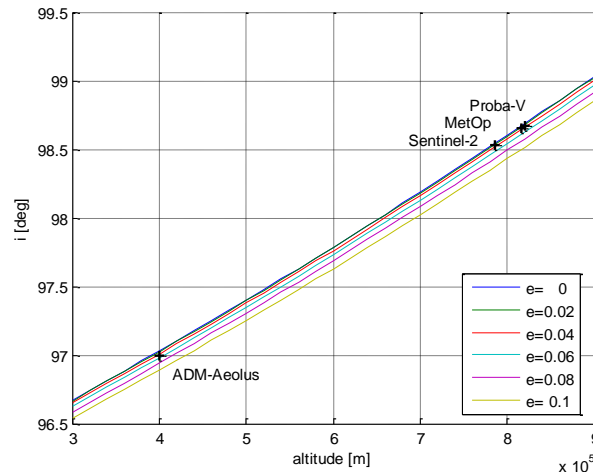


Figure 3.1 – Sun-synchronous nominal inclination for circular orbit as function of altitude

### Sun visibility on a dusk-dawn Sun-synchronous orbit

The desired orbit is a dusk-dawn sun-synchronous orbit in which sun is always in sight. Setting  $\Omega = \alpha_{\text{sun}} \pm 90^\circ$  a dawn dusk sun-synchronous orbit is obtained, where  $\alpha_{\text{sun}}$  is the Sun right ascension. In that way, Local Time of Ascending Node (LTAN) on the equatorial plane is situated nearby 6:00 or 18:00. Descending node is thereby at the opposite side. Essentially the orbit plane faces the sun.

Over a year, Sun declination spans an angle range of  $\pm 23.5^\circ$  respect to equatorial plane, then, for lowest altitudes, eclipse can still occur, as depicted in Figure 3.2, nearby solstices:

- 1)  $\Omega = \alpha_{\text{sun}} + 90^\circ$ : eclipse occurs in boreal summer
- 2)  $\Omega = \alpha_{\text{sun}} - 90^\circ$ : eclipse occurs in boreal winter

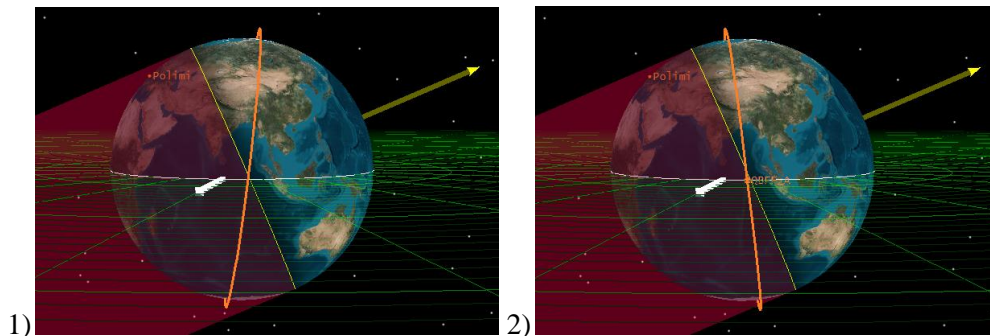
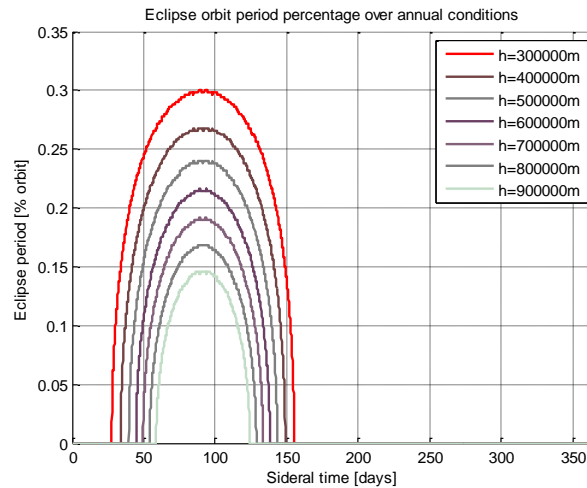


Figure 3.2 - Sun orientation respect to orbit plane at boreal summer solstice, in dawn dusk sun-synchronous conditions with  $\Omega = \alpha_{\text{sun}} + 90^\circ$  (left) or  $\Omega = \alpha_{\text{sun}} - 90^\circ$  (right)



**Figure 3.3 – Eclipse orbit period percentage over a sidereal year, for circular sun-synchronous orbits at various altitudes, for  $\Omega=\alpha_{\text{sun}}+90^\circ$ . Time axis starts at vernal equinox.**<sup>1</sup>

Assuming dawn-dusk sun-synchronous circular orbits, oblate Earth (Earth reference ellipsoid model), given a set of initial semiaxis, sun visibility has been investigated over sidereal year propagation of a J2 only perturbed problem. A long term continuous daylight period effectively results, but it's always interrupted nearby previously mentioned condition at every LEO altitude, as shown in Figure 3.3.

Eclipse periods, at lowest altitude, reach 30% of the orbital period, which is not such a smaller percentage than can be obtained in a general LEO orbit.

In any case, there are no launchers dedicated to a single CubeSat class satellite, so they always take part of a launch program as secondary payload. Typically, already flown picosatellites has been released in LEO orbits or, occasionally, in orbits of particular interest such as sun-synchronous orbits indeed.

It can be reasonably supposed that, if an existing mission is delivered in a dawn-dusk LEO orbit at a certain altitude, it probably has the same long period daylight requirements of current mission and then all considerations already mentioned would be satisfied.

## Section 3.2 - Launch opportunities

Commercial launch vehicles often launch with excess performance capability due to large spacecraft being “volume-limited” rather than “mass-limited”. To fully utilize this excess capability, small secondary payloads can be launched along with the primary payload, providing a means to economically launch small spacecraft, as well providing some additional revenue to the launch provider.

SpaceX<sup>2</sup> and ATK/Lockheed Martin<sup>3</sup> are working to create nanosatellite launch opportunities with NASA support [51]. The agency’s Launch Services Program created the Educational

<sup>1</sup> Time axis starts at vernal equinox, and nearby summer solstice (after about 90 days) there are eclipses periods which duration grows as the altitude reduces. The same graph can be obtained starting from autumnal equinox, for  $\Omega=\alpha_{\text{sun}}+90^\circ$

Launch of Nanosatellite (ELaNa) initiative to provide secondary payload opportunities specifically for student-built CubeSats. Spaceflight provides routine access to space at affordable prices by using standard flight interfaces, frequent flight opportunities and published commercial pricing.

NASA has announced a continuation of an opportunity for small satellite payloads to fly on rockets planned to launch in 2012, 2013 and 2014. These CubeSats could be auxiliary cargo on previously planned missions.

Spaceflight [52] instead is a commercial provider of secondary payload flight services for fixed and deployable cargo and spacecraft for orbital and suborbital vehicles. It provide, other than launch service, payload integration service and on-orbit service.

However, for preliminary analysis, ESA bulletin taken by launch opportunities are subsequently examined. See also ref. [53] and[54].

### **Subsection 3.2.1 - Launcher interface**

Key to the success of the CubeSat concept is the possibility of isolation from the primary payload and launch vehicle that allays launch provider concerns of potential damage to, or impediment to the deployment of, the primary payload.

The most widely used solution is Cal Poly's P-POD, a standard mechanism that attaches a CubeSat to a primary payload or launch vehicle. The P-POD, essentially a box with a spring-loaded "kicker-plate," ejects the CubeSats in "jack-in-the-box" fashion when the door is opened by electrical command. Certified for a wide variety of launch vehicles, the P-POD/Mark III accommodates up to three individual 1U CubeSats or one 3U configuration. Another CubeSat deployer, the UTIAS XPOD (University of Toronto Institute for Aerospace Studies) supports the CubeSat standard while accommodating non-longitudinal configurations as well.

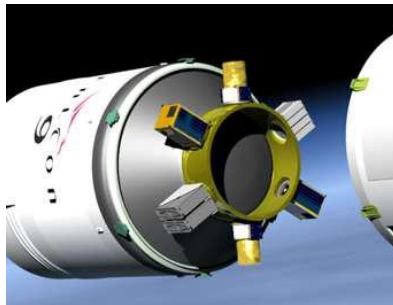


**Figure 3.4 - Example of secondary payload accommodations.**

Secondary Payload accommodations provide the required mechanical, electrical, and thermal interfaces for the Secondary Payloads as agreed-upon in the launch contract. The Secondary Payloads are deployed where required along the mission trajectory, but always on a strict basis of non-interference with the primary payload mission.

---

<sup>2</sup> SpaceX aims to develop a family of launch vehicles which will ultimately reduce the cost and increase the reliability of space access by a factor of ten. This target is direct connect with the newly emerging market for private and commercial space transport.

<sup>3</sup> Alliant Techsystems and Lockheed Martin Corporation developed Athena Launch Vehicle Family for LEO.

---





Figure 3.5 – Cal Poly's and NovaNano FlyMate Picosatellite Deployers.

The tubular design of the POD creates a predictable linear trajectory for the CubeSats resulting in a low spin rate upon deployment. The satellites are deployed from the POD by means of a spring and glide along smooth flat rails as they exit the POD. After a signal is sent from the launch vehicle to the POD release mechanism, a spring-loaded door opens and the CubeSats are deployed by the main spring.

Access ports provided on the side panels of the P-POD allow access to the CubeSats after integration and may be used to charge batteries and run diagnostics. These ports are staked and are not re-opened once CubeSat integration and acceptance testing is complete.

Table 3.1 – Deployment systems (POD)

	NovaNano FlyMate	Cal Poly's P-POD	UTIAS/SFL XPOD
<b>Envelope</b>	3x1U, 2U+1U, 3U, 4U	From 0.5U to 5U 6U in two level	XPOD Triple: 3U XPOD DUO: 20x20x40 cm
<b>Deployment</b>	Controlled and separate orbit insertion Adjustable ejection speed (0.5-2 m/s)	Controlled and separate orbit insertion Adjustable ejection speed (1.6 m/s)	

### Subsection 3.2.2 - Short term scheduled launches

CubeSats are most commonly delivered to LEO, defined as 160–2000 km above the Earth's surface; other orbital details are typically determined by the destination of the primary payload. Choice of orbit is further constrained by current guidelines adopted by UN Inter-Agency Space Debris Coordination Committee (IADC), with which all major space-faring nations are now harmonized: satellites are to either actively or passively re-entry within 25 years after launch. Without active maneuvering or de-orbit capability, a CubeSat is therefore altitude limited, depending on its ballistic coefficient (mass, cross-sectional area) and solar effects on upper atmosphere density, to 500–600 km.

Table 3.2 – Secondary payload launch opportunities

Mission	Orbit	Date launch
<b>MetOp</b>	817 altitude, Sunsynchronous RAAN 9.30	Apr 2012
<b>Proba-V</b>	820 altitude, Sunsynchronous RAAN 10.30	May 2012
<b>Sentinel-2</b>	786 altitude, Sunsynchronous RAAN 22.30	Late 2012
<b>Swarm</b>	490 / 530 altitude, 87.4° / 88° inclined	Jul 2012
<b>ADM-Aeolus</b>	400 altitude, Sunsynchronous dawn dusk	Early 2014

The launches that will be examined are the ESA bulletin[55] next mission which will be delivered in sun-synchronous orbits. In Table 3.2 are listed the features of the possible launches.

ADM-Aeolus orbit is set as reference in order to conservatively evaluate relative position and attitude control capability. This orbit is sun-synchronous dawn dusk to have the better sun visibility, but is also the worst condition in terms of atmospheric drag acceleration and of magnetic, aerodynamic and gravity gradient disturbance torques.

An alternative to secondary payload launch, CubeSat launch mission can be considered. GAUSS Group (Gruppo di Astrodinamica Università degli Studi "la Sapienza"[56]) frequently organizes CubeSat or nanosatellite dedicated launches. In this case we could have mayor influence on orbit choice and launch date. In the following, environmental effects will be still investigated at every LEO altitude, to provide sufficient criteria in case of an alternative orbit selection is necessary.

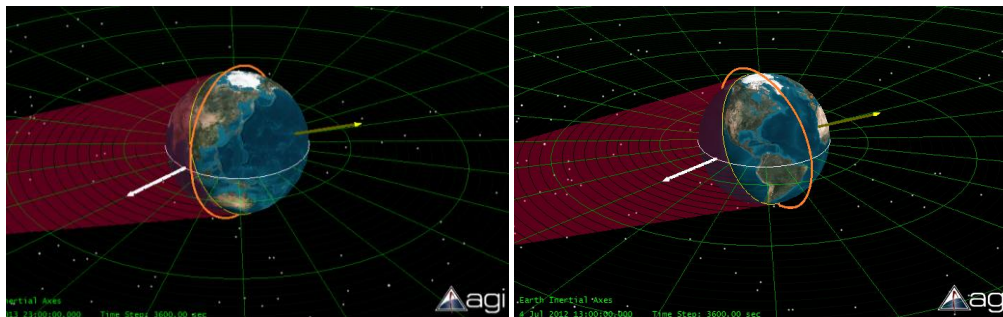


Figure 3.6 – Visualization of dawn dusk RAAN condition: the sun visibility in Aeolus orbit (Left) is continuous, while eclipse occurs for a RAAN different to 6.00 h (Right).

### Subsection 3.2.3 - ADM-Aeolus

In this subsection the ADM-Aeolus orbit features are examined. Considering the launch date is now defined nearby early 2014, the orbital propagation was conducted from the hypothetical date of March 1<sup>st</sup>, from which a continuous sun visibility period starts, at this altitude.

LOP propagator, 12-order spherical harmonic gravity model, aerodynamic, solar and third body force models have been selected, applying typical 3U CubeSat cross area to mass ratio of about 0.01 m<sup>2</sup>/kg.

Figure 3.8 shows semi-major axis, apogee and perigee altitude decay during lifetime. Because of the low semiaxis, the lifetime is about 5 month as shown. However the sun visibility is guarantee for all the life time (Figure 3.7).

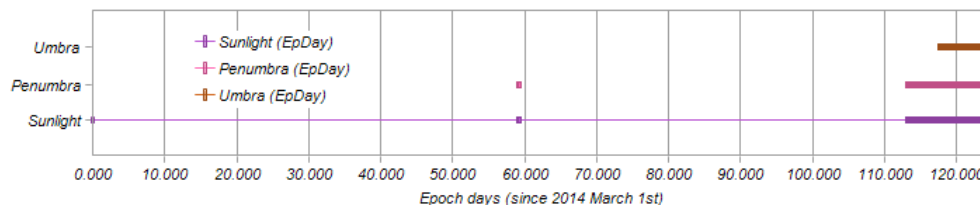


Figure 3.7 – ADM-Aeolus orbit sun visibility during lifetime. Only immediately before final atmospheric re-entry eclipses can occur, even nearby sun-synchronous RAAN and inclination.

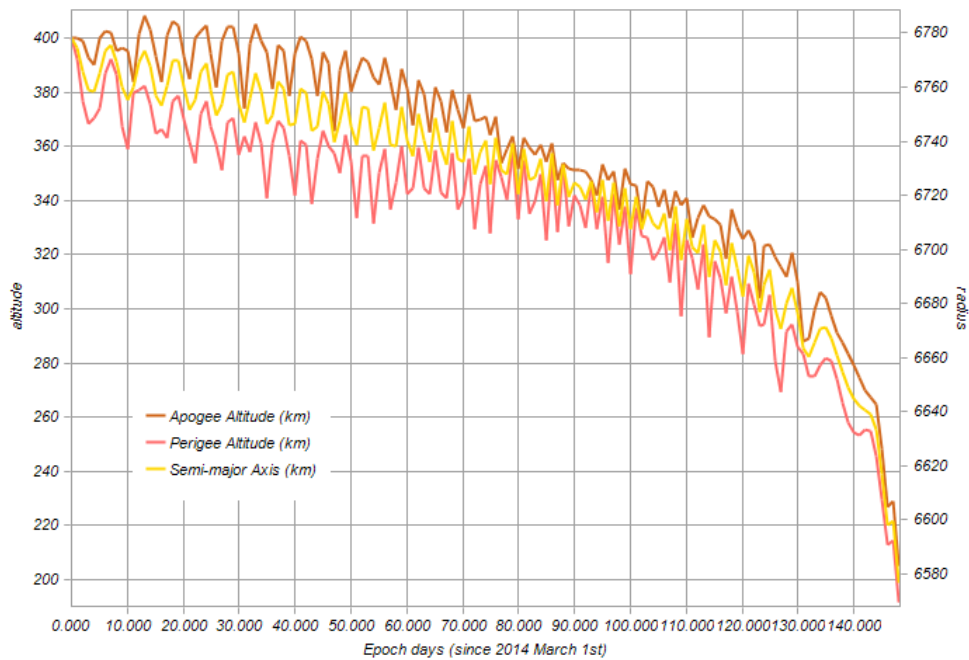


Figure 3.8 – ADM-Aeolus orbital parameters time evolution due to atmospheric drag.

## Section 3.3 - Launch selection criteria

ADM-Aeolus scheduled launch is an affordable choice, but its launch date and vector have still to be defined, up to now. It is expected to launch on a small-capacity booster such as Vega, Rockot and Dnepr. Then, secondary payload participation has to be negotiated.

It's thereby necessary to define some acceptance criteria in case of launch delays or even in case of it becomes necessary to identify an alternative mission to participate to. The reference orbit definition must be seen as a definition of a series of requisites to choose an existing planned launch which participate to.

### Subsection 3.3.1 - Atmospheric drag

#### Orbit degradation due to atmospheric drag

Atmospheric drag is a disturbance force acting opposite the velocity vector and proportional to local atmospheric density. Its effect is directly traduced in decreasing the orbit kinetic energy (and thus total energy) and it's more incisive nearby perigee passages. In this manner, in a first phase, there is an apogee radius and eccentricity decreasing, then, also perigee radius decreases, as orbit becomes more circular. Disturbance acceleration in LVLH frame is:

$$\mathbf{d}_{drag} = -\rho(\mathbf{r})|\mathbf{v}^*|^2 \left( \frac{A_{cross} C_D}{2m_{sat}} \right) \hat{\mathbf{t}} = -\rho(\mathbf{r})|\mathbf{v}^*|^2 \left( \frac{A_{cross} C_D}{2m_{sat}} \right) \sqrt{\frac{\mu}{p}} \begin{bmatrix} e \sin \theta \\ 1 + e \cos \theta \\ 0 \end{bmatrix}$$

Where  $A_{cross}$  is section area perpendicular to relative wind vector  $\mathbf{v}^*$ ,  $C_D$  is drag coefficient, (which for simple shapes is commonly set equal to 2.2) and  $\rho(\mathbf{r})$  is the atmospheric density, which determination is the main issue. Accurate Earth atmospheric models take in account solar cycles, seasons, local light condition and, first of all, geographical coordinates. That's

why it's important to investigate since the beginning perturbation effects on highly inclined orbits.

As purely tangential force, atmospheric drag never affects plane orientation that is  $\Omega$  and inclination. Out of plane component is null, unless rotating atmosphere is considered in relative wind calculation and such this effect is still not critical.

### Long period propagation techniques

Applying GVE (see Appendix B), equations to the following expression of atmospheric drag:

$$\mathbf{d}_{drag} = -\rho(\mathbf{r})|\mathbf{v}|^2 \left( \frac{A_{cross} C_D}{2m_{Sat}} \right) \hat{\mathbf{t}} = -\rho(\mathbf{r})|\mathbf{v}| \left( \frac{A_{cross} C_D}{2m_{Sat}} \right) \sqrt{\frac{\mu}{p}} \begin{bmatrix} e \sin \theta \\ 1 + e \cos \theta \\ 0 \end{bmatrix}$$

consequent semiaxis and eccentricity variation during one orbit period are respectively, [50]:

$$\Delta a = -\frac{A_{cross} C_D}{m_{Sat}} a^2 \int_0^{2\pi} \rho(\mathbf{r}) \frac{(1 + e \cos E)^{3/2}}{(1 - e \cos E)^{1/2}} dE$$

$$\Delta e = -\frac{A_{cross} C_D}{m_{Sat}} a (1 - e^2) \int_0^{2\pi} \rho(\mathbf{r}) \frac{(1 + e \cos E)^{1/2}}{(1 - e \cos E)^{1/2}} \cos E dE$$

They are function of the eccentric anomaly, and then they are function of initial true anomaly and perigee argument, which determine the radius trend at any latitude over an orbit. In order to obtain a lifetime estimation, using a long period propagation, spherical Earth model and near circular orbits should be assumed, neglecting geographical dependency on MSISE00 atmospheric model, so that density depend only from orbit radius absolute value.

### Long term propagation varying initial semiaxis and eccentricity

On the other hand, STK software already implements a long term propagator for this model, averaging atmospheric effects over orbit periods, using various atmospheric model types. We can then evaluate MSISE00 model, including latitude, local apparent time and solar flux dependence, identifying as worst case an initial perigee nearby equator. A 3U CubeSat structure is assumed to be invested on its lateral side, and then ballistic coefficient is set to 0.03 kg/m<sup>2</sup>. Rotating atmosphere is considered.

The effect of initial eccentricity has been investigated. Eccentricity critically reduces perigee altitude at the same semiaxis, determining a lifetime decreasing. Generally it's possible to set perigee altitude of an eccentric orbit in correspondence to the Earth South Pole, in order to reduce altitude at passages over South-Atlantic anomaly to mitigate radiation effect. However, this strategy is immediately discarded, because if reference orbit is not controlled perigee argument exhibits high variations, causing orbit major semiaxis to quickly overturn.

**Table 3.3 – Small launcher vehicles typical injection orbital parameters accuracy for LEO circular orbit, comprising polar and sun-synchronous orbits. (Rockot user manual [57])**

Orbital parameter	Accuracy (3 $\sigma$ )
Altitude	$\pm 1.5\%$
Inclination	$\pm 0.06^\circ$
RAAN	$\pm 0.05^\circ$
Eccentricity	$\leq 0.005$

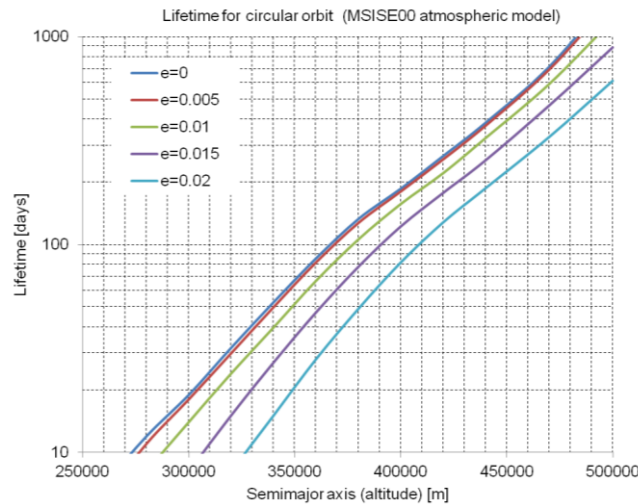


Figure 3.9 - STK propagation results for lifetime at various initial semi-axis and eccentricity

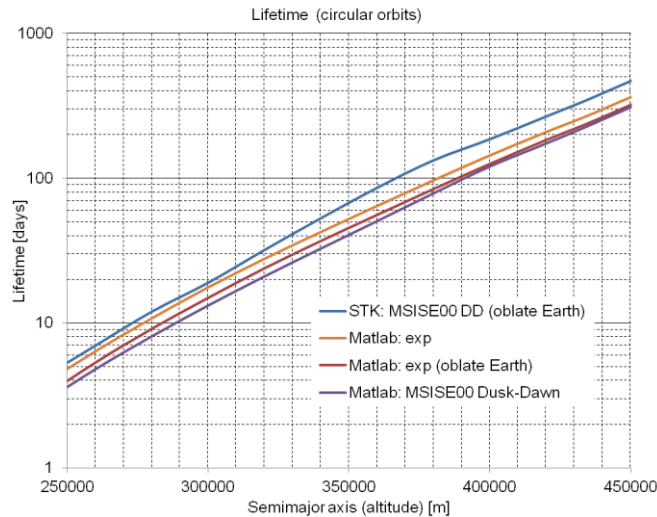


Figure 3.10 – STK and Matlab propagation results comparison, for circular orbit lifetime at 0.005 initial eccentricity, with various model and hypothesis

In conclusion, a circular orbit is indeed preferred and it is in general, the common choice in case of sun-synchronous orbits. We assume from now on initial eccentricity null, taking in account a 0.005 error due to launcher injection accuracy, reported in Table 3.3. A dedicated model has been implemented in MATLAB environment, to be integrated in previous continuous visibility analysis propagator. Under the hypothesis of oblate Earth, 0.005 initial eccentricity, MSISE00 atmospheric model, at AMD-Aeolus launch date, its results are validated comparing to STK simulations and show to be conservative, as depicted in Figure 3.10.

### Subsection 3.3.2 - Continuous sun visibility propagation including drag

As depicted at the beginning of the present chapter, continuous visibility condition can be obtained if spacecraft is injected in a dawn-dusk sun-synchronous orbit at the proper LTAN and launch dates.

Assuming desired date and RAAN launch condition is obtained, corresponding to a starting continuous daylight period, both drag and J2 effects have been propagated, in order to evaluate how much lifetime elapses, before atmospheric orbit degradation causes re-entry or simply before an eclipse period prematurely occurs due to semiaxis lowering and loss of sun-synchronicity.

In Figure 3.11, propagations are conducted at various altitudes, starting in such this continuous visibility start condition. Lifetime results for a controlled orbit (only J2 effect) and an uncontrolled one (J2 and drag effect) are compared.

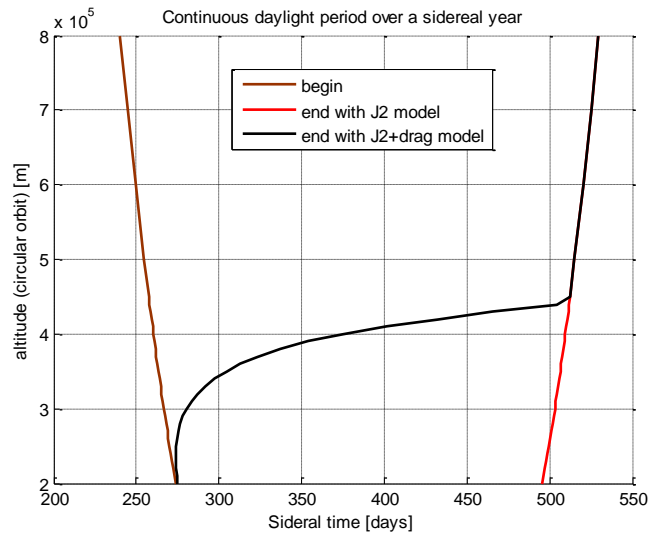


**Figure 3.11 - Continuous daylight periods start times and end times, in elapsed days since 2014 vernal equinox. Simulation are started at each considered altitude at the corresponding visibility period start time and then propagated till atmospheric re-entry or first eclipse period occurred.**

### Subsection 3.3.3 - Preliminary analysis for spacecraft charging

A preliminary Total Dose analysis was implemented in function of orbital altitude. The orbital inclination was fixed on  $98^\circ$ , the inclination variation of a few degrees does not cause substantial changes in the results. To calculate spacecraft charging was used SPENVIS (ESA's Space Environment Information System)[58].

SPENVIS' code for space-shielding radiation dose calculations determines the absorbed dose as a function of the thickness of spacecraft aluminium shielding material, given the electron and proton fluences encountered in orbit.

SPENVIS calculates, for arbitrary proton and electron incident spectra, the dose absorbed in small volumes of different detector materials (silicon in this case) at the centre of a aluminium shield solid sphere, as a function of sphere radius. The shield geometries are illustrated in Figure 3.12.

The overall uncertainty of the final results, including the uncertainties in cross sections used and those due to statistical fluctuations and smoothing of the Monte Carlo data, is estimated to be 10%.

Total Dose trend is plotted in Figure 3.13 in function of thickness of aluminium shield for different orbital heights, from 350 km to 1000 km. Circular sunsynchronous orbits are considered for a lifetime of 365 days.

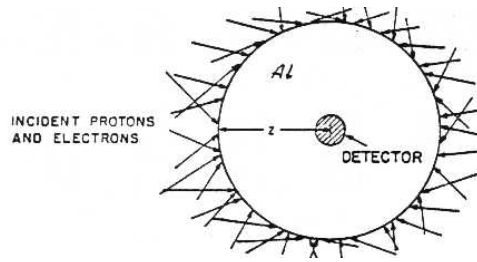


Figure 3.12 – Shielding configuration.

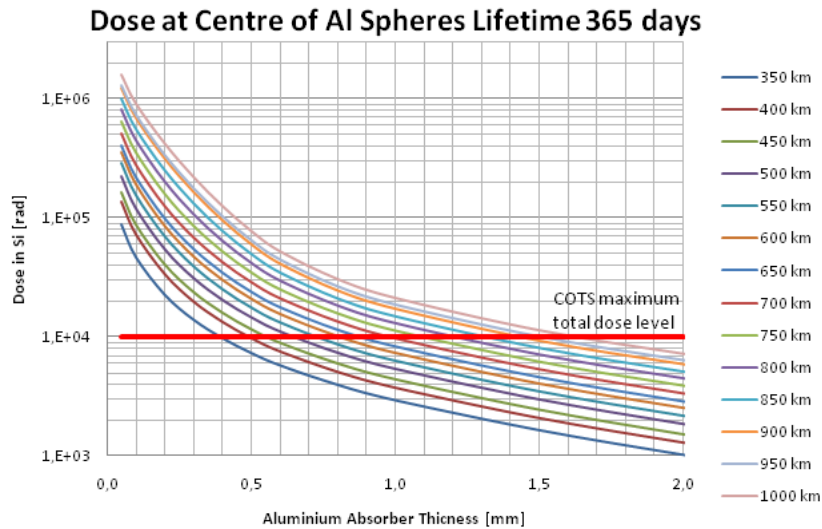


Figure 3.13 – Total Dose vs. aluminium shielding thickness.

Aluminium required thickness increases with altitude. In order to shield total dose up to 10 krad, the maximum total dose commonly considered for COTS devices, shielding thickness results very low. However, solar panel substrate material is not aluminium, but polychlorinated biphenyls (PCB). Carbon fiber composite and aluminium substrate are available on request. It is necessary to calculate the aluminium equivalent thickness relative to PCB solar panel.

Considering the calculation result of a study to develop composite material for LEO uses [59], showed in Figure 3.14, it's easy to notice that the curves relative to polymer are nearly coincident. So the curve relative to polyethylene (PE) can be considered for the equivalent Aluminium thickness calculation.

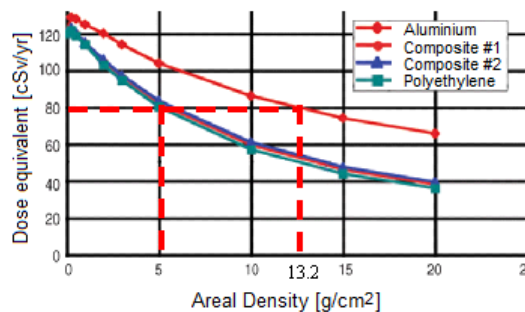


Figure 3.14 – Dose Equivalent vs. areal density.

Table 3.4 – Aluminium and PE density features for a reference 80 cSv/yr equivalence dose.

	Density [g/cm <sup>3</sup> ]	Areal density[g/cm <sup>2</sup> ]
Aluminium	2.70	13.2
Polyethylene	0.91	5

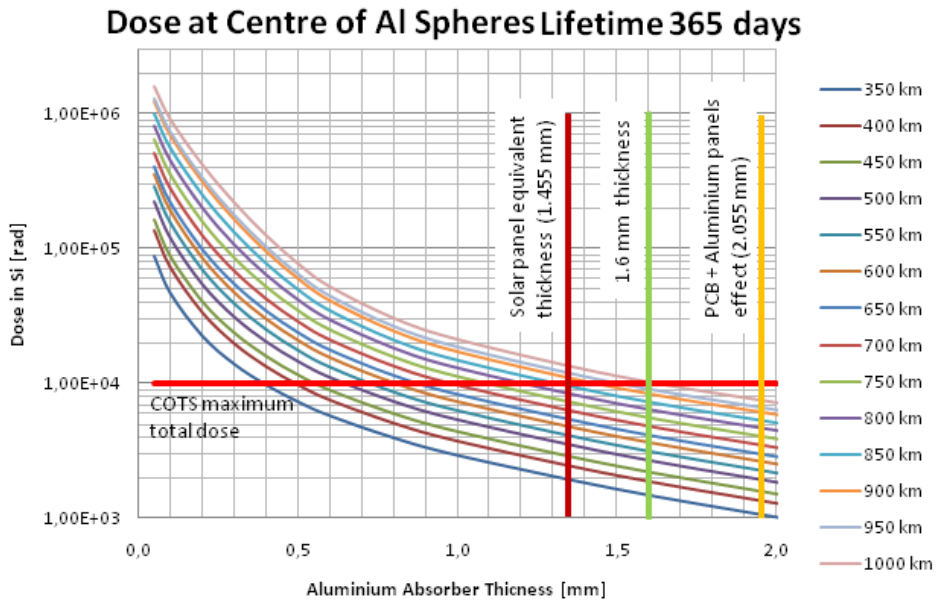


Figure 3.15 – Total Dose vs. Al thickness: comparison between PCB and Al shielding performance.

The thickness equivalence can be calculated through the following proportion using data shown in Table 3.4:

$$l_{PE} : l_{Al} = \frac{\rho_{Al}}{P_{Al}} : \frac{\rho_{PE}}{P_{PE}}$$

where  $\rho$ ,  $P$ ,  $l$  are respectively the material density, areal density and thickness. The equivalent thickness is:

$$l_{PE} ; 1.1 l_{Al}$$

For a 1.6 mm solar panel thickness (Clyde Space solar panel [60]), the equivalent Aluminium thickness is 1.455 mm (Figure 3.15). Since that solar panels are located on Aluminium structural panels 0.6 mm thick, an additional thickness must be added to the equivalent thickness just calculated (Figure 3.15).

From the analysis results one can infer that for a lifetime of 365 days the total dose level remains under the COTS limit level of 10 krad. No additional shielding is needed.

### Subsection 3.3.4 - Lifetime

AMD-Aeolus 400 km nominal orbit is the only orbit that we can accept. We can notice in Figure 3.8 that the orbit remains above 350 km for the most part of the time, 90 days more or less. It's still a very low releasing altitude.

Combining previous analysis of various effects respect to initial altitude, as shown in Figure 3.16, we can individuate a target altitude nearby 450/500 km, which would be strongly



preferred, as the maximum lifetime advantage respect to initial altitude, and then respect to launch cost, would be obtained.

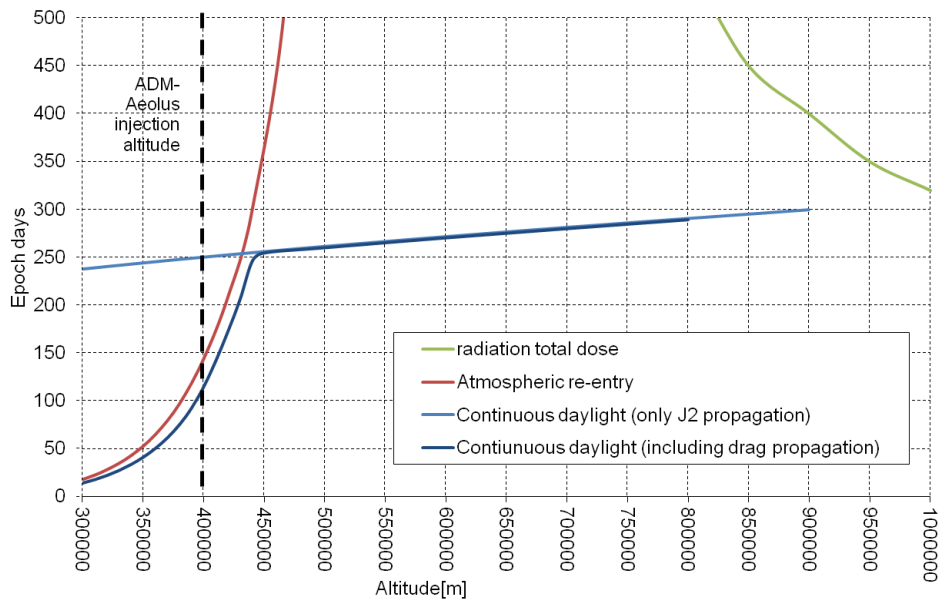


**Figure 3.16 - Lifetime respect to initial altitude summary, at occurring of considered critical effects**

In Figure 3.18, adopting the same hypothesis of previously presented ADM-Aeolus orbit propagation, an equivalent 450 km altitude sun-synchronous circular orbit is examined, confirming a lifetime due to drag over a sidereal year, but a shorter continuous daylight period, as resumed in Figure 3.17.

From now on, all analysis will be conducted at the nominal 400 km altitude of ADM-Aeolus solution, but altitude variation effects will be still verified.

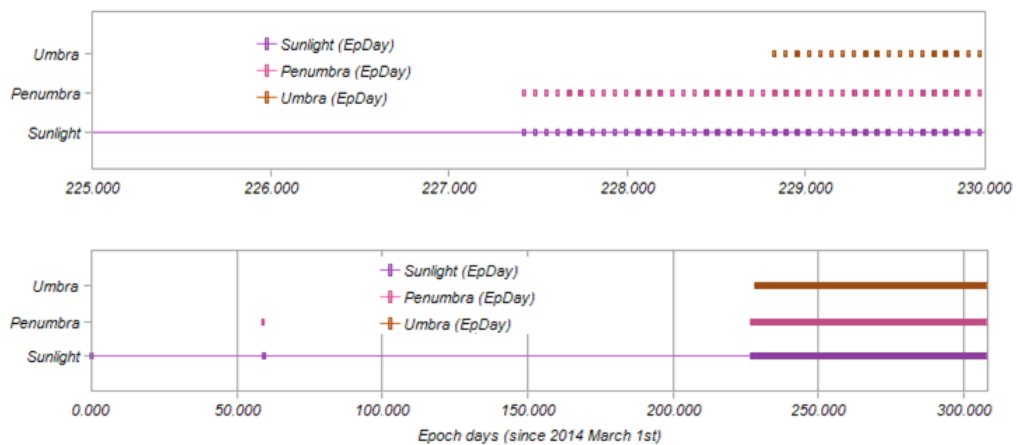


**Figure 3.17 – Sun visibility analysis over entire lifetime (below) and zoom in (above) that highlight the loss of continuous visibility after 228 days. Only a short penumbra condition is earlier experienced.**

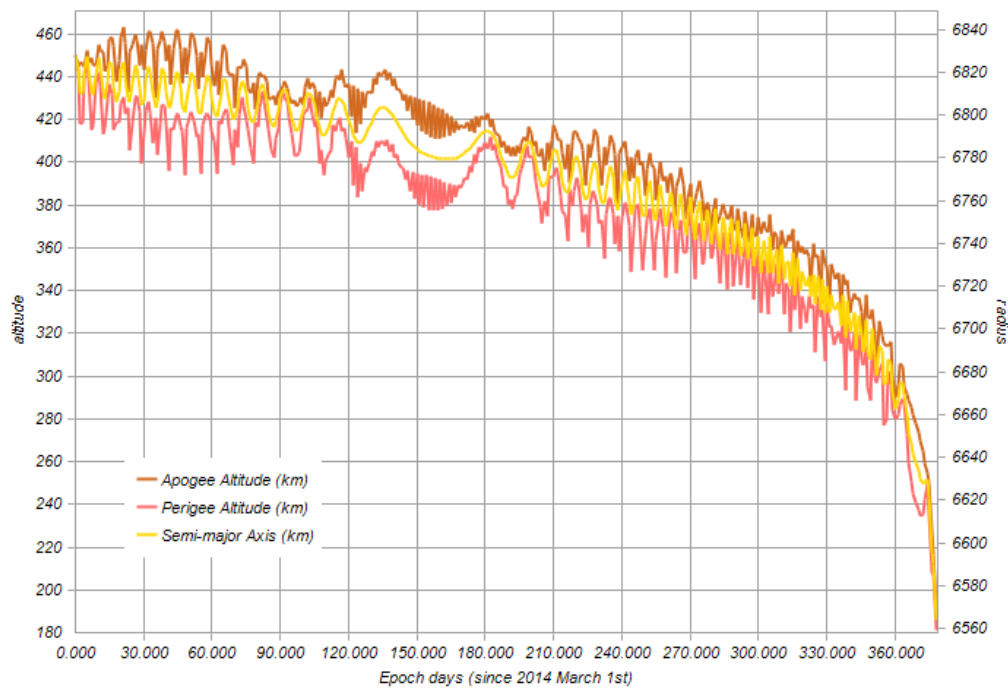


Figure 3.18 –LOP propagation results for desired 450 km altitude sunsynchronous circular orbit, starting from an hypothetical launch date of March 2014.

## Section 3.4 - Relative position control strategy

As a consequence of mission requirements it's necessary to maintain relative position within maximum ranges dictated by inter-satellite link budget. Minimum range is not an explicit requirement, but is indeed a relative position control performance output. Of course, the formation separation shall be as less as possible. As a secondary mission objective, formation control performance shall be investigated for a variety of achievable geometries. At this aim, it's sufficient to separately demonstrate in-plane and out of plane control capabilities for a dual satellite formation. Once these motions are properly combined, each relative trajectory can be realized, as described in Chapter 1 and even complex Cartwheel configurations can be designed for a larger number of involved spacecraft. The whole formation relative motion resolves itself simply coordinating in-plane and out-of-plane respect a common reference orbit, reducing to a dual formation problem.

### Subsection 3.4.1 - Disturbance mitigation strategies

In a LEO environment, main disturbance sources usually involved in orbit propagation, that is aerodynamic drag, gravitational harmonics and solar pressure, act on relative motion as differential accelerations.

#### Gravity field

Gravitational harmonics, as well as usually neglected third body effects, out comes from different orbital parameters between chief and deputy and doesn't depend on spacecraft masses and physical characteristic. Differential disturbance from Earth gravity field first zonal harmonic is the main source and it occurs whenever the constraint  $\delta a = \delta e = \delta i = 0$  is not satisfied (see Appendix B).

This condition is satisfied only for **L-F and pendulum configurations**, when along track separation is provided through perigee argument and/or true anomaly differences and the eventual out-of-plane motion is caused only by a RAAN difference.

#### **Differential pressure accelerations**

On the other hand, other disturbance forces are caused by accelerations on spacecraft surfaces and then does not depend on relative trajectory geometry, or depend on it in a minor part (in example, atmospheric density depend on altitude and then on radial coordinate, but for small separations this effects is rarely modelled). Solar and atmospheric drag pressure strongly depends on ballistic coefficient difference, which is on area-to-mass ratio differences. Not only ballistic coefficient can vary between identical spacecraft in the measure of its mass uncertainty, but it depends also on actual attitude respect to relative wind and radiant source direction.

Then, in order to minimize ballistic mismatch, it's very important to have **gemellar spacecraft**, maintained at the same nominal attitude respect to the orbiting frame, which is respect the velocity vector. Attitude manoeuvres shall be minimized and conducted without incurring in cross-section areas variations.

#### **Subsection 3.4.2 - Operative relative trajectory definition**

Simple leader-follower geometry must be initially achieved as nominal condition, as primary mission requirement to permit payload testing. Depending on effective relative control performances, the nominal separation can even be furthermore a posteriori reduced. Also a pendulum configuration is nice to have, as second step, in order to investigate out-of plane behavior.

Operative phase will comprise two steps:

- Main Leader-Follower target trajectory, with periodical separation variation, until full wireless payload testing achievement.
- Leader-Follower target trajectory with out of plane motion (Pendulum) to better investigate relative position determination and control accuracy.

As a first try, we set a nominal separation between spacecraft of the order of 100 meters, sufficient to achieve WLAN and reasonably controllable with single frequency spaceborne GPS devices. This separation can be achieved even in a simple L-F configuration, but it is a very tight value, compared to typical L-F ranges, often over the kilometer level. At this point it must be kept in mind that meter level errors in differential semiaxis determination and control traduces in an in-track drift of about hundreds of meters per orbit [16].

#### **Subsection 3.4.3 - Risk reduction strategies**

All trajectories already defined to minimize gravitational harmonics differential accelerations periodically intersect the along track axis and need an active collision avoidance control.

Fortunately, within a dual formation, each spacecraft can perform formation maintenance alone. So they can achieve this task in turn, distributing  $\Delta V$  budget each other. That means also that in case of deputy propulsion failure, the pair can fulfil control acceleration in place of it.

A conventional UHF/VHF transceiver subsystem, necessary for ground link, is necessary mounted on board. In case of WLAN failure, it can fulfil position data sharing for relative parameters calculation within the formation.

No risk reduction strategy can be implemented to counteract risk of GPS failure. In this case, unless a cold redundancy is adopted on both spacecraft, with great mass and volume waste, navigation and timing is totally compromised not only for the spacecraft itself, but also for the pair. It's then important to pay attention on technology reliability in navigation components selection.

### Subsection 3.4.4 - Relative control architecture trade-off

Following, most frequently discussed formation control techniques are resumed.

**Table 3.5 – Main relative position control architecture performances**

	Pros	Cons
<b>N-Impulse</b>	<ul style="list-style-type: none"> <li>• Low thrust cycles number</li> <li>• Fuel saving</li> <li>• Occasional attitude pointing requirement from propulsion</li> </ul>	<ul style="list-style-type: none"> <li>• Low position accuracy</li> <li>• High OBDH demand for trial solutions techniques</li> <li>• High relative errors propagations in orbital elements calculations</li> </ul>
<b>Limit Cycle</b>	<ul style="list-style-type: none"> <li>• Low thrust cycles number</li> <li>• Occasional attitude pointing requirement from propulsion</li> <li>• Very low OBC demand</li> </ul>	<ul style="list-style-type: none"> <li>• Low position accuracy</li> <li>• Low flexibility respect to</li> <li>• Low robustness</li> </ul>
<b>LQR</b>	<ul style="list-style-type: none"> <li>• Easy OBD implementation</li> <li>• Fast time response</li> <li>• High position accuracies</li> <li>• Integrates GPS position measurements dynamic filtering</li> <li>• Simple and accurate linear dynamic models in case of close separations (HCW equation)</li> </ul>	<ul style="list-style-type: none"> <li>• High thrust cycles number</li> <li>• High fuel consumption</li> <li>• Continuous attitude pointing requirement from propulsion</li> </ul>

### Limit-Cycle

It represents the simplest method, directly derived from general orbit maintenance. It consists in a series of pre-fixed control manoeuvre triggered once a parameter (that is relative position or derivate quantities) exceeds a prefixed tolerance. It's substantially similar to the previous case, but usually implement.

### N-Impulse control strategy

This category involves long coast phases (fractions of orbit periods) and impulsive firings, calculated after trial solution techniques as function of relative orbital elements differences. It can be seen as a periodical reconfiguration from perturbed to nominal condition. In this way, this technique is very versatile, because it can be implemented even outside the operative conditions.

Usually this scheme involves relative orbital parameters differences and the relative position determination system has to handle their small variations relatively to nominal values. As demonstrated in various studies, [61] [62] [63] and most of all [16], for long term maintenance based on orbital elements, it's fundamental to numerically obtain and use within the control loop mean elements and averaged elements, in order to neglect short periodic perturbation and save fuel, greatly increasing OBC demand.

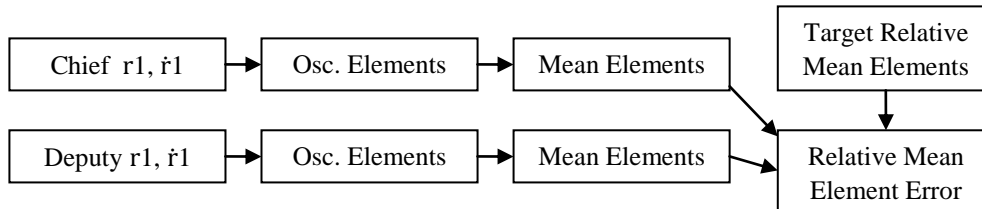


Figure 3.19 – Relative position measurement and control scheme for geometric control methods

### Linear Quadratic Regulation (LQR)

Classical linear control theory involves a linearized model of the relative dynamic, to implement a continuous-time regulator state-space model (or its discrete-time counterpart), by minimization of a selected performance.

Linear Quadratic Regulation approach is strongly preferred because it should incur minimal risk. All the tools of linear control can be used to analyse stability and properties and, even if it generally waste more fuel than an impulsive scheme, it offers the best position accuracy performance. Moreover, to prevent continuous firing, an LQR controller can be combined with a dead-band, obtaining great fuel saving, but extreme care of stability reductions has to be taken.

This approach has no restrictions in relation to target relative orbit selection, at the only condition that the chosen target trajectory is an equilibrium solution. For the separation effects principle, each relative trajectory can be seen as the sum of an equilibrium trajectory and a perturbation respect to it, as far as dynamic models linearization hypothesis are still satisfied.

Retroacting relative state, that is position and velocity, either observed or measured, the LQG control scheme, stabilizes deputy motion around the origin of the EH frame. Retroacting the difference between the relative state and the target state, it can counteract only this deviation, tracking any equilibrium target condition exactly as it would be tracking a virtual reference orbit.

### Subsection 3.4.5 - Commissioning and formation acquisition

A contemporary releasing of the two spacecraft is not recommended, because relative position control cannot immediately operate in safety.

A GPS cold start generally takes at least a minute, nominal attitude settling can take several minutes, depending on control bandwidth, and so on. This phase can be accomplished in two ways:

- at the same time, but in a docked configuration
- by two subsequent independent releasing phases.

**Table 3.6 – Releasing conditions constraints**

	<b>Subsequently releasing</b>	<b>Contemporary releasing</b>
<b>Pros</b>	<ul style="list-style-type: none"> <li>• No constraint on releasing POD</li> <li>• No undocking risks</li> </ul>	<ul style="list-style-type: none"> <li>• No relative control needed in early commissioning phase</li> </ul>
<b>Cons</b>	<ul style="list-style-type: none"> <li>• High initial drift to be counteracted</li> <li>• Formation acquisition in early commissioning phase</li> </ul>	<ul style="list-style-type: none"> <li>• Close proximity operations risk during undocking</li> <li>• Undocking failure risk</li> <li>• Single dedicated 6U POD needed</li> </ul>

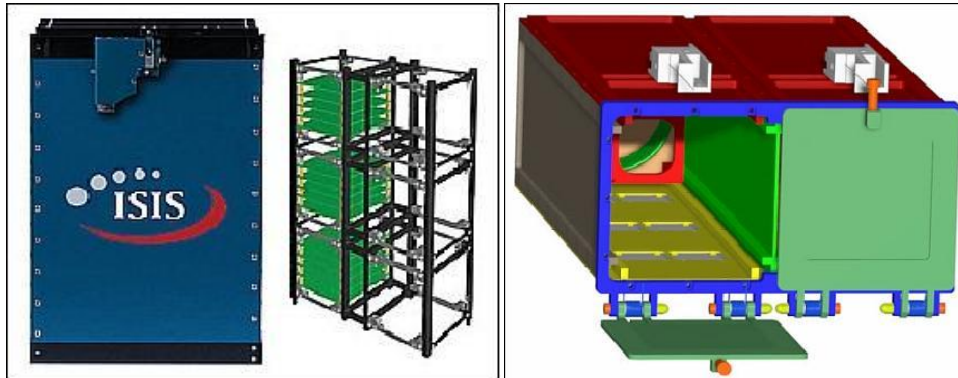


**Figure 3.20 – Left: 6-Pack ISIPOD (ISIS[64]), Right: double P-POD design (CalPoly).**

### Contemporary releasing

Both spacecrafts are released at the same time, in a docked configuration. The formation acquisition can be achieved after undocking at the end of the entire commissioning phase, comprising antennae deployment, GPS cold start, first contact and so on. A particular releasing POD is requested, to accommodate the pair, in example a 6-pack POD to stow two 3U laterally docked spacecrafts.

### Subsequent releasing

Each spacecraft is released from launcher by its own releasing POD and then, orbital periods mismatches between the pair, that is semiaxis differences, must be immediately corrected, to prevent along track drift (see Appendix B). The  $\Delta V$  impulse provided by the POD spring must be oriented towards orbital velocity direction, and have to produce an in-track drift respect to the launcher upper stage equal to the desired separation during the time interval before the second spacecraft releasing.

Releasing POD impresses a  $\Delta V$  from 0.5 up to 2 m/s. If the relative velocity impulse respect to launcher upper stadium is provided in along track direction, which would produce the maximum semiaxis difference, which can be evaluated differentiating energy equation:

$$-\frac{\mu}{2a} = \frac{V^2}{2} - \frac{\mu}{r}$$

$$\delta a = \frac{\mu}{2} \left( \frac{\mu}{r} - \frac{V^2}{2} \right)^{-2} V \delta V \simeq 2 \sqrt{\frac{r^3}{\mu}} \delta V$$

For a 400 km altitude circular releasing orbit, and 2m/s in-track velocity impulse, semiaxis increasing can be evaluated as 3535 m. Its related drift per orbit  $\Delta y$  is of the same magnitude, little above 10 km:

$$\delta T = 2\pi \frac{3}{2} \sqrt{\frac{a}{\mu}} \delta a$$
$$\Delta y \simeq V \Delta T = \sqrt{\frac{\mu}{a}} 3\pi \sqrt{\frac{a}{\mu}} \Delta a = 3\pi \Delta a$$

We can say that in a subsequent releasing scenario, it's sufficient to perform second spacecraft releasing after a time delay equal of a fraction of orbit. After 1/10 orbit separation would reach about 1 km.

The second releasing would be affected by a  $\Delta V$  error, which leads the orbital semiaxis of the pair not to be the same. The effective error on the first impulse is not important, but it's important the effective difference between the pair. For a 10% error on the spring impulse, the formation is subjected to an initial differential semiaxis value of more than 300 meters. Nominal leader follower separation of 100 meters is obviously inappropriate, in the formation acquisition phase. It's necessary to perform this phase at the maximum possible relative distance.

#### **Subsection 3.4.6 - Relative attitude configuration**

The current mission has not particular requirements of relative pointing accuracy, such stereo imaging or other formation flying application demands.

The only constraint on relative attitude derives from coarse inter-satellite link antenna pointing and on thrust vector control. Each spacecraft has still to ensure UHF/VHF antenna nadir pointing for link to ground station and GPS antenna pointing towards zenith direction to maximize GPS constellation visibility.

Regardless the selected control class, it's widely demonstrated that the out of plane relative motion, which is totally decoupled, can be controlled with only actuation acceleration directed in normal direction. In addition, the in-plane motion is completely controllable either applying only radial accelerations or only in-track accelerations. The only in-track actuation solution is strongly preferred, because of its double efficiency, for low-eccentric orbits [65] [66]. So, only thrust in transverse and out-of-plane direction is necessary for each spacecraft.

A nadir-pointing configuration can fulfill all these task, taking advantage of gravity gradient torque, due to stretched CubeSat configuration. Commonly adopted quadrifilar dipole array antenna can be easily oriented toward nadir direction and provide at least a dipole pair in proper direction to also fulfill a backup inter-satellite link, while GPS antenna can be easily accommodates on top surface. Finally, propulsion can be fulfilled by laterally pointed thrusters, eventually oriented by yaw attitude maneuvers.

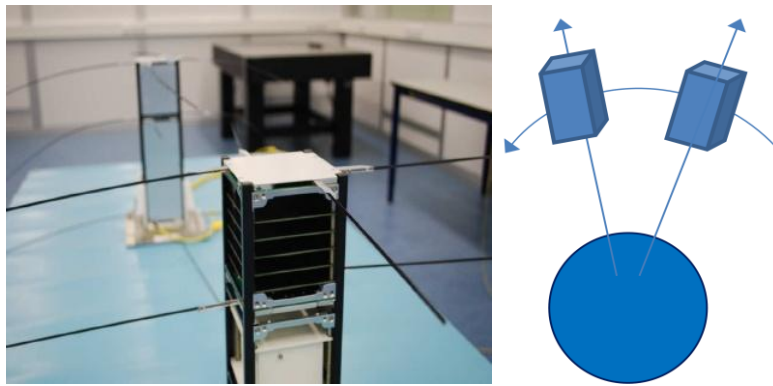


Figure 3.21 – UHF/VHF dipole antenna disposition (left) and nadir pointing relative attitude between spacecraft in the current leader-follower configuration (right).

## Section 3.5 - System configuration

### Subsection 3.5.1 - Critical issues

In general, CubeSat mission has low (or not at all) attitude control demands and rarely propulsion is implemented, because suggested CubeSat propulsion and attitude control solutions requires high power levels and volumes (see [64]). Usually, in technological demonstration mission, nominal orbit maintenance and attitude control is not implemented and, at the utmost, a passive magnetic stabilization and the only position and attitude determination are performed.

In example, a variety of miniaturized reaction wheel cluster assembly are available (see Chapter 5), but they usually take a lot of mass and volume. In Pumpkin Kit, wheel assemblies are presented with already integrated ADCS electronics, within a 1U CubeSat unit volume occupation. Also a 0,5U envelope cold gas propulsion system is available (see Chapter 4). Moreover these two solutions need 12 V regulated supply, achievable only with 3U lateral solar panels. Otherwise a dedicated power supply line has to be converted.

### Subsection 3.5.2 - CubeSat X-U bus trade-offs

Satellite power generation strongly depends from structure configuration choice. Table 3.7 resumes typical mass and power characteristics which depend on the configuration choice.

In relation to other CubeSat mission with complex mission requirements, such as RAX, STRaND-1, Delfi-C3 and so on, we will consider since the beginning a 3U baseline solution, which would provide high voltage and power generation. Despite a desirable mass saving and then significant cost reduction, 2U and smaller configuration would probably result insufficient, in terms of volume and power. Moreover in nadir pointing attitude, 3U stretched configuration can take advantage of gravity gradient disturbance torque as much as its moment of inertia ratio grows.

Table 3.7 - Properties and performances depending on modules architecture

	1U	2U	3U	Deployable 3U (QBX)
<b>Power [W] (See [60])</b>	2.1	5.2	7.3	14.6
<b>Voltage reg. [V]</b>	4.7	4.7/11.7	4.7/16.4	4.7/16.4
<b>Area/Mass [m<sup>2</sup>/kg]</b>	0.01	0.01	0.01	0.02



	1U	2U	3U	Deployable 3U (QBX)
<b>Mass [kg]</b>	1	2	3	3
<b>Ix/Iz</b>	1	5/2	5	>5
<b>Pros</b>	Low mass			High power generation
<b>Cons</b>	Low volumes Low voltage and power generation			Attitude constraints Low ballistic coefficient Center of mass displacement

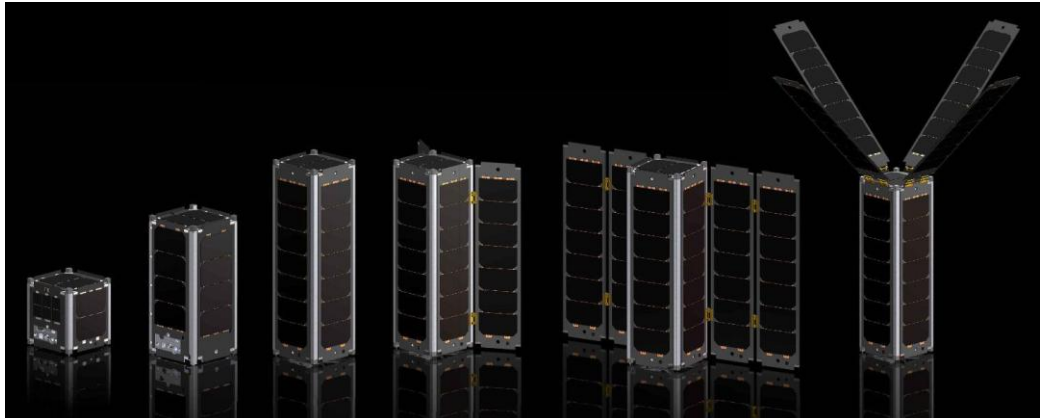


Figure 3.22 - Deployable solar panels architectures

Deployable solar panel architecture, depicted in Figure 3.22, has been developed and would result quite attractive because they would extend cross areas exposed to sunlight. However, that would mean to constrain attitude towards sun direction, losing body mounted panels advantage and they would greatly increase area to mass ratio and center of mass displacement uncertainty. So, aerodynamic disturbance counteraction and thrust vector alignment respect to center of mass would become unaffordable.

In conclusion, a 3U accommodation is strongly preferred, even if a smaller 2U solution will be still investigated, and the need for deployable solar panels will be avoided.

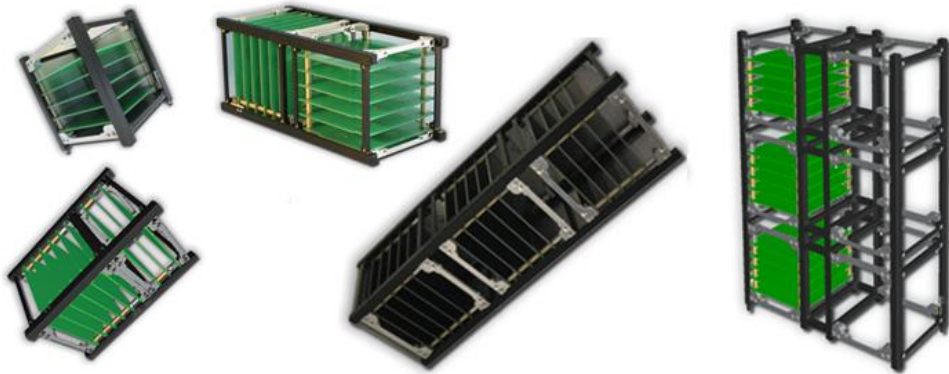


Figure 3.23 – Isis family modular CubeSat structures [64]

### **Subsection 3.5.3 - Summary: Baseline definition**

A formation flying Leader-Follower geometry will be achieved. The satellite separation will be set at 100 meters to permit WLAN payload testing. A single frequency spaceborne GPS device will be used for position determination. Depending on relative control performances, this distance can even be reduced. In a second step a pendulum configuration can be achieved. A Linear Quadratic Regulator (LQR) will be implemented as relative control technique.

A nadir-pointing configuration will be adopted. The quadrifilar dipole array antenna points to nadir direction for the ground link, and provide at least a dipole pair in proper direction to fulfill a backup inter-satellite link, while GPS antenna points on zenith direction. Propulsion system will be positioned to orient thrust in-track and cross-track directions.

Formation acquisition can be accomplished in two ways: in a docked configuration or by two subsequent independent releasing phases.

Using 3U configuration permit to have systems redundancy and the two satellites can perform the Chief and Deputy roles in turn. In particular propulsion system is mounted in every satellite to guarantee the formation control redundancy. In addition, they have the same mass distribution and volume, these features minimize the ballistic coefficient mismatch and the perturbation effect will be the same on both.

Deployable solar panel will be considered only in case of inadequate power generation.

# Chapter 4 - Relative position determination and control

## Section 4.1 - Formation control requisites

### Subsection 4.1.1 - Guidance Navigation and Control subsystem requisites

#### Reference orbit only determination

In this mission, the Guidance Navigation and Control (GNC) subsystem is only responsible to determine and not to maintain operative orbit of each spacecraft. In any case, this monitoring is necessary to determine whenever visibility to the ground station is available, to update on-board parameters such as magnetic field prediction in case of magnetometer output management, local orbiting frame for attitude control, semiaxis and eccentricity in relative position dynamic prediction and so on.

Each spacecraft necessarily mount on board GPS receiver device, which can fulfil this task independently. Even in case of several meters Coarse/Acquisition (C/A) position accuracy, for typical LEO position in Earth-Centered Inertial (ECI) and Earth-Centered Earth-Fixed (ECEF) frame of the order of  $6 \cdot 10^6$  meters, its relative accuracy and the propagated accuracy on position-dependent telemetry and parameters are of the order of  $10^{-6}$ . Except for particular science application, any GPS receiver device can fulfil this requirement with sufficient accuracy, so it's taken for granted.

#### Relative orbit determination and control

The relative position, indeed, have to be determined and maintained with an on board autonomous close loop control, because long time intervals between subsequently visibility window from a single ground station, of the order of 12 hours in a LEO orbit, or equivalently, 7-8 orbit periods, make this task unaffordable by ground segment. At this aim, both GNC and propulsion subsystem are entirely analysed in this chapter.

### Subsection 4.1.2 - Propulsion subsystem requisites

In general, for a CubeSat class mission, no orbit maintenance strategy is implemented and the operative orbit definition process takes into account disturbances propagation, in order to accommodate them. In this particular case, even if the same mission analysis approach is adopted, the propulsion subsystem is still necessary provide formation control. We then analyzed suggested solutions for CubeSat primary and secondary propulsion solution and their possible application on formation control, in terms of achievable thrust level in particular.

## Section 4.2 - Uncontrolled dynamics analysis

### Subsection 4.2.1 - Disturbance accelerations within formation

#### Disturbance sources

As we can see in the following disturbance analysis, atmospheric drag and first zonal harmonics  $J_2$  surely are the main disturbance acting on relative motion, at low altitudes. The lowest altitude considered in reference orbit selection represent the worst case scenario for

relative position control, because both aerodynamic and Earth asphericity effects reduce at altitude increasing.

### Analysis approach and tools

First of all, effects of disturbance acceleration on relative dynamic have been investigated. At this aim, a dedicated model was implemented, using MATLAB Simulink software [67], to be easily integrated in an optimum control loop algorithm. Uncontrolled dynamic results were compared to corresponding propagations conducted on AGI Satellite Tool Kit software [68].

Then the uncontrolled relative trajectory time evolution and the impact of differential disturbance accelerations has been analysed

In this section, a circular sun-synchronous reference orbit at 400 km altitude is considered in all simulations, to include the worst case differential disturbance accelerations and validate formation maintenance capability. Performance will be finally evaluated also for different altitudes.

MATLAB model has been developed taking in account only zonal harmonics effects on gravity acceleration, which are most important disturbance respect to keplerian model, on which HCW equations are related. On the other hand, it has been specifically adapted to the present case, modeling atmospheric drag and solar pressure effects with more details, distinguishing pressure accelerations on each spacecraft side:

$$\mathbf{d} = \sum_{i=1}^{N_{sides}} (\mathbf{F}_{aer,i} + \mathbf{F}_{rad,i})$$

$$\mathbf{F}_{aer,i} = -\frac{1}{2} \rho(\mathbf{r}) |\mathbf{v}| (\mathbf{v} \cdot \hat{\mathbf{n}}) C_D A_i$$

$$\mathbf{F}_{rad,i} = -P_{rad} A_i (\hat{\mathbf{s}} \cdot \hat{\mathbf{n}}) \left( (1 - c_{s,i}) \hat{\mathbf{s}} + 2 \left( c_{s,i} \cos(\alpha_i) + \frac{1}{3} c_{d,i} \right) \hat{\mathbf{n}} \right)$$

where  $\mathbf{F}_{aer/rad}$  are modeled aerodynamic, solar, Earth albedo and infrared pressures acting on each spacecraft side, with area  $A_i$  and normal direction  $\mathbf{n}_i$ ,  $c_s$  and  $c_d$  are respectively specular and diffuse reflectivity, in first analysis equally distributed for each side ( $c_s=c_d=0.33$ ).

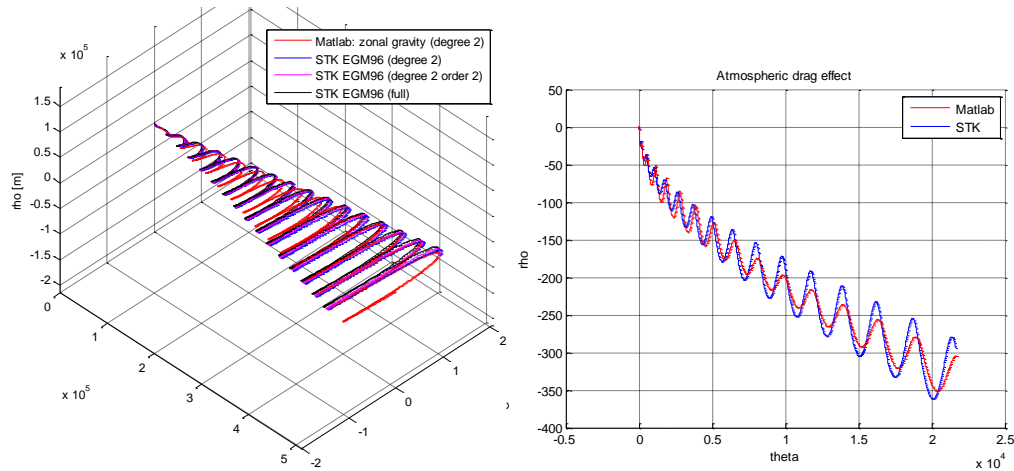
### Dynamic model validation

Figure 4.1 represent the trajectory derived from different gravitational models, respect to a virtual body in keplerian motion. This particular point of view highlights as, in a circular high-inclined LEO orbit of 400 km of altitude, the main disturbance effects comes from first zonal harmonic,  $J_2$  and involving higher order degrees in STK scenario doesn't significantly change the result.

At the same manner, also the effects of atmospheric drag on a typical 3U CubeSat nadir-pointed spacecraft (3 kg mass and cross and radial sectional areas of 0.03 m<sup>2</sup> and 0.01 m<sup>2</sup> respectively) are shown, comparing Simulink and STK.

Aerodynamic pressure effect is surely the principal disturbance to take in account at low altitudes, because they produce an in-track drift progressively increasing, as far as semiaxis decrease. The MSISE00 atmospheric model (standard solution for LEO applications) was implemented, function of geopotential altitude (that means an oblate Earth model is considered), local apparent time and medium solar flux. Also rotating atmosphere has been

considered in velocity direction calculation (particularly important in high-inclined orbits). The initial date is set at 1 March 2014, which is nearby ADM-Aeolus scheduled launch, and the simulation has been run for one sidereal day.



**Figure 4.1 – Effects of including Earth gravity harmonics (left) and atmospheric acceleration (right) respect to unperturbed keplerian problem, for a 400 km circular orbit, over a sidereal day.**

Solar pressure has constant component perpendicular to orbit plane and a minor in-plane cyclic component, but it is a very low effect compared to drag and  $J_2$  perturbation. IR and albedo was included, but their effects are negligible and make simulation time to excessively rise up. However, ballistic coefficient mismatch between spacecraft make this disturbance still important within a formation, so it will be implemented, even in a simplified way, neglecting albedo and IR minor effects.

#### Subsection 4.2.2 - Uncontrolled relative dynamic

In either case, two independent orbit propagations were conducted, each for deputy and chief spacecraft, considering a 2% ballistic coefficient mismatch. Then the free perturbed relative motion in LVLH frame has been algebraically calculated. The simulation was run for a time interval of ten orbit periods, starting from nominal condition.

Starting from nominal condition, an in-track drift immediately occurs because of continuous differential aerodynamic acceleration in tangent direction, as shown in Figure 4.2, at a rate below 10 meters per orbit, but rapidly increasing and causing several hundred meters offset after one day, while differential semiaxis is increasing/decreasing. The minor ripple effect is caused by differential eccentricity variations and by  $J_2$  effects. Far less evident is the out of plane motion, which is still present. Differential radiant pressure mainly acts in normal direction, opposite to Sun direction, and have only periodic effect over an orbit. Differential accelerations are reported in detail in Figure 4.4.

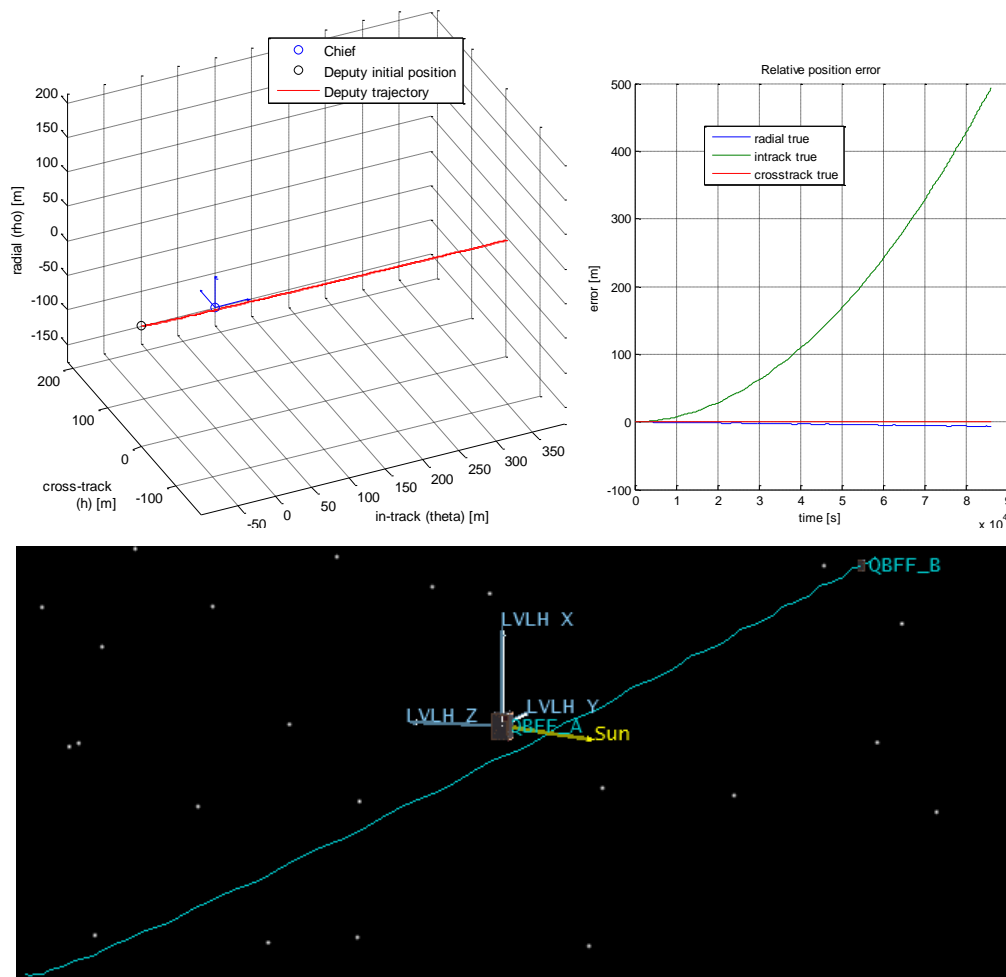
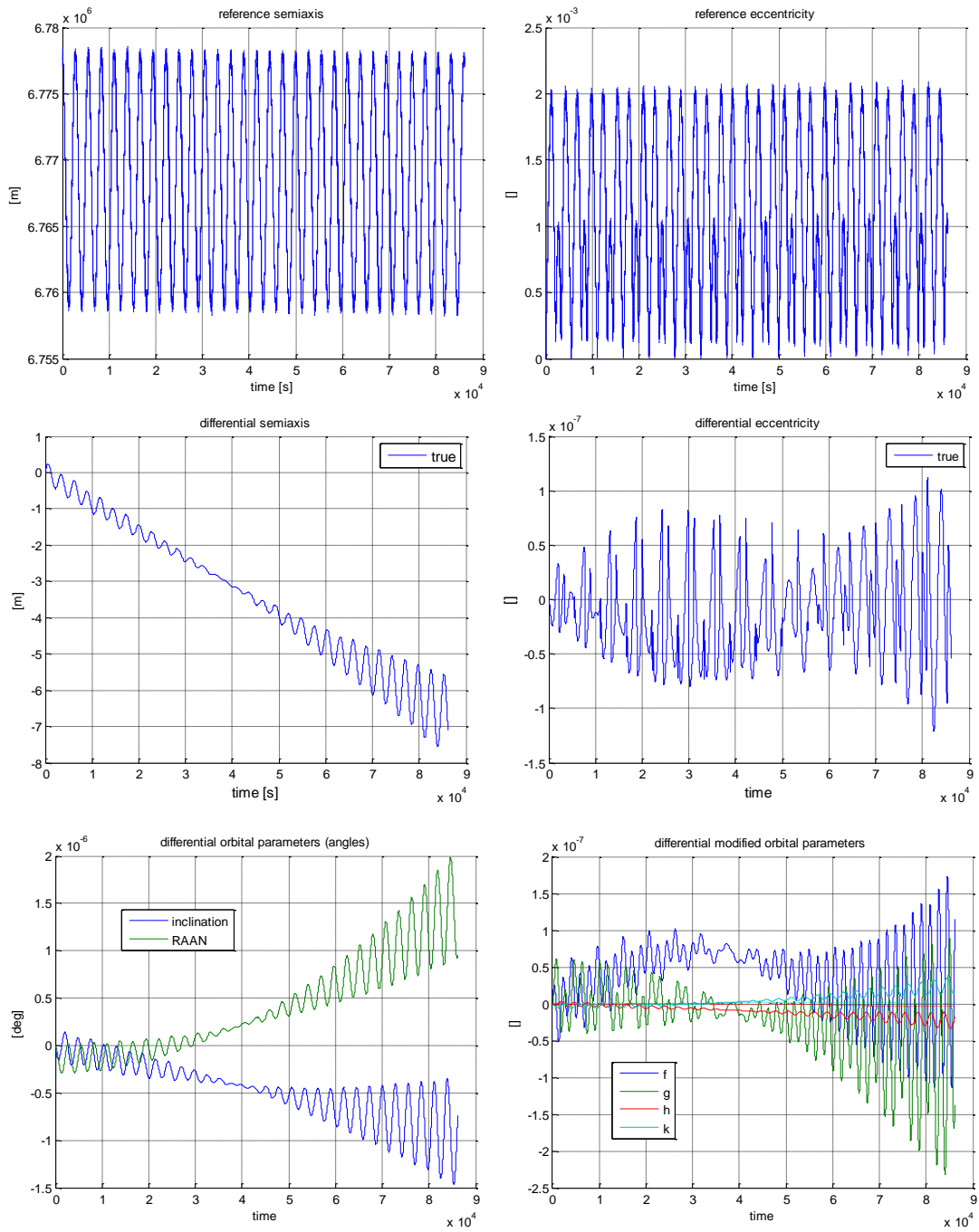


Figure 4.2 – STK (below) and MATLAB Simulink (above) perturbed uncontrolled relative dynamic propagation over a sidereal day

In order to evaluate differential parameters entity, time trend of differential semiaxis and eccentricity between chief and deputy are reported Figure 4.3. For such close separations, only a few meters change in semiaxis is responsible of the huge experienced relative drift. Differential eccentricity is even more difficult to detect, because of high periodic variations within an orbit period, respect to average time trend. Similar, less critical periodic trends are also present in semiaxis and in angle time histories.

Then, unless they are very effective in terms of fuel saving, geometric control methods, based on orbital parameters differences, would suffer from numerical errors and propagated uncertainties, in addition to great computational demand. Moreover, in case of uncontrolled reference orbit, its semiaxis and eccentricity time evolution makes even more difficult to implement a control scheme because the state transition matrix, which surely is true anomaly dependent, is also highly sensitive to reference orbit parameters.



**Figure 4.3- Reference (above) and differential (center) semiaxis and eccentricity, and differential classical and modified orbital angle parameters (below), on uncontrolled relative dynamic of a 100 m separation L-F formation, at 400 km circular 98° inclined LEO.**

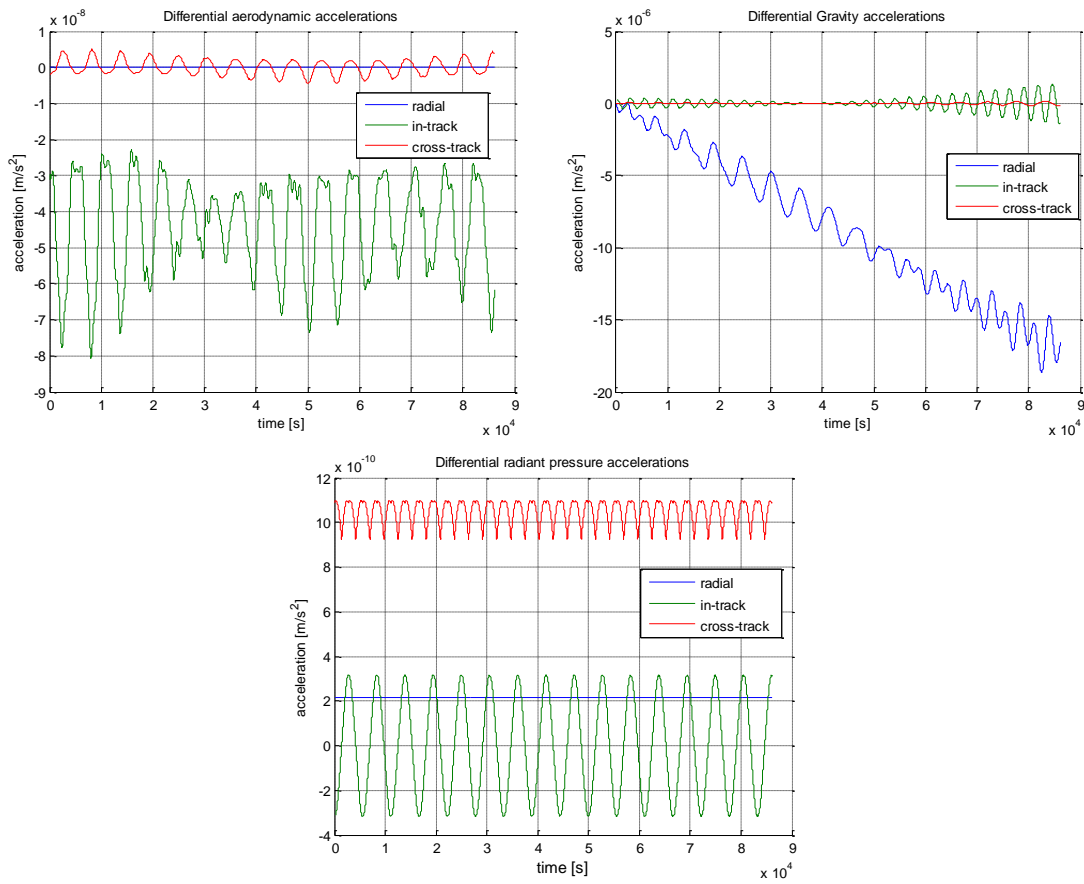


**Figure 4.4 – Differential disturbance accelerations acting on uncontrolled relative dynamic of a 100 m separation L-F formation over 10 orbit periods, with 2% ballistic coefficient mismatch, at 400 km 98° inclined LEO.**

## Section 4.3 - Guidance, Navigation and Control with GPS

### Subsection 4.3.1 - Single frequency spaceborne GPS receivers trade-off

A trade-off between spaceborne receivers early lead to the only product that fits CubeSat envelopes, integrated on Printed Circuit Board (PCB), SSTL SGR-05U [24], similar to Phoenix DLR device. Some US and Canadian CubeSat missions (RAX, CanX) mount commercial device, such some Novatel Original Manufacturer (OEM) family PCBs [69], which has high accuracy and sufficiently small dimensions, but suffer CoCom limits.

**Table 4.1 – Single frequency Spaceborne GPS receiver benchmark [70]**

	Ch.	Antenna	Power [W]	Mass [kg]	Mission
<b>SSTL, SGR series [24]</b>	12-24	1-4	0.8-6.3	0.02-1	STRaND-1
<b>Phoenix, DLR</b>	12	1	0.9	0.02	PRISMA
<b>Accord, NAV2000HDCP</b>	8	1	2.5	0.05	X-Sat
<b>Alcatel, Topstar 3000</b>	12-16	1-4	1.5	1.5	
<b>EADS, Mosaic GNSS</b>	6-8	1	10	1	TerraSAR-X, Aeolus

Surrey Satellite Technology Limited (SSTL) GPS receiver family is specifically designed for application onboard small satellites. The smallest model, Spaceborne GPS Receiver SGR-05U



in Figure 4.5, with only a single receiving antenna input, for its active quadrifilar antenna operating in L1 frequency, has flight heritage and it's specifically suited for. SGR-05U accuracy performances, resumed in Table 4.2, refer to navigation on highly inclined LEO orbit and consider typical ionospheric and ephemeris error levels on signals. They are compared to a NovaTel COTS component, which declared performance are referred to ground operations.



Figure 4.5 – SSSL SGR-05U hardware (left) and host interfacing diagram (right)



Figure 4.6 - NovAtel OEM4-G2L hardware

Table 4.2 - Characteristics of on board GPS receiver

		SSSL SGR-05U	NovAtel OEM4-G2L
<b>GPS signal processing</b>		12 Ch. (L1, C/A)	24 Ch. (L1-L2, C/A-P(Y))
<b>Power consumption [W]</b>		0.8	<1
<b>Voltage regulation [V]</b>		5 V	3.3
<b>Dimensions [mm]</b>	PCB	70x45x10	100x60x16
	Antenna	13x13x40	-
<b>Mass [g]</b>	PCB	40	56
	Antenna	12	-
<b>Cold start [s]</b>		550	50
<b>Hot start [s]</b>		50	30
<b>Temperature limits [°C] (operating)</b>		-20 to 50	-40 to 85
<b>Vibration tolerance [g]</b>		15	4
<b>Radiation tolerance [kRad]</b>		>10	-
<b>Position accuracy [m]</b>	total	10 (95%)	0.45 (RMS)
	pseudo-range	0.9	
	carrier-smoothed range	0.15	
	carrier-phase noise	0.002	
<b>Velocity accuracy [m/s]</b>		0.15 (95%)	0.03 (RMS)
<b>Time accuracy [μs]</b>		0.5 (95%)	0.02 (RMS)
<b>CoCom restrictions</b>	altitude [ft]	none	<18300
	velocity [m/s]	none	<514

### Subsection 4.3.2 - GPS position measurement implementation

GPS measurement accuracy has been taken in account assuming Gaussian distribution on random errors, for discrete-time position acquisition, both for chief and deputy spacecrafts (see BAND-LIMITED WHITE NOISE Simulink block in [67]).

Reasonably, nominal accuracy for this device contains also bias errors in absolute measurement, which are cancelled in relative position calculations. So we can assume zero-mean random noise on relative navigation. In fact, bias errors, which depend strongly on relative geometry and velocity between receiver and GPS constellation, are presumptively the same for both chief and deputy within a close formation flying.

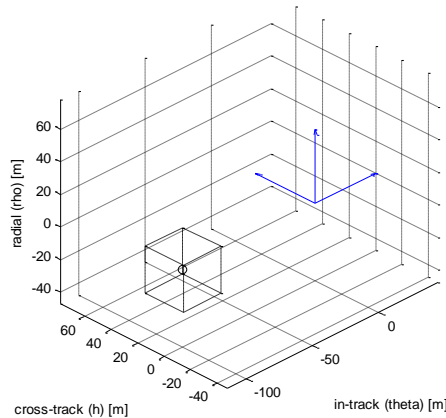


Figure 4.7 - Envelope of relative position measurement accuracy with onboard GPS receivers, for a 100m leader-follower nominal configuration respect to the chief position.

Applying uncertainty propagation on the relative position and velocity, via Root Sum Square (RSS) rule, this lead again to Gaussian distributed random errors with the same standard deviation as absolute measurement. Figure 4.7 shows the envelope of resulting measured relative positions, compared to 100 meters separation leader follower geometry.

### Subsection 4.3.3 - Discrete-time filtering

Under the hypothesis of Gaussian distribution errors, outputs can be filtered to reduce high frequency noises, adding a discrete-time filter on each position and velocity component, leading to a tighten position accuracy, but introducing a phase delay.

Due to the introduced time delay, this rough technique can be applied only to an L-F formation, in which the nominal trajectory is not time-varying. For the same reason, it's important to filter only the relative position after it's been calculated and not to filter absolute position of the single spacecraft, because the fast orbit dynamics would produces high position errors, compared to the formation characteristic dimension.

The effects of a digital filter has been investigated, inserting 1-order low-pass discrete filters on each channel in relative position and velocity, after they are calculated in the relative EH frame as function of each spacecraft position measurements. The results inevitably exhibited a time delay in relative state determination, because its dynamic is not taken in account.

### Subsection 4.3.4 - Kalman filtering

The Kalman Filter (KF) [71] is a recursive scheme that propagates a current estimate of a state and the error covariance matrix of that state forward in time, blending the new information introduced with measurements with a Kalman gain matrix  $L$ . The gain matrix balances uncertainty in the dynamics model and guarantees minimum estimation errors (in the sense of minimizing the 2-norm-squared) for linear system with linear measurements. The  $L$  matrix determination leads to the solution of an Algebraic Riccati Equation (ARE). Improvements on the KF to handle non linearity, such J2 effect in HCW equations [72], were proposed for use in LEO, as i.e. the Extended Kalman Filter (EKF) [73].

#### Relative dynamic system model

Several approximated model of the unperturbed relative motion, respect to a target reference orbit, and even model which take in account J2 effect and drag, are present in a wide literature, [16] [74] [75] and [76], and resumed in Appendix B. In any case, for LQG applications, the selected dynamic model entirely determine the state matrix  $\mathbf{A}$  and any neglected disturbance acceleration acts as an input line disturbance vector  $\mathbf{d}$ . In case of GPS implementation, that is position measurements, and to the utmost velocity digital calculation, the feed through matrix  $\mathbf{D}$  is null:

$$\begin{cases} \dot{\mathbf{x}} = \mathbf{A}\mathbf{x} + \mathbf{B}_u\mathbf{u} + \mathbf{B}_d\mathbf{d} \\ \mathbf{y} = \mathbf{C}\mathbf{x} + \mathbf{v} \end{cases}$$

$$\mathbf{x} = [x \quad y \quad z \quad \dot{x} \quad \dot{y} \quad \dot{z}]^T$$

In following simulations, the state space matrix refers to the HCW equations:

$$\mathbf{A} = \begin{bmatrix} \mathbf{0}_{3 \times 3} & \mathbf{I}_{3 \times 3} \\ 0 & 0 & 0 & 0 & 2n_0 & 0 \\ 3n_0^2 & 0 & 0 & -2n_0 & 0 & 0 \\ 0 & 0 & -n_0^2 & 0 & 0 & 0 \end{bmatrix}$$

The input matrix differs from actuation and disturbance inputs, because thrust component in radial axis has been removed. The output matrix selects the only position components states.

$$\mathbf{B}_u = \begin{bmatrix} \mathbf{0}_{3 \times 2} \\ 1 & 0 \\ 0 & 0 \\ 0 & 1 \end{bmatrix} \quad \mathbf{B}_d = \begin{bmatrix} \mathbf{0}_{3 \times 3} \\ \mathbf{I}_{3 \times 3} \end{bmatrix} \quad \mathbf{C} = [\mathbf{I}_{3 \times 3} \quad \mathbf{0}_{3 \times 3}]$$

In this particular case, which is for very close separations and low eccentricity reference orbit, even the simplest model of HCW equations adequately predicts the relative dynamic. Errors between estimated and true position comes widely from drag acceleration. All other error sources, that is Earth gravitational harmonics, solar pressure acceleration and first-order approximation of gravity acceleration lead to drift errors far below the onboard device's position measurement accuracy.

Implementation of higher accuracy time-variant state space models would certainly increase prediction accuracy, but at the cost to have a time-variant Kalman Filter. At the best, ARE can be preventively solved for several time step at operative conditions to provide data for onboard

L matrix interpolation, otherwise, its solution has to be implemented in the control loop, excessively increasing OBC demand.

### Gain matrix evaluation

Being HCW equation a linearized time-invariant state space model, we then evaluated a constant gain matrix L, as classical theory suggest, as a function of a rough estimation of disturbance covariance matrix on input line (differential accelerations) and on output line (random position measurements error), out coming from a simplification of the same propagator used in this simulation.

$$\hat{\mathbf{x}} = \mathbf{A}\hat{\mathbf{x}} + \mathbf{B}_u \mathbf{u} + \mathbf{L}(\mathbf{y} - \mathbf{C}\hat{\mathbf{x}} - \mathbf{D}_u \mathbf{u})$$

$$E(\mathbf{d}) = E(\mathbf{v}) = 0$$

$$E(\mathbf{v}^T \mathbf{v}) = \text{diag}(\sigma_{GPS}^2)$$

$$E(\mathbf{d}^T \mathbf{d}) = \begin{bmatrix} 1.5 \cdot 10^{-11} & 4 \cdot 10^{-15} & -1.6 \cdot 10^{-15} \\ 4 \cdot 10^{-15} & 3.9 \cdot 10^{-14} & -6.6 \cdot 10^{-17} \\ -1.6 \cdot 10^{-15} & -6.6 \cdot 10^{-17} & 6.2 \cdot 10^{-16} \end{bmatrix}$$

Measurement error covariance is a priori known and corresponds to a diagonal matrix containing GPS error variances along the three axis, but the differential disturbance covariance, strongly depends on relative position and is difficult to evaluate, because position itself depends on control strategy. Thereby an adaptive technique shall be preferred for final implementation, with in-the-loop disturbance evaluation, but this is beyond the purpose of this work. Not only, this would require a lot of real time in-loop calculation on board, determining time-varying L and control gain matrix.

As it is the common way, the estimator optimization is conducted alone and does not take in account effective control strategy. The effective performance will be simply verified once optimum control is integrated. Moreover, the same observer model can even be implemented in an impulsive control, during long term coasting phases. We roughly consider input line disturbance covariance matrix, which refers to differential accelerations, registered on uncontrolled relative motion propagation over about 5 orbits, a sufficient time to lead the formation drift of several meters, but not too far away from typical controlled dynamic ranges.

### Considerations on altitude variation

Including differential solar pressure accelerations and Earth oblateness effects does not produce significant variation on disturbance covariance, dominated by differential aerodynamic acceleration, at this altitude of 400 km. The disturbance covariance, as well as the L-matrix and the state transition matrix, has to be recalculated for any upper altitude. This must be periodically done even during mission, while reference orbit semiaxis will decrease over lifetime.

### Subsection 4.3.5 - Digital Implementation

Once a continuous state-space estimator model has been calculated (see KALMAN command in [67]), a discrete-time state space model has implemented in the simulation (see KALMD command in [67]), to evaluate real-time on board calculation. GPS devices have an output rate of two measurements per second, and the observed time period has no reason to be smaller.

We assume synchronized GPS timing between spacecraft, instantaneous data packet transmission from the Chief to Deputy, and instantaneous state calculation, with a simple Forward Euler technique, on board the deputy satellite. This hypothesis is as best satisfied as larger the integration time period is, respect to GPS output time period.

**Table 4.3 – Standard deviation comparison of relative position and velocity and propagation on differential classical and modified orbital parameters with and without filtering.**

$\ \text{std}(\rho_{\text{meas}} - \rho_{\text{true}})\ $	Surrey SGR-05U	NovAtel OEM4-G2L	SGR-05U Discrete filter T=4s; $\tau=20$ s	SGR-05U Kalman filter T=4s
Position [m]	7.04829	0.06524	1.56633	0.40577
Velocity [m/s]	0.156633	0.0312	0.02333	0.001924
Semimajor axis [m]	188.50758	37.81053	41.02499	3.75828
Eccentricity	$1.56 \cdot 10^{-5}$	$4.93 \cdot 10^{-6}$	$6.03 \cdot 10^{-6}$	$5.13 \cdot 10^{-7}$
Inclination [deg]	$9.69 \cdot 10^{-6}$	$1.11 \cdot 10^{-6}$	$2.10 \cdot 10^{-6}$	$1.98 \cdot 10^{-7}$
$\Omega$ [deg]	$9.88 \cdot 10^{-6}$	$1.12 \cdot 10^{-6}$	$2.15 \cdot 10^{-6}$	$1.99 \cdot 10^{-7}$
$f = e \cdot \cos(w)$	$2.20 \cdot 10^{-5}$	$4.43 \cdot 10^{-6}$	$4.75 \cdot 10^{-6}$	$4.24 \cdot 10^{-7}$
$g = e \cdot \sin(w)$	$2.19 \cdot 10^{-5}$	$4.38 \cdot 10^{-6}$	$4.84 \cdot 10^{-6}$	$4.41 \cdot 10^{-7}$
$h = \tan(i/2) \cdot \cos(W)$	$1.10 \cdot 10^{-5}$	$2.20 \cdot 10^{-6}$	$2.38 \cdot 10^{-6}$	$2.18 \cdot 10^{-7}$
$k = \tan(i/2) \cdot \sin(W)$	$1.12 \cdot 10^{-5}$	$2.22 \cdot 10^{-6}$	$2.45 \cdot 10^{-6}$	$2.32 \cdot 10^{-7}$

For this reason, Kalman filtering has been implemented and investigated for a time periods above two times this value, which is 1 second. Figure 4.8 shows the trend of position error as the integration time grows up. The error is evaluated, in order to take in account both medium and standard deviations errors in all axis.

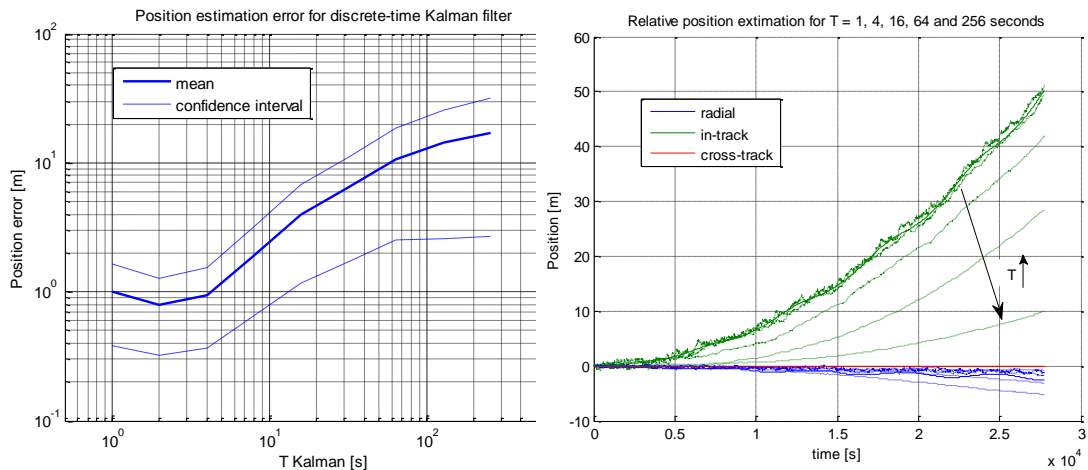


**Figure 4.8 - Discrete-time Kalman filter position error respect to integration time period, during an uncontrolled dynamic propagation over 5 orbit periods.**

Under our hypothesis, the observer minimizes state error, under the effects of white noises, but input line disturbances have a non-zero mean value. That leads to a non-steady free dynamic, characterized by a quadratic in-track relative position time history. The observer state can still follow the real state for sufficiently slow variation rates. In particular, error index excessively grows up for values above 4 seconds, because the observer response progressively slows down.

In Table 4.3, results of SGR-05U output filtering are compared to a typical dual frequency COTS competitor for ground operations. Kalman filter smooth the position determination within accuracy limits which are comparable to CDGPS outputs. Moreover, high frequency cut-off improves significantly propagated accuracy on orbital parameters estimations. Despite that, errors in semiaxis determination are still high, compared to order of magnitude which has to be detected, previously shown in uncontrolled dynamic propagations.

## Section 4.4 - Optimal control

It's assumed that a stable L-F formation is initialized, so the control scheme has to correct deviations caused by main identified disturbances, that is differential drag, solar radiant pressure and J2 effect.

As previously discussed, an LQR control regulator is preferred for its continuous disturbance counteraction, without involving long term coast phases, and its minimal risk, complexity and on-board computational demand. A LQR gain matrix is then evaluated, minimizing performance index:

$$J = \int_0^{\infty} (\mathbf{x}^T \mathbf{Q} \mathbf{x} + \rho \mathbf{u}^T \mathbf{R} \mathbf{u}) dt$$

where Q and R weight matrix, contain the inverse of target position accuracy, set as 10 m, and control acceleration, for a target daily consumption of 0.01 m/s/orbit. After accurate tuning, the best compromise between consumption and control accuracy out come from a ratio  $\rho$  equal to 1000 and without involving relative velocity (at this point, a null weight factor cannot be set, or the algorithm cannot converge to a gain matrix solution, but it's necessary to set a sufficiently small value).

$$\mathbf{Q} = \begin{bmatrix} \text{diag}(1/\mathbf{p}_{\max}) & \mathbf{0} \\ \mathbf{0} & \text{diag}(1/\dot{\mathbf{p}}_{\max}) \end{bmatrix} = \text{diag} \left( \begin{bmatrix} \text{diag}(1/10m) & \mathbf{0} \\ \mathbf{0} & \text{diag}(\ll 1) \end{bmatrix} \right)$$

$$\mathbf{R} = \left[ \text{diag}(1/\mathbf{u}_{\max}) \right] = \left[ \text{diag} \left( 1 / \left( 1 \cdot 10^{-4} m/s^2 \right) \right) \right]$$

Then the same control will be applied inserting actuation errors and, most of all, thruster modulators nonlinearities.

### Subsection 4.4.1 - Discrete time implementation

As resulting from digital implementation of Kalman filter, a time period equal to 4 seconds is sufficient to obtain sufficiently accurate estimation, without excessive time delays. The main OBC demand come from Kalman filtering, while LQR consist in a simple matrix operation, so there is no valid reasons to implement LQR at higher time periods, multiples of KF time period, because performances would lower, without significant computing cost reduction. Then the closed loop Discrete-time Linear Quadratic Regulator (DLQR) (see LQRD command in [67]) has been simulated, retroacting ideal required accelerations on deputy spacecraft in EH frame. That means that the actuation acceleration is constant at any time within the k-th interval:

$$\mathbf{u}(k) = -\mathbf{K}\mathbf{x}(k)$$

Relative trajectory is shown in Figure 4.10, and related performance in Figure 4.11. The relative trajectory is stable, but it manifests a constant steady-state offset, typical of proportional-derivative feedback (LQR is proportional to state, that is position and its derivative) respect to a constant disturbance. This can be negated adding a position integral feedback, or simply correcting target position, once the formation is established and differential aerodynamic acceleration can be a posteriori estimated.

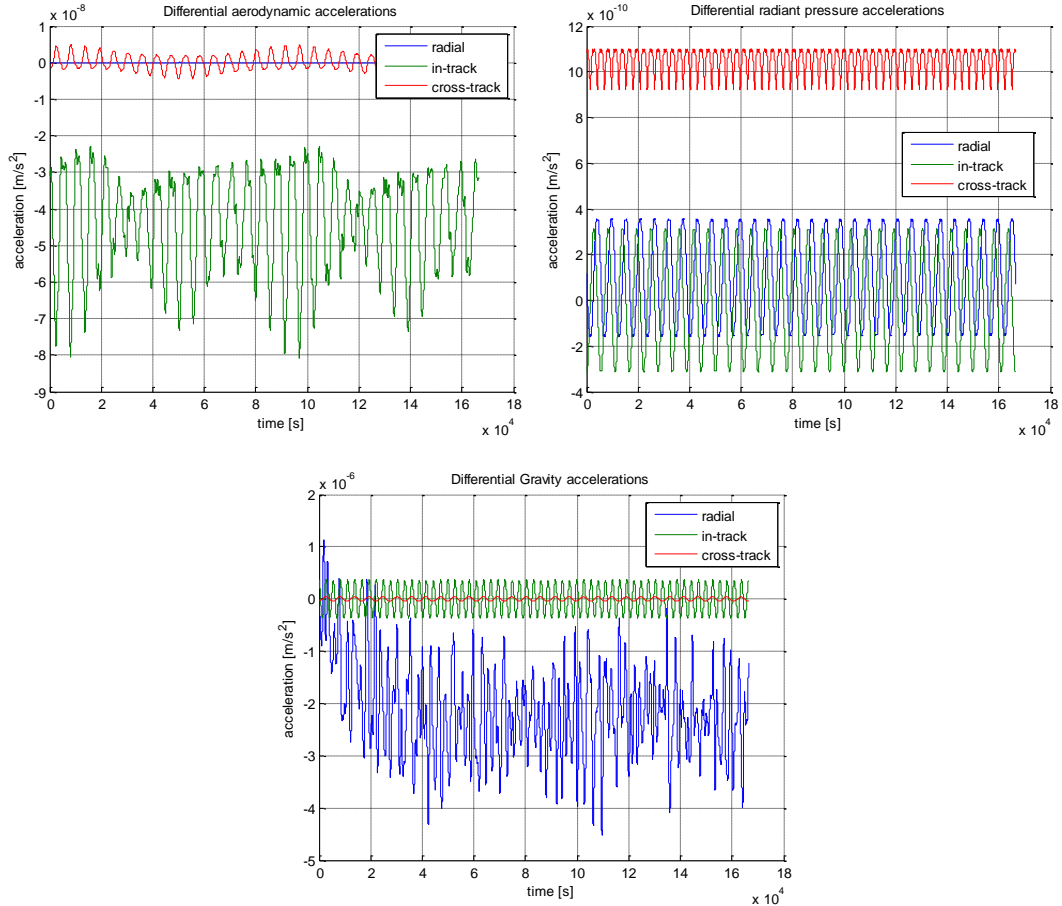


**Figure 4.9 – Differential aerodynamic (above) and radiant pressure (below) time trends, in case of DLQR, with 2% ballistic coefficient mismatch, over 30 orbit periods.**

#### Subsection 4.4.2 - Optimum control with integral feedback

Either a optimum control, with output integral retroaction has been implemented, to counteract constant disturbance effects, but full controllability of the dynamic system, with augmented state cannot be achieved in case of only in-track and cross-track actuation.

$$\mathbf{u}(k) = -\mathbf{K}\mathbf{x}_{aug}(k) = -\mathbf{K} \begin{bmatrix} \mathbf{x}(k) & \mathbf{x}_I(k) \end{bmatrix}^T = -\mathbf{K} \begin{bmatrix} \mathbf{x}(k) & \int_0^{t(k)} (\mathbf{y}_T - \mathbf{y}) dt \end{bmatrix}^T$$

$$\begin{Bmatrix} \dot{\mathbf{x}} \\ \dot{\mathbf{x}}_I \end{Bmatrix} = \begin{bmatrix} \mathbf{A} & \mathbf{0} \\ -\mathbf{C} & \mathbf{0} \end{bmatrix} \begin{Bmatrix} \mathbf{x} \\ \mathbf{x}_I \end{Bmatrix} + \begin{bmatrix} \mathbf{B}_u \\ \mathbf{0}_{3 \times 3} \end{bmatrix} \mathbf{u} + \begin{bmatrix} \mathbf{0}_{6 \times 3} \\ \mathbf{I}_{3 \times 3} \end{bmatrix} \mathbf{y}_T$$

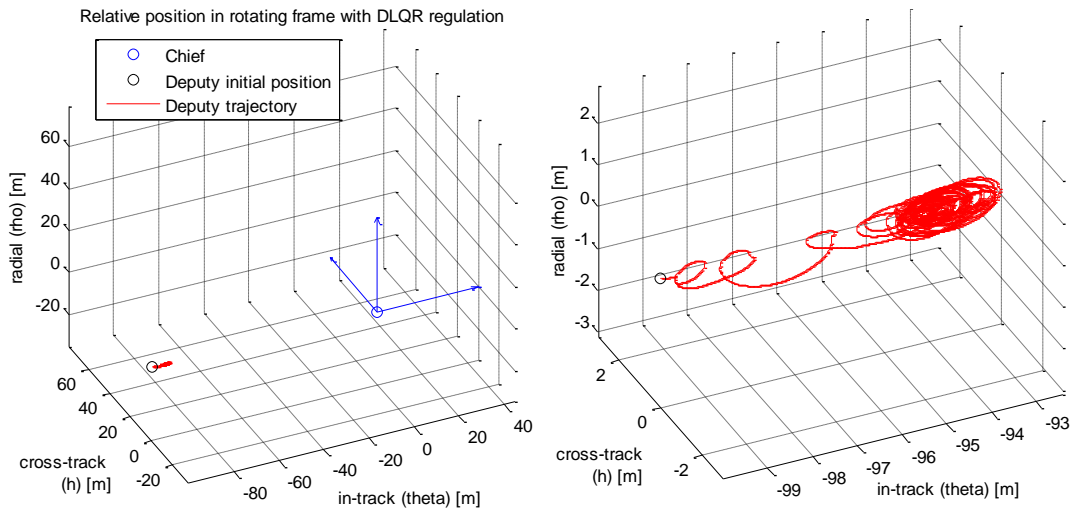


Figure 4.10 - Relative position propagation in case of DLQR ( $T=4s$ )

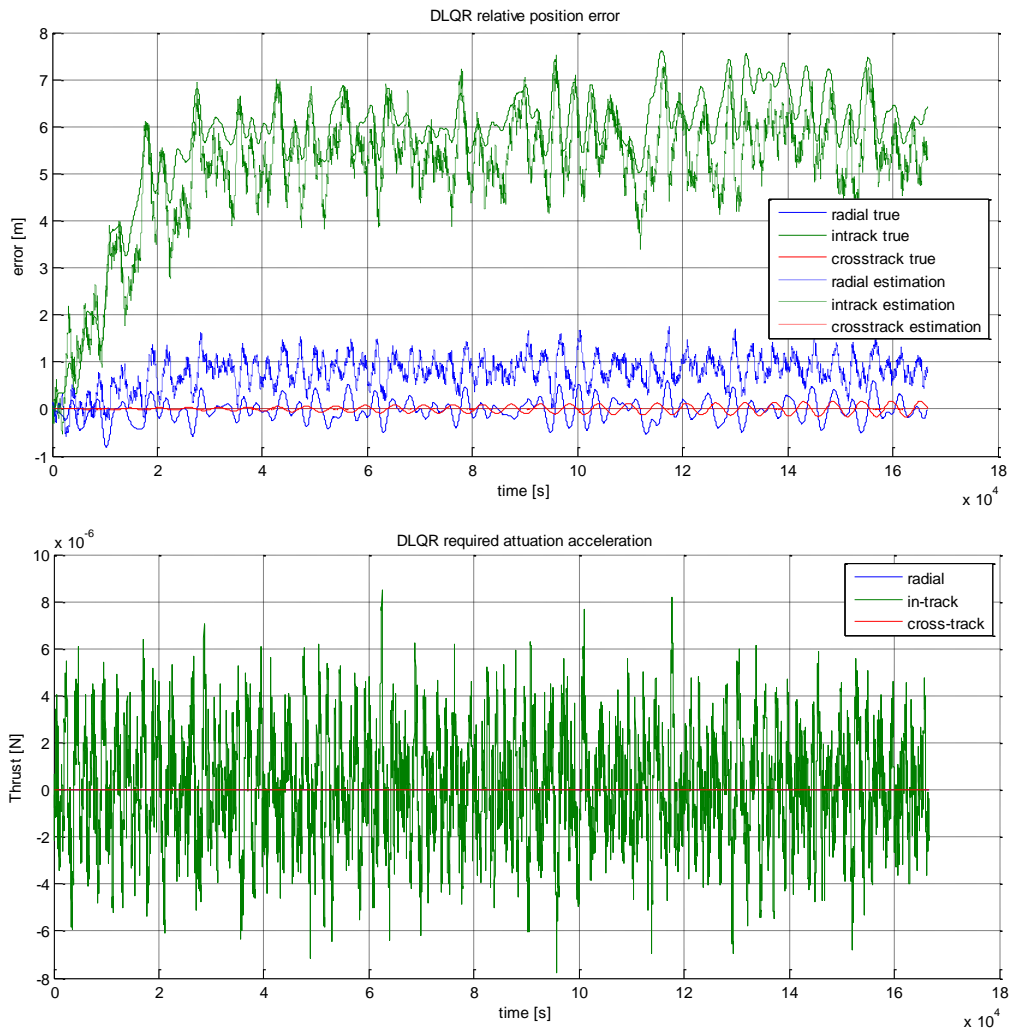


Figure 4.11 - Relative position errors time trend in EH frame (above) and control thrust (below), in case of DLQR ( $T_s=4s$ ), over 30 orbit periods



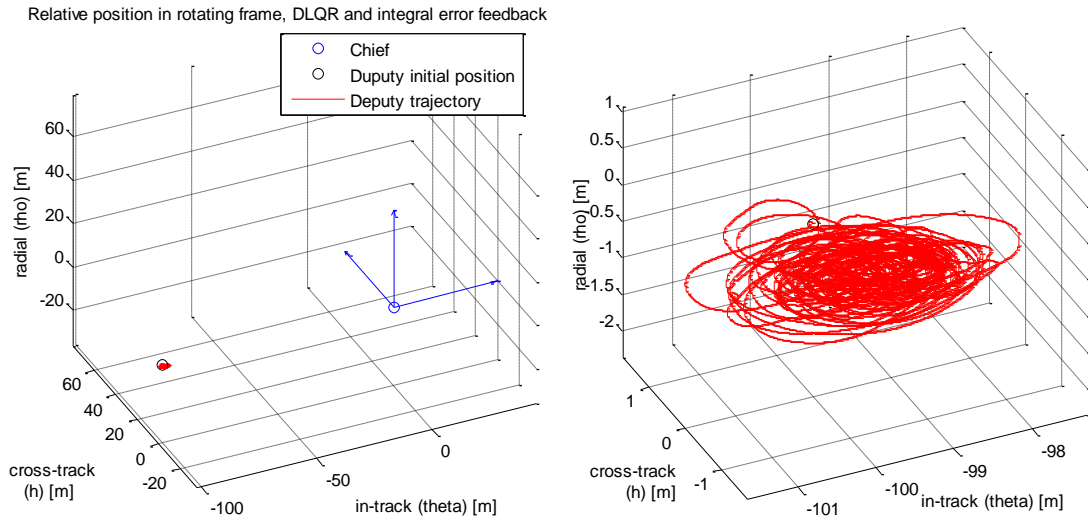


Figure 4.12 - Relative position propagation in case of DLQR ( $T=4s$ ) with integral error feedback.

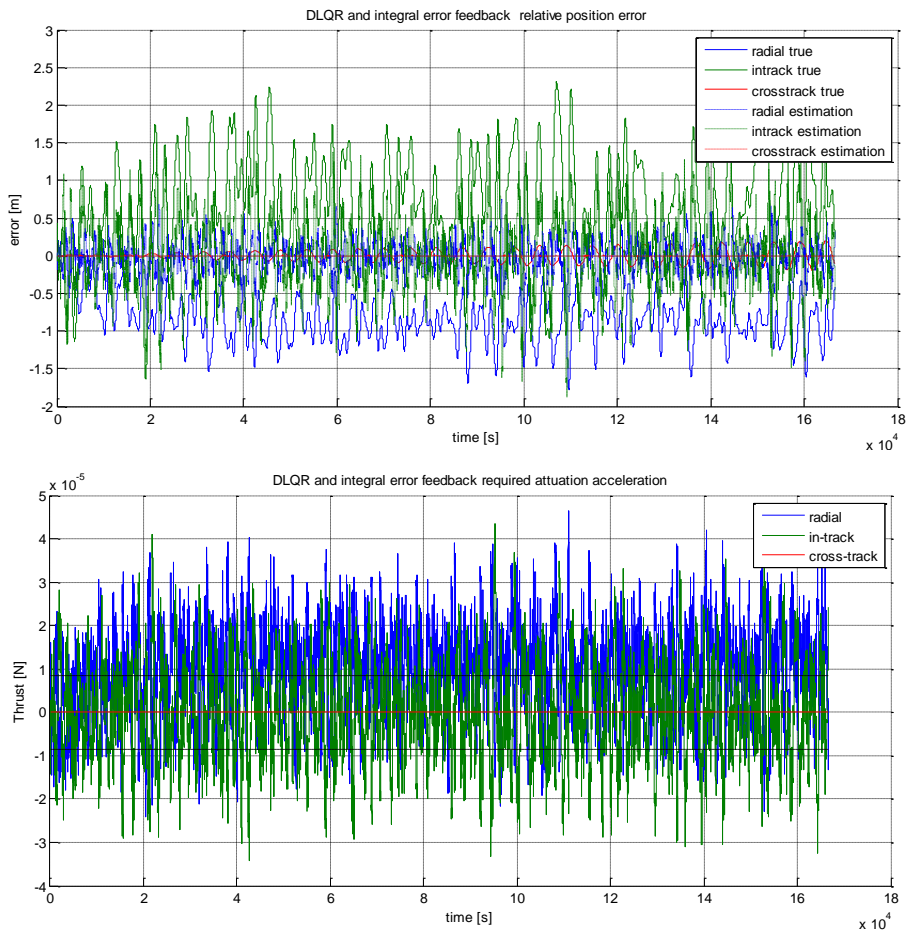


Figure 4.13 - Relative position errors time trend in EH frame (above) and control thrust (below), in case of DLQR with integral error feedback ( $T=4s$ ), over 30 orbit periods

A gain matrix for a generic three axis actuation has been calculated and implemented in the model, effectively improving position accuracy, in terms of steady state errors, setting:

$$\mathbf{Q}_{aug} = \text{diag} \left( \left[ \frac{1}{\rho_{\max}}; \frac{1}{\dot{\rho}_{\max}}; \frac{1}{T_0 \rho_{\max}} \right] \right) = \text{diag} \left( \left[ \frac{1}{10m}; 0; \frac{1}{5 \cdot 10^4 ms} \right] \right)$$

Then the same matrix has been truncated and applied to our condition of no radial thrust, but this rough attempt led to an unstable controlled dynamic. Thereby, this technique can be only applied using actuators in any direction, losing all advantages of neglecting radial thrust to control the in-plane dynamic.

## Section 4.5 - Propulsion subsystem, relative position control

Let's consider PCI-104 embedded propulsion systems already developed, which have sufficiently fine thrust level and modulation for relative position control. We focus on two technologies: cold gas and simple chemical propulsion or Pulsed Plasma Thruster.

### Subsection 4.5.1 - Chemical thrusters

In general, chemical propulsion MEMS (ChEMS) are oriented to reliable and less complex blow-down and cold gas technologies. Rarely Monopropellant solutions have been developed. The only solutions at the required  $\mu\text{N}$  thrust level are resumed in Table 4.4.

#### MicroSpace Cold Gas Micropropulsion System

The micropropulsion system, produced by MicroSpace [77] in Trieste, Italy, is initially designed for attitude control. It is composed by a pressurized nitrogen tank and thruster modules each one using micronozzles producing nominal forces between  $100 \mu\text{N}$  and  $10\text{mN}$  depending on the micronozzle model selected for use. Each micronozzle is coupled with a microvalve for the control by Pulse Width Modulation (PWM) mode so that very fine attitude control and formation flight are enabled also for the CubeSat class. Control of the thrust is achieved by a 1% resolution control of the valve duty cycle and results in a 1% to 5%. [78].

The propulsion system can be mounted inside the satellite body with nozzles operating through appropriate openings, or can be mounted outside the body frame as structural section of the satellite itself and occupies  $90 \times 90 \times 37 \text{ mm}$  ( $100 \times 100$  with nozzles). The entire system has a minimum total mass of 300 g and draws less than 2 W, at 12 V, of peak power consumption, lowering to 1 W while not thrusting. An  $85 \times 40 \times 10\text{mm}$  sized dedicated electronic board is provided (also in PCI-104 format) with RS232 command and telemetry interface. Extendable tanks are available to increase total impulse, up to a 1U cube envelope. Other information is reported in Table 4.4.

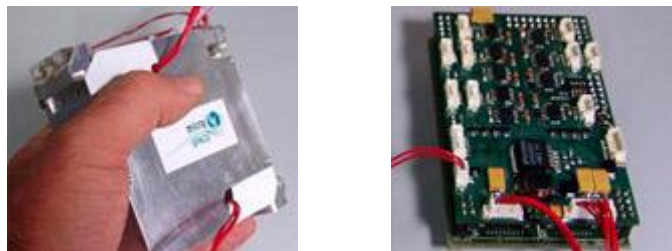


Figure 4.14 - MicroSpace Cold Gas Micropropulsion, nozzles module (left) and control PCB (right) [77]

### Vacco Micro Propulsion System

A valid alternative is VACCO MiPS, a highly integrated all-welded manifold system, employing self-Pressuring Isobutane  $C_4H_{10}$  propellant (it is stored as Liquid and expelled as cold gas). Depending on effective tank pressure thrust varies between 25 (18 psia) and 55 mN (40 psia) at 20°C, with minimum pulses from 0.25 to 0.55 mNs.

Table 4.4- Available CubeSat chemical propulsion subsystems

	MicroSpace Cold Gas Microprop.	VACCO/JPL MiPS Microthr.
Isp [s]	50 to 100	65
Power [W]	<2	<1
Voltage [V]	12	TBD
Thrust [ $\mu$ N]	100 to 10000	25000 to 55000
Min Imp bit [ $\mu$ Ns]	0.2 to 20	25 to 55
Min Imp bit [s]	0.002	0.001
Total Impulse [Ns]	TBD	34
Mass [kg]	0.300	0.509
Price [euro]	81000	TBD
Dim [ $mm^3$ ]	100×100×37	91×91
References	[77][78]	[79] [80]

Also this product is declared to be expandable for increased propellant capacity. Normal version provides a total impulse up to 34 Ns, with a total system mass of 509 g (dry mass: 456 g; propellant: 53 g), while an extended version is mentioned, providing a total Impulse of 239 N-Sec, but increasing total mass up to 980 g (dry mass: 620 g; propellant: 350 g) [80].

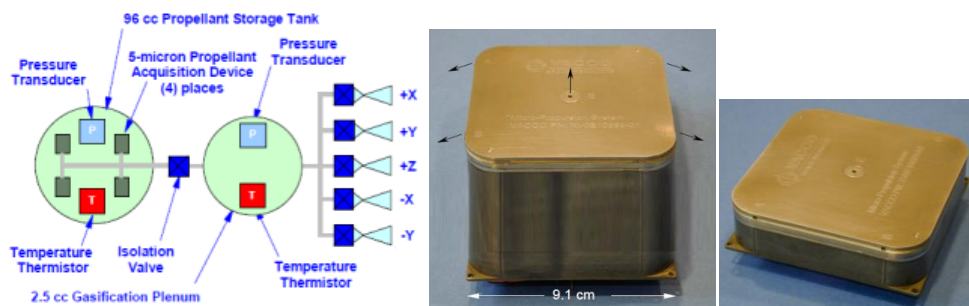


Figure 4.15 - Vacco MiPS propulsion system, system diagram (left) and enclosures, with (center) and without (right) extended tank [80]

### Subsection 4.5.2 - Pulsed Plasma Thrusters

PPTs are long-standing, space-qualified electric propulsion thrusters of proven reliability, relatively simple and low-cost. The PPT is a solid state device, using Teflon fuel and high voltage discharge to ablate, vaporize and ionize the propellant, accelerating it through an electric field to high velocity. A  $\mu$ N Lorentz force propels the plasma out of the nozzle to generate a not-steady thrust (i.e. pulsed).

Energy is stored in the thrusters' capacitors and, at the receiving command, a spark plug circuit is activated eroding the electrode itself. The PPT consists of two main components: the discharge chamber and a Power Processing Unit (PPU), to generate the required excitation voltages and the control circuitry for the firing process.

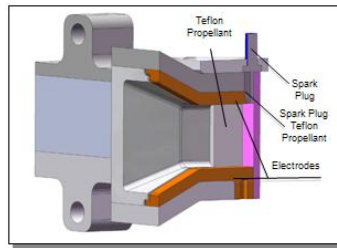


Figure 4.16 – Pulsed Plasma Thruster, nozzle section CAD [81]

### Clyde Space PPT

This product is provided by Clyde Space [82], in collaboration with Mars Space Ltd [81], and extensively tested at Southampton University and Institute for Space Systems, Stuttgart. It consists in single nozzles, fed by a condensers array, collocated on a single PC-104 format board, compatible with CubeSat I2C bus, within 90x90x27mm envelope. Unit mass is less than 200g, including 10g of propellant, providing a total impulse of 30Ns. Experimental data reported in [83], states an impulse bits up to 34  $\mu$ Ns, at the specific Ibit of about 17  $\mu$ Ns/J and a power draw a less than 0.5W, which then corresponds to a medium continuous thrust of 8.5  $\mu$ N, for an impulse every 4 seconds.

According to available information on the website [81], also lateral oriented thruster geometry, represented in Figure 4.17, is under development and custom geometry, such as a cluster of independent thrusters in all four lateral directions is presumably possible to develop, even accommodating electronic board and capacitors in a separate PCB.

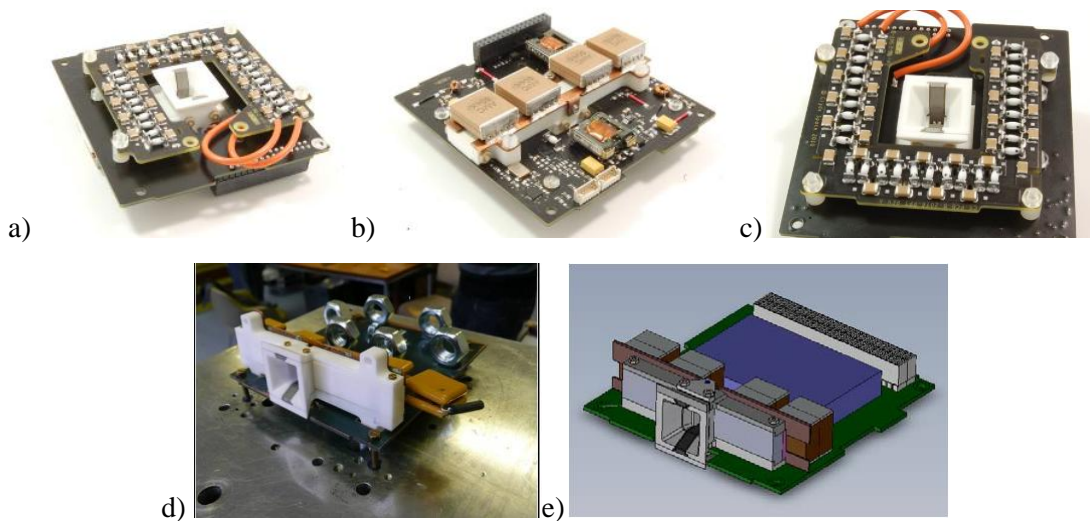


Figure 4.17 – Clyde Space CubeSat Pulsed Plasma, external (nozzle) side view (a), internal view (b) and nozzle close up view (c) and its lateral nozzle version, during vibration tests (d) and CAD model (e) [81]

### Surrey PPT

The Surrey pulsed plasma propulsion system [84] is made from three PC104 Boards, expressly designed for a 3U CubeSat, two boards house four PPTs each and the third acts as PPU. It is designed to charge up two 4 $\mu$ F capacitors within one second allowing firing two thrusters at any one time at a discharge rate of 1Hz. In this configuration the combined PPTs have a total propellant mass of 1.12g, equal to a total  $\Delta V$  of 2.72ms<sup>-1</sup>, at a specific impulse of 321s, with a

satellite mass of 4.5kg. However with the insertion of copper blocks into the established discharge chamber of the current design the total  $\Delta V$  could be increased  $76.34\text{ms}^{-1}$ .

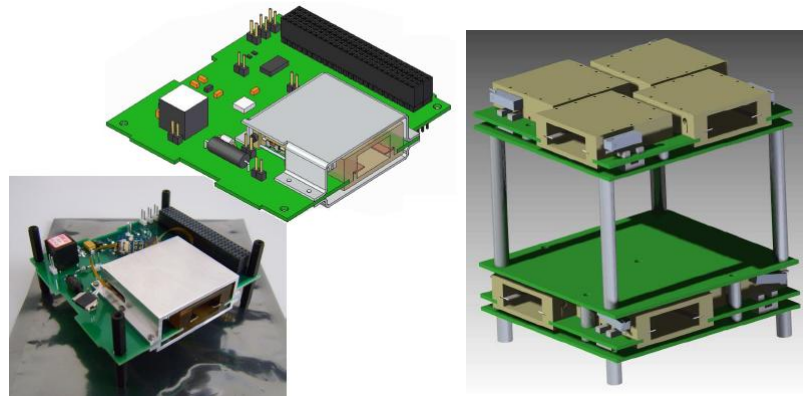


Figure 4.18 – Single (left) and cluster (right) configuration of 8 PPT thruster within PC104 form factor

Additional testing performed on future version at the University of Stuttgart [10] has revealed a true specific impulse of 1340 seconds, 1.5W of power consumption and a thrust of  $0.9\mu\text{N}$ .

The thruster housing measures  $40\times 40\times 12\text{mm}$ . One of these can be easily placed alone on a PC104 board, for lateral oriented thrust, allowing space for corner support and the bus connector. Four of these can be still situated on a PC104 form factor board in a rotational symmetric off axis configuration, as in Figure 4.18, but this design conflicts with structural supports at the board corners and the bus connector and they must be set on outside the stack.

Table 4.5- Available CubeSat PPT propulsion subsystems

	Clyde Space $\mu\text{PPT}$	Surrey $\mu\text{PPT}$
Isp [s]	590	320
Power [W]	0.5	<1.5
Voltage [V]	TBD	5
Period [s]	4	4
Thrust [ $\mu\text{N}$ ]	8.5	0.225
Imp bit [ $\mu\text{Ns}$ ]	34	0.9
Total Impulse [Ns]	30	8.1 to 228.9
Mass [kg]	0.2	0.336
Price [euro]	12000	TBD
References	[82] [83] [81]	[84] [10]

### Subsection 4.5.3 - Analyzed propulsion subsystems

Among considered Off-the-Shelf available device, none of them have flown yet, but they are all selected for different incoming missions. All of the listed products can be also fitted in a cluster of four independent thrusters for our particular configuration.

The driving criteria is first of all the lowest thrust level, or, in case of PWM modulation is implemented, the lowest obtainable impulse bit, in order to achieve fine formation maintenance. In this case, Microspace Cold Gas Micropropulsion, despite a relatively high nominal thrust, not less than  $100\mu\text{N}$ , due to very tight minimum impulse duration can obtain impulse bits even lower than PPT counterparts.

However, as already mentioned, power consumption is a major issue, in the current mission, so, both Pulsed plasma Thruster models presented, are still a valid option, most of all Clyde Space's device, for its extremely low consumption, despite a bit high impulse bit magnitude.

**Table 4.6- Existing CubeSat propulsion subsystem driving selection criteria summary**

	<b>Clyde Space <math>\mu</math>PPT</b>	<b>MicroSpace Cold Gas Microp.</b>
<b>Power [W]</b>	0.5	2
<b>Voltage [V]</b>	TBD	12
<b>Thrust [<math>\mu</math>N]</b>	34	100 to 10000
<b>Min Imp bit [<math>\mu</math>Ns]</b>	34	0.2 to 20
<b><math>\Delta</math>V budget [m/s]</b>	10	TBD
<b>Mass [kg]</b>	0.2	0.3 + fuel
<b>Price [euro]</b>	10000	81000
<b>Pros</b>	Low cost Defined $\Delta$ V budget Low power consumption Easy PCI-104 integration	High thrust modulation Fine impulse level

All these devices have been tested in relative position control simulations, and then Vacco MiPS was early discarded, due to its higher thrust levels. Both MicroSpace Cold Gas Micropropulsion and Vacco MiPS microthruster has been implemented, but the latter has shown to be much more versatile and performing, due to its finest minimum impulse bit and throttling. Surrey PPT showed instead insufficient thrust authority at low altitudes and it is discarded too.

Both Clyde Space PPT and Microspace Cold Gas resulted feasible for formation maintenance. Despite better cold gas performance, the PPT solution is strongly preferred, due to its cost and reliability. Moreover, little information about cold gas fuel mass and total impulse is available, up to now. Early estimates state standard fuel storage of about 20 g. In order to obtain the same  $\Delta$ V budget of 10 m/s provided by PPT device, about 60 g of fuel mass are necessary. Storing this fuel amount is reasonable, with provided additional tanks, increasing the subsystem envelope up to 1U cube.

#### **Subsection 4.5.4 - Simulation implementation**

In order to model the real actuation thrust that can be implemented on board, the required acceleration has been filtered with algebraic non linear relations, which simulate the modulation implemented by the selected propulsion system. We investigate the two best solutions outlined, one for each actuation technology type: Clyde Space PPT and MicroSpace cold gas Micropropulsion System.

In this section, only results for an oriented thrust along in-track and cross-track directions are presented, that is in case of a single thrusters and yaw manoeuvring capability, and not for independent thrusters for each axis. The latter case has been modelled and verified anyway, but does not lead to significantly different results in terms of thrust modulation and consumption.

Then, the modulated required acceleration, a priori known on board, can be sent as input to the Kalman estimator, instead of the original required acceleration out coming from optimum control, reducing predicted state errors.

**Table 4.7 – Performance indexes, calculated from propagation data over 30 orbit periods, in case of DLQR, with and without integral error feedback, with and without PPT or cold gas actuation**

		DLQR	Int. DLQR	DLQR + cold gas	LQR + PPT
<b>Position accuracy<sup>4</sup></b> <b>[m]</b>	Radial	0.2406	0.3346	0.2665	0.5488
	In-track	1.414	0.7306	1.3724	1.5228
	Normal	0.07438	0.0846	0.0666	0.0840
<b>Position steady state error [m]</b>	Radial	0.1915	0.8351	-0.0238	-0.0186
	In-track	5.744	0.8283	5.7355	5.8077
	Normal	0.05930	0.06752	0.0018	0.0019
<b>Mean acceleration [m/s<sup>2</sup>]</b>	Radial	0	$3.756 \cdot 10^{-6}$	0	0
	In-track	$6.068 \cdot 10^{-7}$	$3.005 \cdot 10^{-6}$	$5.487 \cdot 10^{-7}$	$3.404 \cdot 10^{-7}$
	Normal	$1.277 \cdot 10^{-9}$	$3.568 \cdot 10^{-9}$	$1.091 \cdot 10^{-9}$	$5.387 \cdot 10^{-10}$
<b>Consumption [m/s/day]</b>		0.0525	0.5845	0.0474	0.0294

Finally, the real acceleration is modelled rotating the input acceleration by random error angles which depends on attitude control accuracy, set to 5% coarse radial pointing, and multiplied by one plus specific thrusters magnitude accuracy. The error angle is introduced via a small rotation technique. Both small angles and magnitude errors are random generated (see BAND-LIMITED WHITE NOISE Simulink block in [67]).

Results are compared to previous simulations, conducted with ideal actuation acceleration, and resumed in Table 4.7.

#### Subsection 4.5.5 - Actuation with Cold Gas Micropropulsion

MicroSpace cold gas device can provide, by integrated Pulse Width Modulator (PWM) circuit, from 1% to 100% percentage of nominal thrust set at minimum available level of 0.1 mN.

Within the simulation, the required thrust has been limited from minimum (function of minimum impulse) and maximum value (that is nominal thrust, at full throttle), then, for intermediate values, it's rounded off by 1% steps of maximum thrust. The very fast PWM dynamic has been modelled at first time, and then neglected, because no more accurate results have been experienced, while the model became greatly stiff and simulation time critically slowed down. So we assume constant thrust acceleration at each time interval.

A very similar behaviour respect the ideal actuation (required acceleration direct feedback) of previous DLQR simulation is obtained, as results in Figure 4.19 and Figure 4.20.

#### Subsection 4.5.6 - Actuation with Pulsed Plasma Thruster

Both Surrey and Clyde Space PPT has been implemented, but Surrey device thrust level simply results insufficient to counteract differential disturbances and it has been discarded.

The Clyde Space PPT thrust impulse is generated every 4 second, exactly as the defined LQR period. A simple ON/OFF modulation has been modelled. It's possible to increment control period to multiples of the original value, to achieve some level of thrust modulation, having the possibility to switch on and off propulsion device for fractions of the period itself, but the control period has to grow too much, i.e. up to 40 s to achieve a 10% modulation step.

<sup>4</sup> accuracy =  $std(|\mathbf{p}_{real} - \mathbf{p}_{target}|)$  steady-state =  $mean(|\mathbf{p}_{real} - \mathbf{p}_{target}|)$  acceleration =  $mean(|\mathbf{u}_{effective}|)$

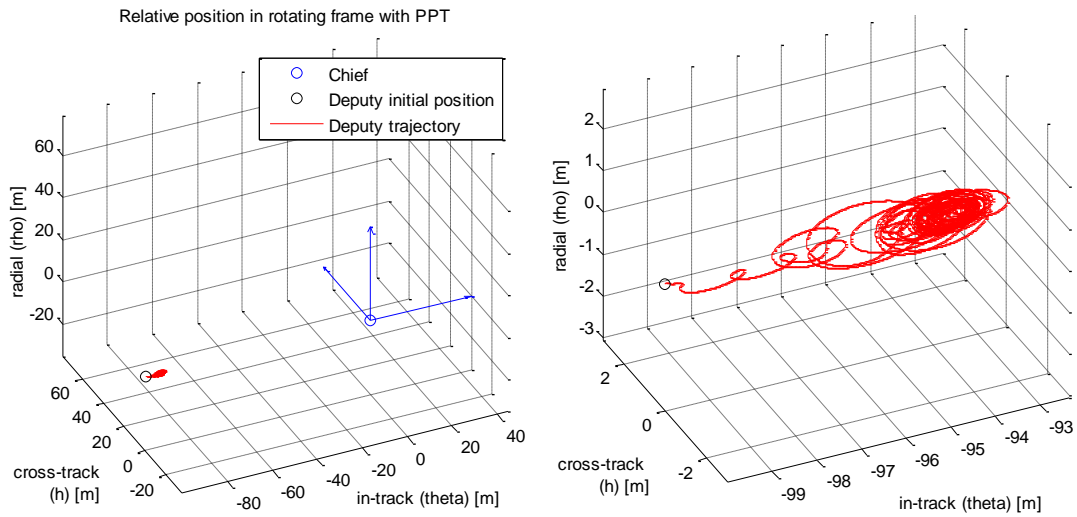


**Figure 4.19 - Relative position propagation in case of DLQR ( $T=4s$ ) with Micro Space cold gas (left) and zoom in (right), over 30 orbit periods**

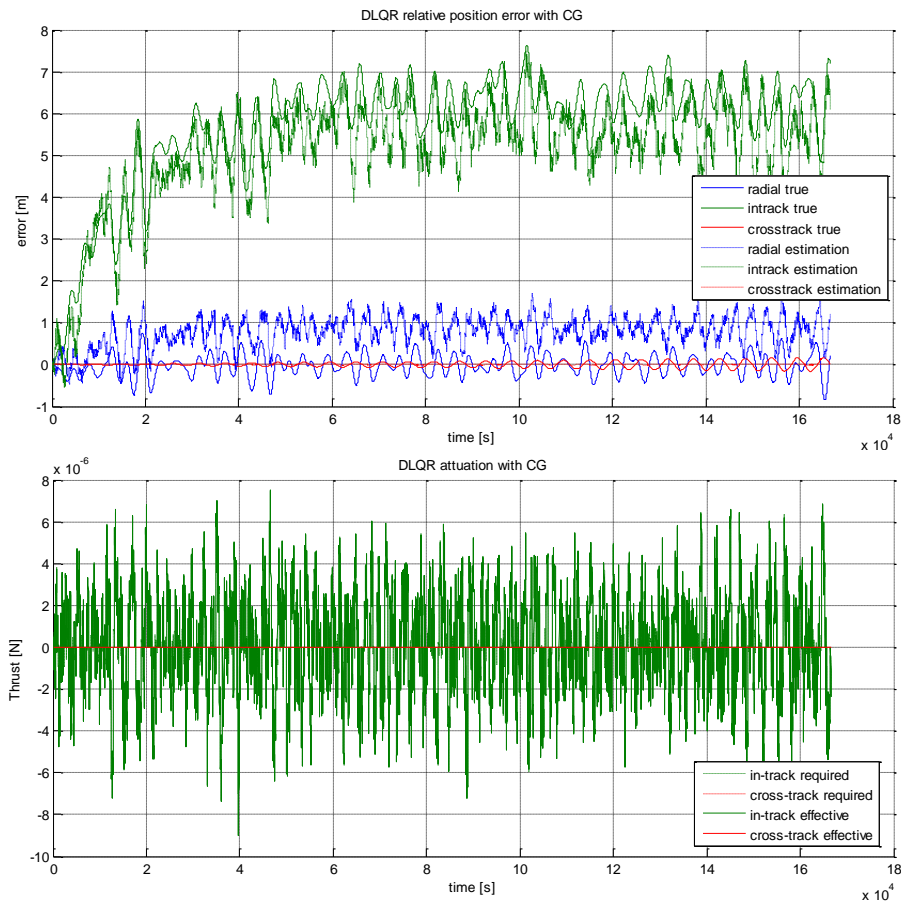


**Figure 4.20 - Relative position errors time trend in EH frame (above) and control thrust (below), in case of DLQR ( $T=4s$ ) with Micro Space cold gas (left) and zoom in (right), over 30 orbit periods**



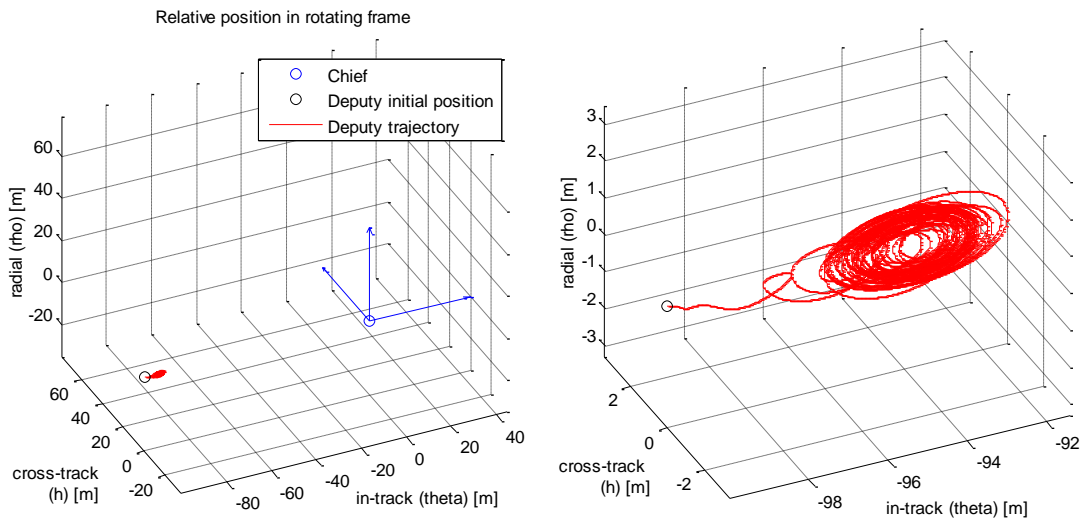


Figure 4.21 - Relative position propagation in case of DLQR ( $T=4s$ ) with Clyde Space PPT (left) and zoom in (right), over 30 orbit periods

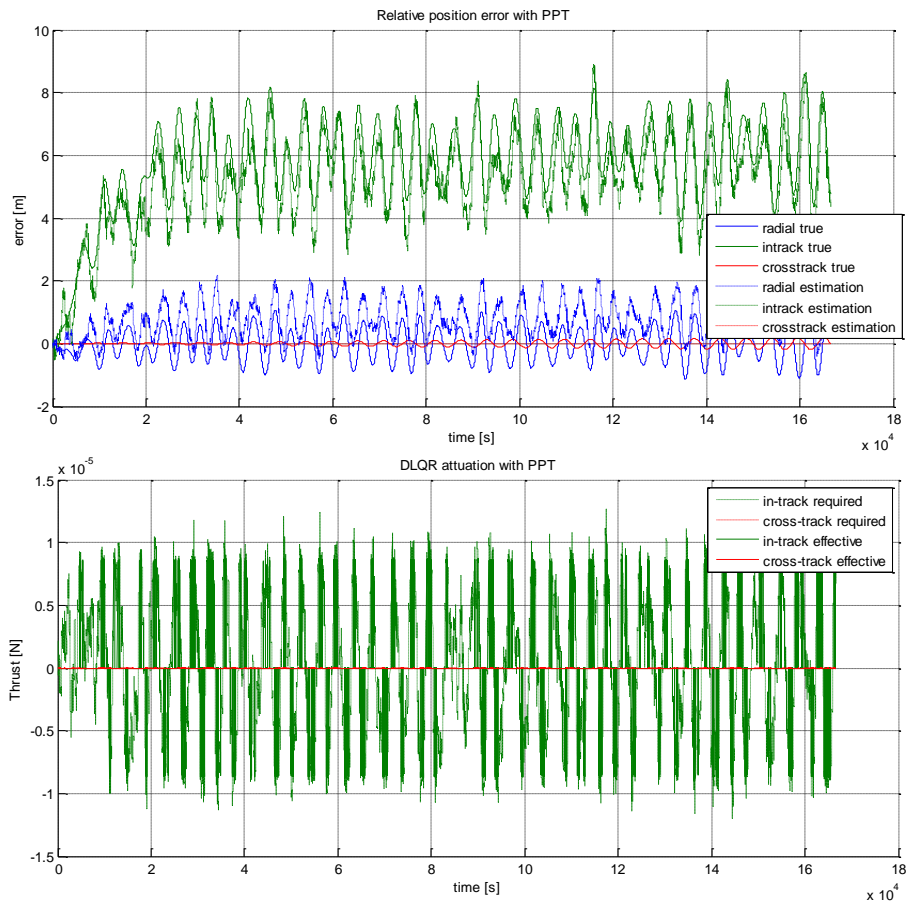


Figure 4.22 – Relative position errors time trend in EH frame (above) and control thrust (below), in case of DLQR ( $T=4s$ ) with Clyde Space PPT (left) and zoom in (right), over 30 orbit periods

In theory, little level of modulation can be obtained acting on PPU supply power, increasing or decreasing condenser charging time and then pulses time period. In absence of detailed information, a constant time period is set and then worst case non-linearity is taken in account.

In Figure 4.21 and Figure 4.22, respect to cold gas, a constant pulsed thrust magnitude is evident and it traduce in a hysteresis effect and in a cyclic motion. The amplitude of this motion reflects the error in relative position and velocity necessary to trigger actuation acceleration.

In conclusion, both actuation propulsion systems are feasible, but PPT solution, considering its low cost, mass and power, is the most attractive solution, despite high non-linearity and performances degradation. For these reasons, subsequent analysis, which explores in detail each phase of the current control strategy and its robustness against parameters variation, is oriented towards the PPT solution, assumed as worst case obtainable performance. Cold gas is still investigated, but results will not be reported, while not significant issues are revealed.

## Section 4.6 - Collision avoidance strategy

### Subsection 4.6.1 - Passive collision avoidance nominal trajectory

As the uncontrolled dynamic results suggest, the main drift from nominal position is in in-track direction, due to position deviation from nominal condition (that is primarily semiaxis differences), caused by momentary control failures, measurements and actuation errors within the control loop, or simply by aerodynamic secular disturbances.

That means that the leader-follower geometry, characterised by a separation in the only in-track direction, is the most dangerous choice, despite its simplicity and its disturbances minimization properties. Even a pendulum configuration, that reduces risks of collision, that can only occur two times per orbit, due to the cross-track periodic motion, cannot negate this risk at all.

As suggested in [85] and [66], a nominal trajectory in which in-plane and cross-track relative motion combined produce a projection on the radial-normal plane that doesn't intersect the reference (chief) trajectory, as depicted in Figure 4.23.

Instead of complicating control architecture, inserting an in-loop sub-routine, that it shall be implemented in any way at least in a simple form, a passive collision avoidance strategy relies only on the nominal trajectory definition. At this aim it's sufficient to modify initial conditions of the previous L-F nominal trajectory, setting in-plane motion by introducing an eccentricity difference and a synchronized cross-track motion, setting an inclination difference, if reference orbit  $\omega=0+k\pi$ , or a RAAN difference if  $\omega=\pi/2+k\pi$ . That is exactly the opposite combination that to obtain a PCO, see Figure 4.24.

Respect to an L-F configuration, which nullify differential J2 effect satisfying the constraint  $\delta a = \delta e = \delta i$  (see Appendix B), such this trajectory type can't do so. The supplementary disturbance accelerations depend on periodic motion amplitude, which is not the effective separation between chief and deputy.

### Subsection 4.6.2 - Effects on control performance, simulation results

The relative trajectory periodic motion shall not be excessively wide, to mitigate J2 effects, but it have to be large enough to mitigate collision risk. We set  $\rho_x$  and  $\rho_z$  as function of position control accuracy  $\sigma$ , in each respective axis, equal to 2 m ( $3\sigma$ , that correspond to 2.2% probability to intersect in-track axis on EH frame, that is still not the probability of a collision event, which would be even lower). Also higher apertures have been investigated. The case for a 10 m aperture, in Figure 4.25 and Figure 4.26, highlights previously mentioned effects

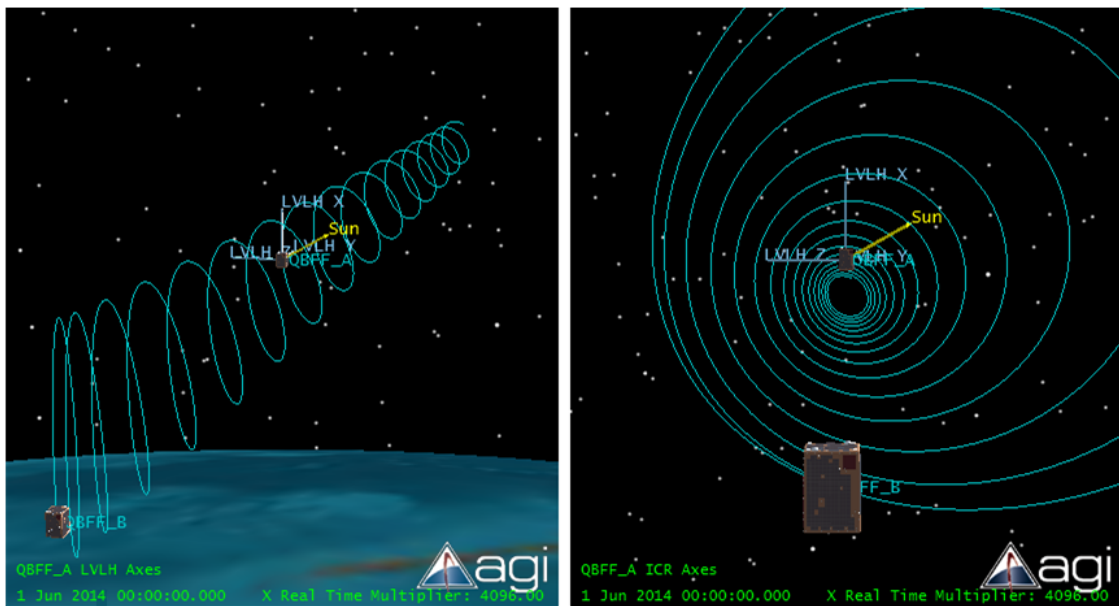


Figure 4.23 - Passive collision avoidance strategy. Propagation over a sidereal day of uncontrolled relative motion, setting initial  $\delta e$  and  $\delta i$ .

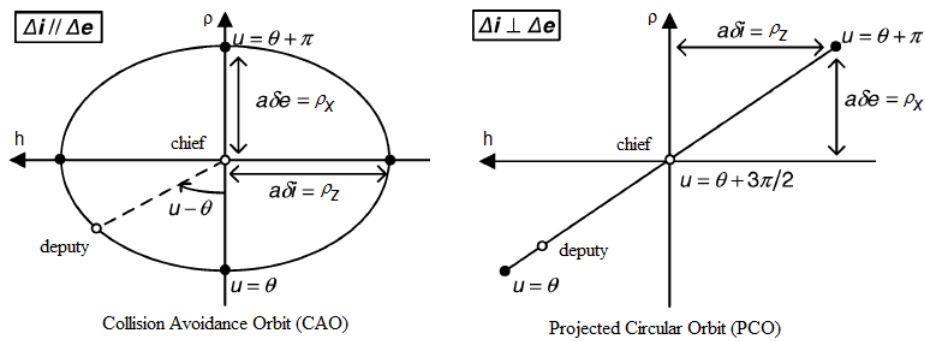
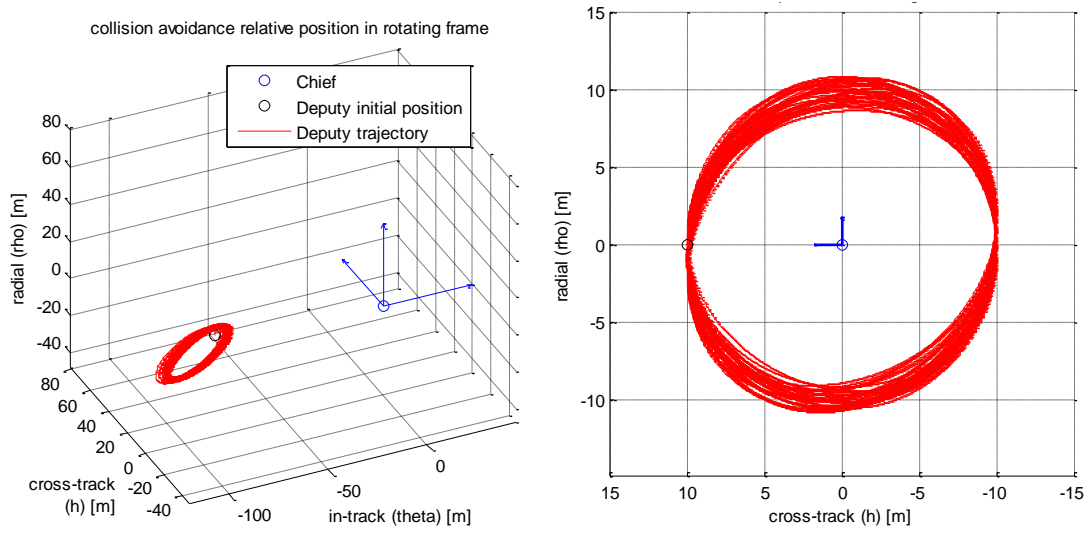


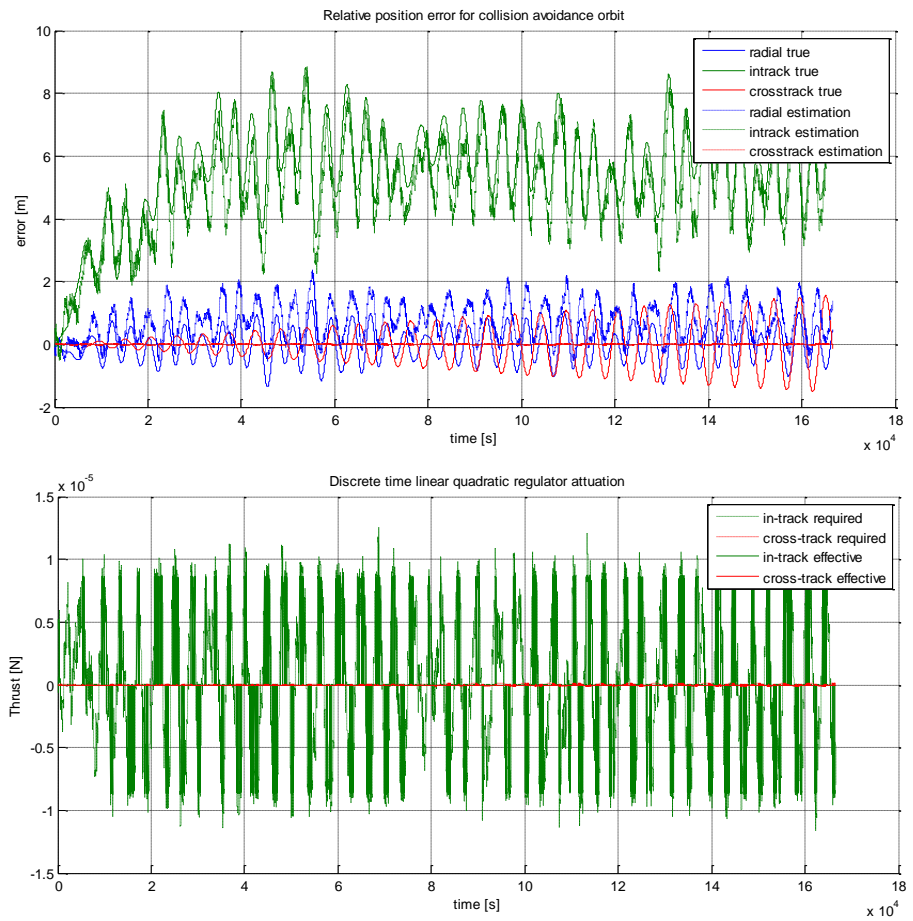
Figure 4.24 - Relative out-of-plane and in-plane motion synchronization

Table 4.8 – Performance indexes, calculated from propagation data over 30 orbit periods, for the only case of PPT actuation, at different relative orbit apertures

KF + LQR + PPT architecture		Leader Follower	CARO 2 m aperture	CARO 10 m aperture
Position accuracy [m]	Radial	0.5488	0.5074	0.5556
	In-track	1.5228	1.6021	1.6110
	Normal	0.0840	0.1927	0.6487
Position offset [m]	Radial	-0.0186	-0.0251	-0.0238
	In-track	5.8077	5.6416	5.5803
	Normal	0.0019	0.00464	0.0157
Actuation acceleration [m/s <sup>2</sup> ]	Radial	0	0	0
	In-track	$3.404 \cdot 10^{-7}$	$3.579 \cdot 10^{-7}$	$3.825 \cdot 10^{-7}$
	Normal	$5.387 \cdot 10^{-10}$	$6.936 \cdot 10^{-10}$	$2.337 \cdot 10^{-9}$
Consumption [m/s/day]		0.0294	0.0309	0.0330



**Figure 4.25 – Controlled relative position propagation (left) and projection in radial-normal plane (right), in case of DLQR ( $T=4s$ ) with Clyde Space PPT (left) and zoom in (right), over 30 orbit periods, with Collision Avoidance Relative Orbit (CARO) starting conditions**



**Figure 4.26 - Relative position errors time trend in EH frame (above) and control thrust (below), in case of DLQR ( $T=4s$ ) with Clyde Space PPT (left) and zoom in (right), over 30 orbit periods, with Collision Avoidance Relative Orbit (CARO) starting conditions**

Simulation has been run with the so defined target relative trajectory and the optimum control plus Kalman filter architecture works well, taking in account GPS accuracy and PPT modulation non-linearity. There are some losses in position accuracy performance differences respect to classical L-F case, but the trajectory is still controlled without instabilities or undesirable behaviours.

The fuel increasing is still significant and the implementation of such this geometry would be inconvenient, especially for separation far above the position control accuracy. This strategy has been investigated. It guarantees that in case of control failure, the unperturbed dynamic passes nearby the chief at a safety distance, and it would be an appreciable addition but it is not strictly necessary in the present case, because the chief itself can take on formation control duty, in case of deputy temporary failure.

## Section 4.7 - Formation acquisition and reconfigurations

### Subsection 4.7.1 - Relative dynamic after second spacecraft releasing

Acquisition phase is the most critical condition in LQR control, especially in case of subsequently releasing from launchers. In track relative velocity errors lead to fast drift rates along orbit track, in uncontrolled dynamic, as it is represented in Figure 4.27, for an initial separation of 1 km. Error in other direction does not produces semiaxis error, but drift still triggers due to disturbances.

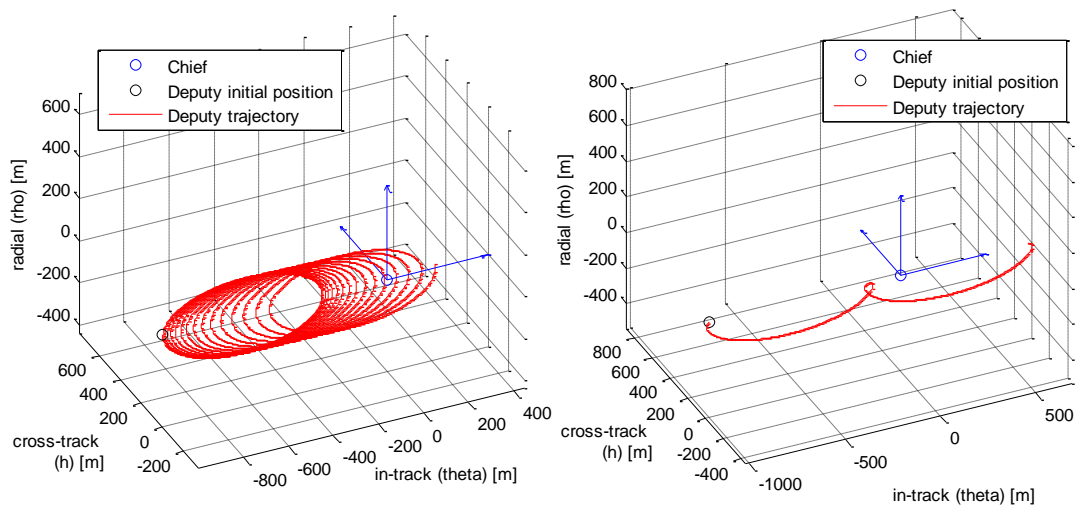


Figure 4.27 – Relative uncontrolled trajectory evolution in EH frame, after deputy releasing with 0.2 m/s radial (left) or in-track (right) velocity , for 1 km separation L-F formation

### Subsection 4.7.2 - Formation acquisition with continuous control

The LQR control has been tested, setting such this prohibitive initial conditions. The worst case, identified in this way, is an initial error of 0.2 m/s (10% spring impulse) in relative in-track velocity component. No position error has been introduced, considering it negligible respect to semiaxis error already introduced.

Simulations results for cold gas propulsion are shown in Figure 4.28, over a 10 orbit period interval. The relative trajectory immediately converge to the nominal condition, but this result has been achieved modifying the control gain matrix previously tuned for the maintenance phase, reducing position weight factor and increasing velocity one. With nominal gain matrix,

the relative motion showed an unstable behaviour, due to thrust saturation non-linearity. In such this condition, the position accuracy obviously decreases, but the control system can counteract even this critical initial condition.

Also an alternative strategy has been implemented, in which nominal DLQR gains are initialized after semiaxis difference is reduced below a defined tolerance, with a different control law, defined as:

$$u_y(k) = -K_{acquisition} (2n_0 x + \dot{y})$$

That is, in particular, acting on errors in the commensurability condition. This technique does not produce significantly better results and the previous technique is preferred, because doesn't imply semiaxis tolerance setting and other evaluations. Moreover, the LQR approach already implements this commensurability condition establishment and counteracts not only semiaxis mismatch, but also differential eccentricity and out-of plane motion.

PPT propulsion, in Linear Quadratic Gaussian LQG loop (DLQR and Kalman Filter), shows an unstable behaviour and an alternative control strategies has to be developed. With very low PPT thrust level, only a docked configuration releasing strategy becomes possible, setting a low level spring impulse during separation, which ensures safe relative drift of the pair and subsequent settling of the nominal 100 m separation, using the same control loop matrix gains implemented during nominal trajectory maintenance analysis, as shown in Figure 4.30 and Figure 4.31.

Performance in both cases and the fuel amount over the first day (comprising acquisition increment) is resumed in Table 4.9.

**Table 4.9 – Formation acquisition performance, calculated from propagation data over 10 orbit periods, for a relative velocity error of 0.2 m/s initial conditions.**

Formation acquisition		Cold Gas	PPT
<b>Position max deviation<sup>5</sup> [m]</b>	Radial	507.4	5.838
	In-track	2442	23.51
	Normal	0.3847	0.1056
<b>steady state position accuracy [m]</b>	Radial	3.801	0.5858
	In-track	7.015	1.343
	Normal	0.0467	0.0515
<b>Starting condition</b>		Sequential releasing	Undocking after contemporary releasing
<b>Velocity starting error [m/s]</b>		0.2	0.005
<b>Settling time [orbits]</b>		≈6-7	≈2-3
<b>Consumption over 1 day [m/s]</b>		0.6554	0.03498

<sup>5</sup> max deviation =  $\max(|\mathbf{p}_{real} - \mathbf{p}_{target}|)$

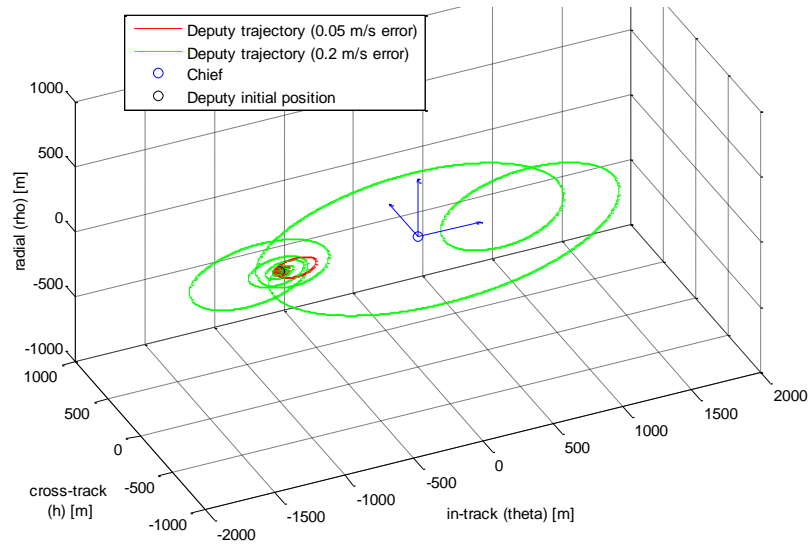


**Figure 4.28 - Relative trajectory in EH frame during formation initialization, with Cold Gas Micropropulsion, for 0.2 m/s in-track velocity error**

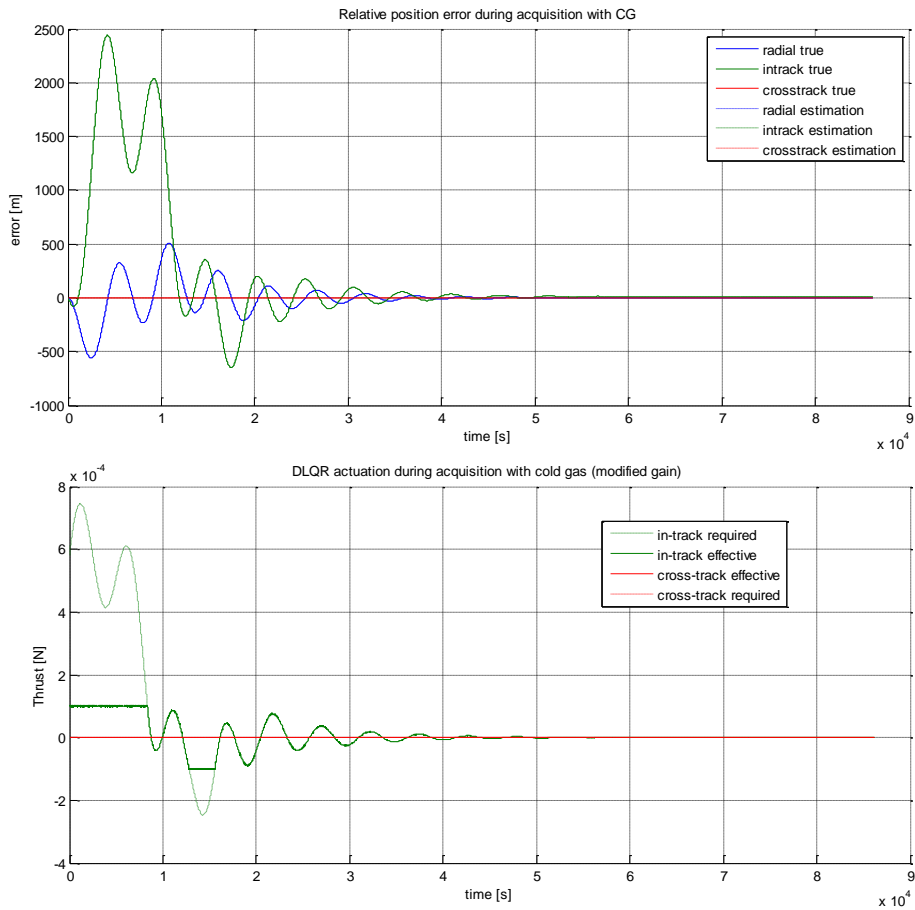


**Figure 4.29 - Formation initialization with Cold Gas Micropropulsion. Position in EH frame (above) and control thrust (below) time-trend for 0.2 m/s in-track velocity error**

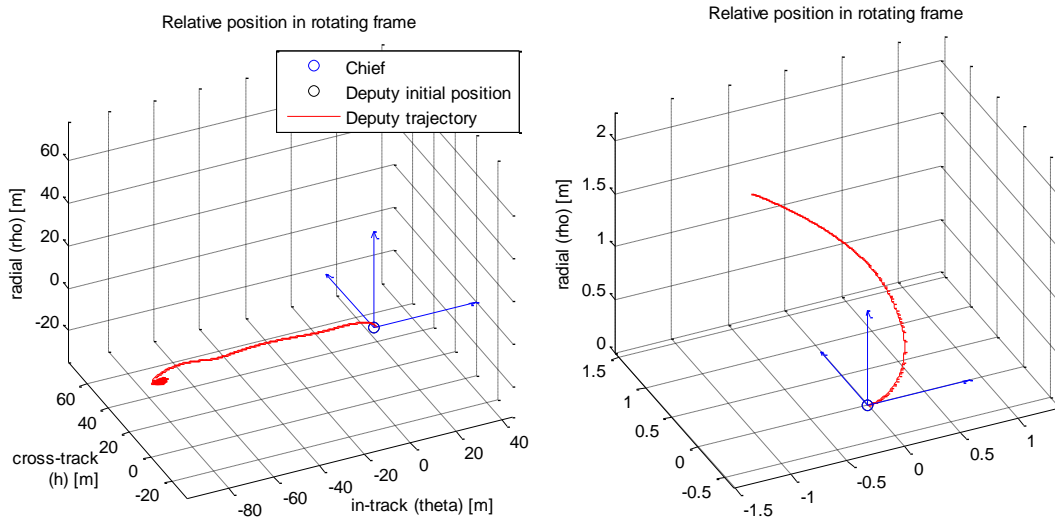


Figure 4.30 – Relative trajectory (left) in case of formation acquisition after deputy and chief undocking, highlighted in close up view (right), with an in-track 1 cm/s impulse.

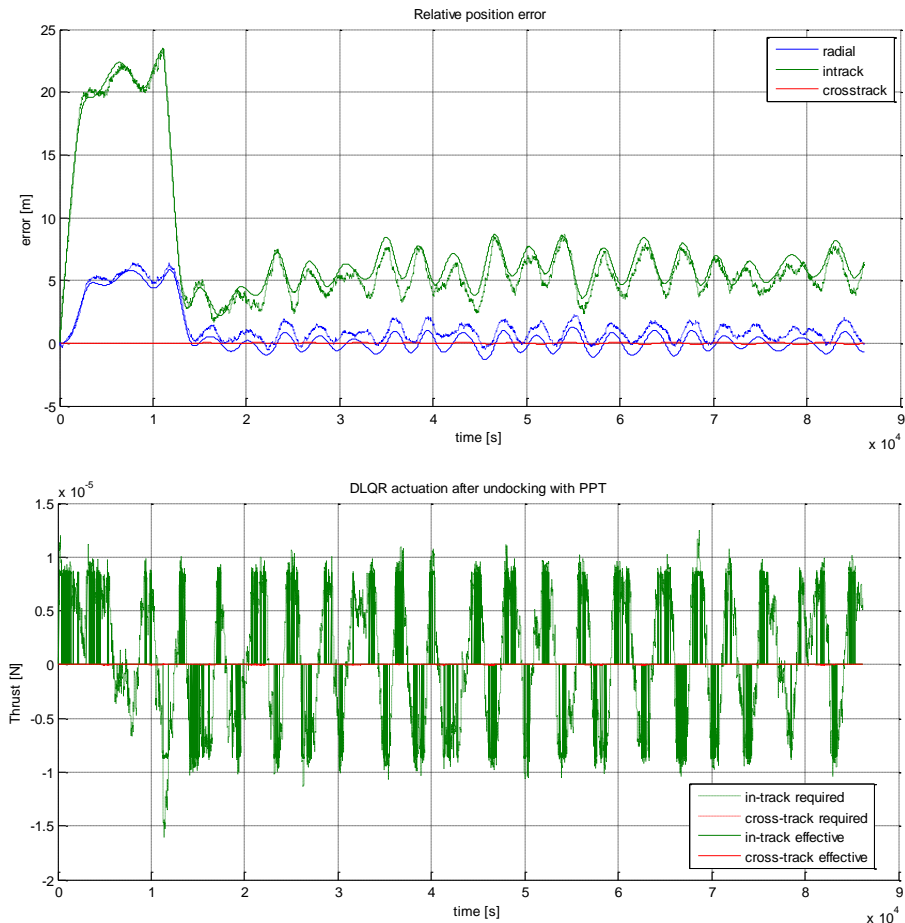


Figure 4.31 – Acquisition performance position (above) and required control acceleration (below) in case of L-F formation acquisition after Deputy undocking from Chief, with an in-track 1 cm/s impulse.



### Subsection 4.7.3 - Formation acquisition with impulsive control

To the only formation acquisition phase, a simple 2 impulse maneuver is sufficient to counteract initial semiaxis mismatch. Once the relative position velocity errors are sufficiently reduced, the continuous LQR control can be initialized nearby nominal conditions.

With STK Astrogator tool, an impulsive formation acquisition has been simulated, after a releasing in a 1km separation leader follower configuration, with 0.2 m/s in-track relative velocity error. The maneuver starts after 1 orbit period of uncontrolled dynamic, surely sufficient time interval to perform commissioning and WLAN acquisition, collect enough relative position sampling data for semiaxis difference evaluation and calculate  $\Delta V$  impulses on board. The adopted control sequence is defined as follows:

- Propagation till true anomaly is  $0^\circ$  (waiting for perigee condition)
- First impulsive firing
- Propagation till  $m$  orbit periods are elapsed
- Second impulsive firing

It has to be iterated until semiaxis matching condition at the end of the sequence is satisfied, respect to the two  $\Delta V$  impulse unknown components. In Table 4.10,  $\Delta V$  budget for this control sequence, for a 2 orbits intermediate coast phase is resumed and it results not very greater than the actual velocity error of 0.2 m/s to be corrected. However, this strategy is unaffordable with selected propulsion devices, because of too high firing time periods. Moreover, that involves a trial solution technique to be performed on board and a STK model doesn't implement measurements and actuation accuracies and non-linearity, which effects shall be carefully investigated. In conclusion, in case of PPT actuation, a releasing in docked configuration has to be necessarily developed.

**Table 4.10 – STK Astrogator results for a 2-impulse maneuver formation acquisition, for an initial relative velocity error of 0.2 m/s (after 1 orbit free dynamics, with 2 orbit coast phase between the two firings).**

	Impulse magnitude [m/s]	$T_{\text{firing}}$ with cold gas [s]	$T_{\text{firing}}$ with PPT [s]
$\Delta V1$	0.1349	1349	15875
$\Delta V2$	0.1161	1161	13659
<b>Total</b>	<b>0.2510</b>		

### Subsection 4.7.4 - Reconfigurations with continuous control

Once formation is initialized and huge semiaxis differences are removed, optimal control technique, with nominal K and L gain matrices, can counteract smaller deviations from equilibrium conditions.

Thereby, the same LQR control loop is also able to follow time-varying target signals, allowing formation reconfigurations in terms time-varying periodic motion aperture, as shown in Figure 4.32, or in-track separations, as shown in Figure 4.33. As example, time profile of relative position and control acceleration transient response, only for the case of a periodic motion aperture time-varying input signal is reported in Figure 4.34.

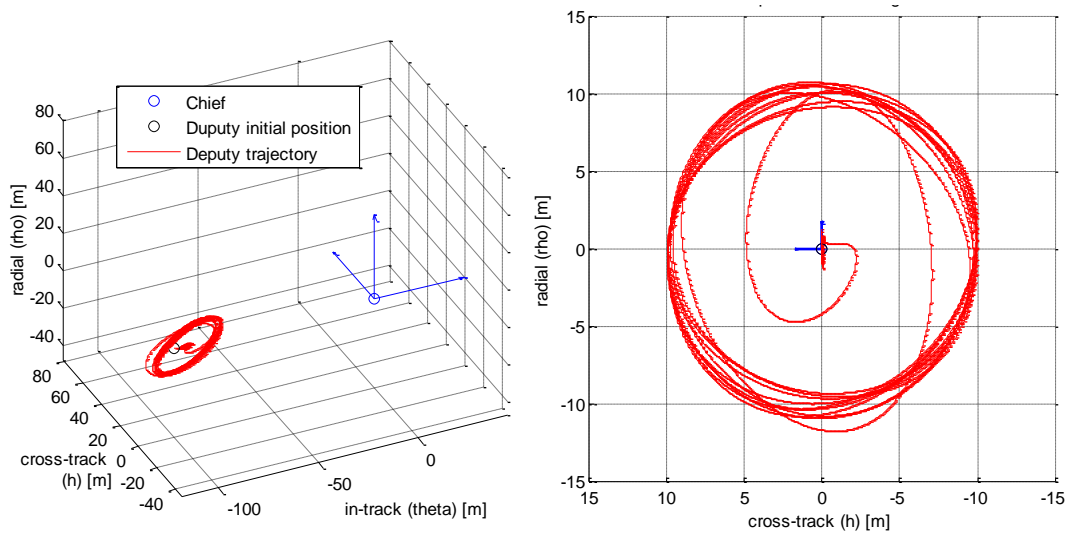


Figure 4.32 - Relative trajectory in EH frame (left) and projection on normal-radial plane, during reconfiguration from leader follower to a 10 m aperture periodic relative motion relative trajectory.

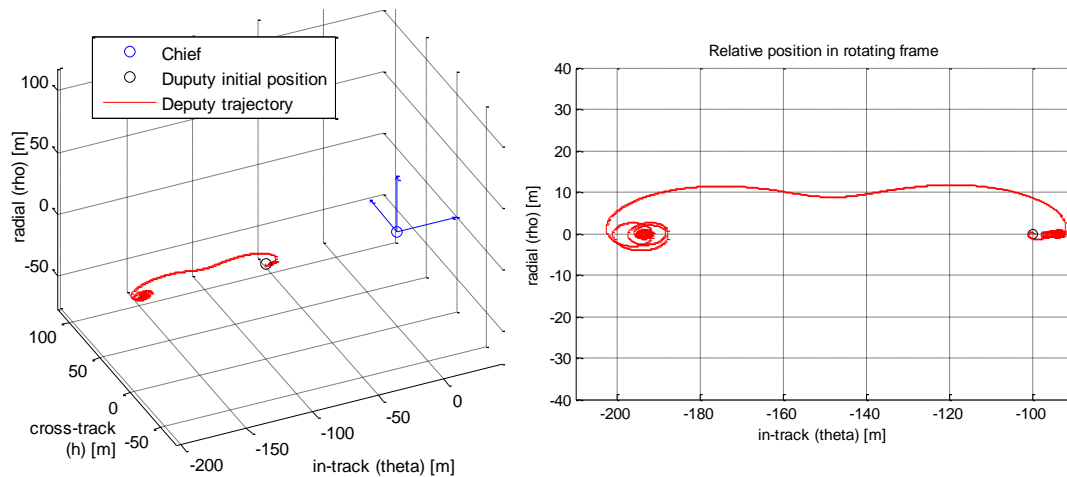
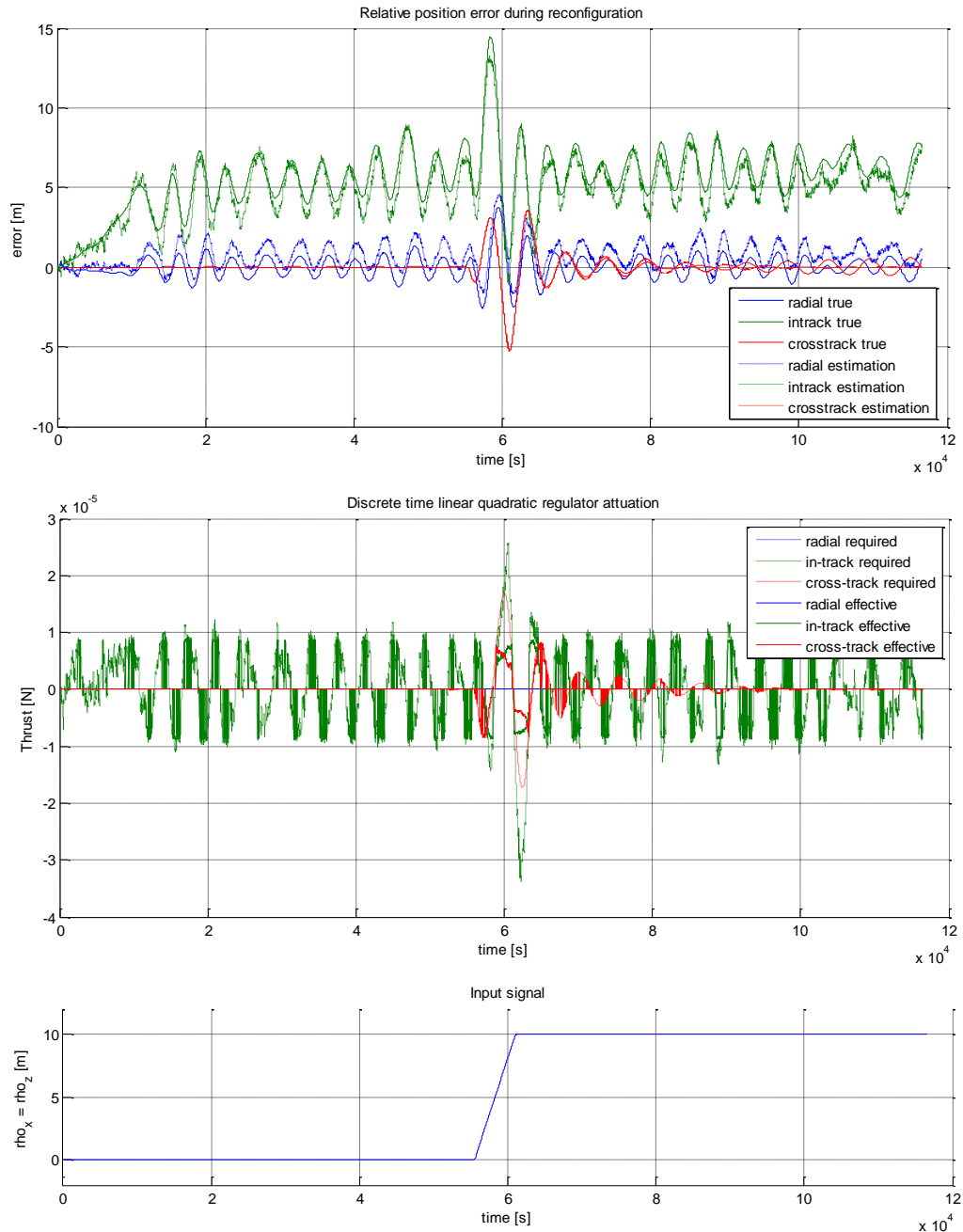


Figure 4.33 - Relative trajectory in EH frame (left) and projection on intrack-radial plane, during reconfiguration from 100 m to a 200 m in-track separation in a leader follower configuration.

Table 4.11 – Performance indexes, calculated from propagation data over the three different input target signal phases, in case of PPT actuation, for a reconfiguration strategy, starting from a leader follower steady state.

Reconfiguration		100 m separation L-F (10 orbits)	Into 10 m aperture CARO		Into 200 m separation L-F	
			Reconfig. (1 orbit)	Settling (10 orbits)	Reconfig. (1 orbit)	Settling (10 orbits)
Position accuracy [m]	Radial	0.574	2.04	0.693	4.97	2.37
	In-track	1.97	4.35	1.25	11.8	5.08
	Normal	0.0242	2.41	0.819	0.0553	0.0858
Position max deviation [m]	Radial	1.31	3.76	2.01	11.9	11.6
	In-track	8.82	14.5	8.84	47.1	46.1
	Normal	0.0545	3.56	3.56	0.0799	0.151
Mean acc. [m/s <sup>2</sup> ]	In-track	$3.65 \cdot 10^{-7}$	$1.48 \cdot 10^{-6}$	$5.75 \cdot 10^{-7}$	$1.81 \cdot 10^{-6}$	$8.59 \cdot 10^{-7}$
	Normal	$4.39 \cdot 10^{-10}$	$1.24 \cdot 10^{-6}$	$1.52 \cdot 10^{-7}$	$2.52 \cdot 10^{-9}$	$5.92 \cdot 10^{-10}$

Respect to corresponding steady state 100 meters separation leader-follower maintenance, in order to obtain a circular projection in radial-normal plane of 10 meters radius, consumption increasing during transient phases amounts to 0.0222 m/s.



**Figure 4.34 – Relative position in EH components (above) and required control acceleration (center) during reconfiguration from L-F to a 10 m aperture periodic relative motion relative trajectory (below)**

Alternatively, in order to obtain an in-track separation variation from 100 m to 200 m, additional fuel consumption results 0.0370 m/s. Relative trajectories in EH frame for this two example cases are shown respectively in more details are reported in Table 4.11.

This  $\Delta V$  budget can be furthermore reduced, requesting the same manoeuvres in a shorter time period, lowering fuel consumption and maximum position excursion during transient phases. So, more detailed analysis is beyond the purpose of this work. They depend on the definitive mission plan and they otherwise have minor impact on final budget.

In conclusion, a continuous LQR control has also the advantage to allow freedom of reconfiguration, without significantly greater fuel consumption respect to the nominal maintenance condition, paying attention to give a sufficiently slow varying target time-signal.

## Section 4.8 - Effects of parameters on control performance

### Subsection 4.8.1 - Separation effects

HCW equations model cannot take in account the effect of spacecraft separation. The major effect is that, as the hypothesis of close proximity relative position respect to orbital radius falls, higher order terms in gravity gradient model lead to high position estimation and control errors (See Appendix B).

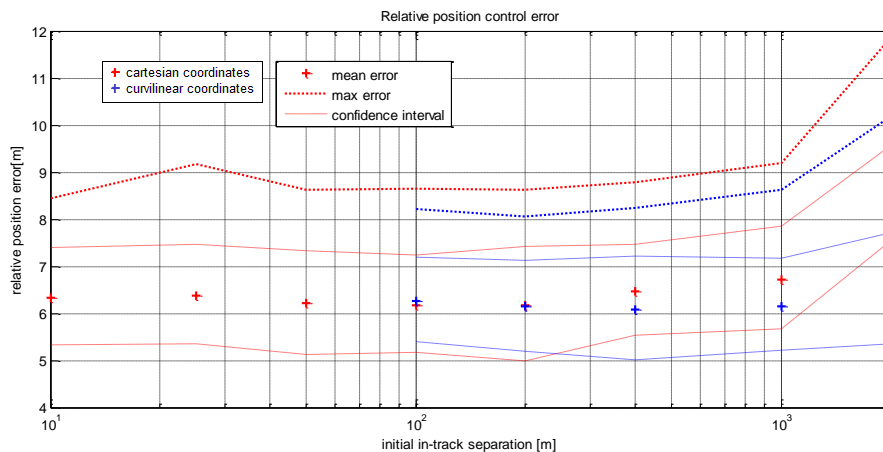


**Figure 4.35 – Steady state distance error respect to target relative position and maximum value experienced during transient**

As depicted in Figure 4.36, neither position estimation errors nor control accuracy show significant effects respect to distance between chief and deputy, unless, for higher baseline, above kilometer-level, these errors start growing, before rapidly bring to instability in the current LQG architecture with PPT actuators. In particular, measured position is affected by a standard deviation rising, which means less accurate estimation, but no bias errors. Control accuracy is affected, as a consequence, by higher steady state errors.

Figure 4.35 shows mean position error absolute value respect to target relative orbit during the initial transient state, highlighting deviation standard and max registered value intervals. In this case, results are shown also in case of curvilinear coordinates conversion, highlighting error reduction for higher separations.

PPT and cold gas propulsion follows similar trends. These errors are then probably due to position determination and estimation, and not due to propulsion, even if for even higher separations, cold gas still works at lower accuracies, while PPT propulsion incurs in occasional instability effects, caused by non-linear actuation.

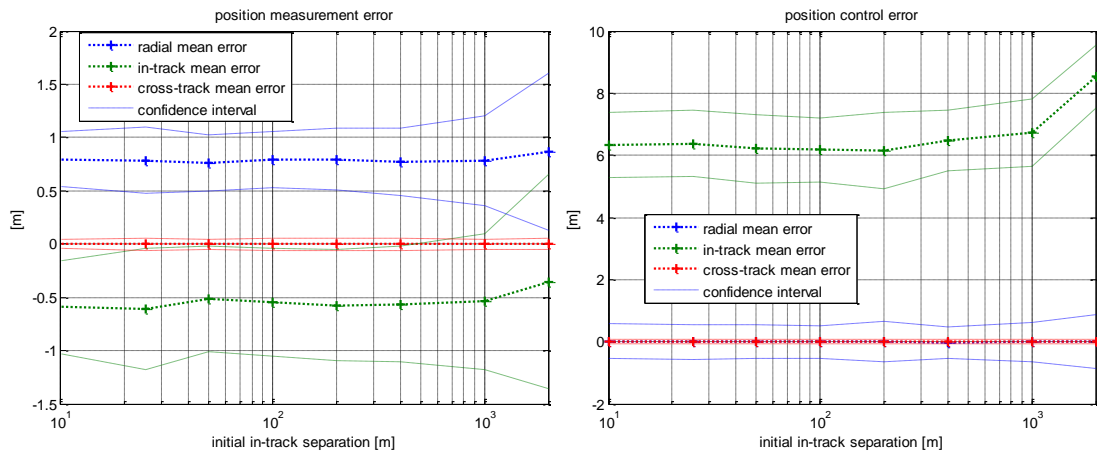


Figure 4.36 – Steady state relative position measurement (above) and control (below) statistical values over a sidereal day, respect to target L-F in-track separation in all three EH frame direction.

### Subsection 4.8.2 - Altitude variation effects

DLQR design was oriented to obtain achievable daily fuel consumption at acceptable position accuracy, acting on state and control weights, that is  $\rho$  ratio, within gain matrix determination.

Maintaining the same gain matrices, both in control and estimation, the same LQG loop has been applied at different altitudes. Obviously, the result is a position accuracy reduction and an overall consumption increasing. The correct procedure would consist in a fine weight factors tuning at each altitude, but it is beyond the purpose of this work.

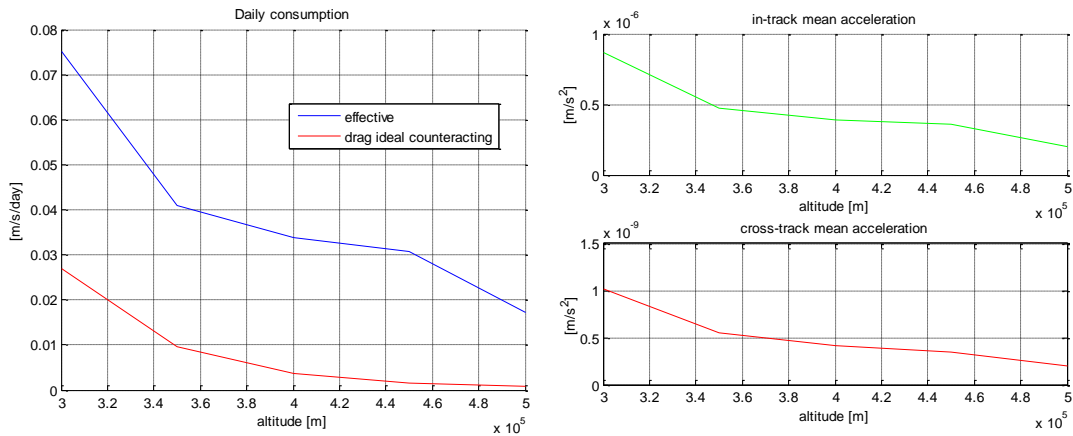


Figure 4.37 - Daily  $\Delta V$  budget (left) and mean accelerations (right) respect to reference orbit altitude

As shown in Figure 4.37, mean control acceleration increase at altitude lowering, due to higher mean disturbance accelerations, mainly atmospheric drag, leading to higher consumption. Higher disturbance acceleration also affect estimated state, incurring in high offset errors. Current Kalman filter implementation can be improved to take in account constant disturbance acceleration on input line, which implies constant acceleration estimation inclusion within the augmented state vector. However, estimation errors remain much smaller than controlled position errors, then it's more effective to concentrate on control gain tuning, rather than on estimator gain.

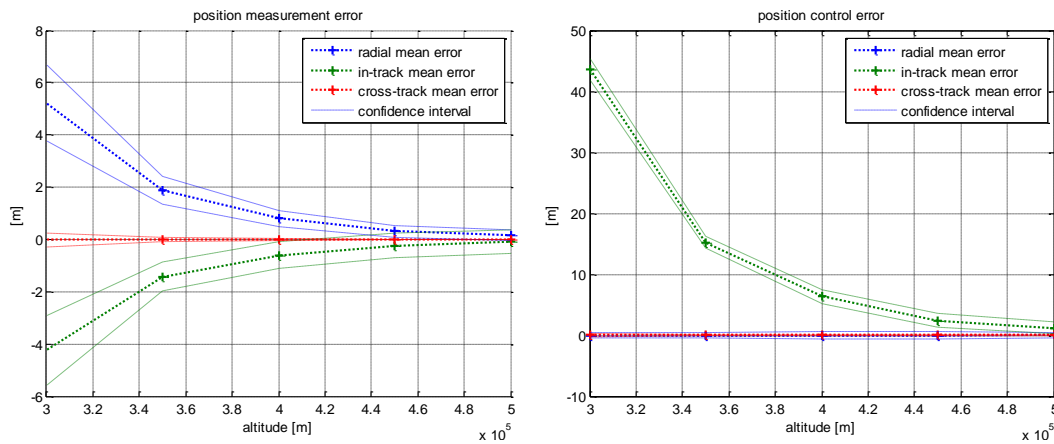


Figure 4.38 – Steady state relative position measurement (left) and control (right) respect to reference orbit altitude, in all three EH frame direction

## Section 4.9 - Summary

In conclusion, C/A GPS device can reach sufficient accuracy, within an adequate state-space estimator implementation, avoiding more massive and CDGPS solutions. Even HCW equation system provides good estimation within close formations, where model hypothesis are best satisfied. Moreover, it remains the only LTI model for relative dynamic prediction, extremely reducing algorithm complexity and onboard implementation. Eventually curvilinear coordinates can greatly improve results at middle range separation.

Considered propulsion technologies have been finally investigated and results both feasible. In particular, PPT provides mass and power saving and smaller envelopes, but its lack of thrust modulation compromise control robustness, occasionally leading in instability outside nominal condition, such in acquisition phases. Then, it needs a particular docked configuration release sequence. Cold gas propulsion is quite more expensive, but offers great modulation, and greater control stability.

Table 4.12 – Propulsion solution trade off.

Actuation solution	Clyde Space PPT	MicroSpace Cold Gas
<b>Pros</b>	Low cost Low envelope	Extendable tank Fine thrust modulation High control accuracy
<b>Cons</b>	Less control robustness (highly non linearity in actuation)	High cost

Daily consumption for formation maintenance results a little less than 0.03 m/s per day, which lead to a total lifetime of 300 days, in case of 34 Ns PPT total impulse, that is exactly a 10 m/s  $\Delta V$  budget for a 3.4 kg CubeSat.

Each spacecraft can perform formation control alone, and only in case of one of the propulsion systems failure, this budget equals the total. Otherwise this amount can be doubled.

Moreover, designating deputy role to the more massive spacecraft of the pair (it can be determined by a simple analysis of the unperturbed motion), ballistic coefficient mismatch can be continuously reduced, incurring in lower disturbance and lower consumption.

A single reconfiguration, like the two considered examples, takes approximately a daily formation maintenance budget. Then, even considering a large number of reconfiguration and the negligible undocking phase consumption increasing, there is plenty of margin to maintain L-F geometry up to the ADM-Aeolus orbit lifetime equal to only 200 days.

In case of alternative launch selection, LQG loop can still be refined and adapted to different altitudes to obtain smaller consumption, at cost of reduced accuracies.





# Chapter 5 - Attitude Determination and Control subsystem

## Section 5.1 - Pointing requisites

As already depicted in Chapter 3, a nadir pointing attitude, constraining minor inertia axis along radial direction, is the best solution in order to:

- GPS, zenith pointing (top panel mounted)
- ground link nadir pointing (bottom panel mounted)
- Inter-satellite link in-track pointing (laterally oriented main lobe)
- Thrust at least in in-track and out-of-plane directions (lateral thrusters)

GPS and ground link antennas pointing, respectively in zenith and nadir direction is immediately resolved for any yaw angle, providing yaw axis nadir constantly aligned. Moreover, commonly adopted quadrifilar dipole array, used in ground-link and also in inter-satellite link, in case of WLAN failures, is characterized by two orthogonal dipoles. Then it performs as an omnidirectional antenna and has very low pointing requirement. Inter-satellite link antenna lobe, in case of a radially oriented dipole, that is in case of WLAN transceivers, provide maximum gain in any direction in the horizontal plane.

At this point control around radial direction is not required, but laterally pointed thrusters may require yaw attitude maneuvers. In the following, the selected solutions to provide horizontal thrust vector will be presented.

## Section 5.2 - Attitude control architectures

### Subsection 5.2.1 - Maximum torques estimation

Maximum disturbance torques acting on a typical 3U CubeSat at LEO altitudes have been estimated and reported in Figure 5.1.

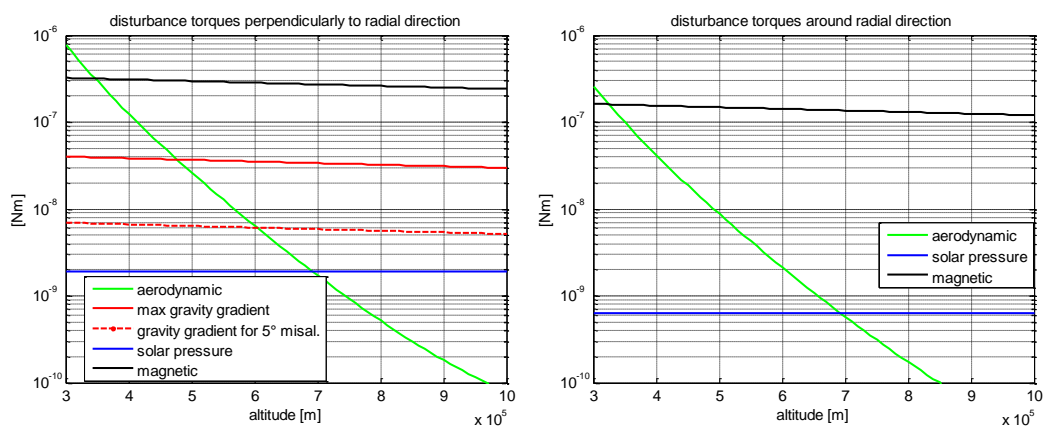


Figure 5.1 – Maximum disturbance torques respect to LEO altitude, on a 3U nadir-pointing CubeSat

Assuming a uniform internal mass density and neglecting center of mass and geometric center mismatch, minimum and maximum moment of inertia are respectively  $I_x=0.005 \text{ kgm}^4$  and  $I_y=I_z=0.025 \text{ kgm}^4$ . Center of mass position misalignment respect to geometric center is set to

10% of each edge, and aerodynamic coefficient is set to  $C_D=2.2$ , that is the common value adopted in literature for simple external shapes;

Due to stretched configuration, magnetic dipole is generally oriented towards maximum spacecraft length. In first hypothesis, it has been oriented in  $x$  (radial) direction and perpendicular components, proportional to the CubeSat dimension ratio were added. Magnetic dipole magnitude is carefully set at  $10 \text{ mAm}^2$ , for our 3U CubeSat, which dimensions are comparable (even less stretched than) to Space Dart geometry. Typical solar panel integrated magnetic coils provide at least  $50 \text{ mAm}^2$  capability for a 1U side panel and surely can compensate and overcome satellite residual dipole. Moreover, they can counteract disturbance torques magnitude at every LEO altitude, as reported in Table 5.9.

### **Subsection 5.2.2 - Some considerations on passive stabilization**

A passive magnetic stabilization is often implemented in most of low cost CubeSat missions, which involve only attitude determination requirements and not necessarily control. In this solution, the spacecraft would be constantly aligned with local Earth magnetic field vector, with only very poor maneuvering possibility around this direction. Moreover, In case of high inclined orbits, magnetic field vector orientation continuously tumbles and nadir pointing results unaffordable.

For a nadir nominal attitude, a gravity gradient stabilization would be preferred, especially if multiple unit CubeSat structures are chosen, which elongated shape would provide appropriate inertia properties. Unfortunately, a purely passive gravity gradient stabilization is ineffective at lowest LEO altitudes, where atmospheric and magnetic torques overcome gravity gradient stabilizing torque, even for high angles errors respect to radial direction. Gravity gradient has no authority at all below 500 km and would not control the yaw axis in any way.

A gravity gradient stabilized configuration, augmented with magnetic actuation is the minimum active strategy to be implemented. In such case, despite magnetotorquers would have sufficient authority against aerodynamic, they still cannot provide control around all three direction at the same time, but only perpendicularly to Earth magnetic field vector.

In any case, a purely passive stabilization technique is not recommended, because it offers no maneuvering possibility. With particular antenna configurations, like commonly used quadrifilar dipole array, antenna pointing requirements can be avoided, but thrust vector still has to be provided in any direction.

### **Subsection 5.2.3 - Attitude control possible solutions**

The selected propulsion devices can both be configured with multiple thrusters, but only lateral thrusters are preferred, in order to avoid excessive structural complications and taking advantage of the possibility to control relative position only with along-track and out-of-plane accelerations.

Then, two different active control architectures can fulfill propulsion orientation requisites, both based on a **nadir-aligned minor inertia axis**, ensuring proper inter-satellite antennas orientation and lateral oriented thrust and taking advantage of gravity gradient disturbance, as suggested in Table 5.1 and in Figure 5.2:

- a) **Dual spin configuration:** locking attitude on to the Local Vertical Local Horizontal LVLH frame, with a single Inertia Wheel (IW) oriented on pitch axis (that is aligned

with orbit angular rate). In this case, an independent thruster becomes necessary for each in-track and cross-track directions.

- b) **Three-axis control configuration:** involving a cluster of three Reaction Wheels (RW) and providing maneuvering capability. In this case a single thrusters can be properly oriented (even in radial direction, unless not necessary in nominal condition).

**Table 5.1 - Attitude control architecture comparison**

	Passive	Dual spin	3 Axis
<b>Maneuvering</b>	No	Pitch axis only	Full
<b>Pointing accuracy</b>	Very poor	Medium	High
<b>Relative cost</b>	None	Low	High
<b>Power consumption</b>	None	Medium	High
<b>Mass</b>	None	Medium	High

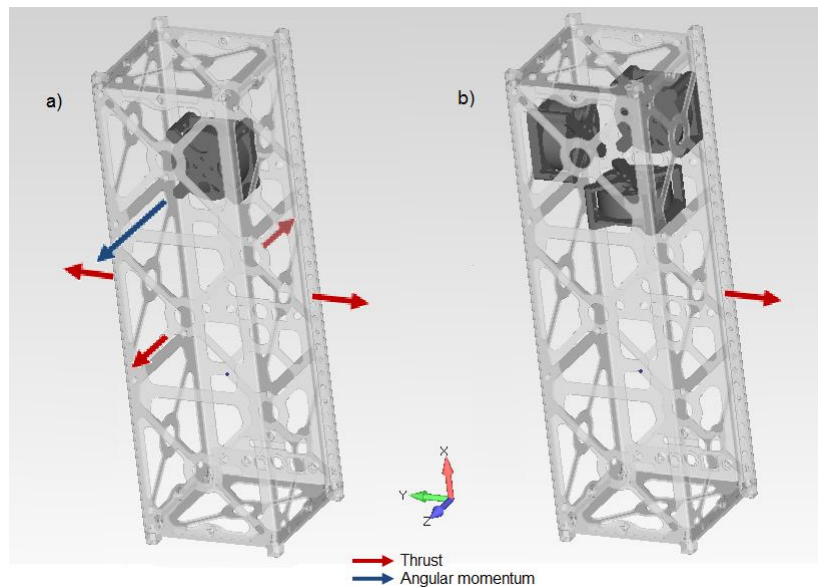


**Figure 5.2 – Attitude control analyzed architectures**

#### Subsection 5.2.4 - Disturbance torques at nominal attitude

Magnetic  $\mathbf{M}_{mag}$ , aerodynamic  $\mathbf{M}_{aer}$ , solar, Earth albedo and Earth infrared radiation pressure  $\mathbf{M}_{rad}$  torques, acting on each spacecraft of the pair nominal attitude, are shown in Figure 5.3, for a 400 km circular sun-synchronous orbit. They have been evaluated within Euler's equations propagation conducted in MATLAB Simulink and they have been modeled as follows. Magnetic torque can be expressed as:

$$\mathbf{M}_{mag} = \mathbf{m} \times \mathbf{B}$$

where  $\mathbf{m}$  is magnetic residual dipole,  $\mathbf{B}$  Earth magnetic field. Residual magnetic dipole has been modeled as sum of a constant vector, as in previous estimation, plus a 10% random component in each direction. Its magnitude has been estimated in relation of other satellites existing data. There are only a small number of nanosatellite residual dipole strengths declared in the literature [86], that is for Space Dart (a QBX structure), and for PACE mission (2U CubeSat), respectively equal to 9 and 0.5 mAm<sup>2</sup>. That produces fast time-varying magnetic

torques, which is mainly periodic over an orbit period, due to magnetic field tumbling (12-th order IGRF2000 Earth Magnetic Field model applied). Pressure torques are:

$$\mathbf{M}_{\text{aer/rad}} = \sum_{i=1}^{N_{\text{sides}}} \left( (\mathbf{r}_{CG,i} - \mathbf{r}_{CG,Sat}) \times \mathbf{F}_{\text{aer/rad},i} \right)$$

where  $\mathbf{F}_{\text{aer/rad}}$  are modeled aerodynamic, solar, Earth albedo and infrared pressures acting on each spacecraft side. Aerodynamic torque has constant components mainly around pitch axis, but also around yaw axis, and a periodic component around roll axis, only because of relative wind oscillations. In the same way, radiation pressure torque has constant components around roll and yaw axis and little periodic oscillations around pitch axis.

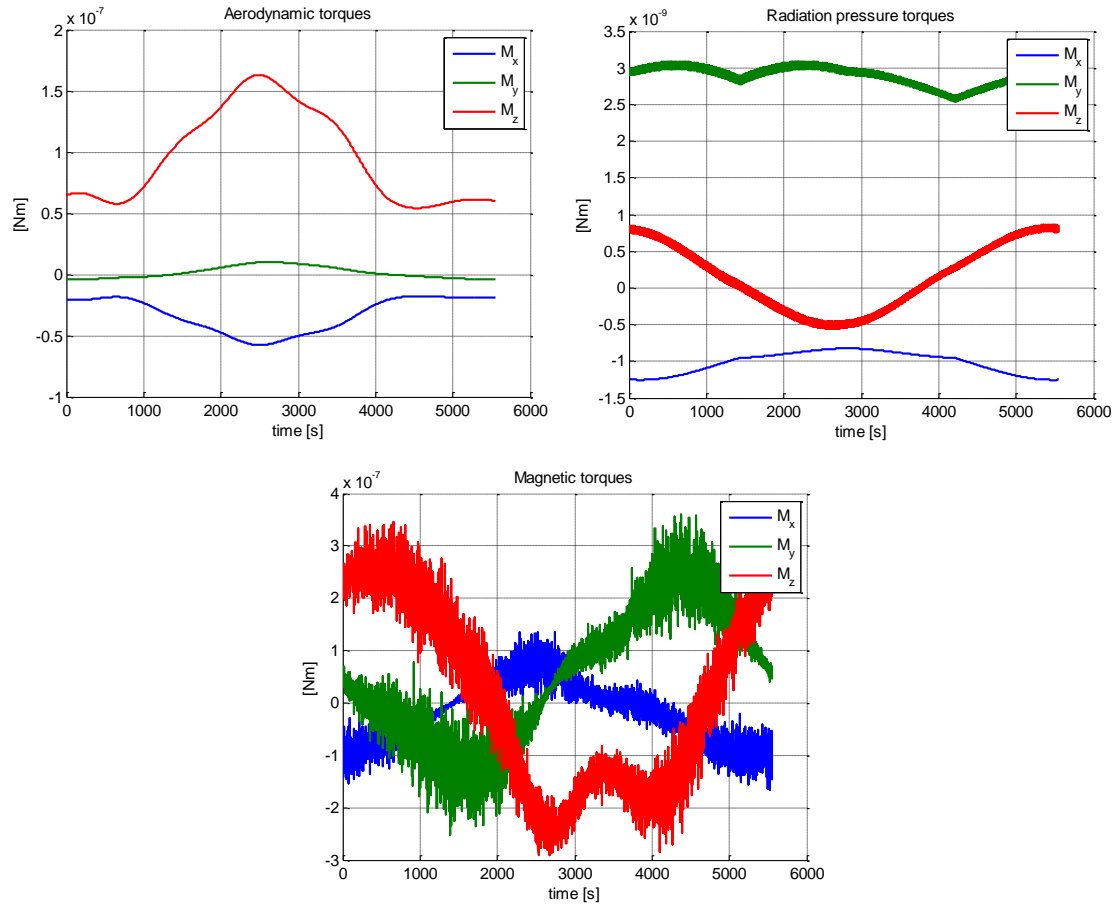


Figure 5.3 - Environmental conditions at nominal nadir-pointing attitude, at 400 km altitude LEO, over an orbit period. Aerodynamic (a), radiation pressure (b) and magnetic (c) torques.

Finally gravity gradient is stabilizing torque acting only around pitch and roll, in case of perturbations respect to nominal attitude.

$$\mathbf{M}_{\text{gg}}^{\text{Body}} = \begin{Bmatrix} (I_z - I_y)(\mathbf{r}_0 \cdot \hat{z})(\mathbf{r}_0 \cdot \hat{y}) \\ (I_x - I_z)(\mathbf{r}_0 \cdot \hat{x})(\mathbf{r}_0 \cdot \hat{z}) \\ (I_y - I_x)(\mathbf{r}_0 \cdot \hat{y})(\mathbf{r}_0 \cdot \hat{x}) \end{Bmatrix} \frac{3\mu}{r_0^3} = \begin{Bmatrix} 0 \\ (I_x - I_z)c_x c_z \\ (I_y - I_x)c_y c_x \end{Bmatrix} 3n_0^2$$

### Subsection 5.2.5 - Free dynamic

As shown by short term MATLAB Simulink propagation results in Figure 5.1, uncontrolled dynamic drift apart very rapidly from the nominal nadir pointing condition, primarily due to constant aerodynamic torque components. In fact, roll axis, on which main disturbance is magnetic torque, exhibit slower drift.

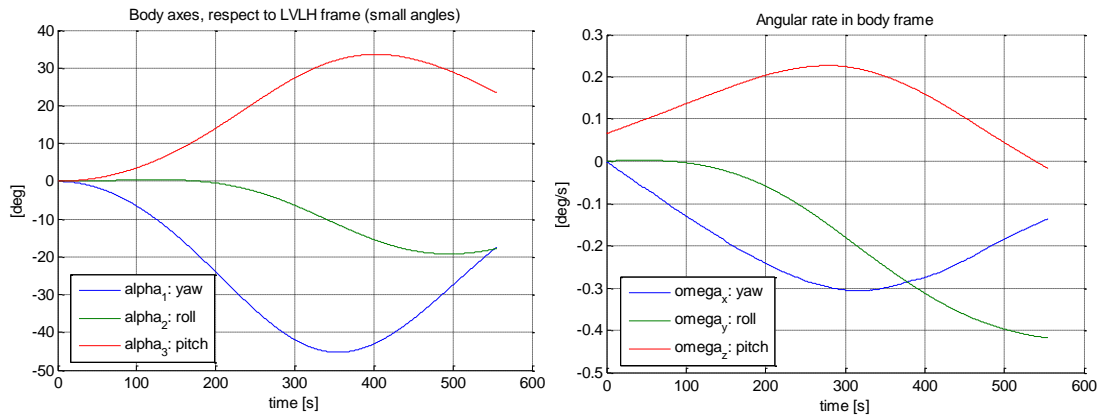


Figure 5.4 – Uncontrolled attitude angles rates over short time period, expressed as small angles rotations, starting from unperturbed nominal attitude.

Dual-spin architecture would mitigate these high drift rates, stiffening roll and yaw axis dynamics, as shown in Figure 5.5.

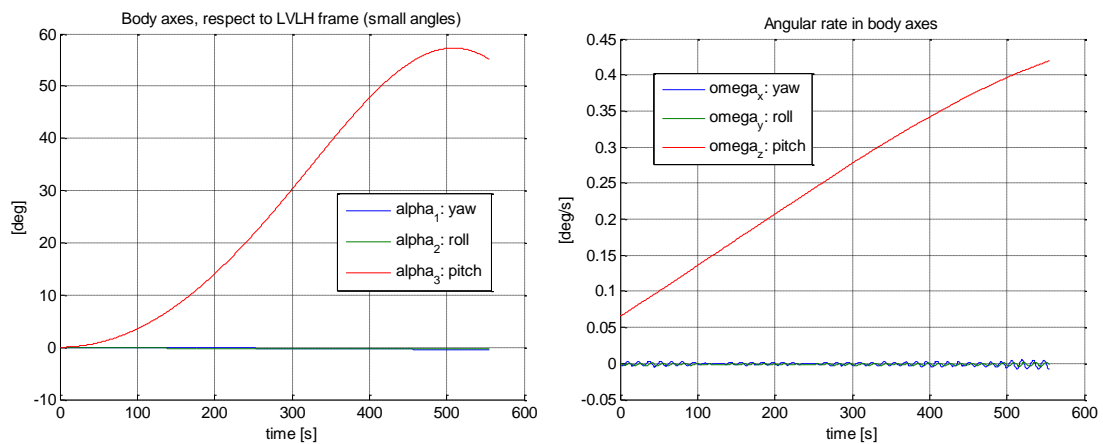


Figure 5.5 – Uncontrolled attitude angles rates over short time period, expressed as small angles rotations, starting from unperturbed nominal attitude, in case of pitch axis inertia wheel ( $h_1 = 4$  mNms).

## Section 5.3 - Attitude determination

Given two measured vectors in body axes, which true directions in inertial frame are known or modeled with sufficient accuracy, it's possible to estimate the rotation cosine matrix from inertial to body frame, providing these direction are not aligned.

There are three common measurements performed in LEO: radial direction, via horizon sensors, sun direction and magnetic field directions. In our purposes, for a dawn-dusk sun-synchronous orbit, a solution involving horizon sensors and magnetometers incurs in singularity at high latitudes. Moreover, Earth horizon sensors miniaturization technology

hasn't still reach affordable levels. They are fairly more massive and power expensive than other two sensor classes. Measurement of magnetic field and sun direction vector is the best choice, because of its low cost and high reliability. As shown in Figure 5.6, those vectors never align along orbit path and no singularities can occur.

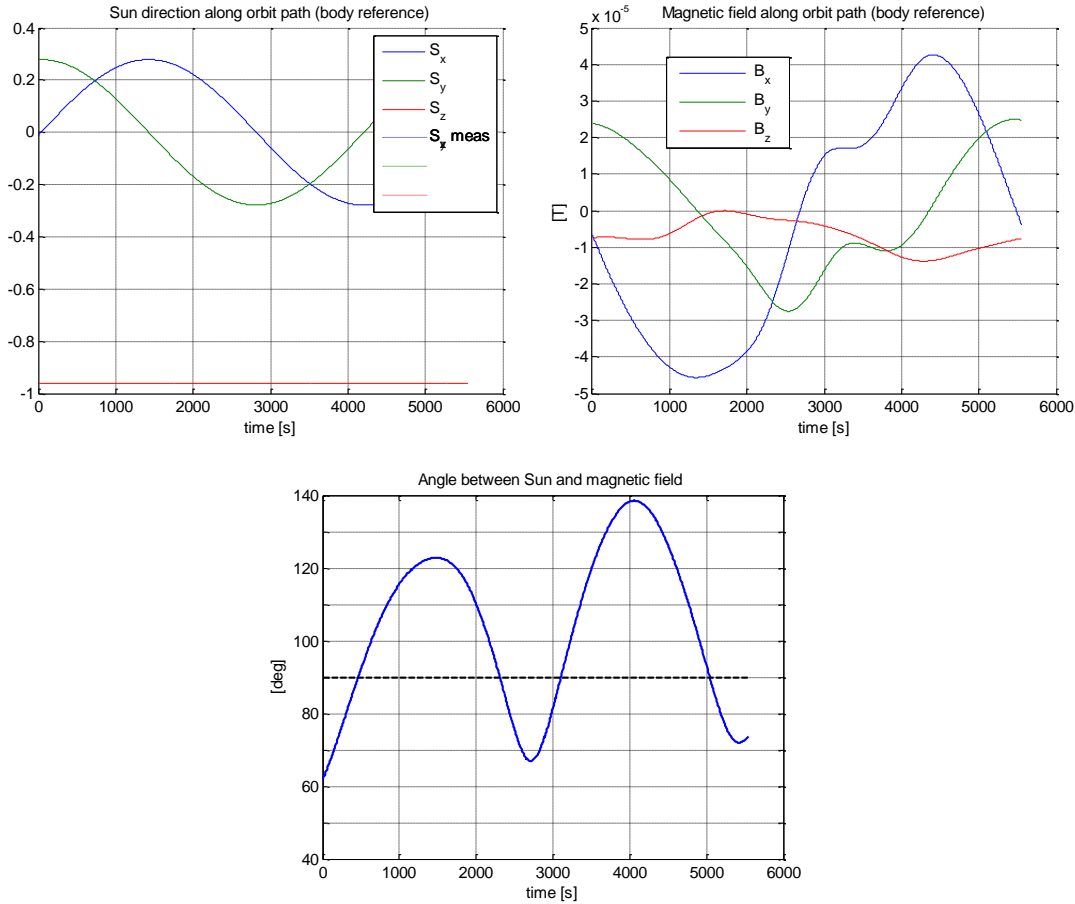


Figure 5.6 - Relative angle (d) between sun direction (e) and Earth magnetic field vector (f)

### Subsection 5.3.1 - Magnetometer

Selected solution for magnetic field measurements are reported in Table 5.2. SSBV device requires external mounting, that greatly complicates releasing POD accommodations, and its output has to be manipulated and interfaced via a dedicated PCI board. Sparkfun device is strongly preferred, because it is designed to fit in Pumpkin interface board, as shown in Figure 5.7, which is already necessary to provide correct I2C interface to other sensors and actuators.

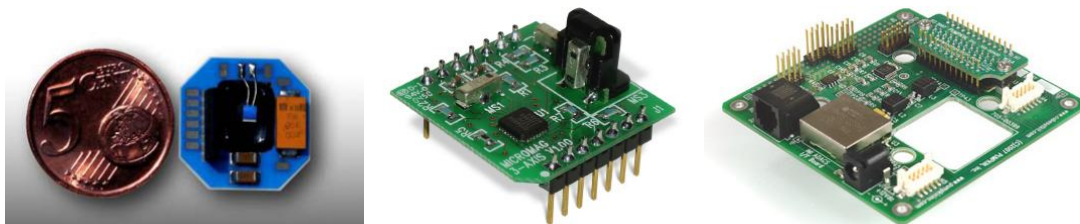


Figure 5.7 - SSBV Magnetometer hardware (left, sensor only), Sparkfun Electronics MicroMag3 sensor (center) and its dedicated interface provided in Pumpkin ADCS package (right)

Table 5.2 – Magnetometer performances for CubeSat applications

	SSBV Magnetometer	Sparkfun Electronics MicroMag3
Mass [g]	15 (+150 PCB)	Negligible (+ADCS PCI-104)
Power [W]	0.4	0.0015
Voltage [V]	5 to 15	3
Accuracy [deg]	1 (Rigid boom suggested)	0.7 Typ. (<1.1 Max) <sup>6</sup>
Linearity		
Interface	RS422, I2C	PCB, SPI
Sample rate [Hz]		2000
Dimension [mm <sup>3</sup> ]	10x10x5 (+ 90x30x11 PCB)	25x25x19 (+ADCS PCI-104)
Temperature [°C]	-50 to 85	-20 to 70
Radiation toll. [krad]	15	
Vibration toll. [g]	16	
Price [€]	9000	39 (+ ADCS interface)

### Subsection 5.3.2 - Sun sensor

If only one sun sensor is intended to be mounted onboard, it have to be aligned with pitch axis, but that would constrain the considered maneuvering possibility around yaw axis, so this solution fits the only dual spin control architecture. In case of 3-axis control and also to provide an acceptable level of redundancy, a sun sensor in each lateral side is necessary. In such this case, full coverage around radial axis is provided for sun direction detection, except for two cones around nadir and zenith direction, smaller than 45° angle, but power and masses are multiplied.

Table 5.3 – Sun sensors performances for CubeSat applications (see also Figure 5.8)

	Isis Analog Fine Sun Sensor	Solar MEMS SSOC-D60	SSBV CubeSat Sun Sensor	Sinclair Digital Fine Sun Sensor
Mass [g]	50	40	5	35
Power [W]	Peak	0	0.025	0.778
	Nominal	0	0.025	0.224
	Sleep	0	0	0
Voltage [V]		5 to 12	3.3 to 5	5 to 50
Accuracy [deg]	0.3	0.1	0.5	0.1
Interface	MDM 9-S	SPI, RS-422	9-way Nano-D	UART, I2C, RS-485
FOV [deg]	128	120	120	140
Dimension [mm <sup>3</sup> ]	46x45x14	50x30x12	33x11x6	34x32x21
Temperature [°C]	-50 to 85	-40 to 85	-25 to 50	-25 to 50
Radiation toll. [krad]	100	300	10	20
Vibration toll. [g]	TBD	10	25	16
Price [€]	TBD	8550	2500	9900

<sup>6</sup> Calculated as function of linearity errors reported in **Specificata fonte non valida.**, setting full scale (FS) equal to  $5 \cdot 10^{-5}$ , feasible for Earth magnetic dipole magnitudes span from  $2.02 \cdot 10^{-5}$  to  $4.57 \cdot 10^{-5}$  Tesla.

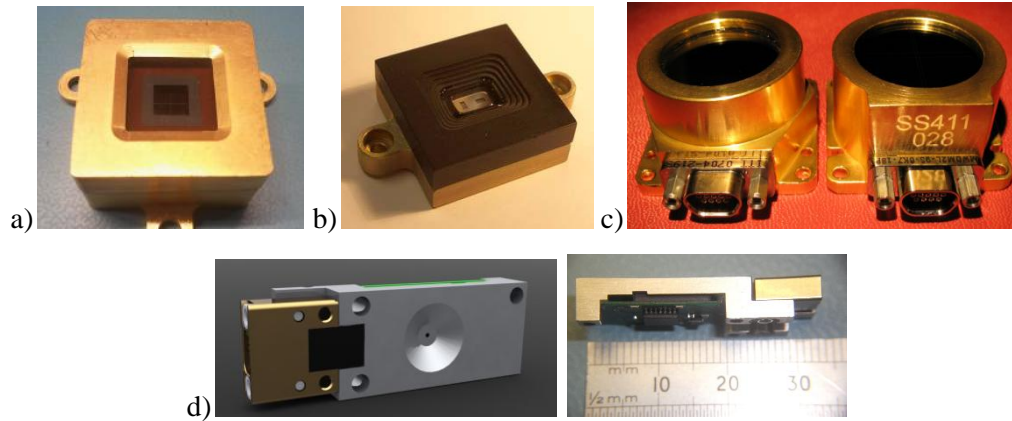


**Figure 5.8 - Isis Analog Fine Sun Sensor (a), Solar MEMS SSOC-D60 (b), SSBV CubeSat Sun Sensor (c) and Sinclair Digital Fine Sun Sensor (d)**

There are several available choices within miniaturized sun sensor COTS device and they are resumed in Table 5.3. Most of them are characterized by significant envelopes, still feasible with CubeSat applications, but involving configuration complications, particularly if more devices have to be oriented towards several directions. The best choice, in terms of price, power consumption and masses consists in four SSBV CubeSat sun sensors, taking also advantage of their thin shape to mount them directly onto solar panels.

### Subsection 5.3.3 - Determination method

Common recursive methods are based on minimization of a quadratic error index, weighted function of  $i$ -th measured vector  $\mathbf{v}_i$  in body frame, such as:

$$J = \frac{1}{2} \sum_{i=1}^{N_{meas}} \left( \alpha_i |\mathbf{e}_i|^2 \right) = \frac{1}{2} \sum_{i=1}^{N_{meas}} \left( \alpha_i \left| \mathbf{v}_i^{Body, meas} - \mathbf{T}_{Body}^{IN} \mathbf{v}_i^{IN, true} \right|^2 \right)$$

In our case, involving only two measured vectors, sun and magnetic field directions, this technique corresponds to a direct method [87], which aligns first the most accurate measure, resolving singularity around its axis with the second one:

$$\mathbf{T}_{Body}^{IN} = \left[ \mathbf{v}_i^{IN, true} \right] \left[ \mathbf{v}_i^{Body, meas} \right]^T$$

$$\left[ \mathbf{v}_i \right] = \left[ \mathbf{v}_1, \frac{\mathbf{v}_1 \times \mathbf{v}_2}{|\mathbf{v}_1 \times \mathbf{v}_2|}, \mathbf{v}_1 \times \frac{\mathbf{v}_1 \times \mathbf{v}_2}{|\mathbf{v}_1 \times \mathbf{v}_2|} \right]^T$$

**Table 5.4 – Attitude determination direct method performances in operative orbit conditions, with SSBV CubeSat Sun Sensor and Sparkfun Electronics MicroMag3 magnetometer. Angle rates results from random simulations and are calculated via finite differences (FD).**

Determination accuracy	Angles [deg]	Angle rates (T <sub>s</sub> =0.5s) [deg/s]	Angle rates (T <sub>s</sub> =1s) [deg/s]	Angle rates (T <sub>s</sub> =4s) [deg/s]
<b>Yaw</b>	0.612	1.80	0.869	0.361
<b>Roll</b>	0.623	1.78	1.27	0.152
<b>Pitch</b>	1.57	4.45	2.95	0.247



Both methods have been implemented, obtaining same accuracies. Then the direct method is adopted, avoiding the onerous iterative algorithm. Small angles and their derivatives, via finite differences, are on-board calculated.

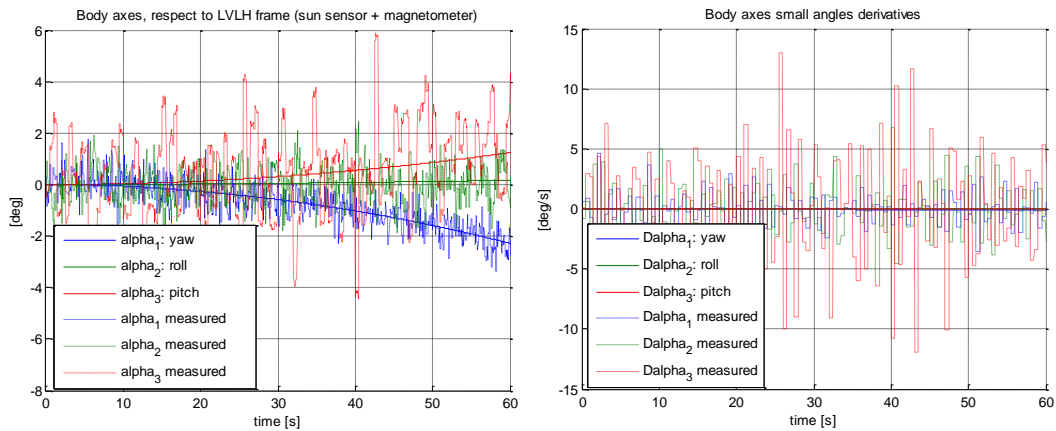


**Figure 5.9 - Angles and angular rates measurements (dashed line) over short period free dynamic, with direct determination from sun sensor and magnetometer measurements (left). Angle rates (right) are calculated via finite differences.**

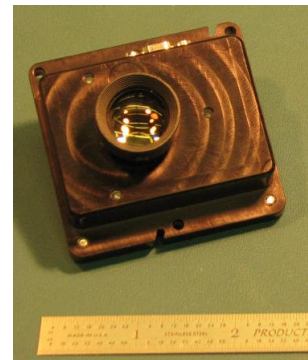
### Subsection 5.3.4 - Star tracker

A possible alternative solution is represented by recent improvements in low-cost miniaturized star tracker technologies. The Sinclair Interplanetary S3S device, which characteristics are resumed in Table 5.5, would be able to provide complete attitude determination with affordable mass and power consumption, but at a price to be still defined.

Star tracker performs 2 acquisition outputs per second of attitude and rates, then with a sufficient bandwidth for attitude control applications, with a higher order level precision, as shown in Figure 5.10. Power consumption is while the sun sensor with magnetometer solution requires a direct or iterative method onboard solution.

**Table 5.5 – Sinclair Interplanetary S3S Star tracker performances**

Sinclair Interplanetary S3S Star tracker	
Mass [g]	90
Power [W]	Peak
	Nominal
Voltage [V]	3.4 to 6
Accuracy [deg]	0.01 (85%)
Interface	RS-485, CAN, UART
Max slew rate [°/s]	>3
Sampling period [s]	0.5
Dimension [mm <sup>3</sup> ]	59×56×32.5
Temperature [°C]	-30 to 50
Radiation toll. [krad]	9
Vibration toll. [g]	14



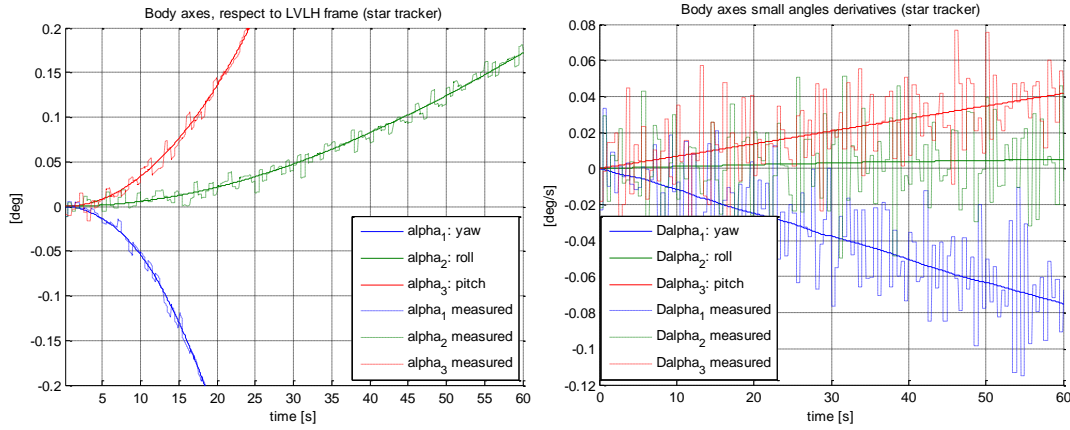


Figure 5.10 - Angles and angular rates measurements (dashed line) over short period free dynamic with Sinclair S3S star tracker (left). Angle rates are calculated via finite differences.

Table 5.6 – Attitude determination solutions and performances summary

	SSBV CubeSat Sun sensor	Sparkfun MicroMag3 Magnetometer	ADCS interface PCI + 4 x Sun sensor + Magnetometer	Sinclair S3S star tracker
Mass [kg]	0.005	negligible	0.069	0.090
Power [W]	0.025	0.0015	0.1	1
Angle acc. [deg]	0.5°	1.5°	(see Table 5.4)	0.007
Rate acc. [deg/s]	via FD	via FD	(see Table 5.4)	0.02

## Section 5.4 - Attitude control

### Subsection 5.4.1 - Dynamic model for nadir-pointing attitude spacecraft

Starting from Euler's equations, we can express 3-axis equilibrium equations system for each spacecraft of the pair as:

$$\mathbf{I}\dot{\boldsymbol{\omega}} + \boldsymbol{\omega} \times (\mathbf{I}\boldsymbol{\omega}) = \mathbf{M}$$

where  $\mathbf{I}$  is the inertia matrix,  $\boldsymbol{\omega}$  the angular rate vector,  $\mathbf{M}$  external torque. For simplicity, we reorder body axis so that correspond to the LVLH frame in nominal attitude, so that minor inertia axis, which has to be aligned with radial direction, is assigned to be the x body axis. The y body axis then lies on the orbit plane. Dynamic model for nadir-pointing attitude spacecraft

Including gravity gradient torque and a pitch axis rotor's angular moment  $\mathbf{h}_r$ :

$$\begin{cases} I_x \dot{\omega}_x + (I_z - I_y) \omega_z \omega_y + h_r \omega_y = (I_z - I_y) c_3 c_2 3n_0^2 + M_{c,x} + M_{d,x} \\ I_y \dot{\omega}_y + (I_x - I_z) \omega_x \omega_z - h_r \omega_x = (I_x - I_z) c_1 c_3 3n_0^2 + M_{c,y} + M_{d,y} \\ I_z \dot{\omega}_z + (I_y - I_x) \omega_y \omega_x + \dot{h}_r = (I_y - I_x) c_2 c_1 3n_0^2 + M_{c,z} + M_{d,z} \end{cases}$$

Assuming small angles, we express body frame rotation respect to the spacecraft LVLH frame as:

$$\mathbf{T}_{Body}^{LVLH} \simeq \begin{bmatrix} 1 & \alpha_z & -\alpha_y \\ -\alpha_z & 1 & \alpha_x \\ \alpha_y & -\alpha_x & 1 \end{bmatrix}$$

So this cosine matrix corresponds to an identity matrix in nominal condition. Angular rate and radial direction can be linearized nearby equilibrium condition and the state transition matrix can then be expressed, in case of axial symmetric spacecraft  $I_x < I_y = I_z$ , as:

$$\mathbf{A} = \begin{bmatrix} \mathbf{0}_{3 \times 3} & \mathbf{I}_{3 \times 3} \\ \frac{n_0 h_{rz}}{I_x} & 0 & 0 & 0 & n_0(1 - K_x) - \frac{h_{rz}}{I_x} & 0 \\ 0 & -4n_0^2 K - n_0 \frac{h_{rz}}{I_{yz}} & 0 & n_0(1 - K_x) - \frac{h_{rz}}{I_{yz}} & 0 & 0 \\ 0 & 0 & -3n_0^2 K & 0 & 0 & 0 \end{bmatrix}$$

$$K_x = \frac{I_{yz} - I_x}{I_{yz}}$$

$$\mathbf{x} = [\boldsymbol{\alpha} \quad \dot{\boldsymbol{\alpha}}]^T = [\alpha_x \quad \alpha_y \quad \alpha_z \quad \dot{\alpha}_x \quad \dot{\alpha}_y \quad \dot{\alpha}_z]^T$$

$$\mathbf{B}_c = \mathbf{B}_d = \begin{bmatrix} \mathbf{0}_{3 \times 3} \\ \mathbf{I}_{3 \times 3} \end{bmatrix} \quad \mathbf{C} = [\mathbf{I}_{3 \times 3} \quad \mathbf{0}_{3 \times 3}] \quad \mathbf{D}_c = \mathbf{D}_d = \mathbf{0}_{3 \times 3}$$

#### Subsection 5.4.2 - Discrete time linear quadratic regulator implementation

An LQR approach has been adopted, as described in Chapter 4, calculating optimal gain matrix, tuning  $\mathbf{Q}$  and  $\mathbf{R}$  weight matrices and  $\rho$  ratio:

$$\mathbf{Q} = \begin{bmatrix} \text{diag}(1/\text{target}\alpha) & \mathbf{0} \\ \mathbf{0} & \text{diag}(1/\text{target}\dot{\alpha}) \end{bmatrix} \quad \mathbf{R} = [\text{diag}(1/\max \mathbf{M}_c)]$$

Regulator time period has been set to a reasonable value of 0.5 s, higher than implemented sensors sampling time. Moreover, this value would result feasible also performing attitude determination with star-tracker measurements. Either in presence of angular momentum stiffness or not, also an integral error feedback can be implemented, effectively reducing steady state attitude error, but increasing angle rates and then overall accuracy, even involving higher mean control torques, as resumed in early simulation results in Table 5.7, with direct measured state vector feedback and without modeling actuators dynamic.

**Table 5.7 – Optimal control performance comparison attitude determination with sun sensor and magnetometer**

	LQR		LQR + integrator	
	0	4	0	4
<b>Pitch rotor [mNm]</b>	0	4	0	4
<b>Mean attitude error [deg]</b>	0.311	0.307	0.156	0.079
<b>Attitude accuracy [deg]</b>	0.448	0.383	0.663	0.427
<b>Angle rate accuracy [deg]</b>	0.312	0.227	0.888	0.556
<b>Mean control torque [mNm]</b>	0.280	0.264	0.771	0.646

Also in this case, due to coarse accuracy in state vector measurements via finite difference, an estimator filter results necessary. A simpler approach, respect to relative position control analysis can be adopted, calculating an L estimator gain by duality with the same LQR technique and then applied to a discrete time state-space model. The same previous Q matrix is adopted, while:

$$\mathbf{R} = \left[ \text{diag} \left( 1/\sigma_{a_{error}}^2 \right) \right]$$

### Subsection 5.4.3 - Actuators trade off

There are some available attitude control oriented thrusters solutions, as already implemented MicroSpace Cold Gas Micropropulsion system, providing some modifications respect to standard version. In general, such these nanosystems are based on cold gas propulsion and they cannot reach high  $I_{sp}$  values.

Due to high secular effects deriving from aerodynamic disturbance torque, fuel based solution are early discarded and magnetotorquers are preferred, despite their higher electrical power consumption, also in conjunction with rotors, to provide desired short term accuracy pointing. They cannot always provide torque in all three axes, along the entire sun-synchronous orbit path, but they periodically can do. So, wheel desaturation becomes possible.

A reference solution for complete 3-axis control is the MAI-100 ADCS module [88], or its equivalent RW cluster only enclosure, suggested from Pumpkin [89] for 1° pointing accuracy applications, with supplied sensors. The goal is to obtain the same pointing accuracy, decreasing its huge power consumption.

Then, alternative wheel models have been selected and reported in Table 5.8. Magnetic actuators and selected wheel solutions power consumptions are compared in Figure 5.13. In general, wheels have significant non-zero power consumption at no torque, due to electronics and they are less efficient in case of low control torque demands.

Table 5.8 – Reaction Wheels for CubeSat applications performances.

Wheel models	Maryland	Space tech. RW1		Sinclair RW-
	MAI-101 (3x)	1x	PCB	0.01-4 (1x)
Mass [kg]	0.64	0.02	0.049	0.12
Power [W]	Peak	4.5	0.32	0.4
	Nominal	1.5	0.22	0.4
	Sleep	TBD	0	0.4
Angular mom. [mNms]	11	0.58	-	10
Max torque [mNm]	0.635	0.023	-	1.000
Angular rate [rpm]	1000	8000	-	3410
Voltage [V]	12	5		3.4 to 6
Interface/Control mode	RS232	CAN2.0, RS232, RS485, SPI		UART/I <sup>2</sup> C Speed/torque
Dimension [mm <sup>3</sup> ]	762 x 762 x79	21x21x12	95x50x15	50x50x30
Temperature range [°C]	-40 to 80	-20 to 50		-40 to 70
Vibration toll. [g]	12	TBD		12
Radiation toll. [krad]	30	TBD		20

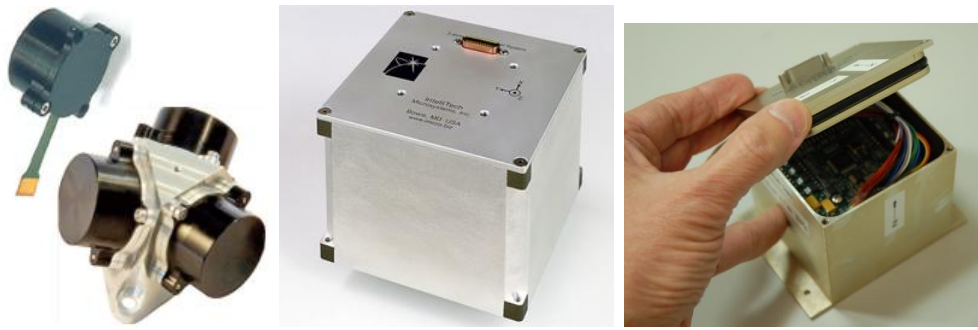


Figure 5.11 - Space technology RW1 wheel and its 4x cluster configuration (left), Maryland Aerospace complete MAI 100 ADCS (center) and the only MAI-101 3x wheels cluster enclosure (right) [88]

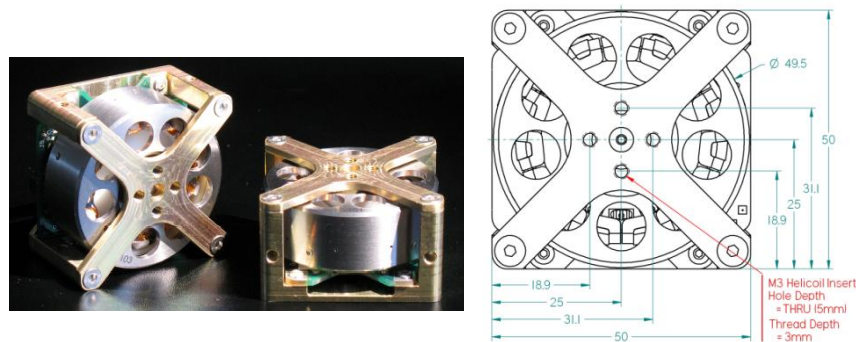


Figure 5.12 - Sinclair Interplanetary RW-0.01-4 wheel hardware (above) drawing (left-below) and power consumption (right-below) [90]

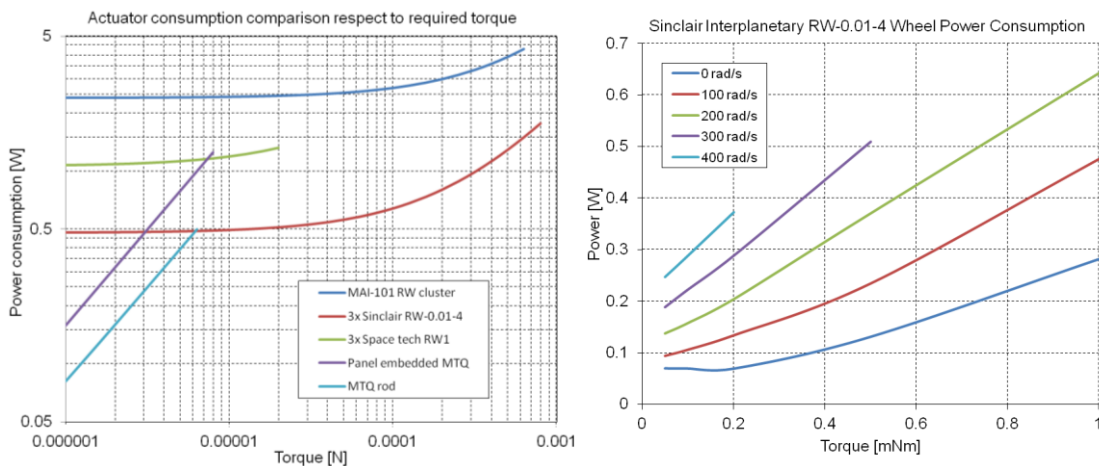


Figure 5.13 – Power consumption comparison for the considered solutions, without spin (left), and more detailed power consumption chart [90] respect to required torque and nominal angular speed

Despite their low mass and envelopes, Space Technology RW1 model, it has been discarded. Its angular stiffness in dual spin architecture resulted insufficient and its implementation in 3-axis architecture doesn't provide higher torque than magnetotorquers alone. On the other hand, a cluster of three Sinclair model, each with dedicated and integrated PCBs, seems to achieve the same torque capability than MAI-100, with very lower consumption, in particular at low control torque demand. Then they have been implemented both in 3-axis case, in cluster configuration, and in dual spin case, as a single pitch axis oriented wheel

**Table 5.9 – Magnetic actuators performance comparison for CubeSat applications at 400 km.**

	coil type	Mass [kg] <sup>7</sup>	Power [W]	Dipole [Am2]	Torque [μNm]
<b>Solar panel</b>	Square Top-Bottom	0.018 <sup>(*)</sup>	0.1	0.05	1.9
	3U Side option 1	0.035 <sup>(*)</sup>	0.340	0.17	6.46
<b>integrated</b>	3U Side option 2	0.055 <sup>(*)</sup>	0.440	0.22	8.36
<b>CubeSat Magnetotorquer Rod</b>		0.030	0.200	0.2	7.6

### Subsection 5.4.4 - Operative mode

Each selected architecture has been evaluated, modeling actuator's dynamic and nonlinearities within attitude dynamic control loop. In each case, a simple LQR control, with can provide attitude accuracy at degree level, far below the 5° accuracy early adopted in formation control simulations.

### Three-axis control

In this case, a cluster of three Sinclair RW-0.01-4 reaction wheels are implemented. They are aligned with each principal axes and their actuation force is simply limited by minimum and maximum achievable output. They are intended to be torque-controlled by integrated electronics at sufficiently high frequency to neglect their second-order internal dynamic.

Non-linearity effects, due to wheels angular momentum accumulation is taken in account, so:

$$\mathbf{M}_{c,RW}^{PI} = \mathbf{M}_{c,required}^{PI} - \boldsymbol{\omega}_{SC}^{PI} \times \mathbf{h}_{RW}^{PI}$$

As long as rotor angular momentum remains nearby nominal null condition, there is no significant loss of performance, as shown in Figure 5.14 and in Figure 5.15.

### Dual spin control

In case of dual spin, only pitch axis can be controlled by inertia wheels, torque around other axis is provided by magnetotorquers, even if the only component perpendicular to magnetic field can be provided at each time:

$$\mathbf{M}_{coil}^{PI} = \frac{1}{\mathbf{B}^{IN} \cdot \mathbf{B}^{IN}} \left( \mathbf{B}^{IN} \times \mathbf{M}_{c,required}^{PI} \right) \times \mathbf{B}^{IN}$$

A single pitch axis Sinclair inertia rotor, at 40% maximum angular rate, provides outstanding angular stiffness to contain this effect, as shown in Figure 5.16.

<sup>7</sup> panel integrated coil masses are intended as increment respect to already mounted solar panel

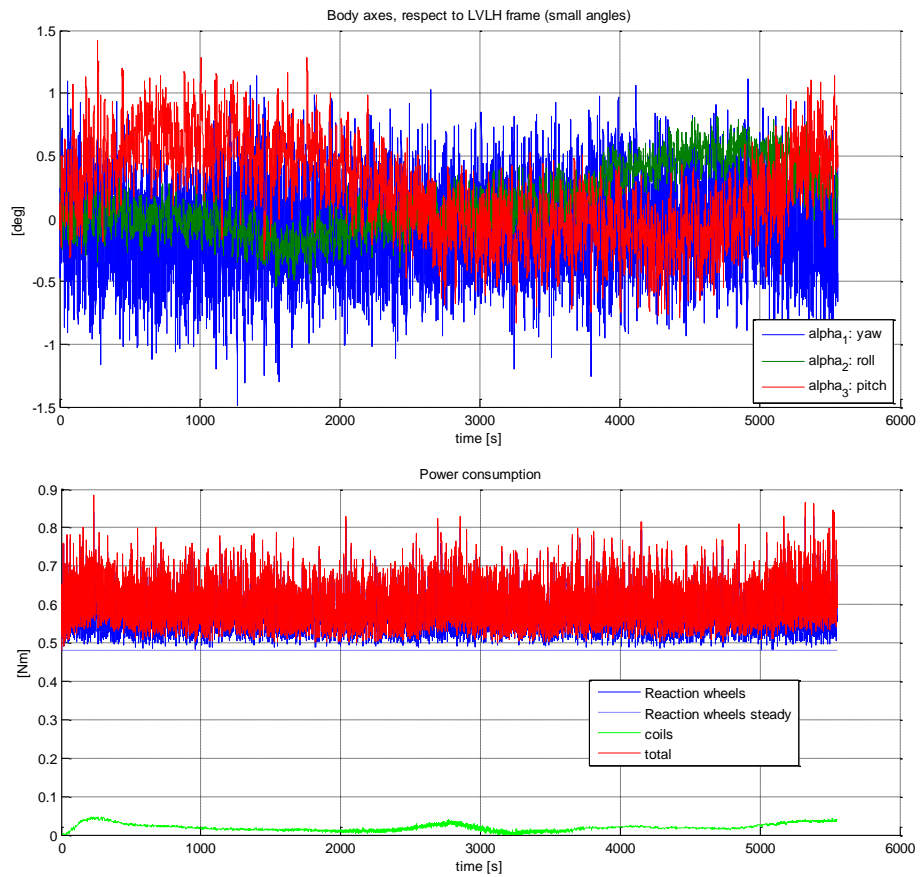


**Figure 5.14 – Attitude respect to LVLH frame (above) and power consumption (center) performances, in case of operative mode 3-axis control.**

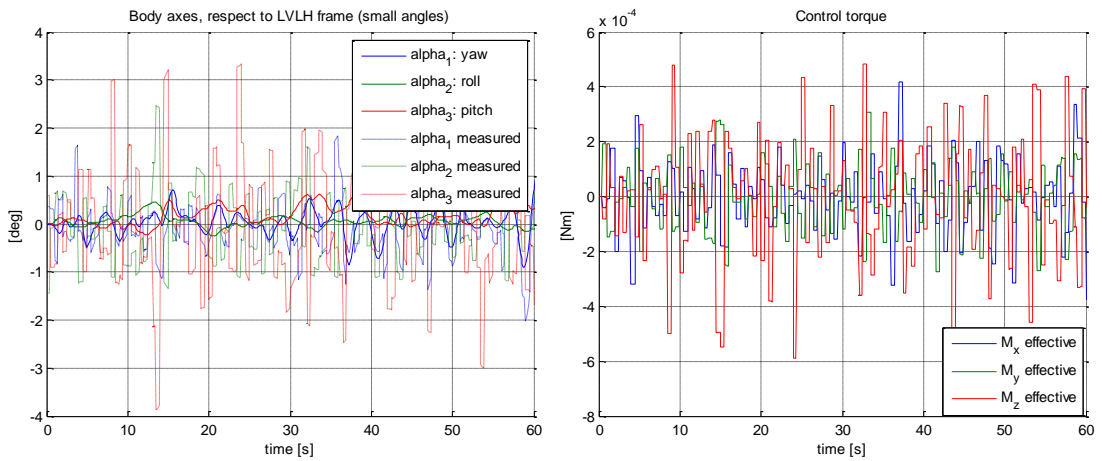


**Figure 5.15 - Zoom in views (below) highlight attitude errors and control torques short period time trend.**

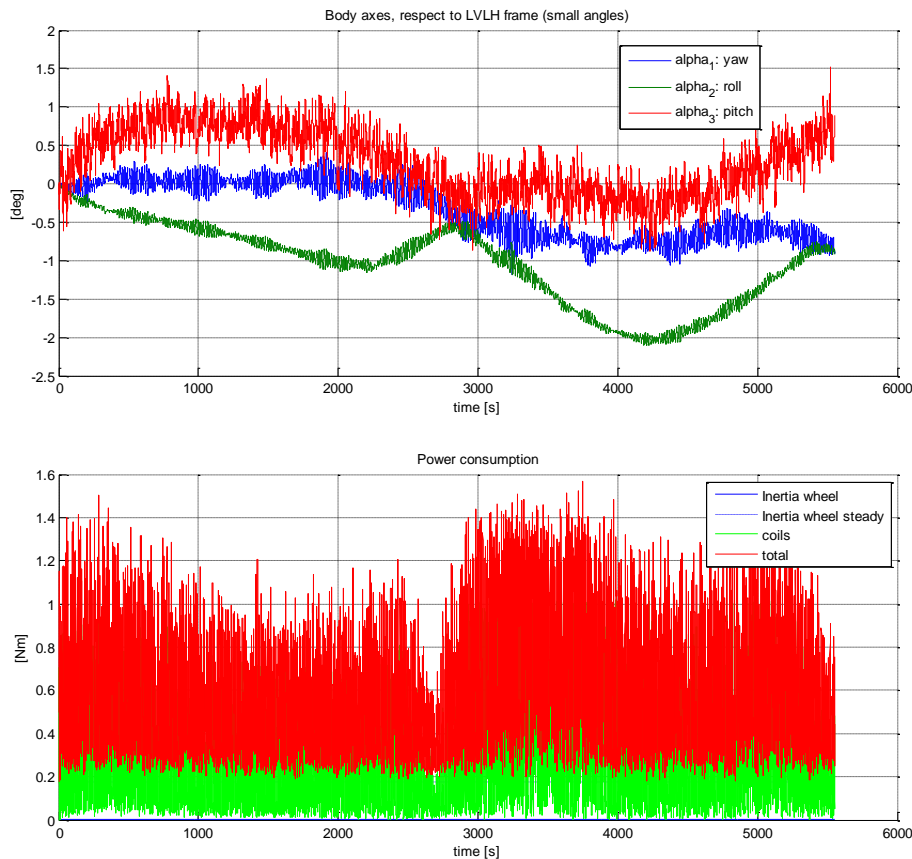


**Figure 5.16 – Attitude respect to LVLH frame (above) and power consumption (center) performances, in case of operative mode dual spin.**

### Subsection 5.4.5 - Thrust misalignment disturbances

Torques due to center of mass and thrust vector misalignment overcomes other disturbances. PPT has a pulsed effect, which produced, for a 5% CG misalignment, up to  $1.25 \cdot 10^{-7}$  Nm around pitch axis, that is comparable to aerodynamic and magnetic torques, but in case of continuous Cold Gas actuation, torque reach  $1.5 \cdot 10^{-6}$  Nm, fully counteracted by wheels, but not by magnetotorquers. So rotor angular momentum storage would rapidly saturate. Fortunately, propulsion never works continuously at full level and rarely overcome 10%, even during formation reconfigurations. Attitude simulations demonstrate the control capability and correct rotor desaturation nearby 25% of maximum cold gas mean continuous thrust. Conservatively, this value is set to evaluate worst case power consumption and attitude accuracy in case of cold gas actuation, while, in case of PPT actuation, full pulsed thrust is considered and modeled as a rectangular wave (see PULSE GENERATOR Simulink block).



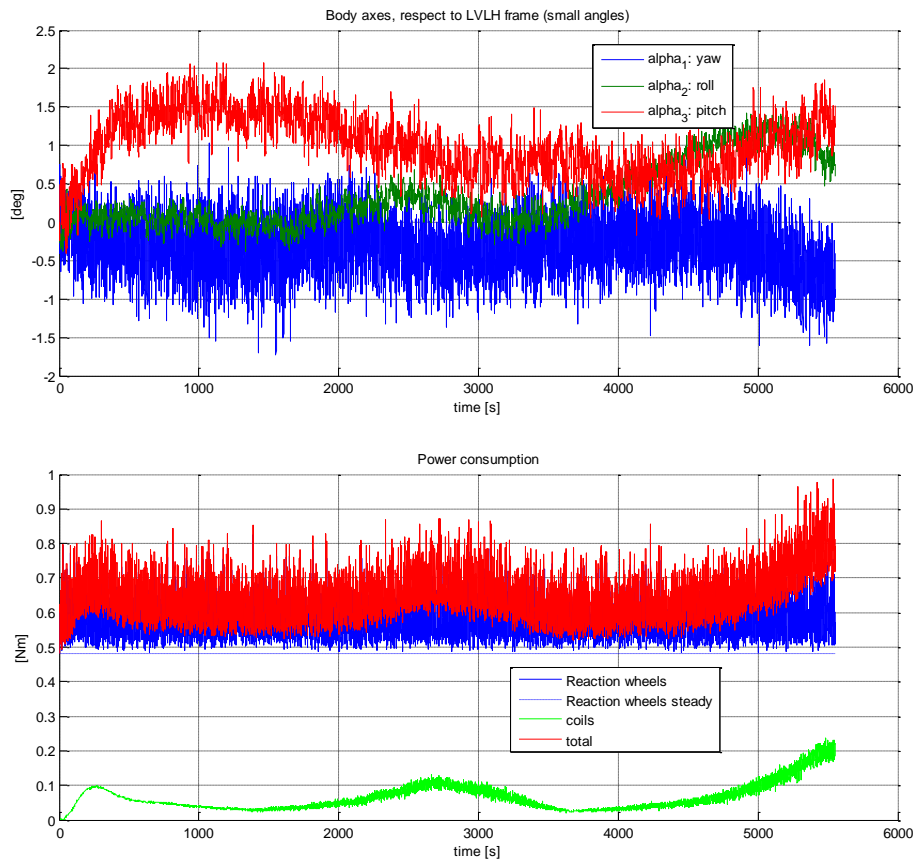


Figure 5.17 – Power (above) and attitude (below) performance in case of 3-axis control, during MicroSpace Cold Gas continuous firing at 25% of maximum thrust.

Table 5.10 – Performance comparison between dual spin and three axis architectures, in case of optimal control and attitude determination with sun sensor and magnetometer

		Chief Operative mode (no thrust)		Deputy Operative mode (with PPT)		Deputy Operative mode (with cold gas)	
		Dual Spin	3-Axis	Dual Spin	3-Axis	Dual Spin	3-Axis
<b>Constant attitude error [deg]</b>	Yaw	-0.328	-0.0712	-0.323	-0.0744	-1.21	-0.315
	Roll	-1.0387	0.138	-1.02	0.149	-5.14	-0.340
	Pitch	-0.289	0.224	0.275	0.227	1.35	-1
<b>Attitude accuracy [deg]</b>	Yaw	±0.37	± 0.332	±0.365	±0.323	±1.10	±0.346
	Roll	±0.531	± 0.255	±0.585	±0.271	±3.96	±0.413
	Pitch	±0.437	± 0.368	±0.421	±0.378	±0.465	±0.394
<b>Consumption [W]</b>	mean	0.586	0.599	0.589	0.599	0.608	0.645
	$\sigma$	±0.27	± 0.050	±0.269	±0.051	±0.273	±0.064

Results are summarized in Table 5.10 and shown in detail in Figure 5.17 and in Figure 5.18. We can then evaluate effective power consumption needed by attitude control actuators in both chief (which doesn't perform thrust) and deputy (which does) operative modes, that is far less than maximum values declared by datasheets.

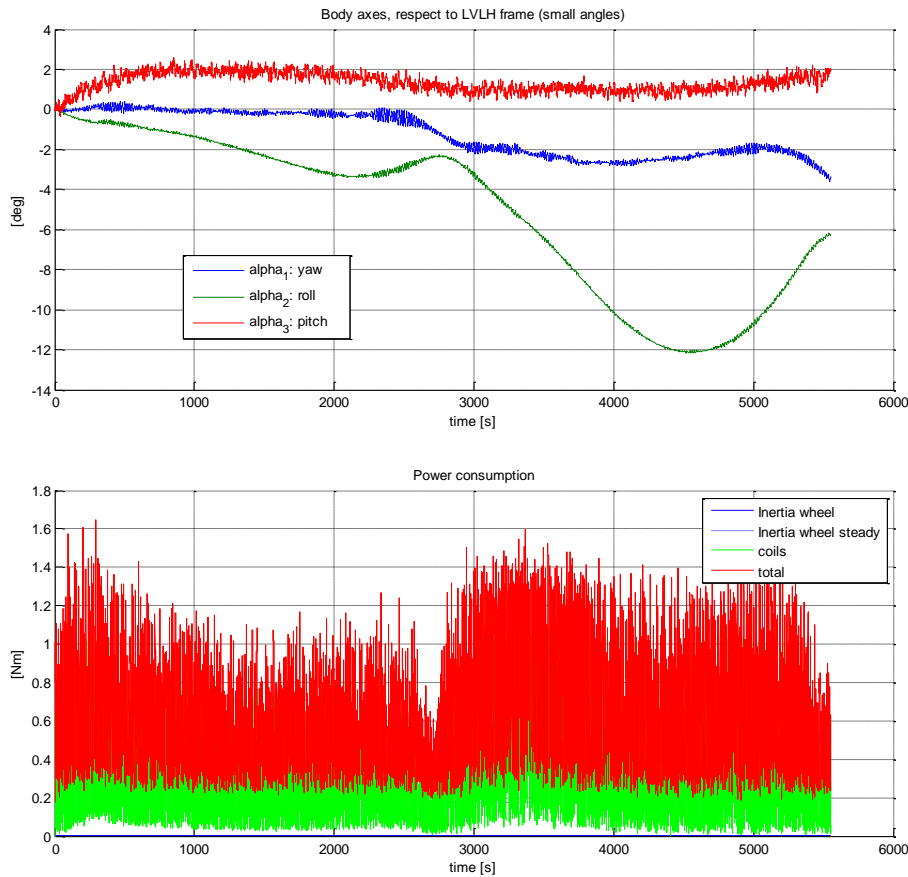


Figure 5.18 – Power (above) and attitude (below) performance in case of dual-spin control, during MicroSpace Cold Gas continuous firing at 25% of maximum thrust.

#### Subsection 5.4.6 - Desaturation strategy

In each case, desaturation with magnetotorquers is still necessary. Instead of applying periodical desaturation torques, which can be only fulfilled in correspondence of desired Earth magnetic field orientation, a continuous desaturation proportional control is performed.

$$\mathbf{M}_{desaturation}^{PI} = -K_p \mathbf{h}_{RW/IW}^{PI}$$

where  $K_p$  is a proportional gain, set to obtain maximum achievable magnetic torque at a tolerance angular momentum value is reached. At feedback signal, a discrete time filter (even a first-order filter is sufficient) to neglect higher frequencies. This procedure still works fine, as shown in Figure 5.19, over an orbit period, taking advantage of  $\mathbf{B}$  vector tumbling.

Only in case of continuous propulsion, at some alignment conditions, a small oscillation occurs in storage momentum, but they immediately recover.

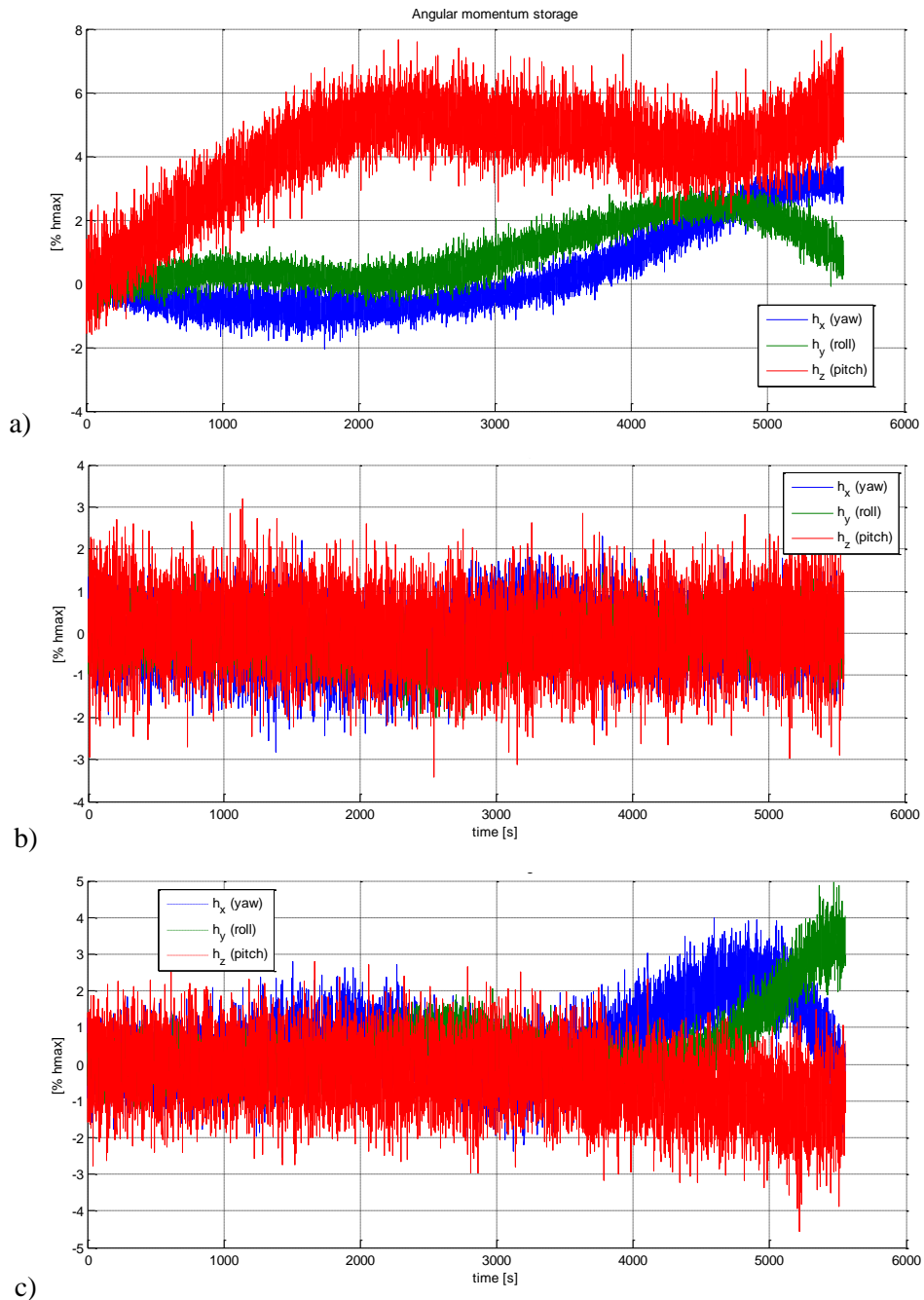


**Figure 5.19 – Wheel angular momentum storage time trend over an orbit, without desaturation control (a) and with proportional desaturation control, in Chief operative mode (b) and in Deputy operative mode (c)**

### Subsection 5.4.7 - Detumbling, commissioning mode

Launcher releasing attitude angle and rates strongly depend on primary payload mission requirements. In case of 3-axis stabilized releasing from small category launchers, typical attitude accuracy angular rate accuracy is about few degrees per second (Rockot specifications states  $3^\circ$  and  $1^\circ/s$  ( $3\sigma$ ) errors [57]).

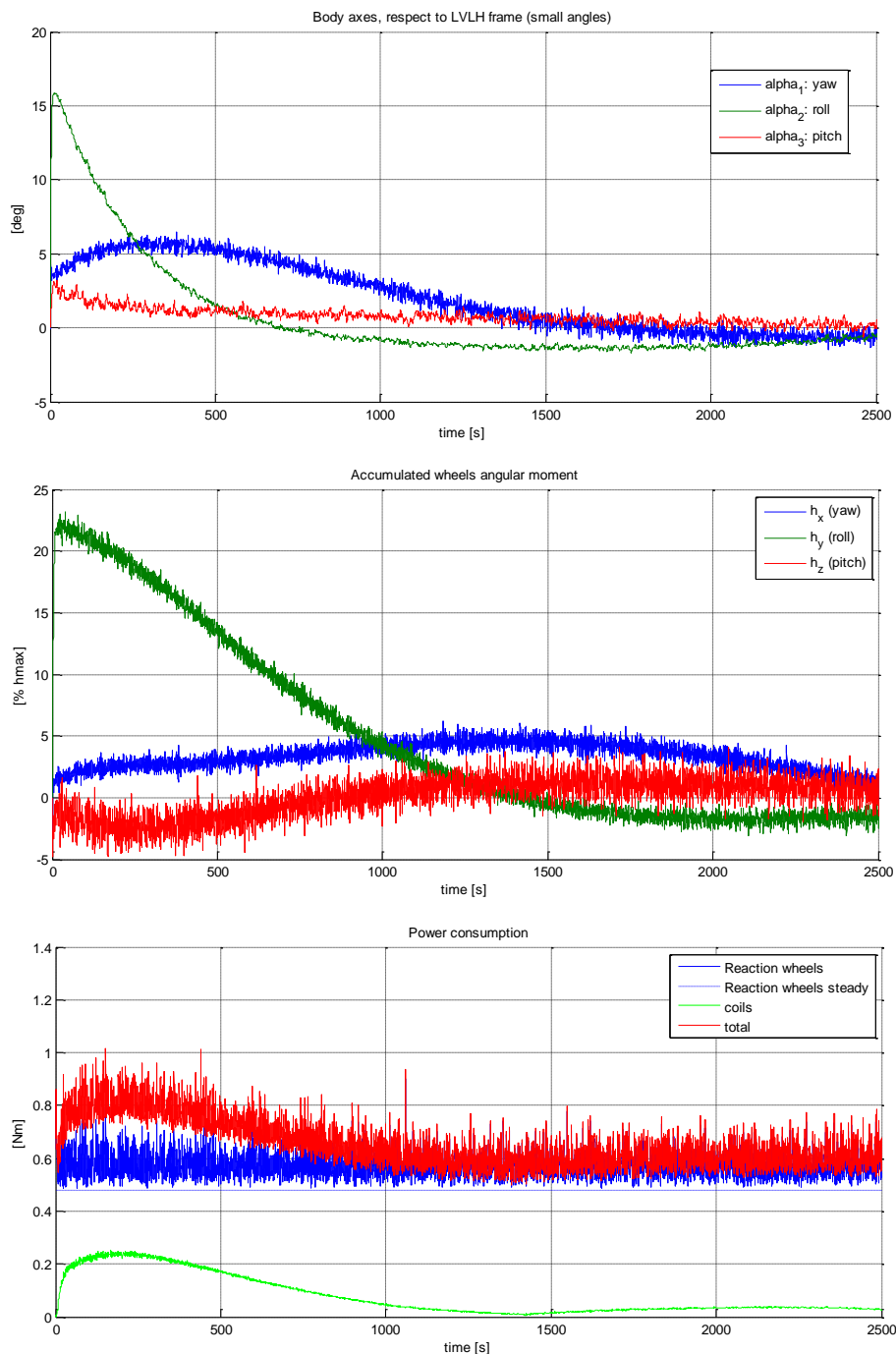


**Figure 5.20 – Attitude (above), stowed angular moment (center) and power consumption (above) performance during transient response after spacecraft releasing with  $5^\circ$  and  $5^\circ/s$  attitude and rate errors.**

In case of spin stabilized releasing, some small launcher can provide up to  $30^\circ/s$  on request. In such this case, quick detumbling phases have to be immediately provided. During this phase, due to high rates, sun direction would drift out from sun sensors field of view. However, an open loop control can still fulfill this task, if the nominal spin rate is a priori known, without needs of attitude and angular rate measurement. Selected wheels cluster can easily accumulate the impressed moment of momentum, up to 0.01 Nms around each axis, which correspond to 5 rad/s, but full rotor desaturation can take much more time.

**Table 5.11 – Performance during detumbling transient and steady state, in case of optimal control three axis architecture and attitude determination with sun sensor and magnetometer**

		Transient peak	Steady state mean	Steady state $\sigma$
Attitude error [deg]	Yaw	0.1135	-0.352	$\pm 0.4307$
	Roll	0.2766	-0.983	$\pm 0.381$
	Pitch	0.0556	0.275	$\pm 0.294$
Consumption [W]		1.0147	0.600	$\pm 0.046$

Simulations results, reported in Table 5.11 and shown in Figure 5.20, correspond to a initial attitude error equal to  $5^\circ$  and an initial angular rate equal to  $5^\circ/s$  around roll axis (typical value for a spin stabilized upper stage around its orbit track), which are fully counteracted within less than half of orbital period.

Maneuver simulations have not been implemented with current LQG, because linearized dynamic system already implemented is referred to the nominal equilibrium attitude condition. Simply setting a non null target attitude to be tracked is not correct. Fortunately, a 3U CubeSat acts as an axial symmetric satellite, having two coincident principal moments of inertia, and then each radial aligned attitude is still an equilibrium condition. The LQG regulator has just to be corrected at each yaw angle, repeating dynamic model linearization.

However, on board actuators have plenty of torque authorities and they can provide yaw maneuver within few seconds. A worst case  $180^\circ$  wide maneuver around x principal axis, at 1 mNm maximum torque, takes 5.605 seconds.

**Subsection 5.4.8 - Attitude variation effects**

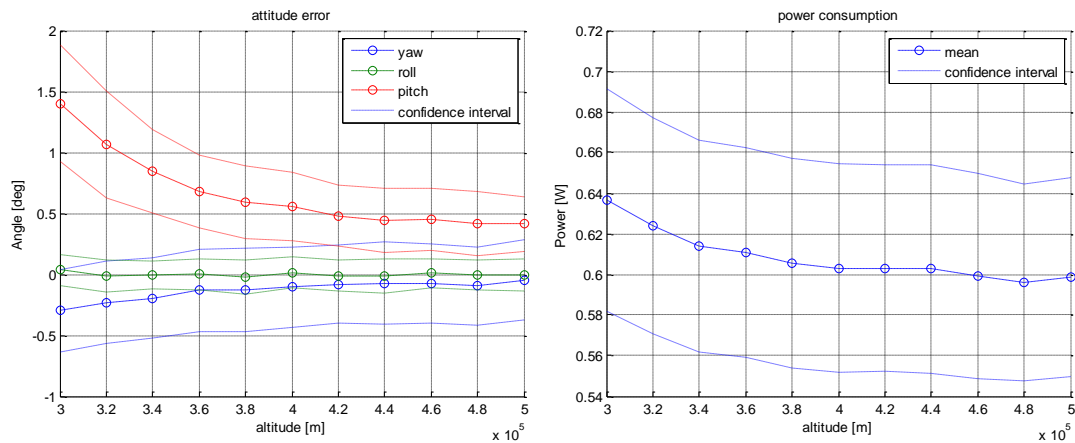


**Figure 5.21 - Attitude error (left) and power consumption (right) trend respect to reference orbit altitude.**

No particularly negative effects occur at reference semiaxis decreasing. As depicted in Figure 5.21, due to aerodynamic torque magnitude increasing, control performances around pitch and yaw axis, but not around roll, decrease significantly, but remaining within acceptable values even at lowest considered LEO altitude of 300 km. Below this value, operative mode control have no meanings, due to imminent atmospheric re-entry.

Measurements angle and rates, which depend on altitude only by linearized dynamic model implemented in estimator state space model, doesn't suffer significant effects.

## Section 5.5 - Final considerations

The most important result is that operative power consumption is demonstrated to be far less than maximum value depicted in datasheets, and they can be applied distinguishing each operative mode, facilitating power system design.

The dual spin architecture mass saving doesn't justify all other disadvantages, most of all power consumption, considering current mission critical power generation issues. Moreover multiple thruster requirements would complicate propulsion system and overall configuration. Yaw maneuvers with 3-axis control to orient propulsion are achievable, even if not simulated. Previous analysis are intended to prove nadir pointing control capability at degree level, involving low power actuators, low accuracy measurements and thrust vector correct orientation is demanded on further design phases and is taken as granted.

Finally, a 3-axis architecture is strongly preferred, because:

- It doesn't imply attitude constraints, facilitating commissioning and undocking phases.
- It adds mission flexibility, permitting eventual additional payloads accommodating.
- It better manages thrust misalignment torques, without significant power increasing
- It offers more accurate attitude control, due to its minor dependence on Earth magnetic field orientation.

**Table 5.12 – Architecture trade-off results. Panel integrated magnetotorquers (2×top/bottom + 4×lateral) on both configuration plus inertia wheel or reaction wheel cluster.**

	Dual Spin (1×IW)	3-axis (3×RW)
<b>Total actuators mass [kg]</b>	0.296	0.536
<b>Max attitude error [deg]</b>	2.5	0.60
<b>Max attitude accuracy [deg]</b>	±2.3	±0.59
<b>Actuation power</b>		
chief	1.39	0.75
<b>budget (mean + 3σ) [W]</b>		
deputy (cold gas)	1.43	0.84
deputy (PPT)	1.40	0.75
<b>Pros</b>	Mass saving Power saving in chief mode	Easy commissioning/detumbling High flexibility Power saving in deputy mode
<b>Cons</b>	Propulsion mass increasing	

# Chapter 6 - On-Board Data Handling and Communication subsystem

## Section 6.1 - On Board Data Handling subsystem

The choosing criteria for the OBDH microcontroller are only relative to CubeSat envelopes, power availability and the quantity of data that it can manage. In particular the PCI-104 standard must be considered and the low power consumption is the more restrictive constrain. Because of the position determination data precision, we need almost a 32-bit Microcontroller Unit (MCU). Standard CubeSat OBDH devices are less efficient in terms of number of data that can be managed. Two devices are now considered: NanoMind A712C GOMspace microcontroller is CubeSat born devices that satisfy mission requirements, and LPC1102 NXP one is a COTS chip shaped microcontroller. The second one needs a host-board PCI-104 compliant. In Table 6.1 the processors main features are showed. Data storages are very small, in particular in case of LPC1102 NXP MCU, so a MicroSD card can be considered. GOMspace device already has a 2GB MicroSD support and it can be added in LPC1102 host-board.

Table 6.1 – OBDH microcontroller data.

	NanoMind A712C	LPC1102
<b>Power supply</b>		
Pick [W]	0.294	0.360
Nominal [W]	0.231	0.330
Voltage [V]	3.3	3.3
<b>Data storage</b>	4 MB	8 kB
Size [mm <sup>3</sup> ]	96 x 90 x 10	2.17 x 2.32 x 18



Figure 6.1 – 32-bit Microcontroller: LPC1102 (left) and NanoMind A712C (right).

## Section 6.2 - Telemetry Tracking & Command subsystem

The TT&C subsystem task is to connect each spacecraft and the ground station in order to communicate telemetry and payload data. In this case payload data are temperature measured by COTS wireless sensors, so they are down in telemetry data. This communication

subsystem represents also a backup solution for the inter-satellite link in case of the failure of Wireless ISL subsystem. Two different tasks can therefore be defined:

- Satellite – ground station
- Satellite – satellite

### Subsection 6.2.1 - Satellite – Ground station link

#### Ground station visibility

Considering the ground station positioned in Politecnico di Milano campus, the visibility of the station from ADM-Aeolus orbit during 10 days is represented in Figure 6.2. Complete tables of accesses are reported in Appendix C.

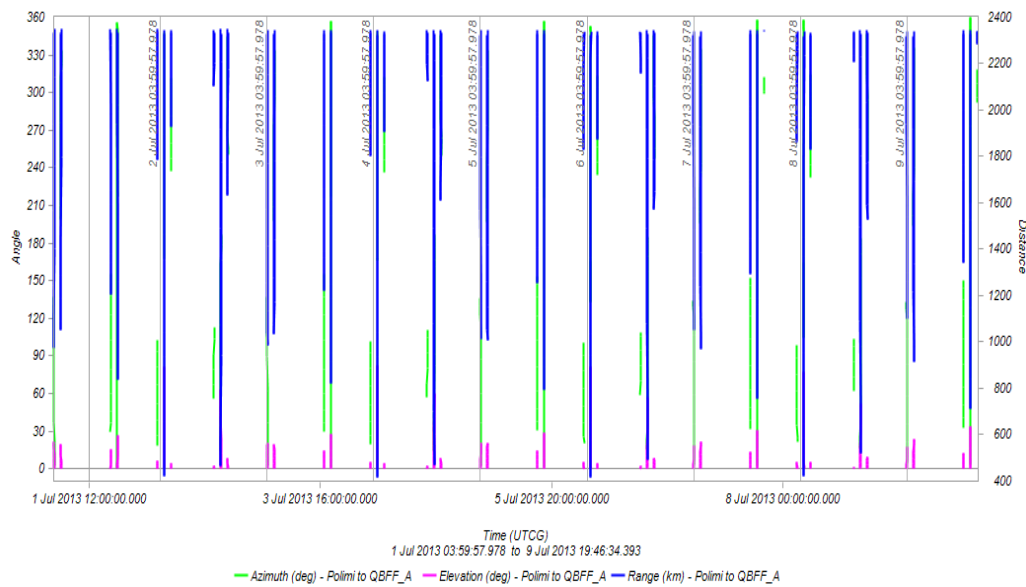


Figure 6.2 – ADM-Aeolus PoliMi accesses, over 10 days.

The ground station can receive data only from one satellite by one, so each satellite can communicate only one time every two available access and the waiting time from one communication link and the follower is calculated between two accesses. The maximum waiting time for one satellite is 12<sup>h</sup> 27<sup>m</sup> 00<sup>s</sup>, corresponding to 44820 s.

#### Packet Telemetry

Packet Telemetry [91] is a concept which facilitates the transmission of space-acquired data from source to user in a standard highly automated manner. Packet Telemetry provides a mechanism for implementing common data transport structures and protocols which may enhance the development and operation of space mission systems. To accomplish these functions, this Consultative Committee for Space Data Systems (CCSDS) Recommendation defines two data structures:

- Source Packet: is a data structure generated by an Application Process (Figure 6.4)
- Transfer Frame: is a data structure that provides an envelope for transmitting packetized data (Figure 6.5)



The multiplexing process to interleave Source Packets from various Application Processes into Transfer Frames as shown in Figure 6.3.

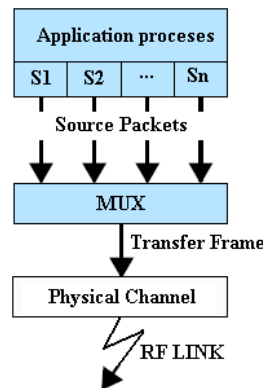


Figure 6.3 – Telemetry data flow.

The Packet Primary Header has a standard size of 48 bits (6 Byte) for every PCI-104 data channel (coming from an Application Process or source). The Packet Data Field contains the data relative to the correspondent channel or Application Process.

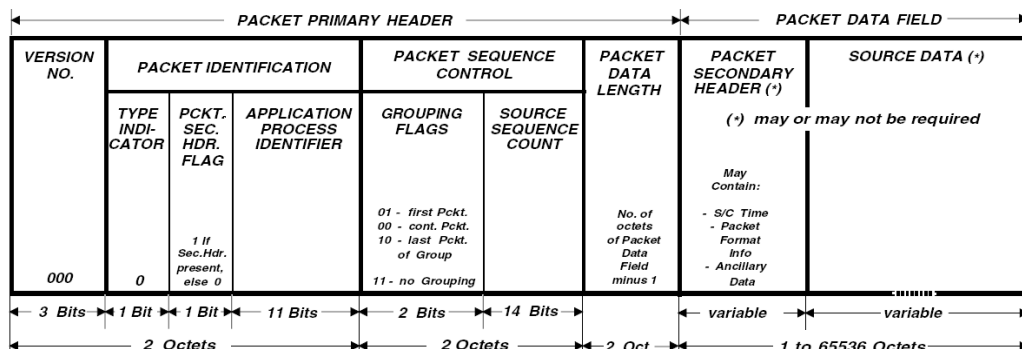


Figure 6.4 – Source Packet Format.

In this specific case, the Application Sources are represented by four categories: **housekeeping** comprehend all subsystems status (temperature, voltage, current, power supply, battery charge and temperature...), 70 channels are reasonably considered; **position and time** coming from GPS receiver are collected in one channel; **attitude** is delivered to the OBDH subsystem by one channel and the string data dimension is relative to the four quaternion's components and the four quaternion rates; as payload, four COTS temperature sensors are considered, so the transceiver collect **data coming from sensors** in one data string delivered by one channel. The Source Packets coming from every Application Source are contained in the Transfer Frame data field.

Packet Telemetry must collect, in the Transfer Frame, housekeeping, position and attitude data and in this case also payload data because they are temperature measurements (so telemetry data). Housekeeping and temperature COTS sensors data can be measured every minute, position and time data are storage each second and attitude data every 4 seconds. Table 6.2 reports the telemetry data dimensions every sampling time for each category.

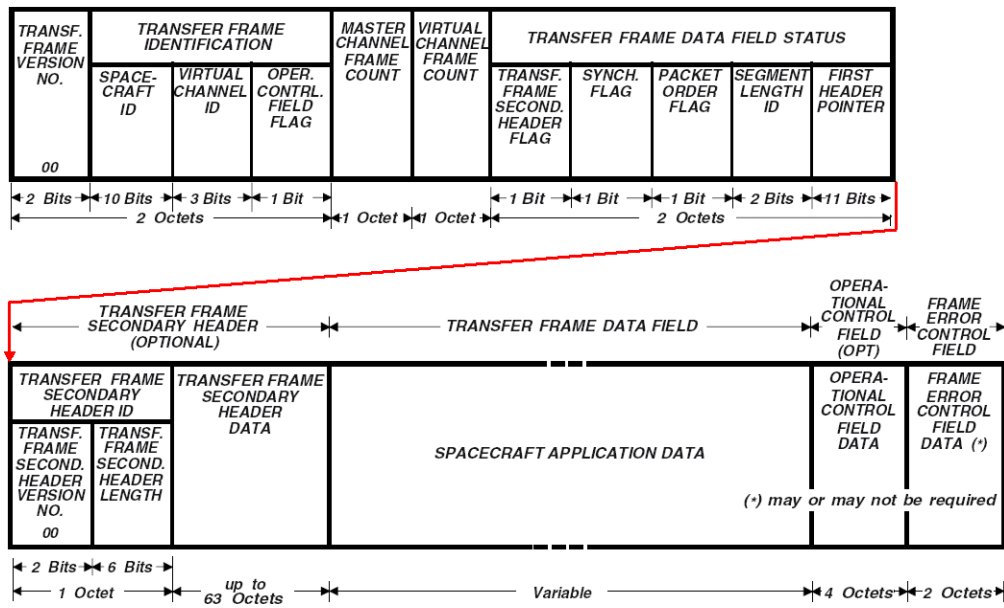


Figure 6.5 – Transfer Frame Format.

Table 6.2 – Telemetry data every sampling time.

	Variable	One Data[bits]	Total Data [bits]
<b>Housekeeping</b>	Subsystems status ( $T_S=60s$ )	16	16 x 70
<b>Position</b>	GPS data ( $T_S=1s$ )	32	32 x 3
<b>Clock</b>	GPS time ( $T_S=1s$ )	32	32
<b>Attitude</b>	Quaternion ( $T_S=4s$ )	16	16 x 4
	Quaternion rate ( $T_S=4s$ )	16	16 x 4
<b>Payload</b>	Temperature ( $T_S=60s$ )	16	16 x 4

Data collected during maximum waiting time divided by categories are:

Table 6.3 – Telemetry data collected during maximum waiting time.

	Variable	Total Data [Byte]
<b>Housekeeping</b>	Subsystems status	104580
<b>Position</b>	GPS data	537840
<b>Clock</b>	GPS time	179280
<b>Attitude</b>	Quaternion	89640
	Quaternion rate	89640
<b>Payload</b>	Temperature from COTS sensors	5976
<b>Data in OBDH memory</b>		<b>1006956</b>

The considered microcontrollers own a data memory, in particular NanoMind A712C (GOMspace device) has a 4MB data storage that corresponds of 15 hours data memory, otherwise LPC1102 (NXP device) has 8kB data storage that can memorizes less than one hour of data collected. If the LPC1102 microcontroller will be selected for the mission, an additional memory must be provided. The Application Source data string often exceeds the

Packet Data Field dimension limit (65536 Byte), so it must be divided into some Packets. In particular, considering the data sources, data can be divided as follow:

- Housekeeping: 70 channels (Source Packet)
- Position + Clock: 11 Source Packet
- Attitude: 3 Source Packet
- Payload: 1 Source Packet

Each Source Packet is structured as in following table:

**Table 6.4 – Source Packet Ground link.**

	Source/Application process	Dimension [Byte]
<b>Housekeeping</b>		
Packet Primary Header		6
Packet Data Field	Subsystems (Data BUS)	1494
<b>Position + Clock</b>		
Packet Primary Header		6
Packet Data Field	GPS receiver	65193
<b>Attitude</b>		
Packet Primary Header		6
Packet Data Field	ADCS interface	59760
<b>Payload</b>		
Packet Primary Header		6
Packet Data Field	COTS Transceiver	5976

Source Packets shall be inserted contiguously and in forward order into the Transfer Frame Data Field, so the Transfer Frame becomes:

**Table 6.5 – Transfer Frame Ground link.**

		Total data [Byte]
<b>Transfer Frame Data Field</b>	70 housekeeping Source Packet	105000
	11 GPS receiver Source Packet	717186
	3 ADCS interface Source Packet	179298
	1 Payload Source Packet	5982
<b>Transfer Frame Primary Header</b>	Without Secondary Header Fields, with operational and error control fields.	12
<b>Total Transfer Frame</b>		1007478

### Data rate calculation

Considering the satellite-ground station access analysis period (10 days), a data rate estimation can be implemented. The total time analysis, from the first contact to the last contact loss, is 9<sup>h</sup> 39<sup>m</sup> 20<sup>s</sup>. During this time period, telemetry data collected are about 18 MB. To this data amount are summed: a Packet Primary Header size every 65536 Byte and the Transfer Frame Primary Header size multiply for the accesses number (46 accesses). In this way the 46 accesses time Transfer Frames are calculated. Dividing the sum of all the 46 Transfer Frames by access total duration, the result is the required data rate: 6735 bps.

**Components description**

Communication devices are chosen between few transmitters, receivers and transceivers compatible with CubeSat bus. There is the possibility to use two different devices for transmitting and receiving in VHF or UHF frequency bands. However a receiver and a transceiver single components need two level bus to be integrated in the satellite, in addition, on equal performances, the two level solution is more expensive than transceiver one. Then, transceivers are preferred. Two transceiver devices are presented in Table 6.6: the choice criteria were the low power consumption and bit rate upper to 6735 bps, as already calculated. It's important to notice that the UHF transceiver communication frequency is between 435 to 437 MHz for the NanoCom U480 and between 400 and 450 MHz for the AstroDev Helium Radios. These frequency bands are quietly close to the SENSEOR TSE AS10 temperature sensors work frequency ( $433.63\text{MHz} \pm 0.2 \text{ MHz}$  and  $434.36\text{MHz} \pm 0.15 \text{ MHz}$ ). However there not should be problems of overlapping of frequency. In case of disturbance between communication transceiver and payload, AstroDev Helium Radios is available also in VHF version.

**Table 6.6 – TT&C transceiver.**

	NanoCom U480 [92]	AstroDev Helium Radios [93]
<b>Data rate [bps]</b>	Up to 9600	Up to 9600
<b>Frequency [MHz]</b>	435 – 437	120 – 150 or 400 – 450
<b>Power supply</b>		
<b>RX[W]</b>	0.240	0.200
<b>TX[W]</b>	1.386	1.700
<b>Voltage [V]</b>	3.3	5
<b>Output power [dBm]</b>	27-28	27
<b>Sensitivity [dBm]</b>	-120	-104.7
<b>Size [mm<sup>3</sup>]</b>	96 x 90 x 17/27	95 x 90 x 18

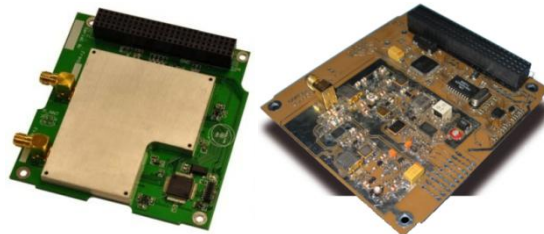


**Figure 6.6 – TT&C Transceiver: at left AstroDev Helium Radios, at right NanoCom U480.**

The antenna system is the Deployable UHF and VHF Standard ISIS Dipole Antenna[94]. The technical data are listed in Table 6.7. A dipole antenna has been chosen because of the high beamwidth at -3 dB (about 74°).

**Table 6.7 – Deployable Dipole Antenna System.**

<b>Antenna features</b>	
<b>Frequency band</b>	VHF - UHF
<b>Power: MAX/Typ.</b>	2 W (deployment) / < 20 mW
<b>Insertion loss</b>	< 1.5 dB
<b>Voltage [V]</b>	3
<b>Size [mm<sup>3</sup>]</b>	98 x 98 x 7

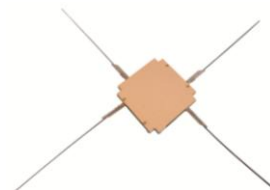


Table 6.8 – Ground station data.

Ground station features	
VHF yagi antenna	12dBic gain
UHF yagi antenna	16dBic gain
Frequency range	VHF 144 MHz – 146 MHz
	UHF 430 MHz – 440 MHz

The ground station supplied by ISIS [95] is capable of providing UHF/VHF/ S-band (downlink only) communications with satellites in Low Earth Orbit and can autonomously track selected satellites by using a steerable antenna system. CubeSat ground station cannot provide Uplink service, so, in case of communication from ground to spacecraft is needed, this service must be purchased. Alternatively SPACEFLIGHT [52] has the ability to provide TT&C services using UHF and S-Band ground stations. Data can be provided to the customer via the internet. Also Uplink service is provided.

### Link Budget

The link budget is calculated following the same method used for ISL WLAN (Chapter 2). In Table 6.9 are reported the dimensioning data and considered losses. The calculation was implemented in conservative condition of link geometry and losses.

Table 6.9 – Data for ground link calculation.

Loss/Gain	Values	Comments
Transmit waveguide	-1.5 dB	Considering Insertion loss (Antenna datasheet)
Receive waveguide	-3 dB	Estimate RF losses between transmitter and antenna
Tx antenna gains	2 dB	Estimated gain for dipole antenna
Rx antenna gains	16 dB	UHF yagi antenna
	12 dB	VHF yagi antenna
Atmospheric	-3 dB	Loss for 1GHz frequency and inclination angle by horizon of 10° (very conservative) (Figure 6.7)
Rain	0 dB	Wave length bigger than rain drop
Free space	Depending on Tx freq.	Distance between S/C and ground station (S/C rising)

In Table 6.10 the link margins relative to the link S/C – ground are showed. The calculation was implemented for both transceivers and considering UHF and VHF bands.

Table 6.10 – Ground link budget calculation.

Features	NanoCom U480	AstroDev Helium Radios	Comments
Frequency [MHz]	437	440 / 146 (take care of ground station)	Allocation of frequency plan[96]: 120-150 MHz: aeronautical, space 400-450 MHz: space
Output power[dB]	27	27	
Data rate [bps]	9600	9600	
Link margin [dB]	41.73	41.67 / 43.25	Threshold Power relative to BER = 10 <sup>-5</sup> ECSS[97]

The link margin is over 3 dB (conventional margin), so the communication between CubeSat and ground station is verified.

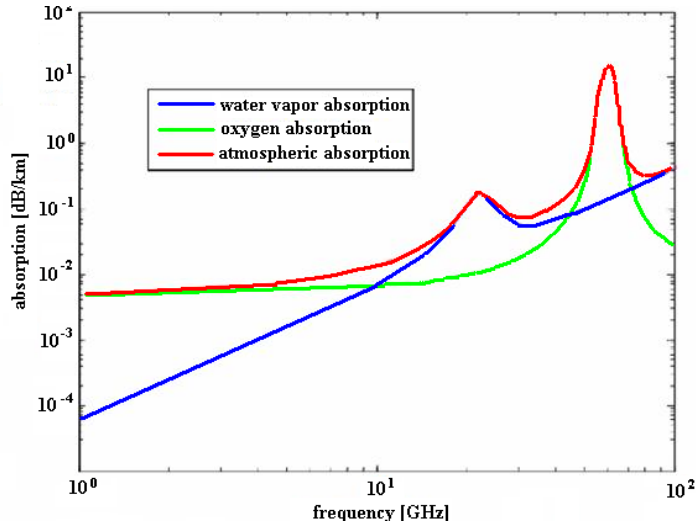


Figure 6.7 – Atmospheric losses diagram.

### Subsection 6.2.2 - Inter-Satellite Link backup

In case of Wireless ISL failure, a backup solution is needed.

TT&C transceiver and antenna are used also to communication between satellite. In Table 6.11 are reported the data for the calculation and, in Table 6.12, the link solution.

Table 6.11 – Data for ISL backup link calculation.

Loss/Gain	Values	Comments
Tx and Rx waveguide	-1.5 dB	Considering Insertion loss (Antenna datasheet)
Antenna gains	2 dB	
Free space	Depending on Tx freq.	Distance between S/Cs (1000 m)

Table 6.12 – ISL backup link budget calculation.

Features	NanoCom U480	AstroDev Helium Radios
Frequency [MHz]	437	450 / 150
Output power [dB]	27	27
Data rate [bps]	9600	9600
Link margin [dB]	88	87.78 / 97.32

Calculated link margins guarantee that the ISL is supported by chosen TT&C devices.

# Chapter 7 - Power generation and Thermal Control subsystems

## Section 7.1 - Components breakdown

We are now able to define a components list. In particular, in this section the list specifies the electrical and the environmental features. In the successive sections the power and the thermal analysis are presented referring to the data reported in Table 7.1.

The chosen components for the Electric and Power Subsystem (EPS) are the standard Clyde Space EPS 3U unit and four side solar panels with integrated magnetotorquer. A 3U battery board is also considered, it's dimensioning is reported in next pages.

**Table 7.1 – Satellite components specifications.**

	#	Power [W]			Voltage [V]	Radiation tolerance [krad]	Temperature range [°C]	
		Nominal	Sleep	Peak			Min	Max
<i>OBDH</i>								
<b>GOMspace NanoMind A712C</b>	1	0.231	0	0.294	3.3	TBD	-40	+85
<i>EPS</i>								
<b>Clyde Space EPS 3U CubeSat</b>	1	-	-	0.100	-	10	-40	+85
<b>Clyde Space 3U battery board</b>	1	-	-	-	8.2/12	500	-10	+40
<b>Clyde Space 3U Side Solar Panel with magnetotorquer</b>	4	-	-	0.34	-	-	-	-
<i>TT&amp;C</i>								
<b>ISIS Deployable Antenna</b>	1	0.020	0	2.000	3.6	TBD	-30	+70
<b>GOMspace NanoCom U480</b>	1	0.240	0	1.386	3.3	TBD	-30	+60
<i>Wi-Fi</i>								
<b>SYNAPSE SM700PC1</b>	1	0.108	1.7E-4	0.695	3.3	TBD	-40	+85
<i>Payload sensor</i>								
<b>SENSeOR TSE AS10</b>	4	-	-	-	-	TBD	-40	+200
<b>Infineon TDA 7255V</b>	1	0.027	2E-5	0.041	3.3	TBD	-40	+85
<i>GPS</i>								
<b>SSTL SGR-05U GPS Receiver</b>	1	0.800	0	0.800	3.3	10	-20	+50
<b>Quadrifilar antenna</b>	1	-	-	-	-	10	-20	+50
<i>ADCS</i>								
<b>Pumpkin ADACS interface</b>	1	-	-	-	12	TBD	-40	+85
<b>Sparkfun microMAG3</b>	1	0.002	0	0.002	3	TBD	-20	+70
<b>SSBV CubeSat Sun Sensor</b>	4	0.025	0	0.025	3.3/5	10	-25	+50
<b>Sinclair RW-0.01-4</b>	3	0.160	0.100	0.700	5	20	-40	+70
<i>Propulsion</i>								
<b>Clyde Space PPT</b>	1	-	0	0.500	5	TBD	TBD	TBD
<b>MicroSpace cold gas micropropulsion</b>	1	-	0	2	12	TBD	TBD	TBD

## Section 7.2 - Operative Modes

Before Electric and Power Subsystem design, the operation modes are introduced to better comprehend the power budget afterwards presented.

Table 7.2 – Mission Operative Modes vs. Subsystems.

Operative Mode	ADCS	GPS	TT&C	EPS	OBDH	Prop	P/L WLAN	P/L TSE
<b>Operational Chief</b>	Coarse	Coarse	TX	Panel	Normal	None	TX	Normal
<b>Operational Deputy</b>	Precise	Coarse	RX	Panel	Normal	Normal	RX	None
<b>Transmitting</b>	Coarse	Coarse	TX	Panel	Normal	None	RX	None
<b>Safe&amp;Hold (Eclipse)</b>	None	Coarse	RX	Battery	Normal	None	TX	None
<b>Safe&amp;Hold (Emergency)</b>	None	None	RX	Battery	Normal	None	None	None
<b>Launch</b>	None	None	None	Battery	Sleep	None	None	None
<b>Deployment</b>	None	Starting Search	Antenna deploy	Panel	Starting	None	None	None
<b>First contact</b>	Coarse	Starting Search	TX	Panel	Starting	None	TX	Normal
<b>Detumbling</b>	Precise	Coarse	RX	Panel	Normal	None	None	None

In each operative mode:

- TT&C subsystem default condition is in transmitting backup solution, in order to verify WLAN ISL: Deputy satellite compares data coming from TT&C link and WLAN link. Only during launch the communication subsystem is turned off. The only mode, in which both satellites transmit, is during the first contact after deployment. Chief satellite can transmit telemetry to ground only in Transmitting mode and it will be set on this mode when ground station is visible.
- The EPS subsystem generates power through solar panel. A battery board is foreseen in case of emergency or eclipse. During launch satellites are powered by battery board.
- OBDH subsystem is always collecting telemetry data from all subsystems and payloads. During launch the On Board Computer is in sleep mode until release from launcher. In following moments, Deployment and First contact modes come one after the other and the computer is started, so this is the time when OBDH is in maximum power consumption condition.
- Propulsion is turned off for all the operative modes in except of Operational Deputy mode in which the satellite is responsible for formation flying maintenance.
- COTS temperature sensors are interrogated (tested) when satellite is in Operational Chief mode. During first contact the transceiver interrogates payload to verify the devices correct functioning.



### **Operational**

- **Chief:** in this operational mode, the COTS temperature sensors are tested. The satellite transmit to the Deputy satellite the Data Packet containing coordinates, attitude and clock using the Wi-Fi ISL (and TT&C backup solution) that will be used to formation flying maintenance.
- **Deputy:** its primary task is to maintain the relative position, so the satellite receives Chief information through Wi-Fi ISL and from TT&C backup solution. Temperature sensors are in sleep mode and the ADCS subsystem is full active to maintain the correct attitude during trusting.

### **Transmitting**

Chief satellite switches into the transmitting mode each time formation will pass in proximity of ground station. The satellite transmits to ground station telemetry and payload data collected from the last ground station access in OBDH data storage.

### **Safe&Hold**

- **Eclipse:** during lifetime, eclipse could occur; in this case power supply is performed by battery as already sad. In this mode ADCS, temperature sensor and propulsion are in minimum power consumption conditions or even turn off. Wi-Fi ISL is maintained to avoid collision and TT&C subsystem is in receiving in case of communication by ground station.
- **Emergency:** in case of emergency all subsystems and payloads skip in sleep mode except TT&C that is in receiving mode waiting instruction from ground, and OBDH that must perform the commands coming from receiver. The system is powered by battery.

### **Launch**

Both spacecraft remain in sleep mode during all launch operations, stowed into the release pod, until sequential releasing. The spacecrafts demand minimum power to all subsystems, which is only OBDH and TT&C, is in sleep mode, while ADCS, GPS and payloads are switched off.

### **Detumbling**

Satellites switch into the detumbling mode directly after release from launcher. TT&C is in receiving mode and all payloads are switched off because sufficient power may not be available.

### **Deployment**

GPS starts and searches GPS satellites, also OBDH starts and TT&C antenna deploys. ADCS and payloads remain switched off.

### **First contact**

ADCS is switched on to acquire radial attitude, so TT&C can take the first contact with ground station. Payloads are tested to verify the devices correct functioning. Probably OBDH and GPS are still starting and searching for GPS satellite.

## Section 7.3 - Electric Power Subsystem

### Subsection 7.3.1 - Power solar panel generation and battery sizing

Maximum power generated by 3U solar panel [60] is 7.3 W as already sad in Chapter 1. However the effective power generated depends on solar vector angle respect to the panel surface, and solar cells degradation.

Power generated at the beginning of life ( $P_{BOL}$ ) is calculated as:

$$P_{BOL} = P_{GEN} \cdot \cos(\beta)$$

where  $P_{GEN}$  is the maximum power that could be generated and  $\beta$  is the solar vector angle that is different depending on operative mode:

- Operational, Detumbling, Transmitting, Deployment: sum of maximum inclination of Earth axis (23.5°) with orbital inclination effect (8°) and attitude accuracy (5°)
- First contact: 30° for hypothesis, considering along track release perpendicular to sun direction and with a coarse attitude accuracy.

Also power generation in the end of life is necessary:

$$P_{EOL} = P_{BOL} \cdot L_d$$

where  $L_d$  depends on solar cells material and is calculated by the formula:

$$L_d = (1 - d)^{Lifetime}$$

where  $d$  is 0.0275 for GaAs solar cells and lifetime is 1 year.

In Table 7.3 are showed the power budget results for each operative mode, a margin of 10% is summed to all results:

**Table 7.3 – Solar panel power generation.**

Operative Mode	$\beta$ [°]	$P_{BOL}$ [W]	$P_{EOL}$ [W]	110% $P_{BOL}$ [W]	110% $P_{EOL}$ [W]
Operational Chief	36.5	5.868	5.707	5.335	5.188
Operational Deputy	36.5	5.868	5.707	5.335	5.188
Transmitting	36.5	5.868	5.707	5.335	5.188
Deployment	36.5	5.868	5.707	5.335	5.188
First contact	30	6.322	6.148	5.747	5.589
Detumbling	36.5	5.868	5.707	5.335	5.188

In case of Safe&Hold and Launch operative modes, a battery is needed. Battery power is calculated by the equation:

$$P_{Batt} = \frac{DOD \cdot N \cdot \eta \cdot C_r}{T_{Batt}}$$

Clyde Space battery board [98] data are listed in Table 7.4.

Table 7.4 – Clyde Space battery board data.

Battery features	
Capacity ( $C_r$ )	10 Whr
Depth Of Discharge (DOD)	0.6
Numbers of batteries (N)	1
Efficiency of line ( $\eta$ )	0.9

In Table 7.5 are reported the solutions of battery sizing: in case of eclipse, the power budget is calculated considering an eclipse time ( $T_{\text{Eclipse}}$ ) equal to 30% of orbital period ( $T_{\text{Orbit}}$ ), for the emergency operative mode is calculated the maximum satellite autonomy before battery complete discharge and the last result represent the maximum satellite autonomy before in orbit release.

Table 7.5 – Battery power supply.

Operative Mode	Eclipse [orbit]	Battery range [hr]	110% $P_{\text{Batt}}$ [W]	Comments
S&H (Eclipse)	0.3	0.462	10.624	$T_{\text{Eclipse}}=30\% T_{\text{Orbit}}$ (see Chapter 3)
S&H (Emergency)	3.3	5	0.966	Maximum battery range in orbit
Launch		11	0.446	Maximum battery range before launcher release

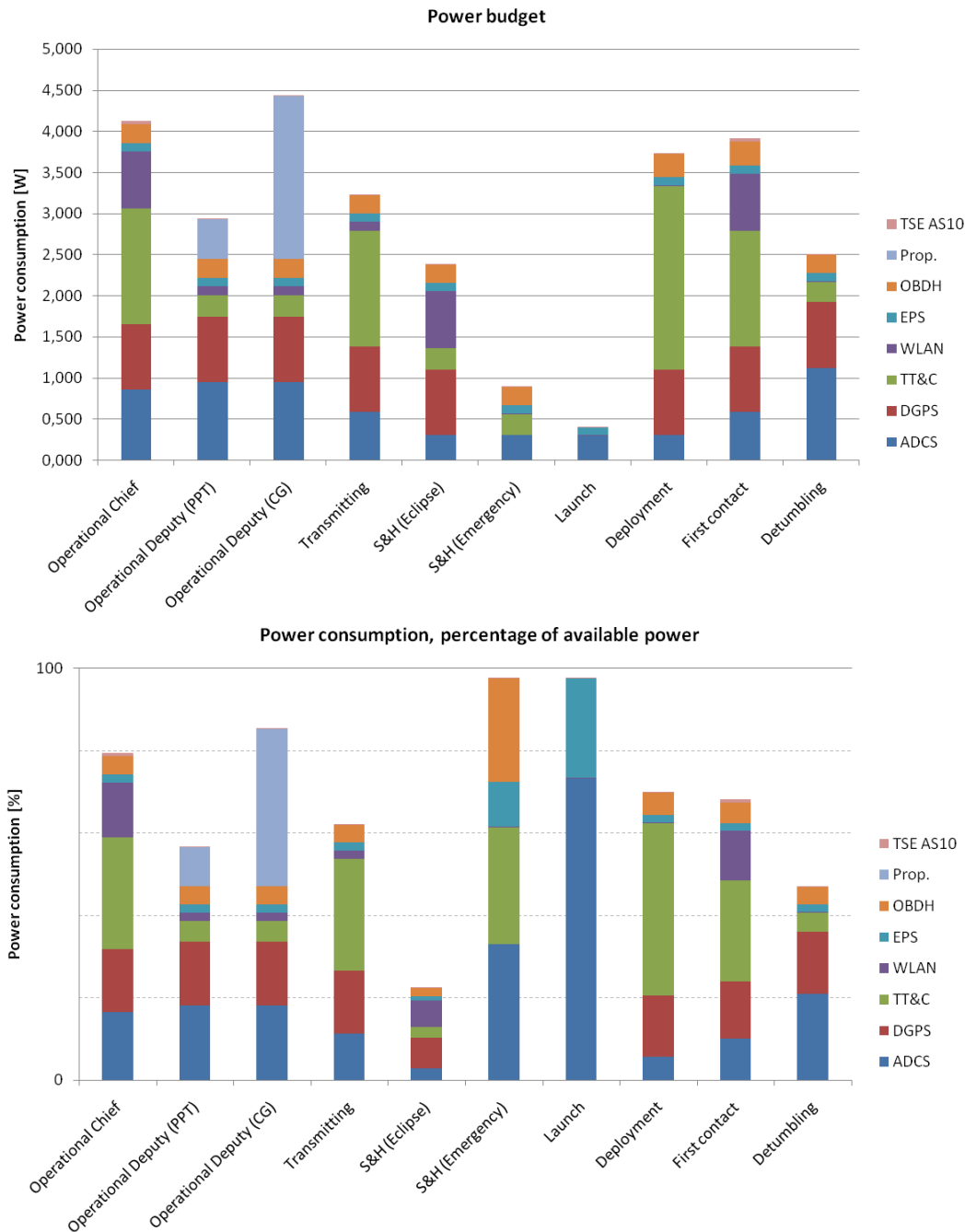
### Subsection 7.3.2 - Power Budget

Table 7.6 summarizes the power consumption of each subsystem for every operative mode. Last column shows the power required from all satellite subsystems. A further Operational Deputy operative mode is added to show the difference between using PPT or Cold Gas thruster.

Table 7.6 – Subsystem Power Consumption vs. Operative Mode.

Operative Mode	ADCS	GPS	TT&C	WLAN	EPS	OBDH	Prop	TSE AS10
Operational Chief	0.852	0.800	1.406	0.695	0.100	0.231	0	0.041
Operational Deputy (PPT)	0.942	0.800	0.260	0.108	0.100	0.231	0.500	0
Operational Deputy (cold gas)	0.942	0.800	0.260	0.108	0.100	0.231	2.000	0
Transmitting	0.582	0.800	1.406	0.108	0.100	0.231	0	0
S&H (Eclipse)	0.300	0.800	0.260	0.695	0.100	0.231	0	0
S&H (Emergency)	0.300	0	0.260	0	0.100	0.231	0	0
Launch	0.300	0	0	0	0.100	0.000	0	0
Deployment	0.300	0.800	2.240	0	0.100	0.294	0	0
First contact	0.582	0.800	1.406	0.695	0.100	0.294	0	0.041
Detumbling	1.117	0.800	0.260	0	0.100	0.231	0	0

Table 7.7 and Figure 7.1 summarize the power budget distinguished for operative mode.



**Figure 7.1 – Power consumption: absolute values and percentage of available power.**

The operations of deployment, first contact and detumbling occur few hours after orbital release, so the dimensioning available power is at the beginning of life. Operational modes and communications with ground station occur for all lifetime, so the dimensioning available power level to consider is the  $P_{EOL}$ . This power budget is calculated considering the typical devices consumption, however sometimes the request of power could increase for various factors. The battery board is also necessary to absorb this peak power request. In particular, ADCS and propulsion subsystems are prone to these power fluctuations, but rarely reach peak power level declared by datasheet. ADCS power budget is calculated on effective operative mean consumption, resulted from simulations reported in relative chapter.

Table 7.7 – Power budget: summary.

Operative Mode	Required Power [W]	Available Power [W]		Budget surplus
Operational Chief	4.124	5.188	$P_{EOL}$	25.8%
Operational Deputy (PPT)	2.941	5.188	$P_{EOL}$	76.4%
Operational Deputy (cold gas)	4.441	5.188	$P_{EOL}$	16.8%
Transmitting	3.227	5.188	$P_{EOL}$	60.8%
S&H (Eclipse)	2.386	10.624	$P_{Batt}$	345.3%
S&H (Emergency)	0.891	0.911	$P_{Batt}$	2.2%
Launch	0.400	0.409	$P_{Batt}$	2.2%
Deployment	3.734	5.335	$P_{BOL}$	42.9%
First contact	3.917	5.747	$P_{BOL}$	46.7%
Detumbling	2.508	5.335	$P_{BOL}$	112.7%

## Section 7.4 - Thermal Control Subsystem

The goal of the thermal control subsystem is to keep spacecraft components whit in their operative temperature ranges. These data are reported in Table 7.1 for each component.

The thermal fluxes considered for the analysis are the classical sources of thermal environment in Earth orbit:

- solar direct radiation: at 1AU is equal to  $1357 \text{ W/m}^2$
- planetary IR radiation: equal to 230 W
- albedo
- IR radiation to deep space: deep space temperature is 3K
- internal dissipation: the only dissipation out of thermal balance is the transmitted power (0.5W for TT&C and 0.1W for Wi-Fi ISL)

Depending on satellite position on orbit and seasons, different orbital conditions are considered. In particular seven cases are analyzed:

- equinoxes, in case of satellite is over passing north pole and south pole. When satellite is on north pole, the Earth under the satellite is in umbra, so the albedo is absent
- summer and winter solstices, in case of satellite is over passing North Pole and South Pole. The albedo is absent in south pole in summer and in north pole in winter
- passage through the orbital node. Sun direction is always perpendicular to the satellite surface and the albedo is referred to a surface covered of forest or water.

In Figure 7.2 are shown the geometries in case of pole position and nodal passage and in Table 7.8 are listed the data relative to the different cases analyzed.

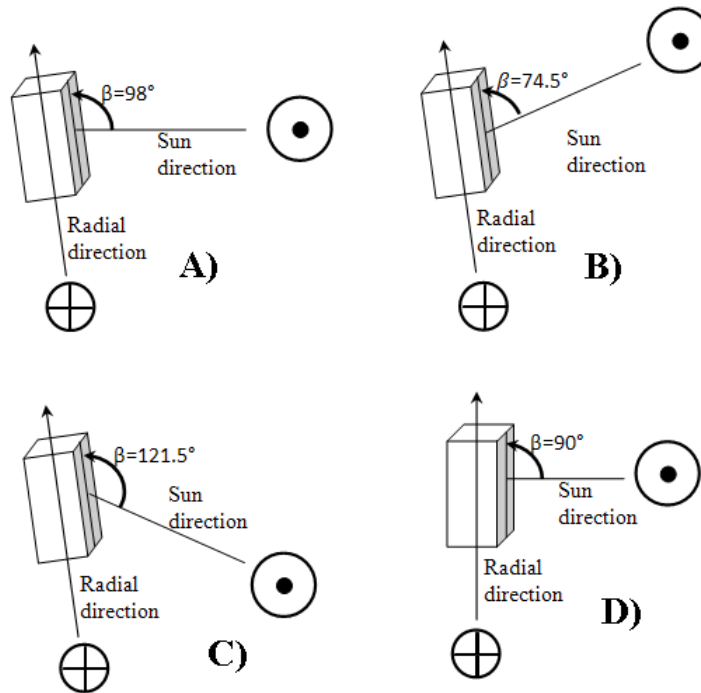


Figure 7.2 – Geometries relative to the analyzed cases: A) equinox, B) summer solstice, C) winter solstice, D) passage on the orbital node. All the figures are relative to the north position on orbit.

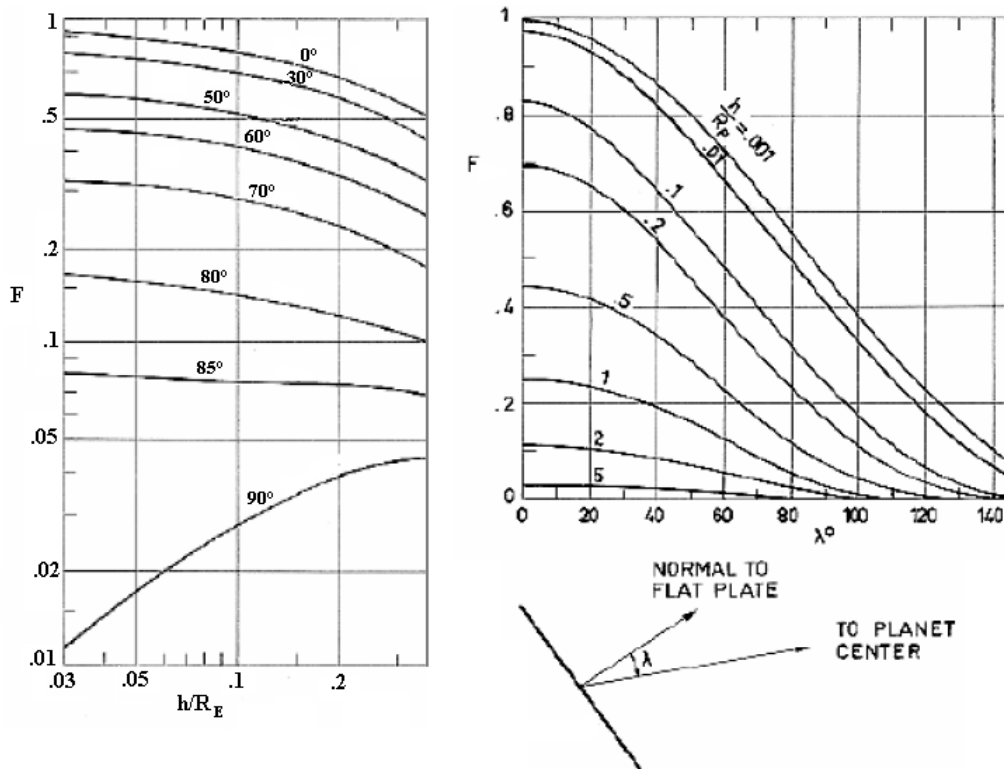


Figure 7.3 – Albedo (Left): view factor ( $F$ ) in function of high on mean Earth radius ( $h/R_p$ ) and  $\beta$  angle; IR radiation (Right): view factor ( $F$ ) in function of angle between normal to S/C panel and planet center direction and high on mean Earth radius ( $h/R_p$ ).

Table 7.8 – Data relative to thermal analysis.

Date	20/03/2014		21/06/2014		21/12/2014		Nodal passage
	North	South	North	South	North	South	
Position on orbit	0.8	0.8	0.8	0.8	0.8	0.8	0.3
Earth surface reflectivity	(Pole)	(Pole)	(Pole)	(Pole)	(Pole)	(Pole)	(Forest)
Angle between S/C panel and sun direction ( $\beta$ )	98	82	74.5	105.5	121.5	58.5	90
View factor Albedo (Figure 7.3)	0	0.12	0.4	0	0	0.5	0.02
View factor IR (Figure 7.3)	0.9	0.8	0.9	0.8	0.8	0.9	0.9

The balance of incoming and out-coming power is expressed by the following equation:

$$Q_{DS} = Q_{Sun} + Q_{IR} + Q_A - Q_{Tx}$$

where:

- $Q_{DS} = \sigma \cdot (4 \cdot A_{Lat} \cdot \epsilon_{Lat} + A_{Top} \cdot \epsilon_{Top}) \cdot (T_{Sat}^4 - T_{DS}^4)$

Is the IR radiation to deep space in which  $\sigma = 5.67E-8 \text{ W/(m}^2\text{K}^4)$  is the Stefan-Boltzmann constant,  $A_{Lat}$  and  $A_{Top}$  are respectively the lateral panel surface and the top panel surface,  $\epsilon_{Lat}$  and  $\epsilon_{Top}$  are the relative emissivity and  $T_{Sat}$  and  $T_{DS}$  are the satellite mean temperature and the deep space temperature.

- $Q_{Sun} = R_{Sun} \cdot \sin(\beta) \cdot A_{Lat} \cdot \alpha$

is the effective solar direct radiation ( $R_{Sun}$ ) absorbed by the  $A_{Lat}$  lateral panel area with an absorbance  $\alpha$ .

- $Q_{IR} = Q_E \cdot F_{IR} \cdot A_{Bot} \cdot \alpha$

is the effective Earth IR radiation ( $Q_E$ ) absorbed by the bottom panel oriented toward Earth surface.  $F_{IR}$  is the IR view factor.

- $Q_A = Q_{Sun} \cdot A_{Bot} \cdot F_A \cdot \rho_E \cdot \alpha$

is the Albedo heat flux calculated in function of Albedo view factor  $F_A$  and the Earth surface reflectivity  $\rho_E$ .

- $Q_{Tx}$  is the power transmitted through the TT&C communication (500 mW).

To calculate the solar panel parameter  $\epsilon$  and  $\alpha$ , we assume the 80% panel covered by solar cells and the remaining area is substrate material. Using a PCB substrate the temperatures that will be calculated are too cold, so aluminium substrate will be required to solar panel supplier.

Table 7.9 – Solar cell and substrates Thermal Properties[99].

	GaAs cell	Aluminium	Polyethylene Black Plastic
Surface proportion	0.8	0.2	0.2
Absorptance	0.9	0.379	0.94
Emissivity	0.87	0.0393	0.92

So, the thermal properties of the total panel, made of solar cells and aluminium substrate, are calculated as weighted mean of the cell and substrate values. The top and the bottom panel are aluminium panel.

**Table 7.10 – Solar panel Thermal Properties.**

	Lateral panel	Top panel	Bottom panel
Area [m <sup>2</sup> ]	0.03	0.01	0.01
Absorptance	0.7958	0.379	0.379
Emissivity	0.70386	0.0393	0.0393

Now is possible to calculate the one node solution on satellite in the seven cases considered with the following formula (caused by the power equilibrium equation):

$$T_{Sat} = \left[ \frac{Q_{Sun} + Q_{IR} + Q_A - Q_{Tx}}{\sigma \cdot (4 \cdot A_{Lat} \cdot \varepsilon_{Lat} + A_{Top} \cdot \varepsilon_{Top})} + T_{DS}^4 \right]^{1/4}$$

In Table 7.11 the one node analysis results are reported. As we can see, the hot case, among the conditions considered, is the nodal passage with  $Q_{Tx}$  null. This is because the sun direction is perpendicular to the satellite side face. Instead, the cold case corresponds to the winter solstice north passage during a ground link. However, both hot case and cold case are very distant from devices operative temperature ranges.

**Table 7.11 – One node analysis results.**

Date	20/03/2014		21/06/2014		21/12/2014		Nodal passage
	North	South	North	South	North	South	
Position on orbit	North	South	North	South	North	South	Nodal passage
T <sub>Sat</sub> [K] (Q <sub>Tx</sub> = 0)	287.49	288.37	289.19	285.39	276.99	282.09	288.24
T <sub>Sat</sub> [°C] (Q <sub>Tx</sub> = 0)	14.34	15.22	16.04	12.24	3.84	8.94	15.09
T <sub>Sat</sub> [K] (Q <sub>Tx</sub> = 0.5 W)	286.39	287.28	288.11	284.26	275.76	280.92	287.15
T <sub>Sat</sub> [°C] (Q <sub>Tx</sub> = 0.5 W)	13.24	14.13	14.96	11.11	2.61	7.77	14.00

A non-stationary analysis is performed to investigate the eclipse case. The satellite is considered as a block characterized by physical features calculated as a weighted mean of the satellite materials features. Approximating the satellite as composed by 55% of PCB, 40% of aluminium and 5% of copper, we can calculate the block specific heat:

**Table 7.12 – Satellite materials specific heats and percents.**

Material	Specific heat [J/(kg K)]	Material proportion
PCB	2300	0.55
Alluminium	900	0.4
Copper	385	0.05
Block material	1644.25	1



Considering a satellite mass of 3kg and an eclipse of 30% of orbit (1663 s), we can calculate the satellite temperature when it come out from the eclipse. In this case the internal heat generation is supplied by battery and no transmitted power is considered.

$$Q = M \cdot c \frac{T_i - T_f}{\Delta t}$$

where Q is the heat power coming from environment and internal generation (battery supply), M is the block mass, c the specific heat, Δt the eclipse time and T<sub>i</sub> and T<sub>f</sub> the entrance and the exit temperature from the eclipse.

**Table 7.13 – Non-stationary analysis results for eclipse case.**

<b>CASE</b>	<b>Q</b>	<b>T<sub>i</sub></b>		<b>T<sub>f</sub></b>	
<b>HOT</b>	2.572 W	288.24 K	15.09 °C	287.17 K	14.02 °C
<b>COLD</b>	2.572 W	275.76 K	2.61 °C	274.69 K	1.54 °C

Hot case is considered because is the most probable eclipse entrance condition, however cold case is analyzed to verify the system thermal protection in the worst case.

In conclusion, the satellite mean temperature stays in components operative temperature ranges also in eclipse.



# Chapter 8 - System overview

## Section 8.1 - Configuration requisites

### Subsection 8.1.1 - Components masses and envelopes

From now on, all components and subsystems are selected and they are listed in Table 7.1. They have just to be accommodated into PCI-104 standard form factor stack and correctly interfaced with available structures.

Table 8.1 – Satellite components physical specifications and cost.

	#	Mass [g]	Envelope [m]			Vibration tolerance [g]	Cost [€]
			length	width	height		
<i>OBDH</i>							
<b>GOMspace NanoMind A712C</b>	1	55	0.096	0.090	0.010	TBD	4750
<i>EPS</i>							
<b>Clyde Space EPS 3U CubeSat</b>	1	93	0.095	0.090	0.015	TBD	3127
<b>Clyde Space 3U battery board</b>	1	110*	0.095	0.090	0.015	TBD	1140
<b>Clyde Space Top-Bottom Panel</b>	2	060	0.454	0.454	0.002	TBD	2265
<b>Clyde Space 3U Side Solar Panel</b>	4	170	0.096	0.002	0.454	TBD	4820.30
<i>TT&amp;C</i>							
<b>Isis Deployable Antenna System</b>	1	100	0.096	0.090	0.007	TBD	4500
<b>GOMspace NanoCom U480</b>	1	75	0.095	0.090	0.017	TBD	8000
<i>Wi-Fi</i>							
<b>SYNAPSE SM700PC1</b>	1	5*	0.025	0.036	0.005	TBD	19.15
<i>TSE</i>							
<b>SENSeOR TSE AS10</b>	4	1	0.005	0.005	0.0015	15.8	300
<b>Infineon TDA 7255V</b>	1	5*	0.007	0.006	0.0009	TBD	26.5
<b>ANT-433-SP</b>	1		0.028	0.0137	0.0015	TBD	1.69
<i>GPS</i>							
<b>SSTL SGR-05U GPS Receiver</b>	1	40	0.070	0.047	0.015	15	13525
<b>Quadrifilar antenna</b>	1	12	0.013	0.013	0.040	15	-
<i>ADCS</i>							
<b>CubeSat Kit ADACS interface</b>	1	49	0.096	0.090	0.015	TBD	10000*
<b>Sparkfun MicroMag3</b>	1	10	0.025	0.025	0.019	TBD	39
<b>SSBV CubeSat Sun Sensor</b>	4	5	0.033	0.011	0.006	25	2500
<b>Sinclair Interplanetary RW-0.01-4</b>	3	120	0.050	0.050	0.030	12	5000*
<i>Propulsion</i>							
<b>Clyde Space Pulse Plasma Thruster</b>	1	200	0.090	0.090	0.027	TBD	10000
<b>MicroSpace cold gas Microprop.</b>	1	300	0.090	0.090	0.037	TBD	81000

### Subsection 8.1.2 - System Chart

The system diagram in Figure 8.1 shows the key subsystems and buses on each CubeSat. Given the adoption of I<sup>2</sup>C by existing CubeSat COTS modules, most of satellites' subsystems operate as slaves, only responding to requests from bus masters. The primary bus master is the GOMspace OBC subsystem.

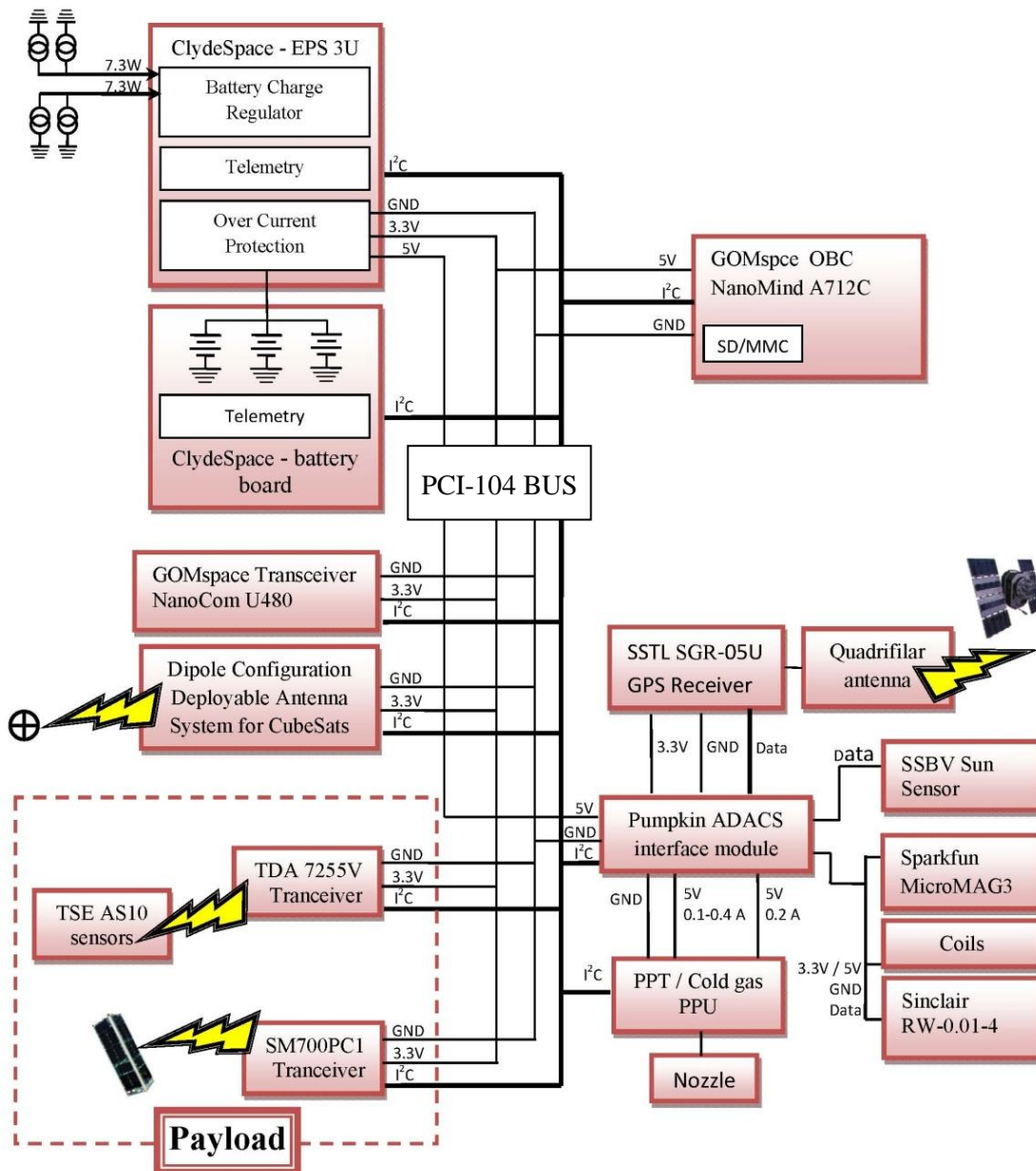


Figure 8.1 - System block diagram.

## Section 8.2 - Primary structure

### Subsection 8.2.1 - CubeSat structures

There are two main CubeSat structure families:

- Pumpkin CubeSat kit models, made of aluminium machined plates, more efficient, available also in fractions of a cube unit. They provide a unique vertical stack, connected to the top and bottom plates and eventually at intermediate heights
- Isis models, composed by frames subframes and panels, available only in multiples of a cube unit. They have the advantage to provide stack rotations, at each module

They are both compliant with CubeSat standards and specifications and able to withstand launch loads, stowed in PPOD interfaces, for maximum payload masses lower than about 2 kg per cube unit [64]. In alternative, ad hoc structure can be designed and tested, if particular interface issues incur, but it doesn't result necessary.

### Subsection 8.2.2 - Propulsion pointing and structural integration

The driving requirement in configuration definition is propulsion components, which has to be necessarily oriented perpendicularly to radial axis, which is the minor inertia axis.

In each case, the structure is constrained to a 3U configuration, due to the very tight power budget, so nozzles have to be aligned with expected center of mass position, in the middle of the central cube. As shown in Figure 8.2, two different configurations have been selected, each one involving different structure types.

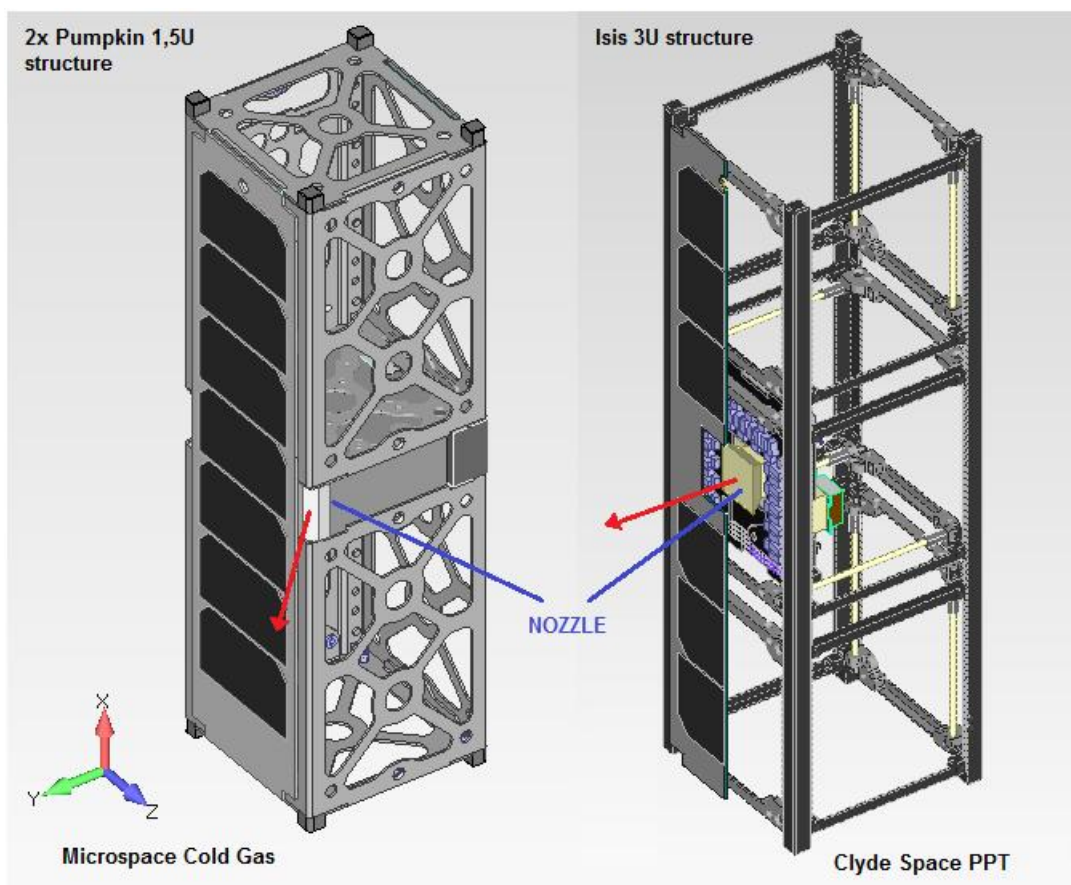


Figure 8.2 – Cold Gas and PPT propulsion system accommodation for lateral thrust

### PPT configuration

Despite a lateral nozzle version is under development, a Clyde Space PPT standard version collocation has been considered, rotating the entire stack of the central block. This solution also offers several possibilities to orient the other PCB mounted components. Lateral plate and corresponding lateral solar panel has to be drilled to allow the nozzle exhaust.

PPT propulsion system occupies about  $\frac{1}{4}$  of a cube, with the possibility to mount other boards within the rotated pile, whenever it's necessary.

### Cold gas configuration

Microspace Cold gas device has nozzle clusters in correspondence of the corners. Such these nozzles can be eventually customized with different orientation. Fortunately, their envelope fits within two adjacent solar panels, but it necessarily interrupts Isis structure's frames. That's because an alternative solution has been studied.

Two 1.5U Pumpkin structures can be directly connected to the cold gas box, at each bottom and top side, with two Pumpkin Payload adapter plates. Fortunately, such this overall height corresponds to a 3U envelope. In this case, the propulsion component itself would become a structural part and more detailed mechanical information, not available yet, would become necessary. In his case, propulsion subsystem occupies up to one module, due to necessary additional tanks, to be collocated within the upper and lower stacks.

### Bus routing within stacks

Involving rotated blocks, PCI bus continuity has to be provided in alternative ways, employing for example discrete wires solutions, bended bus connectors or dedicated boards to rout and convert signal in other serial interfaces, as depicted in Figure 8.3.

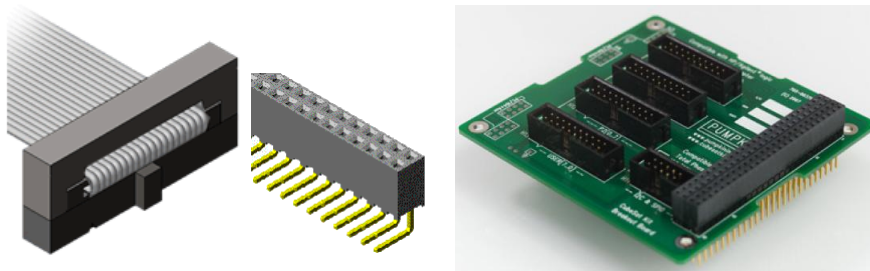


Figure 8.3 – Bus stacking continuity and routing possible solutions, discrete wire and header Samtec products for PCI-104 [100] (left) and Pumpkin breakout board for I/O routing (right).

Even in case of cold gas implementation, there is a discontinuity within the blocks and bus has to be necessarily routed by discrete wires, passing throughout the few millimeters gap between cold gas enclosure and solar panels.

## Section 8.3 - Secondary structures

Some devices are already available in a PCI-104 board, like component specifically designed for CubeSat. Sometimes, also 3D CAD models are provided (these are Clyde Space, GOMspace components and all structural parts). Otherwise, a geometrical representation of their envelopes has been developed, in the best detail as possible.

These devices, in particular WiFi transceivers, GPS receiver and wheels have to be interfaced with PCI-104 bus and stack. However, all of the listed components can fit within a single CubeSat module envelope and can then be mounted within the stack, on empty PCI-104 boards, or alternatively mechanically connected to the four corner bars of the stack. Modal analysis has been performed in order to verify the first vibration frequency of the single board is sufficiently far from minimum 150Hz frequency stated in CubeSat specification [101]. PCB mechanical properties are assumed equal to commonly used FR-4 glass/epoxy ( $\rho=1850 \text{ kg/m}^3$ ,  $E=24\text{GPa}$ ) laminate in PCB industry [102]. Results are reported in Table 8.2.

### Subsection 8.3.1 - Reaction wheels

Wheels have to be aligned with principal axis and connected in some way with the structure. A dedicated box will be soon available, for a three wheel cluster of the selected model; within a 95×95×61 RS232 interfaced enclosure, fully comparable to Maryland models packages, which would also be able to accommodate three of the current RW models, as shown in Figure 8.4.

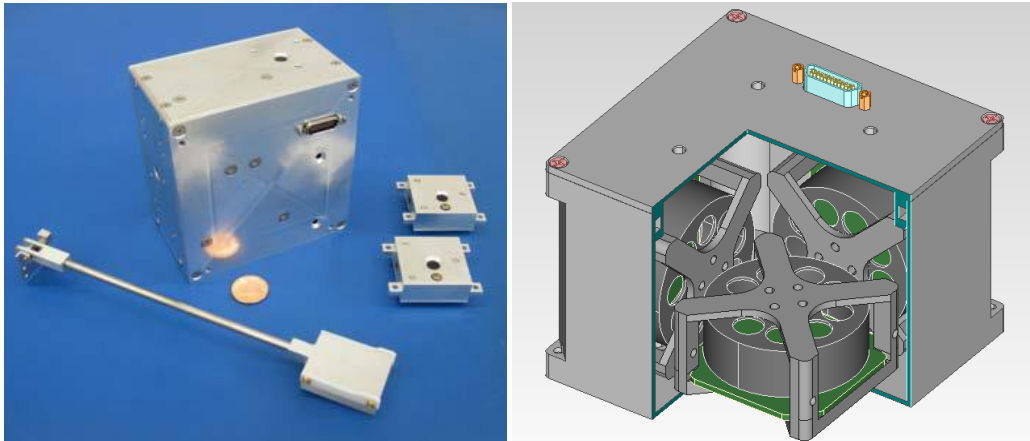


Figure 8.4 – Sinclair 3x cluster enclosure (under development [103]) (left) and Sinclair wheels readjustment within Maryland IMI-100 enclosure (right). Solids have been sliced to aid viewing

Alternatively, a direct PCB mounting has been developed, both in Aluminum plates and in PCBs. Even the second one provides acceptable resonant frequencies, as shown in Figure 8.5.

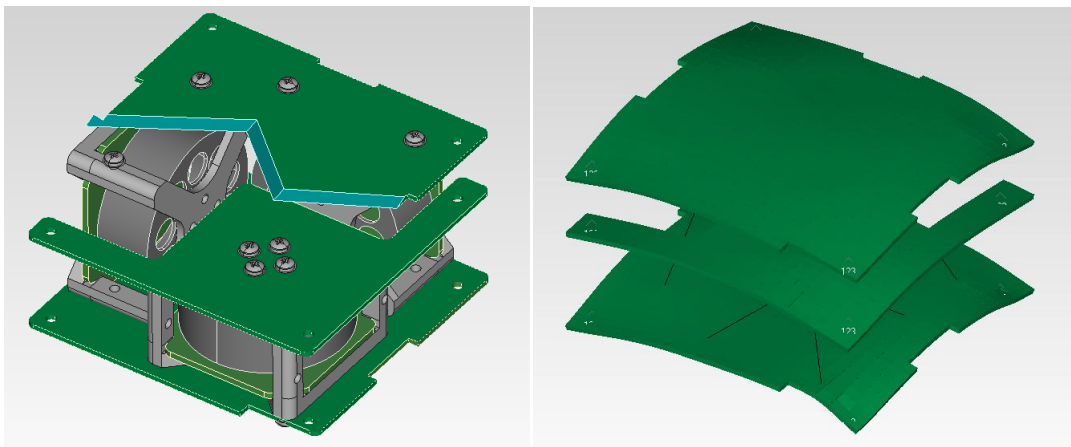


Figure 8.5 – Sinclair wheels cluster PCB stack 3D representation (left) and first vibration mode deformed view of the only interface PCBs (right)

In such this custom configuration also magnetotorquers rod can be distributed and correctly mounted. Despite the use of rods is not actually considered, because attitude control showed to be affordable with panel integrated coils, it would be a valid power saving solution, if additional on-board envelope can be achieved.

### Subsection 8.3.2 - WiFi payload

Both WLAN transceiver and temperature sensing network transceiver and patch antenna are patch components. Then, a direct PCB mounting, glued or soldered, provides easy ad-hoc electrical connections implementation via copper rails. SM700PC1 comprehends its own patch

antenna, which has very low directivity and low pointing constraints. Temperature sensor transceiver, TDA 7255V, utilizes ANT-433-SP antenna, which has a low directivity perpendicularly to its mounting plane. To provide data transmission also within the two spacecraft, the PCB configuration, proposed in Figure 8.6, must be mounted in a rotated stack to obtain in-track pointing, with only yaw attitude maneuvers. .

### Subsection 8.3.3 - GPS receiver

GPS receiver board is provided easy mounting, with four attachment holes at corners, as shown in Figure 8.6. Provided quadrifilar antenna has to be pointed towards zenith direction. External mounting is strongly preferred, but in case it is not possible, it can be even collocated on the PCB, with the receiver itself. Also in this case, PCB must be rotated.

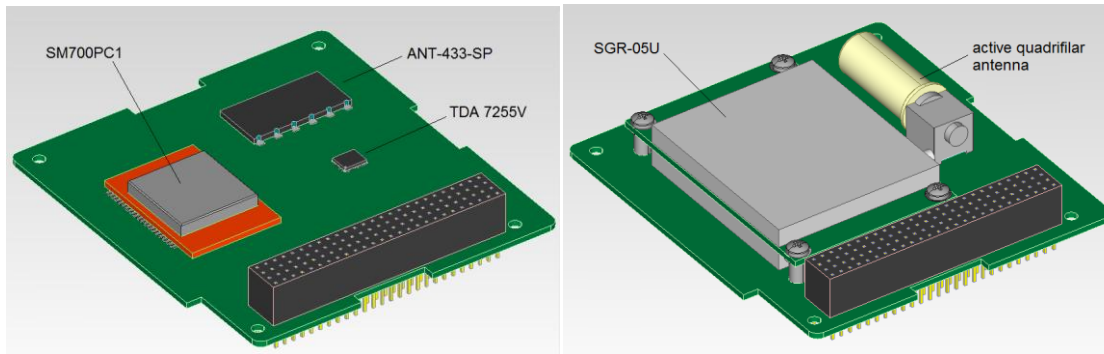


Figure 8.6 – WiFi payload (left) and GPS receiver (right) direct PCB mounting configurations

Table 8.2 – Mechanical interface natural frequencies.

	1st mode frequency [Hz]	2nd mode frequency [Hz]	Structural mass [g]
<b>Wheels cluster (Al board)</b>	386.3	728.6	93.6
<b>Wheels cluster (FR-4 board)</b>	227.7	429.3	61.6
<b>GPS</b>	196.6	318.9	43
<b>Wireless transceiver</b>	182.9	342	43

## Section 8.4 - Spacecraft configuration

A complete configuration 3D model is presented in, for the case of Clyde Space PPT propulsion, to describe the overall stack envelope.

A 2U configuration would indeed be affordable, but it would conflict with power generation constraint to have at least a 3U lateral side panel. As mentioned before, a wide variety of deployable solar panels configurations are available, but none of them is implemented on a 2U structure and then it would be fully designed and tested.

In this low density configuration, a significant advantage can be achieved. By little PCBs translation along the rail, the center of mass can be easily realigned with thrust vector. In this analysis, in lack of detailed information about the effective center of mass position of each component, only a rough mass balancing can be done. As reported in Table 8.3, components



distribution within the modules has been equally distributed, paying attention on upper and lower modules, to facilitate further implementation.

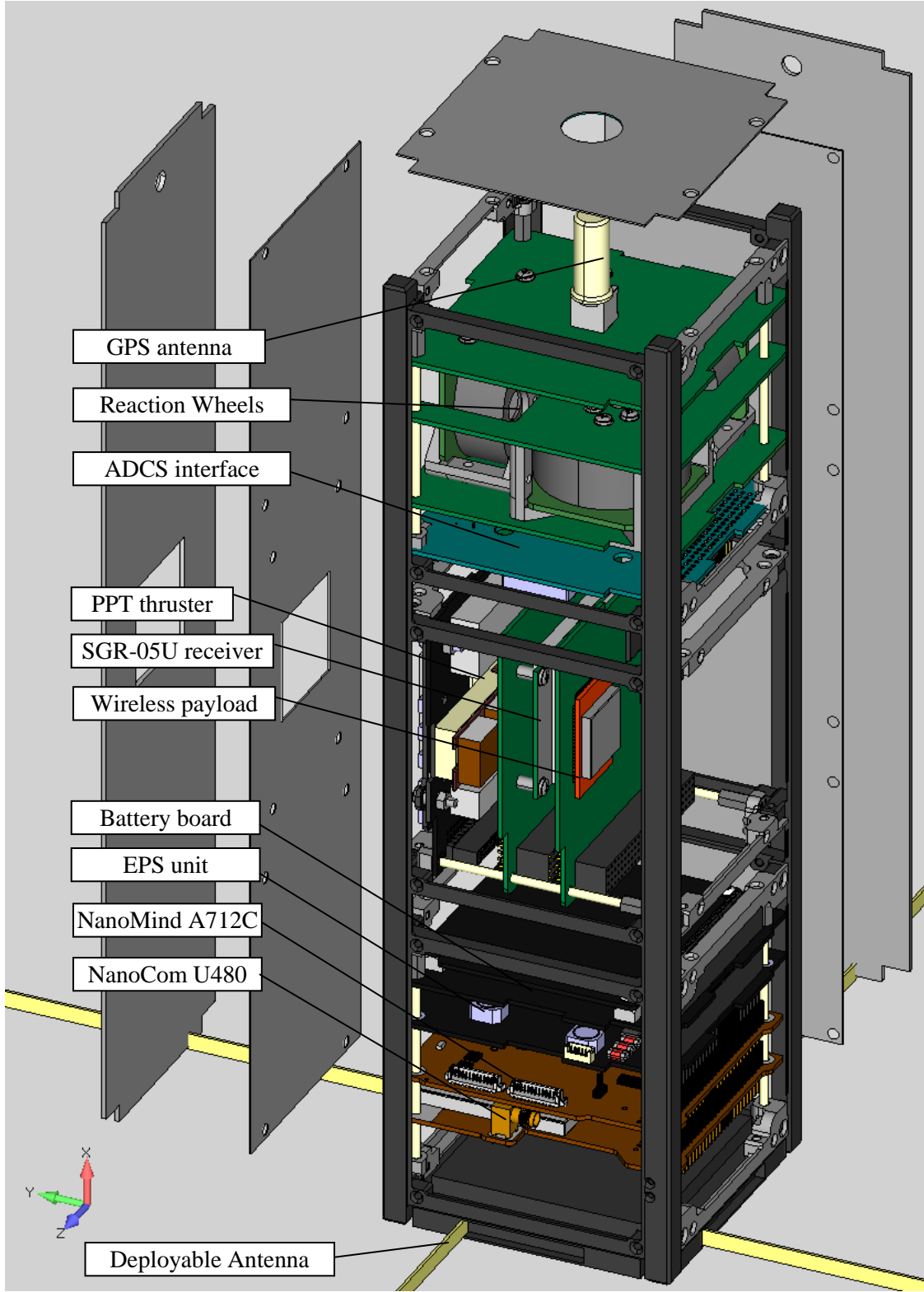


Figure 8.7 – Explode view of the overall configuration, with all components correctly stacked within structures rails.

**Table 8.3 – Mass distribution within cubes**

	PPT		Cold gas	
	Components	Mass	Components	Mass
<b>Upper unit</b>	Top Panel with MTQ Active quadrifilar antenna ADACS interface Sparkfun MicroMag3 4×SSBV Sun Sensor 3×Sinclair RW-0.01-4	491 g	Top Panel with MTQ Active quadrifilar antenna ADACS interface + MicroMag3 4×SSBV Sun Sensor 3×Sinclair RW-0.01-4 SSTL SGR-05U + Empty PCB	574g
<b>Central unit</b>	Clyde Space PPT SM700PC1 + Empty PCB TDA 7255V Ant-433-SP SSTL SGR-05U + Empty PCB	446 g	Microspace cold gas Additional tanks Isis Deployable Antenna	480 g
<b>Lower unit</b>	Bottom Panel with MTQ GOMspace NanoMind A712C Clyde Space 3U EPS Clyde Space battery board Isis Deployable Antenna GOMspace NanoCom U480	493 g	Bottom Panel with MTQ GOMspace NanoMind A712C Clyde Space 3U EPS Clyde Space battery board GOMspace NanoCom U480 Ant-433-SP + SM700PC1 + TDA 7255V + Empty PCB	536 g
<b>Distributed</b>	4×Clyde Space side solar panels Isis 3U primary structure	1250 g	4×Clyde Space side solar panels 2×Pumpkin 1.5U structure	1250 g

## Section 8.5 - Mass & Cost budgets

### Subsection 8.5.1 - Single spacecraft mass and cost budgets

The Mass budget calculated for each satellite is detailed in Table 8.4. Figure 8.8 show the comparison between the two configurations.

WLAN and TSE payload subsystems are integrated with a margin of 20% because are COTS devices and they need additional structure and accessories. ADCS subsystem need interfaces with the bus and this additional mass is integrated in 10% of mass margin. Structural mass comprehend cabling, connectors and additional host boards dedicated to the payloads and ADCS wheels.

Particular attention must be oriented on cold gas propulsion mass budget. No information about propellant and tank are provided by the supplier, so the subsystem mass is increased of the 20% to take account of the tank mass uncertainty. The declared minimum cold gas mass is of 200g, probably the only propulsion system, instead the declared standard mass is 300g, probably with a fuel tank. In the mass calculation above, the fuel mass is taken in account and we are sure to include an eventual additional tank to the standard system increasing the subsystem mass of 20%.

In case of subsequently releasing from launcher the satellites are storage in two 3U PODs whose maximum payload mass is 5kg. If the release is in docked configuration the maximum mass that a 6U POD can carry is 10kg. In both cases the satellites total mass is below the maximum limit.

In Table 8.5 and in Figure 8.8 are shown the costs budget detailed per subsystems. In the first case the PPT propulsion is mounted, in the second one the cold gas propulsion is considered.

**Table 8.4 – Mass budget for each satellite.**

	PPT			Cold gas		
	Mass[kg]	Margin	Mass+Margin [kg]	Mass[kg]	Margin	Mass+Margin [kg]
<b>ADCS</b>	0.439	10%	0.483	0.439	10%	0.483
<b>DGPS</b>	0.052	5%	0.055	0.052	5%	0.055
<b>TT&amp;C</b>	0.175	5%	0.184	0.175	5%	0.184
<b>WLAN</b>	0.005	20%	0.006	0.005	20%	0.006
<b>TSE</b>	0.033	20%	0.040	0.033	20%	0.040
<b>EPS</b>	1.003	5%	1.053	1.003	5%	1.053
<b>OBDH</b>	0.055	5%	0.058	0.055	5%	0.058
<b>Prop.</b>	0.200	5%	0.210	0.300	20%	0.360
<b>Struct.</b>	0.699	10%	0.769	0.699	10%	0.769
<b>Dry mass [kg]</b>			2.857			3.007
<b>Fuel mass [kg]</b>			0.010			0.061
<b>Wet mass [kg]</b>			2.867			3.067
<b>system margin 10%</b>			0.307			0.307
<b>Total launched mass</b>			3.173			3.374
<b>Launcher adapter mass</b>			2.000			2.000

**Table 8.5 – Cost budget for each satellite.**

	PPT			Cold gas		
	Cost [€]	Margin	Cost+Margin [€]	Cost [€]	Margin	Cost+Margin [€]
<b>ADCS</b>	20039	10%	22042.90	20039.000	10%	22042.90
<b>DGPS</b>	13525	5%	14201.25	13525.000	5%	14201.25
<b>TT&amp;C</b>	12500	5%	13125	12500.000	5%	13125
<b>WLAN</b>	19.15	20%	22.98	19.150	20%	22.98
<b>TSE</b>	1226.50	20%	1471.80	1226.500	20%	1471.80
<b>EPS</b>	28775.20	5%	30213.96	28775.200	5%	30213.96
<b>OBDH</b>	4750	5%	4987.50	4750.000	5%	4987.5
<b>Prop.</b>	10000	5%	10500	81000.000	5%	85050
<b>Struct.</b>	1877	10%	2064.70	4500.000	10%	4950
<b>Total cost [€]</b>			98630.09			176065.39
<b>system margin 10%</b>			9863.01			17606.54
<b>Total cost with margin [€]</b>			108493.10			193671.93

Payloads and ADCS cost margins are onerous because manufacturing and service components must be considered for devices integration. In structure cost margin are included additional connectors and cabling.

It's important to notice the enormous gap between satellite cost in case of PPT propulsion mounting or cold gas case.

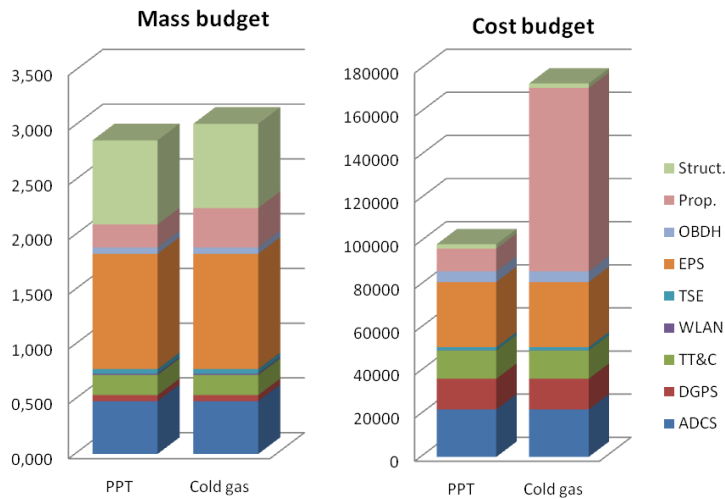


Figure 8.8 – Mass and cost budget comparison: PPT and cold gas thruster.

### Subsection 8.5.2 - Launch cost budget

The launch cost as secondary payload is calculated through the cost/kilogram parameter. These costs range from about 3000€ per kilogram for the Dnepr vehicle to over 30000€ per kilogram for the Pegasus. In next table are reported some examples:

Table 8.6 – Cost per kilogram for some launcher.

Launcher	Cost rate [€/kg]
Atlas V	10354
Ariane 5	7853
Delta IV	9799
Falcon 1	4017
PSLV	3983

However, as already said in Chapter 3, some agencies offer launch service. For example SpaceX recently completed an internal study on the feasibility of flying secondary payloads. He also developed prices for flying those secondary payloads, in particular a POD would cost between 150000€ and 245000€ for missions to LEO. Also Spaceflight provides standard payload dimensions and pricing for planning purposes: about 245000€ for 3U CubeSat (separately release) and 445000 for 6U CubeSat (docked release) to LEO.

### Subsection 8.5.3 - Risks assessment

The risks of CubeSat mission usually concern the redundancies absence and the use of COTS components. In the case of this mission, we guarantee the redundancies of all subsystems planning two identical satellites. Furthermore, in case of WiFi communication failure, the formation flying is maintained thanks the ISL redundancy executed by traditional TT&C subsystem. Anyway this is a CubeSat mission, so the absence of satellite subsystems redundancy inevitably causes a high failure probability. Then our attention has been focused only on payload and formation flying critical issues, accepting standard reliability in relation to remaining CubeSat standard subsystems.

# Chapter 9 - Conclusion

## Section 9.1 - Considerations and analysis results

### Subsection 9.1.1 - Formation performances

#### Scale separation in dynamic analysis

Mission analysis, formation control and attitude control subsystems analysis have been separately conducted.

Reference orbit selection and maintenance has still some impact on other two aspects, especially in relation to disturbance minimization, acting on altitude and inclination. Eccentricity would have impact on dynamic and on its estimation, but it is certainly not the case of LEO orbits, which are commonly assumed as near circular orbits. On the other hand, such these considerations are valid for any kind of mission and no particular issues has been individuated in the current case.

#### Relative position and attitude coupling

Attitude and relative position control involves completely different time periods. In fact, time periods larger than few seconds would be possibly implemented in formation control LQR loop. Instead, attitude dynamics, which is even faster than normal, due to low nanosatellites moment of inertia, required higher attitude control bandwidth.

In this mission, there are no critical relative attitude requirements, so each spacecraft controls its own attitude regardless orbit and formation geometry, within limits and performance dictated by nanosatellite class bus.

On the other hand, many formation flying applications, like stereo imaging or optical links, would require tighter pointing and pointing coordination requirements. In this case, even if dynamic separation principle still applies, the problem is much more interlaced.

This is another reason why a 3-axis attitude control has been selected. It offers great flexibility to future mission application.

#### Position determination performance respect to control performance

GPS low mass and power receivers are already available and they are even easy to implement within CubeSat platforms. Even more complex dual frequency receivers can become affordable in the next future. At the moment, single frequency coarse acquisition GPS devices are available and flight proven. And they result capable of sub-meter level accuracy, while implemented with adequate dynamic estimations models. Adequate models means models compliant with relative motion characteristics, in terms of hypothesis and approximations, and it doesn't necessarily mean complex models.

The critical issue resulted indeed to be nanosatellite class thrust capabilities, most of all in terms of minimum achievable thrust level and in thrust modulation concerns.

### **Subsection 9.1.2 - CubeSat integration**

#### **Flexibility**

PCI-104 form factor provides great modularity, but also strong constraints in configuration design. In relation to our case, simply reorienting thruster pointing can become a critical issue. It's not the bus to be adapted to payload, but in some cases it's exactly the opposite.

It's manifest that structural modifications are still possible, but they usually determine additional interface masses and cabling articulations. Moreover, in this manner, the advantage of having a safe and validated structure configuration can be lost and structural analysis becomes necessary again to verify assembly modifications.

#### **Miniaturization**

It's evident that miniaturization issue becomes critical in case of all devices and subsystem which performances are not related to the overall system dimensions. In particular, attitude actuators, like wheel and magnetometers, still obtain good performance compared to their dimension, once they are scaled down and applied to nanosatellite class. On the contrary, sensors, communications system and on board computers have to fulfill the same tasks with reduced resources.

It's not the case of propulsion, as mentioned before. Propulsion incurs in great miniaturizing difficulties. In general, while thrust level decreases, the trend is to adopt completely different technologies, in particular, simpler and reliable technologies, like considered monopropellant, cold gas systems pulsed plasma thrust.

In particular, the major effect of bus miniaturization is not really a subsystem mass and envelope reduction issue, but the crumbled spacecraft power generation capability

#### **Power system design approach**

Even gaining maximum available surface exposed to sun, power budget is always very tight and the design approach must be oriented to a required power management, rather than available power sizing, defining rigid devices within operative modes. As experienced during presented analysis and sizing, multitasking is always to be avoided and a detailed operative modes definition is the key to fulfill mission requirements.

### **Subsection 9.1.3 - Wireless payloads**

Is important to notice that payload power required is very low in respect to the other subsystems, and the spacecraft integration is very easy: data and power supply bus interfaces are PCI-104 format compliant. In case of the selected transceivers had not been CubeSat Bus compliant, a data bus bridge could be foreseen. An ad hoc PCI-104 board has to be considered to integrate the two transceivers in the CubeSat.

#### **Wireless ISL**

The analysis of the wireless ISL reveals versatility and simplicity of use and integration.

Formation flying geometry is not heavily influenced by wireless payloads. The pointing requirements leave freedom of movement in terms of relative angle. The only constraint is confirmed to be a very close, but even affordable, relative separation.

Both WiFi and ZigBee devices, 802.11 and 802.15.4 protocols, have proved to be useful for the purpose. The final choice is oriented on the compromise between power consumption and outdoor range. For bigger formation distances a WAN network can be considered.

The Packet Format dimension is very big in respect of data packet that must be delivered, so the data string can be repeated more times in the same Packet Format to avoid single events upset (SEU) problem. In alternative, a device tantalum shielding can be adopted, also increasing radiation protection.

### **Wireless temperature sensor**

To integrate wireless sensors some expedients must be considered. First of all the transceiver is too big and expensive in terms of power consumption, a smaller device must be used, however an ad hoc transceiver could be commissioned to device supplier.

Another problem, caused by antenna envelope, is sensors placing within the spacecraft. The solution could be to leave vacant the PCI board level in correspondence of sensors to create space for the antenna.

The working frequency band of this payload is coincident to the frequency band of the TT&C transceiver. This problem can be resolved setting the TT&C transceiver frequency in proximity of the upper limit of the band (payload-TT&C frequency spread is 17MHz), otherwise an alternative TT&C frequency band could be required to the supplier.

## **Section 9.2 - Conclusion and next development**

### **Proposed mission**

The project purpose is the feasibility study of a technical demonstrator mission using CubeSat platform. On decides to use a two satellites formation flying to test payload performances at distances up to 1km. The two designed satellites presented in this paper are identically to permit a role exchange and so guarantee a subsystem redundancy.

Observing already flown CubeSat missions with a similar system complexity, it's clear that the system power request is at least the power generated by a 3U solar panel. Deployable panels are not considered to avoid mechanisms, besides they may impose a continuous solar pointing that constrains attitude and propulsion dynamics, so a 3U structure is considered. Subsystems are chosen among

CubeSat standard components to simplify satellite assembly, however in some cases alternative solutions have been considered, in particular reaction wheels and GPS receiver. For these devices and for payload an interface structure to PCI-104 CubeSat standard format must be prepared. The integration of these devices is not easy, especially for the dimensions, because of the CubeSat modularity characteristic and bus standard. Even preferring CubeSat compliant devices, compatibility problems still may occur. For instance, despite it is sold by CubeSat suppliers, also cold gas thruster is not easy to mount in the satellite system because of the particular nozzles geometry.

Selected payload consists on a WiFi transceiver for the ISL and on a temperature measure wireless system. In the first case the proposed device is a SYNAPSE SM700PC1 RF Engine [39] whose dimension, power supply and outdoor range are conform to our satellite features. In particular this device is 24.5×36×5 mm shaped with integrated F-antenna and maximum

power consumption in transmission of 0.695W and calculated outdoor range up to 2400m. The chosen temperature wireless sensors are the SENSEOR TSE AS10 [45], that are 5×5×1.5 mm shaped and so easy to position in the satellite, however their interrogator transceiver is too large in respect to satellite envelope, so as alternative transceiver the Infineon TDA 7255V [45] is selected. It is chip shaped and requires ultra-low power supply.

The selected GPS receiver is the Surrey SSTL SGR-05U [24] Spaceborne, a more reliable and flight proven solution. A wide variety of low cost commercial GPS receivers, with comparable accuracies and even smaller power drains and envelopes, can be selected and tested as additional payload. However, they suffer legal restrictions and their employment in LEO environment has to be negotiated.

Two different propulsion subsystems are considered, PPT thruster or cold gas thruster, and two consequently configurations are developed. In PPT propulsion subsystem configuration, a vacant volume is available for a further payload. This two propulsion possibility have very different impacts in the cost budget: cold gas thruster almost doubles the budget.

Finally, launch is provided by service agencies [54] as secondary payload or can be planned with other CubeSat mission. The cost is about 500 000€ for LEO.

### **Next development**

A fine internal integration configuration and cabling has to be refined. Payloads and reaction wheels host-boards must be implemented and antennas mounting position shall be verified in Electromagnetic Compatibility/Interference (EMC/EMI) simulations. Eventually COTS devices could be tested in radiative environment, but this test is very expensive and it is not recommended. Instead a charging and thermal more detailed analysis shall be implemented.

A 2U reduction can be examined in particular in case of PPT propulsion subsystem. For this solution must take care to power generation reduction, maybe deployed solar panel can be considered. Alternatively a new payload can be added.

As explained in Chapter 2, WR E010 SENSEOR Transceiver [43] is larger than satellite envelope, however an alternative accommodation could be found or a smaller solution could be designed in collaboration with the constructor.

### **Pre-design platforms and modifications**

The pre-design platform concept imposes standard components utilization and that limits the configuration flexibility and system's capabilities. The design of ad hoc components surely permits a volume and mass saving and increases performances with lower power consumption. The mission can be considerably improved with fine propulsion, with suitable configuration, and with deployable panel projected to no constrain attitude and to permit maneuvering freedom. In this way, 3U configuration constraint should be relaxed and the structure can be reduced even to a 2U envelope.

The mission presented in this paper, strongly rely to the possibility of using low cost systems, but the mission can be refined using the expedients already proposed, accepting the related cost increasing and scheduling delay due to engineering services.



# Appendix A -Global Positioning System overview

Global Positioning System (GPS) is the active US Global Navigation Satellite System (GNSS) and consist in a 24 satellites which form a Walker constellation [104]. They are distributed on six 55.5° inclined, equally spaced, 20200 km altitude orbital planes, with four equally spaced spacecraft for each.

A generic spacecraft can receive signal from each satellite within this constellation, measuring the time delay of each signal in Line Of Sight (LOS), due to differences of path. Then position determination is possible, with a triangulation of at least four relative distances from known sources positions (at least three, plus one to determine the common reference time), by a least square minimization.

## Section A.1 - Signal characteristics

Each GPS satellite signal includes its identification, current position, duration of propagated signal and clock information. GPS signals are 1.023 megabits per second (Mbit/s), modulated on two carrier frequencies in L-band, denoted L1 and L2, generated by integer multiplication of  $f_0$  fundamental frequency (10.23 MHz). Encoded with the identification block, there is a 50 Hz navigation block, composed of a set of frames and subframes, containing clock data parameters, which describe the satellite clock and its relation to GPS time, broadcast ephemeris data parameters of transmitting satellite.

Table A.1 - GPS code frequencies [105]

	Frequency [Hz]	Wavelength [m]
<b>Fundamental frequency</b>	$f_0$	10.23
<b>Carrier L1</b>	$2.77 \cdot f_0$	1575.42
<b>Carrier L2</b>	$2.60 \cdot f_0$	1227.60
<b>CA code</b>	$f_0/10$	1.023
<b>P-codes</b>	$f_0$	29.3
<b>Navigation data</b>	$f_0/204600$	50
		~6 · 10 <sup>6</sup>

Signal generation diagram is explained in Figure A.2, as well as navigation message data format in Figure A.1, while Table A.1 summarizes GPS frequencies and their ratios.

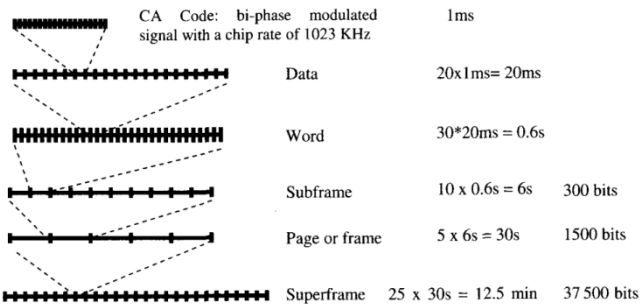


Figure A.1 - GPS data format [105]

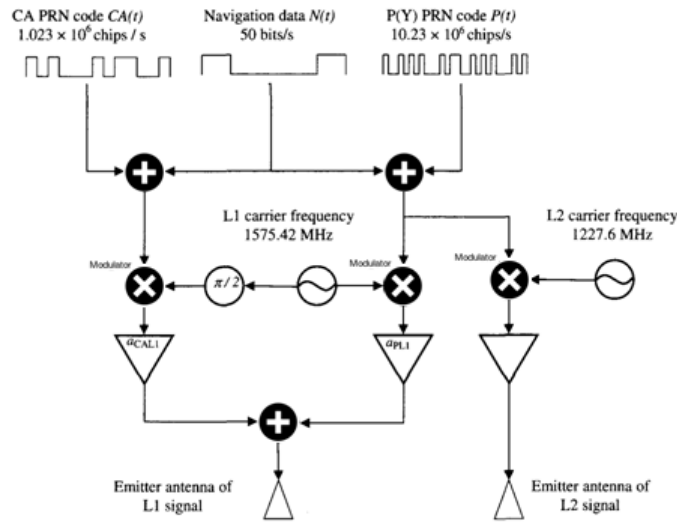


Figure A.2 - GPS signal encoding and modulation [105]

## Section A.1 - Signal processing

There are two main techniques for acquiring time delays from GPS signals: Code Phase method and Carrier phase method.

### Subsection A.1.1 - Code Phase method

The first one typically gathers data via a CA code receiver. Each satellite transmits a unique Pseudo Random Noise (PRN) code, which does not correlate well with any other satellite's PRN code, which means PRN codes are highly orthogonal to one another. This is a form of Code Division Multiple Access (CDMA), which allows the receiver to recognize multiple satellites on the same frequency. A receiver-generated PRN code is correlated to the received signals until a match is obtained. Such this match consist in a peak in time correlation, which identify received signal, and the offset time gives the so called pseudorange between receiver and i-th GPS satellite:

$$P_i = (\tau_{RX} - t_{TX,i})c$$

where  $c$  is speed of light and  $\tau_{RX}$  and  $t_{TX}$  are respectively receiver clock time and transmitter GPS time. The time offset lead to the true range between receiver and emitter if both clock were synchronized. Otherwise, it leads to the pseudorange. Introducing corrections in the receiver clock time, this expression can be related to the true rate.

$$R_i = \sqrt{(x_{RX} - x_{TX,i})^2 + (y_{RX} - y_{TX,i})^2 + (z_{RX} - z_{TX,i})^2}$$

$$R_i = (t_{RX,i} - t_{GPS})c = (\tau_{RX,i} - t_{GPS})c + \Delta t \cdot c$$

That's the reason why a fourth satellite is necessary to obtain four equations and resolve the system in the four unknown: three position components and  $\Delta t$ .

$$\begin{cases} R_1 = (\tau_{RX,1} - t_{GPS})c + \Delta t \cdot c \\ R_2 = (\tau_{RX,2} - t_{GPS})c + \Delta t \cdot c \\ R_3 = (\tau_{RX,3} - t_{GPS})c + \Delta t \cdot c \\ R_4 = (\tau_{RX,4} - t_{GPS})c + \Delta t \cdot c \end{cases}$$

The clear access or coarse acquisition (CA) code is a 1 MHz, 1023 bits PRN code, then repeating every millisecond. Precision or protected code (P-Code), also characterized by a PRN sequence, has the fundamental GPS frequency  $f_0$  and modulates both L1 and L2 carriers. The encrypted P-code which is called Y-code and referred to as the P(Y)-code insures that only authorized users have capability to spoof it. Because of the P-code repeating interval is about 1 week, typical GPS receivers lock first on to the CA code before locking onto the P-code, since there is only 1 ms to search for accurate time information.

### Subsection A.1.2 - Carrier Phase method

Using Carrier phase method, sub-meter accuracy can be achieved for position determination, measuring the phase difference between received carrier signal and receiver-generated carrier signal. The capability of detecting phases at degree level lead to distance measurements of about fractions of a 19 cm wavelength:

At this aim, the receiver must know the exact number of cycles along the path,  $N$ . To approximate the number of these cycles, the code phase method can be initially used, and then the carrier phase method is switched on to determine the actual cycles that identify the timing pulse. Moreover, this technique requires constant view of at least four satellites, avoiding continuous recalculation of cycles for different ones. The integer ambiguity can also be eliminated by making two different measures at subsequent times, then taking the difference.

## Section A.2 - Coverage

GPS system was designed for low-altitude terrestrial application, then constellation architecture allows any user on the Earth to have from five to eight satellites in LOS, and it is optimized to uniform as far as possible medium visible satellite number at any latitude and longitude. Simulations conducted with AGI software Satellite Tool Kit, shows, as expected, that within LEO typical altitudes, GPS satellites visibility change very little respect to Earth ground conditions:

For a LEO receiver, the maximum duration of continuous visibility of a single GPS signal is in the order of 45 min, before the transmitter become shadowed from the Earth.

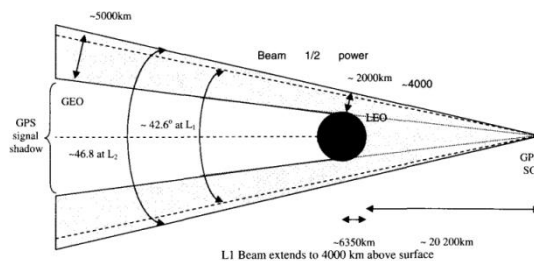


Figure A.3 - Main lobe coverage of GPS signal [105]

The transmission of a GPS signal is pointed towards the center of the Earth and the main beam is  $42.6^\circ$  and  $46.8^\circ$  wide, respectively at L1 and L2 carrier frequencies, as shown in Figure A.3. Thereby, each receiver that is in a LEO orbit and has a GPS satellite in LOS, is automatically within the transmission beam. That's not true for higher altitudes, such MEO, HEO and GEO, which are not in our interest, in which side lobes becomes useful to extend this coverage.

# Appendix B - Notions of relative position dynamics and adopted conventions

## Section B.1 - Relative rotating frame

### Subsection B.1.1 - Cartesian coordinates LVLH

Relative motion in a close proximity formation is generally modeled using a projection of equation of motion in the Local Vertical, Local Horizontal (LVLH) relative frame centered on a Chief spacecraft or in a reference orbit, also called Euler-Hill frame (EH). Rotation matrix from inertial to EH frame is:

$$\mathbf{T}_{EH}^{IN} = \begin{bmatrix} \hat{\mathbf{r}}_0^{IN} & (\hat{\mathbf{h}}_0^{IN} \times \hat{\mathbf{r}}_0^{IN}) & \hat{\mathbf{h}}_0^{IN} \end{bmatrix}^T$$

where  $\mathbf{r}_0$  and  $\mathbf{h}_0$  are respectively reference position and angular momentum vectors in inertial coordinates. This is not an inertial reference, so absolute  $\mathbf{r}$  and relative  $\boldsymbol{\rho}$  position vectors, and their derivatives are related as follows:

$$\begin{aligned} \boldsymbol{\rho}^{EH} &= [x \quad y \quad z]^T \\ \mathbf{r}^{EH} &= \mathbf{r}_0^{EH} + \boldsymbol{\rho}^{EH} \\ \dot{\mathbf{r}}^{EH} &= \dot{\mathbf{r}}_0^{EH} + \dot{\boldsymbol{\rho}}^{EH} + \boldsymbol{\omega}_0^{EH} \times \boldsymbol{\rho}^{EH} \\ \ddot{\mathbf{r}}^{EH} &= \ddot{\mathbf{r}}_0^{EH} + \ddot{\boldsymbol{\rho}}^{EH} + \dot{\boldsymbol{\omega}}_0^{EH} \times \boldsymbol{\rho}^{EH} + \boldsymbol{\omega}_0^{EH} \times (\boldsymbol{\omega}_0^{EH} \times \boldsymbol{\rho}^{EH}) + 2\boldsymbol{\omega}_0^{EH} \times \dot{\boldsymbol{\rho}}^{EH} \end{aligned}$$

where  $\boldsymbol{\omega}_0 = \mathbf{h}_0 / r_0$  is reference orbit angular rate. From now on, we assume the EH frame reference implied. For a general reference orbit, as we refer to a chief perturbed motion, angular rate and its derivative can also be evaluated from its state vector as:

$$\begin{aligned} \boldsymbol{\omega} &= \frac{\mathbf{r}_0 \times \dot{\mathbf{r}}_0}{r_0^2} \\ \dot{\boldsymbol{\omega}} &= \frac{\mathbf{r}_0 \times \ddot{\mathbf{r}}_0}{r_0^2} - 2 \frac{(\mathbf{r}_0 \times \dot{\mathbf{r}}_0) \mathbf{r}_0 \cdot \ddot{\mathbf{r}}_0}{r_0^4} \end{aligned}$$

### Subsection B.1.2 - Curvilinear coordinates

In several applications of close orbit operation, the assumption of relative small separation respect to orbit radius justify first order linear approximations in EH Cartesian frame, such as first order approximation of gravity gradient. These errors can be reduced if a curvilinear coordinate system is used, as depicted in Figure A.4, defining in-track and cross-track distance as arc-lengths:

$$\boldsymbol{\rho}^{EHcurv} = [\delta r \quad r_0 \alpha_y \quad r_0 \alpha_z]^T$$

- $\delta r$  as the difference between deputy and chief radii.
- $\alpha_y$  as the angle between the projection of the deputy radius vector in the chief's orbit plane and the chief radius vector.
- $\alpha_z$  as the angle between the deputy radius vector and its projection in the chief's orbit plane.



$$\ddot{\mathbf{r}}_0 = -\frac{\mu}{|\mathbf{r}_0|^3} \mathbf{r}_0 \quad \ddot{\mathbf{r}} = -\frac{\mu}{|\mathbf{r}|^3} \mathbf{r}$$

$$\ddot{\mathbf{p}} = -\frac{\mu}{|\mathbf{r}_0 + \boldsymbol{\rho}|^3} (\mathbf{r}_0 + \boldsymbol{\rho}) + \frac{\mu}{r_0^3} \mathbf{r}_0 - \dot{\boldsymbol{\omega}} \times \boldsymbol{\rho} - \boldsymbol{\omega} \times (\boldsymbol{\omega} \times \boldsymbol{\rho}) - 2\boldsymbol{\omega} \times \dot{\boldsymbol{\rho}}$$

That means a system of three 2-order scalar differential equation:

$$\begin{cases} \ddot{x} = 2\dot{\theta}_0 \dot{y} + \ddot{\theta}_0 y + \dot{\theta}_0^2 x - \mu(r_0 + x) \left( (r_0 + x)^2 + y^2 + z^2 \right)^{-3/2} + \frac{\mu}{r_0^2} \\ \ddot{y} = -2\dot{\theta}_0 \dot{x} - \ddot{\theta}_0 x + \dot{\theta}_0^2 y - \mu y \left( (r_0 + x)^2 + y^2 + z^2 \right)^{-3/2} \\ \ddot{z} = -\mu z \left( (r_0 + x)^2 + y^2 + z^2 \right)^{-3/2} \end{cases}$$

Integration of the equations above still produces the same results that differentiating two independent state propagations in the inertial frame, both for chief and for deputy spacecraft.

### Circular orbit approximation

In most cases and applications of interest, even in complex models [16],[106], reference orbit is approximated as circular:

$$\mathbf{r}_0 = [a_0 \quad 0 \quad 0]^T$$

$$\dot{\boldsymbol{\omega}} = \bar{\mathbf{0}}$$

$$\boldsymbol{\omega} = [0 \quad 0 \quad n_0]^T = \left[ 0 \quad 0 \quad \sqrt{\mu/a_0^3} \right]^T$$

### First order gravitational acceleration approximation

Small relative distance respect to chief orbit radius suggests a simplification in the gravitational acceleration terms, expanding in Taylor series about the origin the terms:

$$\begin{cases} \mu(r_0 + x) \left( (r_0 + x)^2 + y^2 + z^2 \right)^{-3/2} \simeq n_0^2 (2x - a_0) \\ \mu y \left( (r_0 + x)^2 + y^2 + z^2 \right)^{-3/2} \simeq -n_0^2 y \\ \mu z \left( (r_0 + x)^2 + y^2 + z^2 \right)^{-3/2} \simeq -n_0^2 z \end{cases}$$

Accommodating higher-order nonlinearities, formulation better approximates gravitational acceleration and it's a valid alternative to the curvilinear coordinates approach in first-order equations set, but it becomes not linear, so it cannot be implemented in a linear control theory.

### Subsection B.2.2 - Hill-Clohessey-Wiltshire equations HCW

Under circular reference orbit assumption and first order approximation of gravity gradient, we have the well known Hill- Chohessy-Withshire differential equations:

$$\begin{cases} \ddot{x} = 2n\dot{y} + 3n_0^2 x \\ \ddot{y} = -2n_0 \dot{x} \\ \ddot{z} = -n_0^2 z \end{cases}$$

which can be analytically integrated to obtain:

$$\begin{aligned} x(t) &= \left[ 4x(0) + \frac{2\dot{y}(0)}{n_0} \right] + \frac{\dot{x}(0)}{n_0} \sin(n_0 t) - \left[ 3x(0) + \frac{2\dot{y}(0)}{n_0} \right] \cos(n_0 t) \\ y(t) &= [6n_0 x(0) + 3\dot{y}(0)]t + \left[ y(0) + \frac{2\dot{x}(0)}{n_0} \right] + \left[ 6x(0) + \frac{4\dot{y}(0)}{n_0} \right] \sin(n_0 t) + \frac{2\dot{x}(0)}{n_0} \cos(n_0 t) \\ z(t) &= \frac{\dot{z}(0)}{n_0} \sin(n_0 t) + z(0) \cos(n_0 t) \\ \dot{x}(t) &= \dot{x}(0) \cos(n_0 t) + [3n_0 x(0) + 2\dot{y}(0)] \sin(n_0 t) \\ \dot{y}(t) &= -[6n_0 x(0) + 3\dot{y}(0)] + [6n_0 x(0) + 4\dot{y}(0)] \cos(n_0 t) - 2\dot{x}(0) \sin(n_0 t) \\ \dot{z}(t) &= \dot{z}(0) \cos(n_0 t) - n_0 z(0) \sin(n_0 t) \end{aligned}$$

that is an independent periodic bounded out of plane motion combined to an epicyclical in-plane motion. It becomes also a bounded periodic motion, applying the following condition:

$$\dot{y}(0) + 2nx(0) = 0$$

This condition is called commensurability condition. It is a constraint equation that ensures same orbital periods between chief and deputy orbit, which is the minimal necessary condition to obtain a bounded relative motion, and it traduces itself in a semiaxis condition, or equivalently, an energy condition.

The use of Cartesian rotating coordinates system results in undesirable errors in the solution due to non-linear terms. These effects are reduced using a curvilinear system, and then the HCW equation system would become:

$$\begin{cases} \delta \ddot{r} = 2r_0 n_0 \dot{\alpha}_y + 3n_0^2 \delta r \\ r_0 \ddot{\alpha}_y = -2n_0 \delta \dot{r} \\ \ddot{\alpha}_z = -n_0^2 \alpha_z \end{cases}$$

Alternatively, the Cartesian formulation can be still applied without changes, if x, y and z simply refer to a curvilinear coordinate system.

### Subsection B.2.3 - Tshauner-Hempel equations

Another simple and efficient model, which takes in account also eccentricity, is the Lawden and Tshauner-Hempel (TH) equations [16]:

$$\begin{cases} \ddot{x} = 3n_0^2 x / (1 - e_0 \cos(\theta_0(t))) + 2n_0 \dot{y} \\ \ddot{y} = -2n_0 \dot{x} \\ \ddot{z} = -n_0^2 z \end{cases}$$

which is still a linear model, but it's time variant even in case of keplerian motion, because they are function of true anomaly  $\theta$ .



## Section B.3 - Perturbed motion

Perturbed motion can be obtained adding disturbance accelerations  $\mathbf{d}$ , defined in EH frame depending on applying force models. It's possible to treat differential disturbance effect as linear, respect to a nominal trajectory, generally obtaining a time-varying state-space model. J2 differential disturbance are function of both chief and deputy orbital parameters.

### Subsection B.3.1 - Gauss variational equation

For a generic orbit, defined by its classical keplerian orbital parameters, effects of perturbation forces in the orbiting frame (LVLH) are provided in a wide literature [50] [107].

$$\begin{aligned}\dot{a} &= \frac{2a^2 e \sin \theta}{h} d_x + \frac{2a^2 p}{hr} d_y \\ \dot{e} &= \frac{p \sin \theta}{h} d_x + \frac{p \cos \theta + r(e + \cos \theta)}{h} d_y \\ \dot{\Omega} &= \frac{r \sin(\theta + \omega)}{h \sin i} d_z \\ \dot{i} &= \frac{r \cos(\theta + \omega)}{h} d_z \\ \dot{\omega} &= -\frac{p \cos \theta}{he} d_x + \frac{\sin \theta (r + p)}{he} d_y - \dot{\Omega} \cos(i)\end{aligned}$$

$$\dot{M}_0 = \dot{M} - \sqrt{\frac{\mu}{a^3}} = -\frac{r(2e - \cos(\theta) - e \cdot \cos^2(\theta))}{e\sqrt{\mu a}} d_x - \frac{r \sin(\theta)(2 + e \cdot \cos(\theta))}{e\sqrt{\mu a}} d_y$$

which can be averaged, integrating them on an orbit period, to remove true anomaly dependence and then time-dependence.

### Subsection B.3.2 - J2 effect

In LEO, major disturbance effects derive from Earth oblateness (gravitational potential J2 harmonic), that in the LVLH frame produces:

$$\mathbf{d}_{J2} = \frac{3\mu J_2 R_e^2}{2r^4} \begin{bmatrix} (1 - 3\sin^2(\theta + \omega)\sin^2 i) \\ \sin 2(\theta + \omega)\sin^2 i \\ \sin(\theta + \omega)\sin 2i \end{bmatrix}$$

Averaged orbital parameter derivative are:

$$\begin{aligned}\bar{\dot{a}} &= \bar{\dot{e}} = \bar{\dot{i}} = 0 \\ \bar{\dot{\Omega}} &= -\frac{3}{2} J_2 \left( \frac{R_e}{\bar{p}} \right)^2 \bar{n} \cos \bar{i} \\ \bar{\dot{\omega}} &= \frac{3}{4} J_2 \left( \frac{R_e}{\bar{p}} \right)^2 \bar{n} (5 \cos^2 \bar{i} - 1)\end{aligned}$$

$$\bar{M}_0 = \frac{3}{4} J_2 \left( \frac{R_e}{\bar{p}} \right)^2 \bar{n} \eta (3 \cos^2 \bar{i} - 1)$$

where  $\bar{\eta}^2 = 1 - \bar{e}^2$ . Such this disturbance is a conservative force by assumption, so it cannot vary orbit semiaxis, in the long term, causing only periodic effects on relative motion, in case of eccentricity, chief and deputy orbit semiaxis and inclination are the same, but it produces secular relative drift where not. In addition, perigee different rotation rates causes in-plane and cross track frequencies, equal in the unperturbed relative bounded motion, to no longer be equal.

### Subsection 9.2.1 - Commensurability condition

Despite unperturbed case, commensurability condition doesn't ensure a bounded motion, but it only negates secular in-track drift. In case of exact relative motion differential equations, simply projected in LVLH frame, it yields (Energy-matching condition):

$$a_1 = a_0 \iff \varepsilon_1 = \varepsilon_0$$

$$\frac{1}{2} \left( (\dot{x} - \dot{\theta}_0 y + \dot{r}_0)^2 + (\dot{y} + \dot{\theta}_0 (x + r_0))^2 + \dot{z}^2 \right) - \frac{\mu}{\sqrt{(r_0 + x)^2 + y^2 + z^2}} = -\frac{\mu}{2a_0}$$

In presence of  $J_2$  perturbation, the semiaxis matching condition can be expressed, adopting assertion presented in [16] based on differential orbital parameters, as follows:

$$\delta a = \frac{1}{2} J_2 a_0 \left( \frac{R_e}{a_0} \right)^2 \frac{3\eta_0 + 4}{\eta_0^5} \left( (1 - 3 \cos^2 i_0) \delta \eta - (\eta_0 \sin 2i_0) \delta i \right) = 0$$

$J_2$  perturbation provokes the in-plane and out-of plane motion to have different frequency, as discussed in a wide literature (see [108] [109]), even if no in-track drift condition is satisfied. Imposing the following constraints, in addition to differential semiaxis matching condition, these frequencies are equal and a bounded periodic motion in relative frame is obtained:

$$\delta \eta = \frac{5\eta_0 \sin 2i_0}{4(1 - 5 \cos^2 i_0)} \delta i$$

$$\delta \eta = -\frac{\eta_0 \tan i_0}{4} \delta i$$

That means that both  $\delta \eta$  and  $\delta i$  have to be null to satisfy both equation. To negate  $J_2$  perturbation, the only solution is to set:

$$\delta a = \delta e = \delta i = 0$$

that is the case of a leader-follower formation, with same orbit shape and inclination. Either  $\delta M$  or  $\delta \omega$  can be manipulated to obtain bounded in-plane motion, while, choosing  $\delta \Omega$ , either in-track or pendulum configuration still can be obtained.

# Appendix C - ADM-Aeolus PoliMi communication accesses

In this appendix the results about the ground station positioned in PoliMi campus are reported.

Table A.2 – CubeSat–Ground station PoliMi access.

Access	Start Time (UTCG)				Stop Time (UTCG)				Duration [s]
1	1	Jul	2014	03:59:58	1	Jul	2014	04:09:29	570.615
2	1	Jul	2014	05:32:00	1	Jul	2014	05:41:28	568.221
3	1	Jul	2014	16:45:48	1	Jul	2014	16:54:56	547.979
4	1	Jul	2014	18:17:35	1	Jul	2014	18:27:21	585.202
5	2	Jul	2014	03:15:23	2	Jul	2014	03:22:13	409.897
6	2	Jul	2014	04:45:04	2	Jul	2014	04:55:22	617.321
7	2	Jul	2014	06:19:44	2	Jul	2014	06:25:50	366.388
8	2	Jul	2014	16:01:01	2	Jul	2014	16:05:51	289.771
9	2	Jul	2014	17:30:58	2	Jul	2014	17:41:15	616.284
10	2	Jul	2014	19:03:52	2	Jul	2014	19:11:23	451.411
11	3	Jul	2014	03:59:07	3	Jul	2014	04:08:35	567.877
12	3	Jul	2014	05:31:05	3	Jul	2014	05:40:34	568.831
13	3	Jul	2014	16:44:47	3	Jul	2014	16:53:51	544.94
14	3	Jul	2014	18:16:31	3	Jul	2014	18:26:18	586.447
15	4	Jul	2014	03:14:17	4	Jul	2014	03:20:59	402.734
16	4	Jul	2014	04:43:53	4	Jul	2014	04:54:09	616.189
17	4	Jul	2014	06:18:27	4	Jul	2014	06:24:40	373.113
18	4	Jul	2014	15:59:46	4	Jul	2014	16:04:22	275.393
19	4	Jul	2014	17:29:37	4	Jul	2014	17:39:52	615.499
20	4	Jul	2014	19:02:27	4	Jul	2014	19:10:04	456.58
21	5	Jul	2014	03:57:39	5	Jul	2014	04:07:03	563.806
22	5	Jul	2014	05:29:32	5	Jul	2014	05:39:03	570.875
23	5	Jul	2014	16:43:08	5	Jul	2014	16:52:08	539.949
24	5	Jul	2014	18:14:49	5	Jul	2014	18:24:38	588.685
25	6	Jul	2014	03:12:35	6	Jul	2014	03:19:07	391.93
26	6	Jul	2014	04:42:04	6	Jul	2014	04:52:19	614.972
27	6	Jul	2014	06:16:29	6	Jul	2014	06:22:53	384.232
28	6	Jul	2014	15:57:58	6	Jul	2014	16:02:10	252.043
29	6	Jul	2014	17:27:37	6	Jul	2014	17:37:52	614.354
30	6	Jul	2014	19:00:23	6	Jul	2014	19:08:08	464.317
31	7	Jul	2014	03:55:35	7	Jul	2014	04:04:53	558.258
32	7	Jul	2014	05:27:20	7	Jul	2014	05:36:54	574.2
33	7	Jul	2014	16:40:52	7	Jul	2014	16:49:45	532.745
34	7	Jul	2014	18:12:29	7	Jul	2014	18:22:20	591.778
35	7	Jul	2014	19:47:48	7	Jul	2014	19:48:53	65.882
36	8	Jul	2014	03:10:17	8	Jul	2014	03:16:34	376.993

Access	Start Time (UTCG)				Stop Time (UTCG)				Duration [s]
37	8	Jul	2014	04:39:37	8	Jul	2014	04:49:50	613.542
38	8	Jul	2014	06:13:50	8	Jul	2014	06:20:29	399.119
39	8	Jul	2014	15:55:37	8	Jul	2014	15:59:13	216.119
40	8	Jul	2014	17:25:00	8	Jul	2014	17:35:12	612.673
41	8	Jul	2014	18:57:41	8	Jul	2014	19:05:35	474.356
42	9	Jul	2014	03:52:53	9	Jul	2014	04:02:04	551.019
43	9	Jul	2014	05:24:30	9	Jul	2014	05:34:08	578.585
44	9	Jul	2014	16:37:59	9	Jul	2014	16:46:42	522.947
45	9	Jul	2014	18:09:30	9	Jul	2014	18:19:25	595.541
46	9	Jul	2014	19:44:14	9	Jul	2014	19:46:34	140.014

Table A.3 – CubeSat–Ground station PoliMi access statistic.

Statistics		Start	Stop	Duration
Min Duration	35	7 Jul 2014 19:47:48	7 Jul 2014 19:48:53	65.882
Max Duration	6	2 Jul 2014 04:45:04	2 Jul 2014 04:55:22	617.321
Mean Duration	<b>487.383</b>			
Total Duration	<b>22419.63</b>			

# Bibliography

- [1] I. Bekey, *Advanced Space System Concepts and Technologies: 2010-2030+*, The Aerospace Press, 2003.
- [2] T. Vladimirova, C. P. Bridges, J. R. Paul, S. A. Malik and M. N. Sweeting, "Space-Based Wireless Sensor Networks: Design Issues," 2010.
- [3] CCSDS, *Wireless network communications overview for space mission operations*, December 2010.
- [4] I. Arruego, H. Guerrero, S. Rodríguez, J. Martínez-Oter, J. J. Jiménez, J. A. Domínguez, A. Martín-Ortega, J. R. de Mingo and J. Rivas, "Optical Wireless Links for Intra-Satellite communications Links for Intra-Satellite Communications," 2009.
- [5] "NANOSAT 1," [Online]. Available: <http://www.inta.es/programasaltatecnologia.aspx?Id=1&SubId=2>.
- [6] "Lift-off for Foton microgravity mission," [Online]. Available: [http://www.esa.int/esaCP/SEMQDB13J6F\\_index\\_0.html](http://www.esa.int/esaCP/SEMQDB13J6F_index_0.html).
- [7] V. Aragón, Á. García, R. Amaro, C. Martínez and F. Sarmiento, "OPTOS Communications: A High Performance Solution," 2010.
- [8] [Online]. Available: <http://nuts.cubesat.no/>.
- [9] S. Kenyon and C. Bridges, "STRAND-1: USE OF A \$500 SMARTPHONE AS THE CENTRAL AVIONICS OF A NANOSATELLITE," 2011. [Online]. Available: <http://www.sstl.co.uk/Divisions/Earth-Observation---Science/Science---Exploration/STRaND-nanosatellite/IAC11-Kenyon-STRaND-1-B4-6B-8>.
- [10] Surrey Satellite Technology Ltd, "Science & Exploration - STRaND Nanosatellite," [Online]. Available: <http://www.sstl.co.uk/divisions/earth-observation-science/science-missions/strand-nanosatellite>.
- [11] [Online]. Available: <http://www.delfic3.nl/>.
- [12] T. Vladimirova, C. P. Bridges, G. Prassinis, X. Wu, K. Sidibeh, D. J. Barnhart, A.-H. Jallad, J. R. Paul, V. Lappas, A. Baker, K. Maynard and R. Magness, "Characterising Wireless Sensor Motes for Space Applications," 2007.
- [13] [Online]. Available: <http://www.senseor.com/>.
- [14] S. Y. F. Leung, O. Montenbruck and B. Bruninga, "Hot Start of GPS Receivers for LEO

- Microsatellites". *Department of Aerospace Engineering, Royal Melbourne Institute of Technology University (RMIT)*.
- [15] B. W. Parkinson and J. J. Spikler, *Global positioning System: Theory and Application*, American Institute of Aeronautics and Astronautics, 1996.
- [16] T. K. Alfriend, *Spacecraft Formation Flying: Dynamics Control and Navigation*, Elsevier Astrodynamics Series, 2010.
- [17] "PRISMA Satellites," Swedish National Space Board, [Online]. Available: <http://www.prismasatellites.se/about-prisma.aspx>.
- [18] "PRISMA FFIORD, Technology mission experimenting the Formation Flying," [Online]. Available: <http://smc.cnes.fr/PRISMA/index.htm>. [Accessed september 2011].
- [19] R. J. Carpenter, *Decentralized Control of Satellite Formations*, *International Journal of Robust and Nonlinear Control*, 2002.
- [20] S. D'Amico and O. Montenbruck, "Differential GPS: an Enabling Technology for Formation Flying Satellites," 2009.
- [21] The University of Texas, Department of Aerospace Engineering and Engineering Mechanics, "FASTRAC, the University of Texas Nanosatellite Program," [Online]. Available: <http://fastrac.ae.utexas.edu/>.
- [22] Massachusetts Institute of Technology, "Formation Flying Experiments on the Orion-Emerald Mission," [Online]. Available: [http://web.mit.edu/people/jhow/orion/space2001\\_latest2.pdf](http://web.mit.edu/people/jhow/orion/space2001_latest2.pdf).
- [23] "CANADIAN ADVANCED NANOSPACE EXPERIMENT," [Online]. Available: <http://www.utias-sfl.net/nanosatellites/CanXProgram.html>.
- [24] Surrey Satellite Technology Limited, "SGR-05U - Spaceborne GPS Receiver," [Online]. Available: <http://www.sst-us.com/shop/subsystems/gps/sgr-05u---space-gps-receiver>.
- [25] Deutsches Zentrum für Luft- und Raumfahrt e.V., "Phoenix Spaceborne GPS Receiver," [Online]. Available: <http://www.weblab.dlr.de/rbrt/GpsNav/Phoenix/Phoenix.html>.
- [26] O. Montenbruck, M. Garcia-Fernandez and J. Williams, "Performance comparison of semicodeless GPS receivers for LEO satellites," *DLR, German Space Operations Center*, 2006.
- [27] Inc., NovAtel, "OEM4-G2L datasheet," [Online]. Available: <http://webone.novatel.ca/assets/Documents/Papers/oem4g2l.pdf>.

- [28] [Online]. Available: <http://rax.engin.umich.edu/>.
- [29] Handbook of Wireless Local Area Networks, Mohammad Ilyas and Syed Ahson CRC Press 2005, 2005.
- [30] Handbook of Sensor Networks, Edited by Mohammad Ilyas and Imad Mahgoub CRC Press 2005, 2005.
- [31] M. Ergen, *IEEE 802.11 Tutorial*, June 2002.
- [32] "RF300PD1 Datasheet," [Online]. Available: <http://www.synapse-wireless.com/documents/products/Synapse-RF300xx-Engine-Data-Sheet.pdf>.
- [33] "TelosB Datasheet," [Online]. Available: [http://www.willow.co.uk/TelosB\\_Datasheet.pdf](http://www.willow.co.uk/TelosB_Datasheet.pdf).
- [34] "CC2420 Datasheet," [Online]. Available: <http://www.ti.com/lit/ds/symlink/cc2420.pdf>.
- [35] "SM200P81 Datasheet," [Online]. Available: <http://www.synapse-wireless.com/documents/products/Synapse-RF-Engine-RF200P81-SM200P81-Data-Sheet.pdf>.
- [36] "JN5 148-001 Datasheet," [Online]. Available: [http://www.jennic.com/files/product\\_briefs/JN-DS-JN5148MO-1v4.pdf](http://www.jennic.com/files/product_briefs/JN-DS-JN5148MO-1v4.pdf).
- [37] "WiBear Datasheet," [Online]. Available: [http://www.lesswire.com/uploads/media/WiBear\\_engl\\_v1-12.pdf](http://www.lesswire.com/uploads/media/WiBear_engl_v1-12.pdf).
- [38] "TiWi-R2 Datasheet," [Online]. Available: [http://www.lsr.com/downloads/tiwi\\_r2/TiWi\\_R2\\_Datasheet.pdf](http://www.lsr.com/downloads/tiwi_r2/TiWi_R2_Datasheet.pdf).
- [39] "SM700PC1 Datasheet," [Online]. Available: <http://www.synapse-wireless.com/documents/products/Synapse-SM700xx-Engine-Data-Sheet.pdf>.
- [40] "XG880MU Datasheet," [Online]. Available: <http://www.zcomax.com/embedded/XG-880MU/XG-880MUSpec.pdf>.
- [41] "HW86052 Datasheet," [Online]. Available: <http://www.hoef-wessel.com/en/skeye/products/radio-modules-wlandectfhss/hw-86052-ieee-80211bg-wlan-module/>.
- [42] "GS1011M Datasheet," [Online]. Available: <http://dlnmh9ip6v2uc.cloudfront.net/datasheets/BreakoutBoards/GS1011M%20Datasheet%20ver%201.0.pdf>.

- [43] "WR E010 Datasheet," [Online]. Available:  
[http://www.sensor.com/images/stories/download/Brochures/SENSeOR\\_WRE010.pdf](http://www.sensor.com/images/stories/download/Brochures/SENSeOR_WRE010.pdf).
- [44] "MICRF620 Datasheet," [Online]. Available:  
<http://www.micrel.com/RadioWire/micrf620.pdf#page=1>.
- [45] "TDA 7255V Datasheet," [Online]. Available:  
[http://www.infineon.com/dgdl/TDA7255V\\_DS\\_V1.1.pdf?folderId=db3a3043191a246301192dd3ee2c2ae4&fileId=db3a30432a7fedfc012a84f991c92c1a](http://www.infineon.com/dgdl/TDA7255V_DS_V1.1.pdf?folderId=db3a3043191a246301192dd3ee2c2ae4&fileId=db3a30432a7fedfc012a84f991c92c1a).
- [46] "RFM12B Datasheet," [Online]. Available:  
<http://www.hoperf.com/upload/rf/RFM12B.pdf>.
- [47] "CC1100 Datasheet," [Online]. Available:  
<http://www.ti.com/general/docs/lit/getliterature.tsp?genericPartNumber=cc1100&fileType=pdf>.
- [48] "SRW1011 Datasheet," [Online]. Available:  
<http://www.emartee.com/Attachment.php?name=42090.pdf>.
- [49] "ANT-433-SP Datasheet," [Online]. Available:  
[http://www.rsdoBrasil.com.br/produtos\\_arquivos/926b92f035e9212526584ee20bbfca73\\_25112010151107\\_.pdf](http://www.rsdoBrasil.com.br/produtos_arquivos/926b92f035e9212526584ee20bbfca73_25112010151107_.pdf).
- [50] G. Mengali and A. A. Quarta, *Fondamenti di Meccanica del Volo Spaziale, Plus*, Pisa University Press, 2006.
- [51] J. Foust, "New opportunities for smallsat launches," 22 August 2011. [Online]. Available: <http://www.thespacereview.com/article/1913/1>.
- [52] [Online]. Available: <http://www.spaceflightservices.com/MHome.php>.
- [53] Prof. Jordi Puig-Suari, Prof. Clark Turner, Prof. Robert J. Twiggs, "CubeSat: The Development and Launch Support Infrastructure for Eighteen Different Satellite Customers on One Launch," [Online]. Available:  
[http://zaehring.de/downloads/cubesat\\_standard.pdf](http://zaehring.de/downloads/cubesat_standard.pdf).
- [54] "SpaceFlight Services - Secondary Payload Planners Guide," [Online]. Available:  
[http://spaceflightservices.com/DocFiles/SpaceFlight\\_Services\\_Secondary\\_PL\\_Planner\\_guide.pdf](http://spaceflightservices.com/DocFiles/SpaceFlight_Services_Secondary_PL_Planner_guide.pdf).
- [55] "ESA bulletin 149," [Online]. Available:  
<http://esamultimedia.esa.int/multimedia/publications/ESA-Bulletin-149/pageflip.html>.
- [56] [Online]. Available: <http://www.gaussteam.com/index.php>.



- [57] Eurockot Launch Service, "Rockot User Guide," [Online]. Available: [http://www.eurockot.com/joomla/index.php?option=com\\_content&view=article&id=20040718&Itemid=102](http://www.eurockot.com/joomla/index.php?option=com_content&view=article&id=20040718&Itemid=102).
- [58] "SPENVIS, the Space Environment Information System," ESA, [Online]. Available: <http://www.spennis.oma.be/>. [Accessed september 2011].
- [59] S. Sen, E. Schofield, J. S. O'Dell, L. Deka and S. Pillay, "The Development of a Multifunctional Composite Material for Use in Human Space Exploration Beyond Low-Earth Orbit," *JOM*, vol. January, 2009.
- [60] Clyde Space, "CubeSat solar panel Dasheet," [Online]. Available: <http://www.clyde-space.com/documents/2410>.
- [61] Q. He and H. Chao, "Dynamics and Control of Satellite Formation Flying Based on Relative Orbit Elements" *.AIAA Guidance, Navigation and Control Conference and Exhibit*.
- [62] H. Schaub, S. R. Vadali, J. L. Ju and K. T. Alfriend, "Spacecraft Formation Flying Control using Mean Orbit Elements" *.Journal of the Astronautical Sciences*.
- [63] S. S. Vaddi, K. T. Alfriend, S. R. Vadali and P. Sengupta, "Formation Establishment and Reconfiguration Using Impulsive Control" *.Journal of Guidance, Control, and Dynamics*.
- [64] "CubeSatShop," ISIS - Innovative Solutions In Space, [Online]. Available: <http://www.cubesatshop.com/>. [Accessed september 2011].
- [65] S. R. Starin, R. K. Yedavalli and A. G. Sparks, "Design of a LQR controller of reduced inputs for multiple spacecraft formation flying," *American Control Conference*, 2001.
- [66] S. D'Amico and O. Montenbruck, "Proximity Operations of Formation-Flying Spacecraft Using an Eccentricity/Inclination Vector," *Journal of Guidance, Dynamics and Control*, 2006.
- [67] Mathworks, "Matlab support resources," [Online]. Available: <http://www.mathworks.it/support/product/product.html?product=ML>.
- [68] I. Analytical Graphics, "STK Desktop Application," [Online]. Available: <http://www.agi.com/product-explorer/>.
- [69] N. Inc., "NovAtel GNSS Products," [Online]. Available: <http://www.novatel.com/products/products-overviewnovatel-gnss-products/>.
- [70] O. Montenbruck, M. Markgraf, A. Helm and M. Garcia-Fernandez, "Gps for

- Microsatellites, Status and Perspectives," *DLR, German Space Operations Center*, 2007.
- [71] R. Brown and P. Wang, *Introduction to random signals and Applied Kalman Filtering*, Wiley, 1997.
- [72] M. Sabatini, F. Reali and G. Palmerini, "Autonomous State Estimation in Formation Flight," *Università di Roma La Sapienza, Dipartimento di Ingegneria Aerospaziale e Astronautica*, 2006.
- [73] F. Busse, "Precise Formation-State Estimation in Low Earth Orbit Using Carrier Differential GPS," *Stanford University, Department of Aeronautics and Astronautics*, 2003.
- [74] S. A. Schweighart and R. J. Sedwick, "High-Fidelity Linearized J2 Model for Satellite Formation Flight," *Massachusetts Institute of Technology, Cambridge*, 2002.
- [75] S. Schweighart, *Development and Analysis of a High Fidelity Linearized J2 Model for Satellite Formation Flying*, vol. M.S. Thesis, Massachusetts Institute of Technology, Dept. Aeronautics and Astronautics, 2001.
- [76] M. Sabatini and G. B. Palmerini, "Linearized Formation-Flying Dynamics in a Perturbed Orbital Environment," *Università di Roma La Sapienza, Dipartimento di Ingegneria Aerospaziale e Astronautica*, 2007.
- [77] MicroSpace Srl, "The power of MicroSpace," [Online]. Available: <http://micro-space.org/classic/product.html>.
- [78] G. Manzoni, L. Y. Brama and A. Austin, "Laboratory characterization of a complete Cold Gas Micropropulsion system for Nanosatellite Attitude Control and Formation Flight," [Online].
- [79] J. Mueller, "'Desk Top Safe' Micropropulsion Systems Overview," *Jet Propulsion Laboratory California Institute of Technology*, 2011.
- [80] Vacco Industries Inc., "VACCO ChEMS Micro-Propulsion System - Micro-Propulsion System Overview," [Online]. Available: <http://www.vacco.com/vacco/pdfs/mips2112.pdf>.
- [81] Mars Space Ltd, "Mars Space Cubesat Micro-PPT for CubeSats," [Online]. Available: <http://mars-space.co.uk/MicroPPT.aspx>.
- [82] Clyde Space, "CubeSat Pulse Plasma Thruster datasheet," [Online]. Available: [http://www.clyde-space.com/cubesat\\_shop/propulsion/303\\_cubesat-pulse-plasma-thruster](http://www.clyde-space.com/cubesat_shop/propulsion/303_cubesat-pulse-plasma-thruster).
- [83] F. Guarducci, M. Coletti and S. B. Gabriel, "Design and Testing of a Micro Pulsed

Plasma Thruster for Cubesat Application," *32nd International Electric Propulsion Conference International Electric Propulsion Conference*, 2011.

- [84] P. V. Shaw, V. J. Lappas and C. I. Underwood, "Development and evaluation of an 8  $\mu$ PPT propulsion module for a 3U CubeSat application," vol. International Electric Propulsion Conference Design, 2011.
- [85] S. D'Amico and J.-S. Ardaens, "Spaceborne Autonomous Relative Control System for Dual Satellite Formations," *Journal of Guidance, Dynamic and Control*, 2009.
- [86] J. C. Springmann, J. W. Cutler and H. Bahcivan, "Magnetic Sensor Calibration and Residual Dipole Characterization for Application to Nanosatellites". *American Institute of Aeronautics and Astronautics*.
- [87] C. D. Brown, Elements of Spacecraft design, 2002.
- [88] Maryland Aerospace, Inc., "Products," [Online]. Available: [http://www.miniadacs.com/miniadacs\\_002.htm](http://www.miniadacs.com/miniadacs_002.htm).
- [89] "Begin your CubeSat Mission with the CubeSat Kit," Pumpkin, Inc., [Online]. Available: <http://www.cubesatkit.com>. [Accessed september 2011].
- [90] Sinclair Interplanetary Inc., "Standard Products," [Online]. Available: <http://www.sinclairinterplanetary.com/>.
- [91] "Packet Telemetry," [Online]. Available: <http://public.ccsds.org/publications/archive/102x0b5s.pdf>.
- [92] "NanoCom U480 Datasheet," [Online]. Available: <http://gomspace.com/documents/GS-ICD-U480-4.5.pdf>.
- [93] "AstroDev Helium Radios Datasheet," [Online]. Available: [http://www.astrodev.com/public\\_html/downloads/datasheet/Helium-Specification.pdf](http://www.astrodev.com/public_html/downloads/datasheet/Helium-Specification.pdf).
- [94] "Deployable UHF and VHF antennas," [Online]. Available: [http://www.isispace.nl/brochures/ISIS\\_AntS\\_Brochure\\_v.7.11.pdf](http://www.isispace.nl/brochures/ISIS_AntS_Brochure_v.7.11.pdf).
- [95] "Ground Station," [Online]. Available: [http://www.isispace.nl/brochures/ISIS\\_SmallSatGroundStations\\_Brochure\\_v.8.11.pdf](http://www.isispace.nl/brochures/ISIS_SmallSatGroundStations_Brochure_v.8.11.pdf).
- [96] "TABLES OF FREQUENCY ALLOCATIONS," [Online]. Available: <http://www.ntia.doc.gov/legacy/osmhome/alloctbl/allocmhz.html>.
- [97] [Online]. Available: <http://www.ecss.nl/>.
- [98] "CubeSat Standalone Battery," [Online]. Available: <http://www.clyde->

- space.com/cubesat\_shop/batteries/16\_cubesat-standalone-battery.
- [99] "The Technology Of Solar Cells," [Online]. Available: <http://cubesat.wikidot.com/the-technology-of-solar-cells>. [Accessed 28 3 2012].
- [100] Samtec Inc., "Signal integrity products, Tools and service," [Online]. Available: <http://www.samtec.com/>.
- [101] "CubeSat Structure," [Online]. Available: <http://strathseds.wikidot.com/cubesat-structure>.
- [102] "FR-4 glass/epoxy," [Online]. Available: [http://www.plasticsintl.com/sortable\\_materials.php?display=mechanical](http://www.plasticsintl.com/sortable_materials.php?display=mechanical).
- [103] UTIAS SFL , "CubeSat Compact Three-Axis Attitude Actuator and Sensor Pack with Sinclair Interplanetary," [Online]. Available: <http://www.utias-sfl.net/Products/SFL-SPC-ACS-SYS-3.3-flyer.pdf>.
- [104] J. G. Walker, "Satellite Constellations," *Journal of the British Interplanetary Society*, 1984.
- [105] M. M. Abid, *Spacecraft sensors*, Wiley, 2005.
- [106] P. Gurfil, *Modern Astrodynamics*, Elsevier Astrodynamics Series, 2006.
- [107] M. H. Kaplan, *Modern spacecraft dynamics and control*, Wiley, 1976.
- [108] M. Halsall and P. L. Palmer, "Modelling natural formations of LEO satellites," *Celestial Mech Dyn Astr*, 2007.
- [109] M. Sabatini, D. Izzo and G. B. Palmerini, "Minimum control for spacecraft formations in a J2 perturbed environment," *Celestial Mechanic Dyn Astr*, 2009.